

https://dspace.org/

Assessment criteria for determining the suitability of carbonate rock types for calcination in modern vertical (shaft) kilns in Southern Africa

Potgieter, E.M.

2019

https://hdl.handle.net/10539/29088

Potgieter, Erinus Marius (2019) Assessment criteria for determining the suitability of carbonate rock types for calcination in modern vertical (shaft) kilns in Southern Africa, University of the Witwatersrand, Johannesburg, <http://hdl.handle.net/10539/29088>

Downloaded from a DSpace repository. https://dspace.org/



Assessment criteria for determining the suitability of carbonate rock types for calcination in modern vertical (shaft) kilns in Southern Africa

By E.M. Potgieter



Assessment criteria for determining the suitability of carbonate rock types for calcination in modern vertical (shaft) kilns in Southern Africa

MSc (50/50) Research report

By

E.M. Potgieter (684976)

A dissertation submitted to the Faculty of Engineering and the Built Environment, University of the Witwatersrand, Johannesburg, in fulfillment of the requirements for the degree of Master of Science in Engineering

August 2019

DECLARATION

I declare that this Research Report is my own unaided work. It is being submitted for the Degree of Master of Science in Engineering (Chemical) to the University of the Witwatersrand, Johannesburg. This work has neither been submitted previously for the award of any degree, nor in meeting examination requirements, at any other University

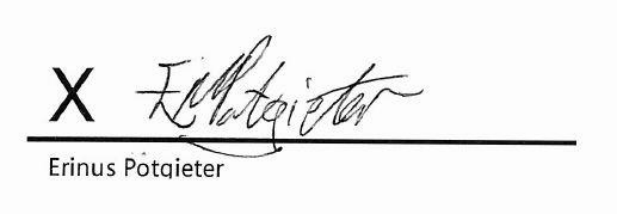

ABSTRACT

Lime kilns have been used through history, initially to produce a key building material, as demonstrated by construction in the days of the Roman empire. Since the time of the Industrial Revolution, the use of lime has developed widely into applications in chemical and metallurgical industries and environmental control.

The production of good quality lime requires a high purity raw material (limestone) and well–controlled kiln operation. Lime kilns developed as shaft or vertical kilns, with rotary kilns being implemented from the early 20th century to meet the increasing demand for production of high quality lime.

In recent times, new global lime kiln projects have seen the implementation of modern, high thermal efficiency vertical kilns in preference to rotary kilns due to lower heat consumption – which also contributes to a reduction in CO_2 emissions – together with their ability to produce lime of competitive quality. In southern Africa, where lime has been produced mainly in rotary kilns since the mid–1950s, the most recent large–scale kiln projects have seen the installation of modern vertical kilns.

Knowledge on the make-up and decomposition characteristics of the stone used for kiln feed is absolutely vital, considering that the quality of the stone directly impacts the quality of the lime product, while the behaviour of the stone under high–temperature calcination conditions can affect kiln operation.

With new kiln installations, there are indications in some cases that – in spite of the established empirical tests done by kiln suppliers – kiln operating problems attributed to the feed stone characteristics have occurred unexpectedly during the commissioning and early operating stages. This research project sets out

to establish a set of assessment criteria for limestone feedstocks in order to assess their suitability for use in shaft kilns.

A range of analytical, visual and thermal investigative methods was used to characterise limestone, including X–ray fluorescence spectrometry (XRF) to characterise the composition, X–ray diffractometry (XRD) to characterise the major phases, Raman spectroscopy to characterise the minor phases, single particle analysis to characterise impurities/phases, petrography to characterise the geological make-up, decrepitation tests and thermogravimetry to characterise the decomposition behaviour.

These techniques were applied to three limestones and one dolomite, all of high grade (purity), from three different geographic regions in southern Africa. Each carbonate rock had a unique chemical composition and geological origin. The complexity of each sample's unique chemical and physical features necessitated a thorough review of each rock's geological history. The review gave a better understanding of the phases and crystal structure in the stone that was formed during sedimentation.

This investigation found that the assessment criteria of limestone had to include physical *and* chemical characterisation methods with an emphasis on physical characterisation. The thermal methods and petrography were used to assess the physical characteristics such as crystal size and decomposition behaviour; while the chemical methods were used to assess the chemical characteristics such as chemical and phase composition. The two types of method were applied in a complementary approach. Thermal methods together with petrography were found to be the most adequate methods for assessing the suitability of stone for use in shaft kilns. Petrography offered information on how the hot gasses move through the crystal structure during calcination and the thermal methods showed how the decomposition was affected by that movement of hot gasses. However, analytical techniques were complementary

to the thermal techniques, offering explanations for observations in the thermal methods.

ACKNOWLEDGEMENTS

The author acknowledges with thanks the cooperation and contribution to this research project from:

- Manchester Metropolitan University (MMU):
  - Dr S Potgieter–Vermaak
  - Dr H Andrews (CCSEM)
  - Dr M Toubes Rodrigo (Single Particle Analysis)
  - Dr G Miller (XRD and hot stage XRD)
- University of the Witwatersrand: School of Geosciences
  Palaeontology
  - Dr C Penn–Clarke (Petrographic analysis)
  Earth lab
  - Mr Marlin Patchappa (XRF)
- University of the Witwatersrand: School of Chemical and Metallurgical Engineering – Chemical Engineering
  - Mrs Janet Smith (TG and technical assistance)
  - Mr Motlatsi Phali (Technical assistance)
  - Mr Rodney Gurney (Cutting of stone)
  - Mr Bennet Shirindza (Technical assistance)
  - Mr Ndivhuwo Nelwalani (SEM assistance)
- University of the Witwatersrand: School of Civil Engineering
  - Mr Edward Pretorius (Compressive strength test)

The author would like to thank the following suppliers of samples as well as all the staff of those companies who assisted in providing the sample:

- PPC Lime: Lime Acres
- PPC Lime: Mooiplaas quarry
- Handyman Lime: Quarry and lime plant

I would like to especially express my gratitude to my primary supervisor, Mr Jeremy Gaylard, for his invaluable help, guidance and input in this project.

TABLE OF CONTENTS

1 Introduction 1

1.1 Quicklime in the industry 1

1.2 Material properties and their effect on quicklime production 2

1.3 Production of quicklime in kilns 4

1.3.1 Rotary kilns 4

1.3.2 Shaft kilns 5

1.4 Project statement 8

1.4.1 Problem statement 8

1.4.2 Research question 9

1.4.3 Aim and objectives of the investigation 9

1.4.4 Hypothesis 11

2 Literature review 12

2.1 Feedstocks for lime production – carbonate rocks 12

2.1.1 South African geology background 12

2.1.2 Zambian geology background 12

2.2 Chemical and physical properties of limestone and dolomite 15

2.2.1 Characterization of carbonate rocks 15

2.2.2 Types of carbonate rock 15

2.2.3 Constituents in carbonate rock 17

2.3 Calcination of limestone 18

2.4 Calcination of dolomite 22

2.5 Impurities during calcination 26

3 Methodology 29

3.1 Limestone sample collection and preparation 29

3.2 Methods 30

3.2.1 X–ray Fluorescence (XRF) 31

3.2.2 Petrographic analysis (petrography) 31

3.2.3 Sample preparation – Crushing and Milling 32

3.2.4 X–ray Diffraction (XRD) 32

3.2.5 Raman Spectroscopy 33

3.2.6 Scanning Electron Microscopy (SEM) 33

3.2.6.1 Scanning Electron Microscopy energy dispersive X–ray spectrometry (SEM–EDX) 33

3.2.6.2 Computer–Controlled Scanning Electron Microscopy (CCSEM) 34

3.2.7 Decrepitation test 35

3.2.8 Thermogravimetry (TG) 36

4 Results and discussion 38

4.1 Chemical composition of Carbonate Rock (XRF results).....38

4.1.1 Dolomite (sample W) – Gauteng.....39

4.1.2 Limestone (Samples X and Y) – Northern Cape 40

4.1.3 Limestone (Sample Z) – Zambia.....40

4.2 Particle size distribution of milled carbonate rock samples.....41

4.2.1 Dolomite (Sample W).....42

4.2.2 Limestone (Samples X and Y): Northern Cape 44

4.2.3 Limestone (Sample Z): Zambia.....44

4.3 X–ray Diffraction (XRD) and Raman Spectroscopy.....45

4.3.1 Dolomite (Sample W) – Gauteng.....48

4.3.2 Limestone (Sample X) – Northern Cape.....53

4.3.3 Limestone (Sample Y) – Northern Cape.....58

4.3.4 Limestone (Sample Z) – Zambia.....61

4.4 Surface Characteristics.....63

4.4.1 Dolomite – Sample W (Gauteng).....64

4.4.2 Limestone – Sample X (Northern Cape).....65

4.4.3 Limestone – Sample Y (Northern Cape).....67

4.4.4 Limestone – Sample Z (Zambia).....69

4.5 Single particle analysis (SPA).....71

4.5.1 Kandler method 73

4.5.1.1 Dolomite – Sample W (Gauteng) Kandler interpretation 77

4.5.1.2 Limestone – Sample X (Northern Cape) Kandler interpretation 78

4.5.1.3 Limestone – Sample Y (Northern Cape) Kandler interpretation 80

4.5.1.4 Limestone – Sample Z (Zambia) Kandler interpretation 81

4.6 Petrographic analysis of carbonate stone samples 83

4.6.1 Dolomite – Sample W (Gauteng) 90

4.6.2 Limestone – Sample X (Northern Cape) 92

4.6.3 Limestone – Sample Y (Northern Cape) 94

4.6.4 Limestone – Sample Z (Zambia) 97

4.7 Decrepitation Characteristics of carbonate rock samples 100

4.7.1 Dolomite – Sample W (Gauteng) 102

4.7.2 Limestone – Samples X and Y (Northern Cape) 103

4.7.3 Limestone – Sample Z (Zambia) 105

4.8 Thermogravimetry of carbonate rock samples 107

4.8.1 Effect of different heating rates (Applied only to Sample W) 108

4.8.2 Decomposition at different CO_2 pressures 111

4.8.3 Sample W – Dolomite 112

4.8.3.1 p_{CO2} = 0 bar – Varying final temperature 112

4.8.3.2 p_{CO2} = 1 bar – Varying final temperature 117

4.8.3.3 Comparison of p_{CO2} = 0 bar vs p_{CO2} = 1 bar 119

4.8.3.4 Impurities 121

4.8.4 Limestone – Sample X (Northern Cape) 122

4.8.4.1 p_{CO2} = 0 bar – Varying final temperature 122

4.8.4.2 p_{CO2} = 1 bar – Varying final temperature 124

4.8.4.3 Comparison of p_{CO2} = 0 bar vs p_{CO2} = 1 bar 127

4.8.4.4 Impurities 128

4.8.5 Limestone – Sample Y (Northern Cape) 129

4.8.5.1 p_{CO2} = 0 bar – Varying final temperature 129

4.8.5.2 p_{CO2} = 1 bar – Varying final temperature 131

4.8.5.3 Comparison of p_{CO2} = 0 bar vs p_{CO2} = 1 bar 133

4.8.5.4 Impurities 134

4.8.6 Sample Z 134

4.8.6.1 p_{CO2} = 0 bar – Varying final temperature 134

4.8.6.2 p_{CO2} = 1 bar – Varying final temperature 137

4.8.6.3 Comparison of p_{CO2} = 0 bar vs p_{CO2} = 1 bar 143

4.8.6.4 Impurities 144

4.9 Comparison 146

4.9.1 At p_{CO2} = 0 bar 146

4.9.1.1 Onset temperature 146

4.9.1.2 Peak temperature 148

4.9.1.3 Decomposition rate 148

4.9.2 At p_{CO2} = 1 bar 149

4.9.2.1 Onset temperature 149

4.9.2.2 Peak temperature 150

4.9.2.3 Decomposition rate 151

5 Conclusions 152

5.1 Correlation between stone properties and its behaviour in thermal environments 152

5.2 Criteria for assessment of the suitability of carbonate rock types for calcination in modern vertical kilns 153

6 Recommendations and future work 154

7 Significance of this work 154

8 Presentations and publication 155

9 References 156

Appendices 164

LIST OF FIGURES

Figure 1.1: Market split for lime products in South Africa, 2004 (Agnello, 2005). 1

Figure 1.2: Temperatures of materials and gases in the different zones of a PFR lime shaft kiln (Piringer, 2017). 7

Figure 2.1: The three main carbonate minerals. 15

Figure 2.2: Equilibrium dissociation temperature of calcite as a function of the partial pressure of CO_2 (Eriksson, 2016). 20

Figure 2.3: Decomposition of the components of dolomite as a function of CO_2 partial pressure 24

Figure 2.4: Phase transitions of inorganic minerals under oxidizing circumstances (Schobert, 2013) 27

Figure 2.5: Carbonates decomposition temperatures as a function of p_{CO2} (Goldin and Kulikova, 1984) 28

Figure 3.1: Powdered sample preparation and analysis route…… 30

Figure 4.1: Particle size distribution of milled limestone and dolomite samples 42

Figure 4.2: Asymmetric carbonate deformation – v4 (Buzgar and Apopei, 2009) 47

Figure 4.3: Symmetric carbonate deformation – v_1 (Buzgar and Apopei, 2009) 48

Figure 4.4: XRD spectrum of carbonate rock W 48

Figure 4.5: Magnesite (purple) match for Raman scan of sample W 49

Figure 4.6: Dolomite (green) match for Raman scan of sample W 49

Figure 4.7: Raman scan of sample W (red) with an unidentified peak at ±370 µm 51

Figure 4.8: Raman scan of Pyrite between 300 cm^{-1} and 400 cm^{-1} (rruff.info) 51

Figure 4.9: Matching phases for the XRD spectra of sample X 53

Figure 4.10: Calcite (blue) match for Raman spectrum of sample X (red) 54

Figure 4.11: Fluoborite match (green) to Raman spectrum of sample X (red) 54

Figure 4.12: Thulite match (green) to the Raman spectrum of sample X (red) 55

Figure 4.13: Eucryptite match (green) to Raman spectrum of carbonate rock X (red) 56

Figure 4.14: Ferroan dolomite match for XRD spectrum of sample X 58

Figure 4.15: Matching phases for the XRD spectrum of sample Y 58

Figure 4.16: Calcite (green) and Fluoborite (blue) match for Raman spectrum of sample Y (red) 59

Figure 4.17: Thulite (purple) match for Raman spectrum of sample Y (red) ... 60

Figure 4.18: XRD spectrum of sample Z 61

Figure 4.19: SEM image of carbonate rock W at 1000x. magnification 64

Figure 4.20: SEM image of carbonate rock W at 4000x magnification. 65

Figure 4.21: SEM image of carbonate rock X at 1000x magnification 66

Figure 4.22: SEM image of carbonate rock X at 4000x magnification. 67

Figure 4.23: SEM image of carbonate rock Y at 1000x magnification. 68

Figure 4.24: SEM image of carbonate rock Y at 4000x magnification. 69

Figure 4.25: SEM image of carbonate rock Z at 1000x magnification 70

Figure 4.26: SEM image of carbonate rock Z at 4000x magnification 70

Figure 4.27: SPA of samples W, X and Y showing percentages of the main elements. 71

Figure 4.28: Kandler interpretation of the SPA results. 74

Figure 4.29: Volumetric mineral composition of each class for aerosols studied by Kandler et al. (2007) 75

Figure 4.30: Formulas of minerals identified by Kandler et al. (2007). 76

Figure 4.31: Graphic (A) and textural (B) classification schemes for carbonate rocks in thin section (Folk, 1962 in Scholle and Ulmer–Scholle, 2003). 85

Figure 4.32: Primary (fabric–selective) (A) and Secondary (non–fabric–selective) (B) porosity types in carbonate rocks (Choquette and Pray, 1970 in Scholle and Ulmer–Scholle (2003). 88

Figure 4.33: Stone classification of carbonate rocks according to depositional texture (Dunham,1962). 89

Figure 4.34: Phase diagram of different forms in which calcite can occur in limestones (Folk, 1959) 89

Figure 4.35: Petrographic features associated with sample W. 91

Figure 4.36: Classification of carbonate clasts. S = Sedimentary clasts. (Note: Conglomerates can be either clast–supported or matrix–supported.) 93

Figure 4.37: Micropetrographic images of carbonate rock X. 95

Figure 4.38: Micropetrographic images of carbonate rock Y. 96

Figure 4.39: Petrographic features associated with sample Z. 99

Figure 4.40: Sample X before (left) and after calcination (right) at 1050 °C for 1 hour. 104

Figure 4.41: Sample Z before (left) and after calcination (right) at 1050 °C for 1 hour. 106

Figure 4.42: Decomposition of carbonate rock W at 5, 10 and 15 °C under a Nitrogen atmosphere. 108

Figure 4.43: Percentage mass as a function of temperature for sample W decomposition – p_{CO2} = 0 bar. 112

Figure 4.44: Derivative mass as a function of temperature for sample W decomposition – p_{CO2} = 0 bar 112

Figure 4.45: Hot stage XRD of sample W under an air atmosphere up to 1150 °C 116

Figure 4.46: Percentage mass as a function of temperature for sample W decomposition – p_{CO2} = 1 bar 118

Figure 4.47: Derivative mass as a function of temperature for sample W decomposition – p_{CO2} = 1 bar 118

Figure 4.48: Sample W decomposition – 0 bar vs 1 bar p_{CO2} 120

Figure 4.49: Percentage mass as a function of temperature for sample X decomposition – pCO2 = 0 bar …… 122

Figure 4.50: Derivative mass as a function of temperature for sample X decomposition – pCO2 = 0 bar 123

Figure 4.51: Percentage mass as a function of temperature for sample X decomposition – pCO2 = 1 bar 122

Figure 4.52: Derivative mass as a function of temperature for sample X decomposition – pCO2 = 1 bar 123

Figure 4.53: Sample X decomposition – 0 bar vs 1 bar pCO2.....125

Figure 4.54: Percentage mass as a function of temperature for sample Y decomposition – pCO2 = 0 bar. 129

Figure 4.55: Derivative mass as a function of temperature for sample Y decomposition – pCO2 = 0 bar. 130

Figure 4.56: Percentage mass as a function of temperature for sample Y decomposition – pCO2 = 1 bar 129

Figure 4.57: Derivative mass as a function of temperature for sample Y decomposition – pCO2 = 0 bar 130

Figure 4.58: Sample Y decomposition – 0 bar vs 1 bar pCO2.....133

Figure 4.59: Percentage mass as a function of temperature for sample Z decomposition – pCO2 = 0 bar. 135

Figure 4.60: Derivative mass as a function of temperature for sample Z decomposition – pCO2 = 0 bar. 136

Figure 4.61: Decomposition of sample Z at different CO2 pressures 137

Figure 4.62: Percentage mass as a function of temperature for sample Z decomposition – pCO2 = 1 bar. 139

Figure 4.63: Derivative mass as a function of temperature for sample Z decomposition – pCO2 = 0 bar. 139

Figure 4.64: Sample Z decomposition – 0 bar vs 1 bar pCO2.....143

Figure 4.65: Decomposition temperatures of inorganic phases that might occur in limestone (Milodowski et al., 1989). 144

Figure 4.66: DTG curves of sample Z at pCO2 = 0 bar showing impurity peaks. 145

Figure 4.67: Decomposition of samples W, X, Y and Z at pCO2 = 0 bar up to 1000 °C. 147

Figure 4.68: Decomposition of samples W, X, Y and Z at pCO2 = 1 bar up to 1000 °C 149

LIST OF TABLES

Table 1.1: Physical and chemical properties of carbonate stone affecting kiln performance (Piringer, 2017). 3

Table 2.1: Location of the Kakontwe limestone formation. 12

Table 2.2: Composition of Kakontwe limestone (Mitchell, 2000). 14

Table 2.3: Grading of high–calcium limestones (Eriksson, 2016). 16

Table 2.4: Dissociation time of calcite as a function of temperature and particle size diameter (Oates, 2008). 19

Table 3.1: Nomenclature of samples and their sources. 29

Table 3.2: Summary of TG variables of each sample. 37

Table 4.1: Chemical analysis – carbonate rock samples (normalised). 38

Table 4.2: Impurities reported as pure elements and not as oxides. 39

Table 4.3: Carbonate content and milled characteristics of limestone and dolomite. 42

Table 4.4: Identified phases from XRD and Raman analysis for samples W, X, Y and Z 46

Table 4.5: The different phases in which $CaCO_3$ occurs in sample W 50

Table 4.6: Sample W (dolomite – Gauteng) wavenumbers 52

Table 4.7: Shifting of wavenumbers between limestone and dolomite 52

Table 4.8: Sample X and Y (limestone –Northern Cape) wavenumbers 60

Table 4.9: Relation of Kakontwe limestone formation 62

Table 4.10: Minerals associated with classification classes (Kandler et al., 2007). 74

Table 4.11: Petrographic features of carbonate stone samples.....84

Table 4.12: Classification of decrepitation performance of a carbonate rock (Vola and Sarandrea, 2013). 100

Table 4.13: Percent decrepitation in each stone sample after heating at 1050 °C for 1h 101

Table 4.14: Petrographic features of the carbonate rocks compared to decrepitation. 102

Table 4.15: Decomposition of sample W up to 1000 °C at different heating rates. 109

Table 4.16: Key characteristics of decomposition of sample W in 1 bar nitrogen atmosphere at different heating rates 110

Table 4.17: Key characteristics of decomposition of sample W in 1 bar nitrogen atmosphere at different heating rates 111

Table 4.18: Calculated theoretical mass loss vs measured mass loss over peak 1.....114

Table 4.19: Calculated theoretical mass loss vs measured mass loss over peak 2.....114

Table 4.20: Characteristics of sample W's decomposition at pCO2 = 0 bar .116

Table 4.21: Characteristics of sample W's decomposition at p_{CO2} = 1 bar ...119

Table 4.22: Characteristics of sample X's decomposition at p_{CO2} = 0 bar. ...124

Table 4.23: Characteristics of sample X's decomposition at p_{CO2} = 1 bar 126

Table 4.24: Characteristics of sample Y's decomposition at p_{CO2} = 0 bar. ...130

Table 4.25: Characteristics of sample Y's decomposition at p_{CO2} = 1 bar 132

Table 4.26: Characteristics of sample Z's decomposition at p_{CO2} = 0 bar.....136

Table 4.27: Characteristics of sample Z's decomposition at pCO2 = 1 bar. .143

LIST OF UNITS

bar = Barometric pressure

°C = Degrees Celsius

h = hour

MPa = mega pascal

kJ = kilojoule

kg = kilogram

kg/m^3 = kilogram per cubic meter

kPa = kilopascal

kV = kilovolt

min = Minute

mg = milligram

mL = millilitre

µL = microlitre

mm = millimetre

rpm = revolutions per minute

NOMENCLATURE AND DEFINITIONS

Al = Aluminium

Al_2O_3 = Alumina

Available lime = The actual amount of CaO in lime that is available to react.

$CaCO_3$ = Calcium carbonate

CaO = Calcium oxide (Quicklime)

CO_2 = Carbon dioxide

Dolomite = An anhydrous carbonate mineral composed of calcium magnesium carbonate, ideally $CaMg(CO_3)_2$.

DTG = Differential Thermogravimetry

Euhedral and subhedral crystal = Euhedral crystals are those that are well–formed with sharp, easily recognised faces. The opposite is anhedral: A rock with an anhedral texture is composed of mineral grains that have no well–formed crystal faces or cross–section shape in thin section. An intermediate texture with some crystal face formation is termed subhedral.

Fe = Iron

Fe_2O_3 = Iron oxide

$FeCO_3$ = Iron carbonate (Siderite)

Lime/Quicklime = CaO. A product produced from the calcination of $CaCO_3$.

Limestone = Limestone is a sedimentary rock composed primarily of calcium carbonate ($CaCO_3$) in the form of the mineral calcite.

$MgCO_3$ = Magnesium carbonate

MgO = Magnesium oxide

Mn = Manganese

Mn_2O_3 = Manganese oxide

N_2 = Nitrogen

O_2 = Oxygen

rpm = revolutions per minute

p_{CO2} = partial pressure of CO_2 gas

PFR: Parallel–flow regenerative

Pyrite = F_2S

Reactive lime = Lime with a high amount of available reaction sites that enables the lime to hydrate quickly.

SEM = Scanning electron microscopy

SEM–EDX = Scanning Electron Microscopy coupled with Electron dispersive X–ray spectroscopy

S = Sulphur

Si = Silicon

SiO_2 = Silica

SPA =Single Particle analysis

TG = Thermogravimetry

wt. = Mass

XRD = X–ray Diffraction

XRF = X–ray Fluorescence

T_f = Final temperature

1 Introduction

1.1 Quicklime in the industry

Quicklime is produced by the thermal decomposition of calcium–carbonate–containing minerals. The most efficient production process is by calcining limestone and dolomite in state–of–the–art shaft kilns. With the production of quicklime it is important that a product of consistent, high quality is produced. This depends to a great degree on the type of carbonate rock used in the kiln. Eighty–eight percent of the 350 million tons of quicklime produced globally each year is required to be of a high degree of calcination (> 80%) (Piringer, 2017).

Lime is primarily used in the steel industry (179 million tons p.a.), the building industry (46 million tons p.a.), the chemical industry (25 million tons p.a.), and for environmental protection through the absorption of SO_x gases (28 million tons p.a.) (Piringer, 2017). In South Africa alone, 1.39 million tons of lime were produced in 2004, with an average value of R325 per ton. The wide variety of uses of quicklime products in South Africa is shown in Figure 1.1.

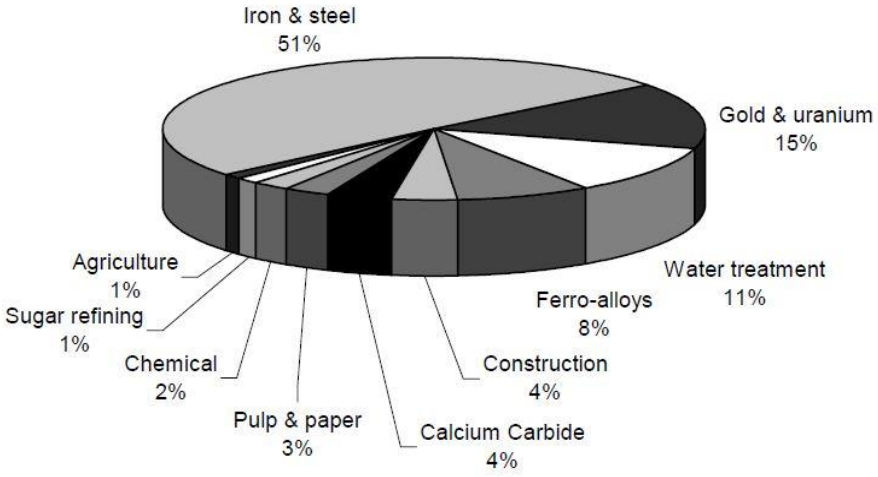

Notes: Excludes by-products & lime generation by paper manufacturers, totalling 363 kt
Excludes all imported material (100 kt, of which 50 kt is used in paper manufacture)
Total lime sales for 2004 amounted to 1,36 Mt
Excludes dolime consumption of 275 kt
Source: Personal communication with mines

Figure 1.1: Market split for lime products in South Africa, 2004 (Agnello, 2005).

1.2 Material properties and their effect on quicklime production

The carbonate rocks used in quicklime–producing kilns have different chemical and physical properties around the world depending on when and how the deposits were formed. The characteristics of the rock can influence the working of a kiln significantly (Piringer, 2017; Vola et al., 2018). Lime shaft kilns are normally designed with a quality limestone (limestone that has a high $CaCO_3$ content and a high mechanical stability) in mind. The lime kiln design is adjusted depending on the results of empirical tests and careful analyses of the quality of the limestone (Piringer, 2017; Vola and Sarandrea, 2013). These analyses cover the stone's physical and chemical properties which will have a significant impact on the burning process and product quality (Vola et al., 2017).

The importance of the characteristics of raw limestone was reiterated by Bresciani *et al*. (2016) with the concluding statement "In today's lime industry, it is no longer sufficient to optimise existing equipment and outdated technology. Companies need solutions that enable the correlation of a multitude of 'data' from different specialities such as geology, mineralogy, crystal chemistry, physics, mathematics, mechanical and valuable experience and insights in an unique environment and share these with professionals of different disciplines."

Table 1.1 shows these qualities, and how they affect the burning process and the product quality (Piringer, 2017). The type of analysis which can evaluate each property is also set out in the table. Piringer (2017) reported that "In order to facilitate the design and the customising of lime shaft kilns and in order to better understand phenomena like surface sintering, further research work is still required as there is still an unanswered key question: "What material properties cause surface sintering?" Surface sintering is the hard burning of a lime surface.

Table 1.1: Physical and chemical properties of carbonate stone affecting kiln performance (Piringer, 2017).

Variable material properties	**Suitable range**	**Influence to the burning process and to the product quality**	**Test allocated to evaluate property**
Carbonate content	> 95 %	product quality, heat consumption, sintering potential	XRF/TGA/XRD
SiO_2 content	< 5 %	product quality, heat consumption	XRF/TGA/XRD
SiO_2 distribution	heterogeneous homogenous	formation of calcium silicate phases, reduction of free CaO	Petrography/XRD
Iron and Manganese content		colour of product	XRF/XRD
Sulphur content	< 0.05 %	product quality	XRF
Organic matter	traces	emissions to air	TGA
Surface contamination	< 1 %	dust, liquid phase sintering depending on the chemical composition	XRF
Enclosed water	unknown	bursting, void space, pressure drop, heat transfer	TGA
Volatile water	0 - 15 %	heat consumption, pressure drop	-
Crystal structure and texture		crumbling, sintering potential	SEM/Petrography
Compression strength	20 - 250 MPa	breakage, void space, pressure drop, heat transfer	Compression strenght test
Thermal expansion	< 3.5 %	bulk movement in the kiln shafts	Decrepitation test/TGA
Porosity of single pieces	0 - 25 %	water absorption, calcination process	BET
Grain size	15 - 150 mm	pressure drop and heat transfer	-
Grain shape	crushed		-
Bulk density of the kiln charge	1.2 - 1.7 kg/m^3	void space, pressure drop, heat transfer	-
Apparent density of the single pieces	2 - 2.8 kg/m^3		-

1.3 Production of quicklime in kilns

Two main kiln types are used to produce lime globally. They are rotary kilns and shaft or vertical kilns (Oates, 2008). Each type has its own advantages and disadvantages. Shaft kilns have, however, been used more widely in recent years because of their ability to produce highly calcined quicklime coupled with economic heat usage. The type of kiln used depends mainly for which industry the quicklime is produced.

1.3.1 Rotary kilns

The traditional rotary kiln is 110 – 140 m long and inclined at 3 – 4°. These kilns rotate slowly with a variable speed drive in order to ensure effective calcination of the feed stone during its passage through the kiln. Rotary kilns typically operate with 0 – 60 mm feed stone and have an output range of roughly 150 – 1500 tons/day (Oates, 2008). Long rotary kilns have a high heat consumption with an average net heat usage of 6480 – 7525 kJ/kg (Oates, 2008). These kilns use metal dividers, lifters, internal refractory dams and oxygen enrichment of the flame in order to reduce the net heat usage (Oates, 2008). The flame length is a crucial variable. If the flame is too long, it does not transfer heat effectively to the limestone in the calcining zone. If the flame is too short, it may give rise to excessive temperatures.

Pre–heater rotary kilns developed from the traditional long rotary kiln and are significantly shorter, with kiln lengths in the range of 40 – 60 m. The significantly lower heat consumption (below 5225 kJ/kg) is the main appeal of this kiln. The lower heat consumption is achieved through reduced radiation heat loss and improved heat recovery by passing exhaust gases from the kiln through a pre–heater (Oates, 2008) where heat in the exhaust gas stream is transferred to the kiln stone feed.

Rotary kilns are characterised by limestone being fed from one end and the calcining heat flowing in the opposite direction. Rotary kilns have the advantage over shaft kilns in that they are able to produce a wider range of reactivity and lower residual CO_2 levels. Some other advantages of rotary kilns are that they can accept moisture in the feed stone and lower–grade limestone feeds. Rotary kilns are most commonly used to produce lime for the iron and steel industries because of the kilns' easy controllability, ability to calcine to varying degrees, and the various fuel options (Oates, 2008). About two thousand rotary kilns are used to supply the global iron and steel industry (Piringer, 2017).

1.3.2 Shaft kilns

A widely used shaft or vertical kiln in the lime industry is the parallel–flow regenerative (PFR) shaft kiln. The PFR shaft kiln technology was developed in Wopfing, Austria in the early 1960s in a lime factory (Piringer, 2017). Maerz Ofenbau AG in Zurich developed the process further after obtaining the patent in 1965. PFR shaft kilns are perfectly suited for producing soft burnt, highly reactive lime owing to the conditions of the parallel flow of the kiln charge and the combustion gases being used for pre–heating.

Considering that the heat consumption of kilns makes up 20 – 50 % of the production costs of quicklime, it is easy to see why PFR kilns (with 87 % heat efficiency compared to 65 – 70 % for pre–heater rotary kilns (Oates, 2008)) have attracted a lot of attention worldwide (Piringer, 2017). The wide size range of limestone charge that the PFR shaft kiln can handle (15 – 150 mm) makes it an ideal candidate for different types of lime production (Oates, 2008).

The heat of dissociation of $CaCO_3$ relative to 25 °C is 3179.84 kJ/kg CaO. The volume of standard PFR shaft kilns is designed to calcine the limestone at an average temperature of 950 – 1050 °C (Piringer, 2017). Based on these limits, the average retention time in the burning zone of the kiln is 8 hours. It is

therefore critical that the kiln charge which is used can be calcined at these conditions and in the specified retention time. PFR kilns typically produce 200 – 400 tons/day, but some kilns in operation can produce up to 800 tons/day. The very low energy consumption in conjunction with relatively high production rates is the main reason why PFR kilns are being favoured instead of rotary kilns.

The PFR kiln is made up of two large inter–connected shafts. Rectangular and cylindrical shafts are both used, with the cylindrical design being more common. The shafts are completely filled with the limestone to be calcined (Oates, 2008), with air and combustion gases flowing through the void space.

In Figure 1.2 (Piringer, 2017), illustrating a PFR kiln arrangement and operation, the left hand shaft (Shaft 1) is the calcining shaft (or burning shaft) during that cycle, where the fuel is fed. The second shaft (Shaft 2) acts as a regenerative shaft, preheating the stone using the combustion gas stream from shaft 1. The lime product is discharged continuously at the bottom of each shaft. The kiln charge moves down the lime kiln at about one metre per hour (Piringer, 2017).

The kiln acts cyclically, going through roughly 90 – 130 cycles per day (Piringer, 2017), with the gas flow being reversed and firing alternating between shafts 1 and 2 with each cycle. During each cycle, fuel is fed to the burning shaft (Shaft 1) through burner lances which are installed vertically in the material bed of the preheating zone. The calcination process absorbs most of the heat at the top of the burning zone, where the fuel is fed. The fuel self–ignites, using the pre–heated combustion air in parallel flow through the material bed (Piringer, 2017). A metered quantity of stone is fed during the reversing time at the end of each cycle.

The average temperature in the burning zone is 950 °C, which is about 150 °C more than the theoretical calcination temperature. The higher temperature

provides an (economic) driving force for calcination. At theoretical temperature, calcination in a kiln on a commercial scale would take much longer. In Figure 1.2, it can be seen that the peak burning zone temperature is close to 1200°C.

Also that the calcination time reduces for each stone size as test conditions approach 1200°C (Oates, 2008). “The burning phase is characterized by the parallel flow of combustion gases and material in Shaft 1 (the burning shaft). The regenerative phase is characterized by the counter flow of hot gases and material in Shaft 2 (the non–burning shaft)” (Piringer, 2017). In Figure 1.2, the combustion gases flow through the cross channel from Shaft 1 to Shaft 2 where they transfer heat exceptionally well to the kiln charge. As in rotary kilns, the kiln flame and fuel burnout are crucial for control for different calcination products.

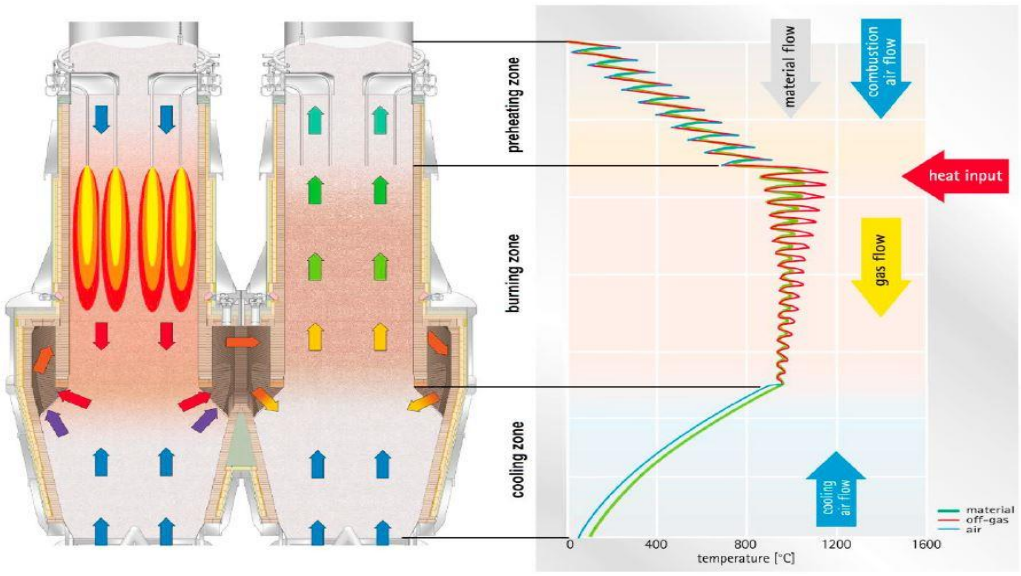

Figure 1.2: Temperatures of materials and gases in the different zones of a PFR lime shaft kiln (Piringer, 2017).

An advantage of these shaft kilns is their ability to produce soft burnt, highly reactive lime perfectly. Using off–gases from the burning shaft for pre–heating purposes, gives PFR shaft kilns the lowest heat consumption of all modern

kilns. Disadvantages of lime shaft kilns are that they cannot process small grain sizes (< 10 mm), and also cannot produce low–sulphur lime when high–sulphur fuels are used. Roughly 600 PFR shaft kilns are in operation globally (Piringer, 2017). Although there are not as many as rotary kilns (2000 used globally), the implementation of lime shaft kilns has increased substantially over the past few years (Piringer, 2017).

1.4 Project statement

1.4.1 Problem statement

During the past decade, attention has increasingly been paid to modern shaft kilns for the production of lime in South Africa. Currently most of South Africa's lime is still produced in rotary kilns situated in the Northern Cape but, in line with global trends, shaft kilns are becoming the more favoured kiln type, primarily because of their low energy consumption. Other factors enabling lime shaft kilns to compete with rotary kilns are significant outputs (up to 800 tons per day (Oates, 2008)), the high quality of lime produced, and flexibility in kiln fuel selection.

Prior to the implementation of a new kiln project, lime kiln equipment suppliers normally conduct empirical tests on samples of the stone type to be used during operation of the kiln, in order to determine whether the stone type is suitable for a shaft kiln. The results of these tests are generally not public knowledge. A standard test that is conducted is the measurement of decrepitation. During this decrepitation test, the structural stability of the stone is evaluated over a specified heating range.

When assessing the suitability of a stone, it is of the utmost importance to investigate whether the structural integrity of the stone allows the kiln gases to reach all voids in the stone, and heat the stone uniformly. It does sometimes

happen that lime shaft kilns do not achieve the rated output or quality of product during the initial period of operation, as a result of operating problems. It is possible that some of these problems arise from unexpected behaviour of the feed stone.

In Southern Africa (Northern Cape and Zambia), two lime plants where PFR (refer to Background for information on PFR kilns) kilns have recently been installed have experienced unexpected problems during kiln operation. Based on the standard tests conducted by the kiln suppliers, these problems were apparently not anticipated during the project design and implementation stages. The cause of these problems is thus unclear and is suspected to arise from the properties of the stone.

Extensive research on the stone or carbonate rock types occurring in Southern Africa, and considered for use in shaft kiln operation, has not yet been done.

This investigation will attempt to establish criteria for assessment of the suitability of limestone and dolomite samples for calcination in modern shaft kilns.

1.4.2 Research question

What are the key physical and chemical properties of the limestone used in lime shaft kilns and how can these properties be used in assessing the suitability of a stone source for kiln operation?

1.4.3 Aim and objectives of the investigation

Aim:

The aim of this project was to characterise limestone from South Africa as well as Zambia by using a range of chemical and physical analyses for assessment of suitability for calcination, and subject to agreement with two operating lime plants, to relate the results to the reported kiln operating performance in respect of each stone type.

A further aim was to recommend, if possible, a test procedure for reliably assessing the suitability of a stone type for calcination in a shaft kiln.

In order to meet this aim the following objectives were defined:

Objectives:

a) Determine the properties that are used to characterise a type of limestone.

b) Decide what range of analysis methods is applicable to assess stone properties.

c) Obtain a complete chemical analysis of each stone type.

d) Determine microstructure and pore features of each stone by use of petrographic analysis.

e) Determine the phases present in each stone using X–ray diffraction, Raman Spectroscopy and Single Particle Analysis.

f) Determine the microscopic structure of each powdered limestone sample.

g) Determine the decomposition characteristics and behaviour of each stone with Thermogravimetry.

h) Determine the decrepitation value of each stone; where the decrepitation value refers to the fractional loss of mass of a defined size fraction.

i) Propose assessment criteria of limestone to be used in shaft kilns.

1.4.4 Hypothesis

A better understanding of the physical and chemical characteristics of feed carbonate rock types, can be used to predict its behaviour in the operating environment of lime shaft kilns.

2 Literature review

2.1 Feedstocks for lime production – carbonate rocks

2.1.1 South African geology background

The largest South African limestone deposit is the Campbell Rand subgroup deposit (part of the larger Transvaal supergroup) which is located in the Northern Cape province of South Africa (Agnello, 2005). The specific formation is the Ghaap formation. This is a primary limestone deposit where medium and high purity limestone occurs. The limestone occurs in a relatively narrow 150 km long belt (Agnello, 2005). Several limestone quarries are situated in close proximity to the Kimberley–Postmasburg railway line. A map of the quarry locations can be seen in Appendix B. The dolomitic limestone deposit in the Gauteng province belongs to the Malmani subgroup deposit. Aggregates for the construction industry are mined there.

2.1.2 Zambian geology background

Table 2.1: Location of the Kakontwe limestone formation.

Nguba group	Muombe subgroup	Kipushi formation
		Kakontwe formation
		Kaponda formation
		Grand conglomerate (Mwale) formation

The larger limestone deposits in Zambia occur in the north and the east of Zambia. Handyman Lime is located only ±10 km east of Ndola Lime which is located in the north of the country, 260 km north of Lusaka, in the copperbelt province (See Appendix B). The limestone occurring in the Ndola region is

known as Kakontwe Limestone. The Kakontwe formation is part of the Muobe subgroup which is part of the Nguba group (formerly lower Kundelungu group) which is part of the Katangan supergroup (Batumike Mwandulo et al., 2007). This formation is summarised in Table 2.1.

The diagenesis is described by Mills (2000) as: “The carbonaceous, pyritic, massive limestone indicates deposition in a reducing environment and its texture suggests deposition as a lime mud. The origin of the organic matter is probably algae and (Binda and Van Eden, 1972) states that the black carbonates contain an abundance of micro–fossils: it is speculated that the pyrite has replaced the algae. A shelf margin is considered to be a possible origin for the limestone with a deposition of algal mud in an environment shallow enough to be slightly affected by wave motion.”

“Limestone and dolomite breccias occur commonly and the large size of the clasts suggest the source to be near, with the limestone breccias grading into micrites, suggesting deposition by turbides. The calcareous shales are rich in organic matter and pyrite and show no internal structure apart from layering. The origin is probably a low energy reducing environment such as deep water and the source is probably wind–blown material.”

Regional geology: (Mills, 2000)

“The top of the Great Conglomerate was deposited in glacio–marine, followed by a brief regression, marking the base of the Kakontwe Limestone. A marine transgression followed, allowing deposition of limestone in shallow water as a shelf deposit, possibly with localized development of reefs. As the water deepened, the lime mud was deposited from pelagic algae and occasional storms produced ripple pavements. Deposition was interrupted by occasional turbidite flows or series of flows. The turbidite flows thinned and the amount of lime mud deposition decreased as the water depth continued to increase. At the

top of the deposit sequence, the sea reached a depth where pelagic sediment dominated over material brought in. Finally the sea level fell with the deposition of limestone resuming. Dolomitisation of the limestone at the base of the Kakontwe Limestone was diagenetic."

The limestone occurring on the east side of the deposit is of low quality, resulting in a higher degree of decrepitation at high temperatures (Mitchell, 2002).

Limited information is available for Handyman Lime but sufficient information is available for Ndola Lime. At Ndola Lime, "the calcitic limestone is divided into ten zones, L1 to L10, of which mainly L1 and L3 are worked (although a small proportion of the other lithologies can be tolerated). L1 is a hard, massive fine–grained grey limestone (80 to 80% $CaCO_3$) with a consistent quality. L3 is a semi–hard medium–grained, light grey limestone (with greater than 90% $CaCO_3$). The dolomitic limestone that bounds the calcitic limestone is white, thinly bedded and contains less than 3.5% MgO (equivalent to 15% dolomite mineral)" (Mitchell, 2002). 35 – 70 mm stone is used in the shaft kiln at Ndola Lime (Mitchell, 2002). The composition of the Kakontwe Limestone has been reported by Mitchell (2000) to be as set out in Table 2.2.

Table 2.2: Composition of Kakontwe limestone (Mitchell, 2000).

Product	**CaO** Wt %	**MgO** Wt %	**SiO_2** Wt %	**Fe_2O_3** Wt %
Ndola lime	53.3	0.5	1.2	0.3

2.2 Chemical and physical properties of limestone and dolomite

2.2.1 Characterization of carbonate rocks

The chemical and physical characteristics of a carbonate rock are often evaluated before use in a shaft kiln. The properties affecting the operation of a kiln are set out in section 1.2 above. In agreement with that, Agnello (2005) stated that the key geological and processing prerequisites of a limestone that must be taken into consideration when producing quicklime are:

- $CaCO_3$ and $MgCO_3$ content
- lack of impurities (trace elements and heavy metals)
- resistance to thermal degradation (decrepitation)
- strength and abrasion resistance
- rate of calcination

2.2.2 Types of carbonate rock

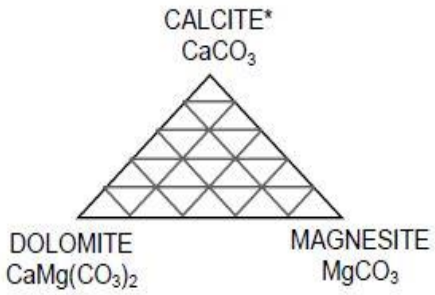

Note: * Aragonite is a less abundant crystalline (orthorhombic) form of calcium carbonate. It slowly recrystallises to calcite (hexagonal structure) in the presence of water.

Figure 2.1: The three main carbonate minerals.

Carbonate minerals can be divided into three primary groups: Calcite ($CaCO_3$), Magnesite ($MgCO_3$) and Dolomite [$CaMg(CO_3)_2$] – Figure 2.1. Calcite and dolomite are the two minerals which are dominantly found in sediments. Calcite (high–calcium limestone) and dolomite (high–magnesium limestone) are differentiated by their magnesium content. Calcium limestone (calcite) is further classified into the varying purities of limestone – see Table 2.3. Calcite and dolomite are categorised as "Anhydrous Carbonates" (Agnello, 2005).

Table 2.3: Grading of high-calcium limestones (Eriksson, 2016).

Weight %	Very high purity	High purity	Medium purity	Low purity	Impure
$CaCO_3$	>98.5	97 - 98.5	93.5 - 97	85 - 93.5	<85
CaO	>55.2	54.3 - 55.2	52.4 - 54.3	47.6 - 52.4	<47.6
MgO	<0.8	0.8 - 1.0	1.0 - 3.0	>3	>3
SiO_2	<0.2	0.2 - 0.6	0.6 - 1.0	<2	>2
Fe_2O_3	<0.05	0.05 - 0.1	0.1 - 1.0	>1.0	>1.0

Depending on its purity, or Iron and Magnesium content, Calcite is found as pure Calcite, Ferro–Calcite and Magnesium Calcite. Similarly, according to the iron content, dolomite may also be regarded as pure Dolomite or Ferrous Dolomite. Other carbonate group minerals are ankerite [$CaFe(CO_3)_2$], siderite ($FeCO_3$), Smithsonite ($ZnCO_3$), Rhodochrosite ($MnCO_3$) and Spherocobaltite ($CoCO_3$).

Despite limestone being synonymous with $CaCO_3$, magnesium often occurs in natural limestone, leading to different qualifications or grades of limestone. A limestone is classified as a Magnesian limestone when it contains 5 – 35 % magnesium. If the limestone contains less than 5 % magnesium, it is classified as a high–calcium limestone (Dollimore et al., 1994).

Different types of limestone have different crystal phase structures and therefore also different characteristics. In nature, anhydrous calcium carbonate occurs in three crystal phases, namely calcite, aragonite and vaterite.

Calcite itself has five structures – calcite I – V (Eriksson, 2016). At ambient temperature and pressure, the calcite crystal phase (I), is the most stable phase (Kontoyannis and Vagenas, 2000). Calcite's crystal structure is rhombohedral whereas aragonite's crystal structure is orthorhombic. Calcite includes common limestone, chalk and marble (Agnello, 2005). Chert or flint nodules are common in limestone layers and crystals of calcite ,dolomite, quartz or barite may line small cavities in the rock (Agnello, 2005).Although aragonite can be found in natural limestone, the limestone of industrial interest consists mainly of calcite (Eriksson, 2016).

The three phases of dolomitic limestone that exist are: dolomite – $CaMg(CO_3)_2$, kutnohorite – $CaMn(CO_3)_2$, and ankerite – $CaFe(CO_3)_2$ (Dollimore et al., 1994).

2.2.3 Constituents in carbonate rock

Typical minor components (<5%) that occur in limestone and dolomite are oxides of Al, Ba, Cr, Cu, K, Mn, Na, Ni, P, Pb, S, Si, Sr, Ti, Zn and Zr (Eriksson, 2016). Manganese oxides in particular occur commonly in limestone deposits of the Northern Cape in South Africa (Beukes, 1987). Different constituents affect the stone properties in different ways. Hogewoning *et al*. (2008) found that an increase in MgO and K_2O resulted in lower sintering potential in limestones because of a boundary layer forming on the CaO crystallites that inhibits sintering.

2.3 Calcination of limestone

As mentioned before, carbonate rock ($CaCO_3$) undergoes calcination in a kiln under high temperatures according to the reaction (Boynton, 1980):

$$CaCO_3 + heat \rightleftarrows CaO + CO_2 \quad (1)$$

Oates (2008) calculated the heat of dissociation of calcite to be 760 kcal/ kg at 900 °C relative to 25 °C.

Calcite, the main occurring phase in high purity limestone, has five crystal structures as mentioned in previously. $CaCO_3$ is expected to occur as calcite I up to 800 °C, and as calcite IV above 800 °C (Eriksson, 2016).

From 800 °C, $CaCO_3$ dissociates into CaO and CO_2 (Oates, 2008). The factors affecting the rate of dissociation are:

a. the characteristics (chemical and physical) of the limestone

b. the particle size distribution

c. the shape of the particles

d. the temperature profile in the calcining zone

e. the rate of heat exchange between the gases and the particles

This dissociation can be described by a shrinking core model (Oates, 2008):

a) Heat is transferred from the kiln gases to the surface of the decomposing particle.

b) Heat is then conducted from the surface to the reaction interface through the micro–porous layer of lime.

c) Heat arriving at the reaction interface causes the dissociation of $CaCO_3$ into CaO and CO_2.

d) The CO_2 produced migrates from the reaction interface, through the lime layer, to the surface of the particle.

e) CO_2 migrates away from the surface into the kiln gases.

Table 2.4: Dissociation time of calcite as a function of temperature and particle size diameter (Oates, 2008).

Diameter of sphere (mm)	**Dissociation time (h)**					
	Temperature (°C)					
	1000	**1100**	**1200**	**1300**	**1400**	**1500**
12	0.8	0.3	0.2			
19	1.1	0.5	0.3	0.2		
25	1.5	0.6	0.4	0.25	0.2	
37	2.3	1.0	0.6	0.4	0.3	0.2
50	3.5	1.5	0.8	0.6	0.4	0.3
75	7.9	3.8	2.0	1.4	1.0	0.8
100	19	8.5	4.8	3.5	2.6	1.9
125	43	19	11	8.3	6.3	4.6
150		45	26	19	15	11

The temperature at which calcination takes place depends on:

1. the diameter or size of the $CaCO_3$ sample (which has been studied by Oates, (2008)) (seeTable 2.4)

2. the partial pressure of the CO_2 in the calcining environment (which has been studied by Eriksson, (2016)) (see Figure 2.2)

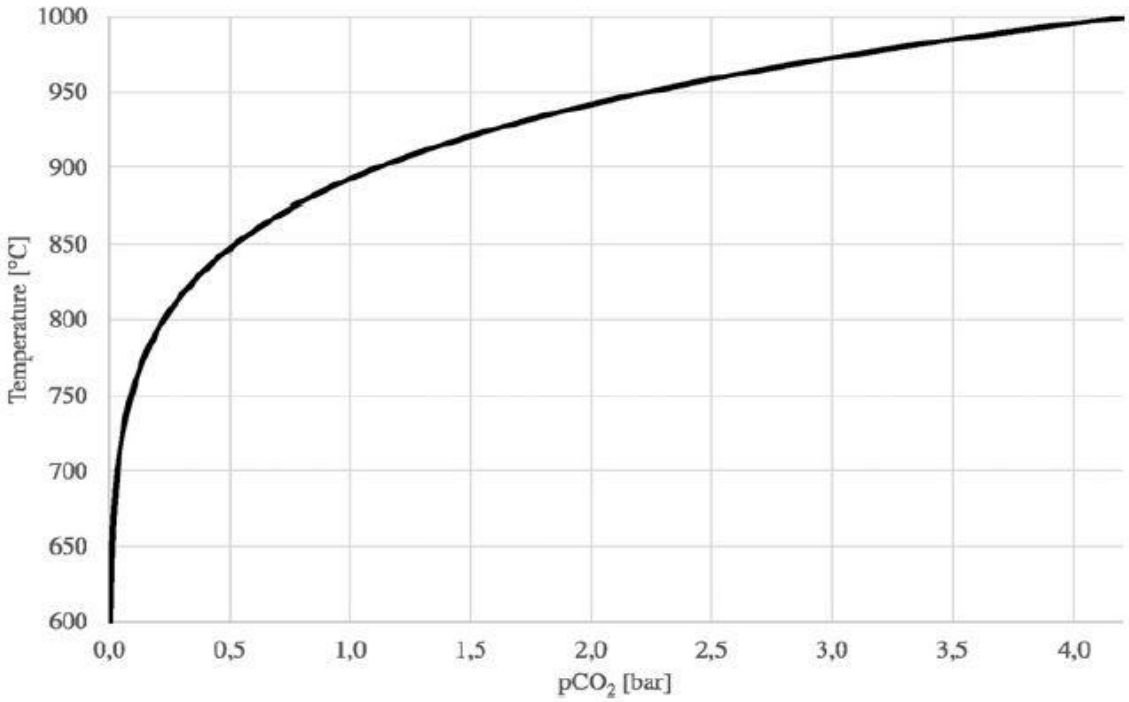

Figure 2.2: Equilibrium dissociation temperature of calcite as a function of the partial pressure of CO_2 (Eriksson, 2016).

In this research the calcination behaviour was studied on limestone that was crushed and milled and was thus in a finely ground particle state.

No conclusion has yet been reached regarding the factors that control the calcination rate of finely ground particles as used in this investigation. Chemical kinetics seem to control the dissociation of 5 – 10 µm particles at temperatures below 900 °C and an Arrhenius activation energy of 46 kcal/mole has been determined (Oates, 2008). At temperatures above 900 °C, the activation energy decreases significantly, which indicates that chemical kinetics no longer control

the rate of dissociation (Oates, 2008). In this temperature range, the time to calcine 80 % of 5 – 10 µm particles varies from 0.55 seconds (at 850 °C) to 0.03 seconds (at 1250 °C) (Oates, 2008). Other research has shown that it takes from 10 seconds to several minutes to calcine particles of 20 – 30 µm at temperatures below 900 °C (Muller and Stark, 1989).

The same literature source has shown that it requires a residence time of only a few seconds to bring about 90 % calcination when operating at temperatures above 900 °C.

Recent research has shown that the physical characteristics, especially petrography of the stone, play a large role in the decomposition characteristics of a stone (Bresciani et al., 2016; Vola et al., 2018, 2017). According to Cheng et al. (2007) the main physical characteristics influencing decomposition temperature are (i) the reaction constant, (ii) pore diffusivity and (iii) thermal conductivity. “High values for the pore diffusivity and the reaction coefficient cause a low decomposition temperature” (Cheng et al., 2007). Conversely high values for thermal conductivity would cause a higher decomposition temperature. The thermal conductivity also determines to a large extent the time it takes for decomposition.

Cheng et al. (2007) is not the only author that has studied the influence of physical characteristic on the decomposition behaviour of limestones. Other authors have paid more specific attention to the petrography and microstructure influence on decomposition (Alaabed et al., 2014; Marinoni et al., 2015; Soltan, 2011). Marinoni et al. (2015) stated that the limestone texture and grain type composition (depending on depositional environment and age of the carbonate rock) seem to be the controlling features on the kinetics of calcination (i.e., T and rate of calcination).

2.4 Calcination of dolomite

The overall decomposition reaction for dolomite in an atmosphere with a low CO_2 partial pressure (0.004 – 0.35 bar) (Dollimore et al., 1994) is given by:

$$CaMg(CO_3)_2 + heat \rightleftarrows CaO + MgO + 2CO_2 \quad (2)$$

In actual fact the decomposition of dolomite in a CO_2 absent atmosphere happens in two stages, often seen as two non–resolved peaks on a DTA/DTG. Literature is still inconclusive on the exact decomposition mechanism. Four mechanisms are prosed for this decomposition:

Mechanism 1 (Hashimoto et al., 1980):

$$CaMg(CO_3)_2 \rightleftarrows CaCO_3(n-1)\cdot MgCO_3 + nMgO + nCO_2 \quad (3)$$

where n ranges from 0 – 1 with time, and

where $CaCO_3(n-1)\cdot MgCO_3$ is in the calcite phase, not the dolomite phase

$$CaCO_3\cdot MgCO_3 \rightleftarrows CaO + MgO + 2CO_2 \quad (4)$$

Mechanism 2 (McIntosh et al., 1990):

$$CaMg(CO_3)_2 \rightleftarrows CaCO_3 + MgCO_3 \quad (5)$$

$$MgCO_3 \rightleftarrows MgO + CO_2 \quad (6)$$

$$CaCO_3 \rightleftarrows CaO + CO_2 \quad (7)$$

Mechanism 3 (Britton et al., 1952):

$$CaMg(CO_3)_2 \rightleftarrows CaO + MgO + 2CO_2 \quad (8)$$

$$CaO + CaMg(CO_3)_2 \rightleftarrows MgO + 2CaCO_3 \quad (9)$$

$$2CaCO_3 \rightleftarrows 2CaO + 2CO_2 \quad (10)$$

Mechanism 4 (Olszak–Humienik and Jablonski, 2015):

$$CaMg(CO_3)_2 \rightleftarrows CaCO_3 + MgO + CO_2 \quad (11)$$

$$CaMg(CO_3)_2 \rightleftarrows MgO + CaO + 2CaO_2 \quad (12)$$

$$CaCO_3 \rightleftarrows CaO + CO_2 \quad (13)$$

Hashimoto et al. (1980) concluded that mechanism 1 is the correct mechanism and McIntosh et al. (1990) concluded that mechanism 2 is the correct mechanism. Olszak–Humienik and Jablonski (2015) concluded that mechanism 4 was correct according to the decomposition of the components of dolomite as a function of p_{CO2} – Figure 2.3.

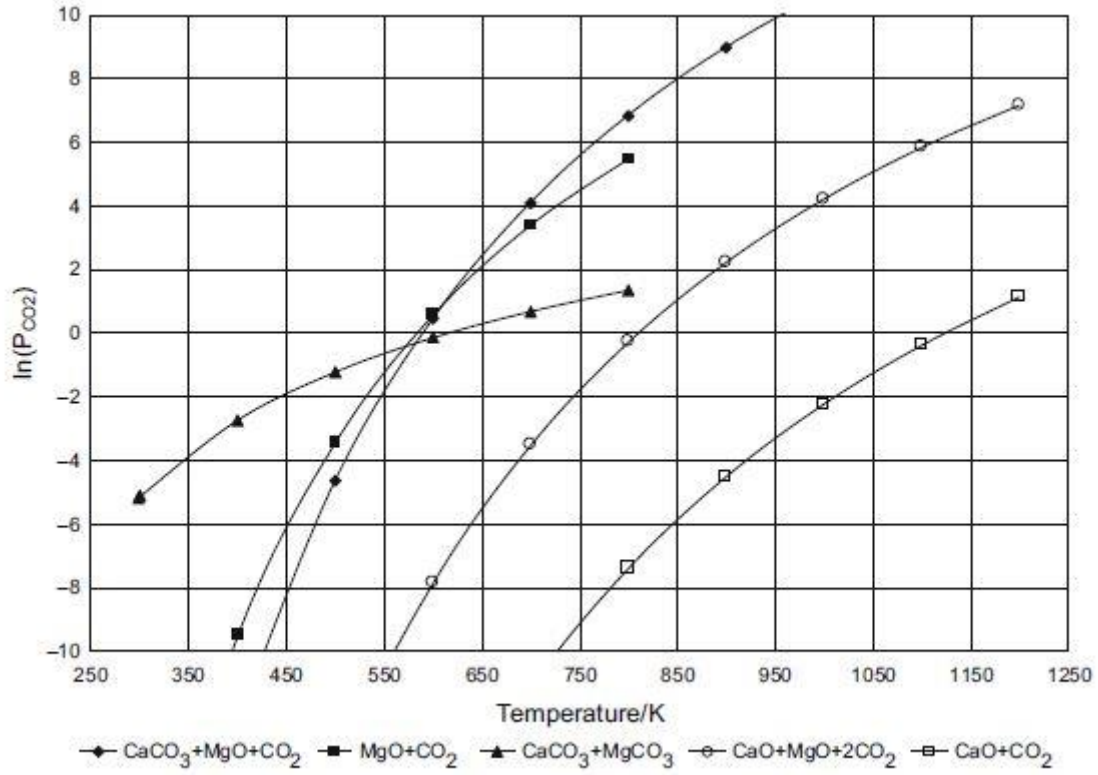

Figure 2.3: Decomposition of the components of dolomite as a function of CO_2 partial pressure

Although there is division about what mechanism is followed, most authors agree that the first peak of dissociation is associated with the formation of MgO and CaO and the second peak is associated with the formation of CaO (Barcina

et al., 1997; Hashimoto et al., 1980; Kök and Smykatz–Kloss, 2008; McIntosh et al., 1990).

Barcina et al. (1997) reported that quarry dolomite decomposition in nitrogen shows two peaks (not perfectly resolved) at 750 °C and at 800 °C. Barcina et al. (1997), in accordance with Boynton (1980), went on to postulate that during decomposition of a dolomite the MgO formation is not yet completed once the $CaCO_3$ decomposition starts. The reason for this is the smaller size of magnesium atoms with respect to calcium atoms, favour the CO_2 in $MgCO_3$ to be driven off first, rather than the CO_2 in $CaCO_3$ (Barcina et al., 1997; Hashimoto et al., 1980). The kinetics of this two–stage decomposition was confirmed by Goldin and Kulikova (1984).

Literature also shows that the decomposition of crushed/milled dolomite decomposes in a two–step process in a nitrogen as well as in an air atmosphere (Kristof et al., 1993; McCauley and Johnson, 1991). According to literature particle size plays a role in the decrepitation characteristics of dolomite (Dollimore et al., 1994; McCauley and Johnson, 1991)

At higher CO_2 pressures, the decomposition of dolomite happens in two stages:

$$CaMg(CO_3)_2 \rightarrow CaCO_3 + MgO + CO_2 \quad (14)$$

$$CaCO_3 \rightarrow CaO + CO_2 \quad (15)$$

The temperatures in both steps are affected by the partial pressure of CO_2:

Step 1 (peak 1):

- The first step takes place at 550 – 756 °C (Eriksson, 2016).

- The first peak temperature decreases as the CO_2 partial pressure increases from 0 – 20 %,reaching a minimum between 10 and 20% (McCauley and Johnson, 1991; McIntosh et al., 1990).

- The first peak temperature in 1 bar CO_2 is lower than in 1 bar N_2 (McIntosh et al., 1990).

- The presence of inorganic salts reduces the decomposition temperature of the first peak (McIntosh et al., 1990).

Step 2 (peak 2):

- The second step takes place at 750 – 785 °C (Eriksson, 2016).

- The second peak temperature increases when the partial pressure increases from 20 % upward (McCauley and Johnson, 1991; McIntosh et al., 1990).

- The second step follows the more expected behaviour of increasing temperature when the CO_2 partial pressure increases (Dollimore et al., 1994; McIntosh et al., 1990).

2.5 Impurities during calcination

The decomposition of some common inorganic mineral phase changes is shown in Figure 2.4 (Schobert, 2013). It should be noted however that these phase transitions are in an oxidizing atmosphere and that the experimental work conducted in this research was done under Nitrogen and CO_2 atmospheres.

Temperature, degrees C	*Reactions or phase transformations*
300	$CaSO_4 \cdot 2H_2O \rightarrow CaSO_4 \cdot \frac{1}{2}H_2O$
400	$K(Al,Mg,Fe)_2(Si,Al)_4O_{10}(OH)_4 \cdot nH_2O \rightarrow K(Al,Mg,Fe)_2(Si,Al)_4O_{10}(OH)_4$
	$CaSO_4 \cdot \frac{1}{2}H_2O \rightarrow CaSO_4$
450	$Al_2Si_2O_5(OH)_4 \rightarrow Al_2Si_2O_7$
600	α-$SiO_2 \rightarrow \beta$-SiO_2
	$FeS_2 \rightarrow FeS$
700	$K(Al,Mg,Fe)_2(Si,Al)_4O_{10}(OH)_4 \rightarrow K(Al,Mg,Fe)_2(Si,Al)_4O_{10}$
750	$CaSO_4$–NaCl eutectic melts
	Clays + $CaCO_3$ + $FeS_2 \rightarrow$ melt phase
	$(Na,Ca)_{0.33}(Al,Mg)_2Si_4O_{10}(OH)_2 \cdot nH_2O \rightarrow (Na,Ca)_{0.33}(Al, Mg)_2Si_4O_{10}(OH)_2$
800	$FeCO_3 \rightarrow FeO + CO_2$
	$Ca(Mg,Fe)(CO_3)_2 \rightarrow CaO + MgO + FeO + CO_2$
900	K_2SO_4–$CaSO_4$ eutectic melts
	$PbS \rightarrow PbO$
	β-$SiO_2 \rightarrow$ tridymite
	$CaMg(CO_3)_2 \rightarrow CaO + MgO + CO_2$
	$3\ CaSO_4 + CaS \rightarrow 4\ CaO + 4\ SO_2$
950	$2\ Al_2Si_2O_7 \rightarrow 2Al_2O_3 \cdot 3SiO_2 + SiO_2$
	FeO–FeS eutectic melts
	$CaCO_3 \rightarrow CaO + CO_2$
	$2\ CaO + Al_2Si_2O_7 \rightarrow Ca_2Al_2SiO_7 + SiO_2$
	$CaO + Al_2Si_2O_7 \rightarrow CaAl_2Si_2O_8$
1000	TiO_2 (anatase) $\rightarrow$ TiO_2 (rutile)
1100	$K(Al,Mg,Fe)_2(Si,Al)_4O_{10}$ forms glassy phase
1200	$Ca_2Al_2SiO_7$ forms glassy phase
1300	Glassy phases transform to spinels and Si-rich glass
1400	$Ca_2Al_2SiO_7$ and $CaAl_2Si_2O_8$ melt
	FeO melts
	Glassy phases $\rightarrow 2Al_2O_3 \cdot SiO_2$
1500	SiO_2 (tridymite) $\rightarrow$ SiO_2 (cristobalite)

Figure 2.4: Phase transitions of inorganic minerals under oxidizing circumstances (Schobert, 2013)

The decomposition of carbonates as a function of CO_2 partial pressure was done by (Goldin and Kulikova, 1984) and is displayed in Figure 2.5.

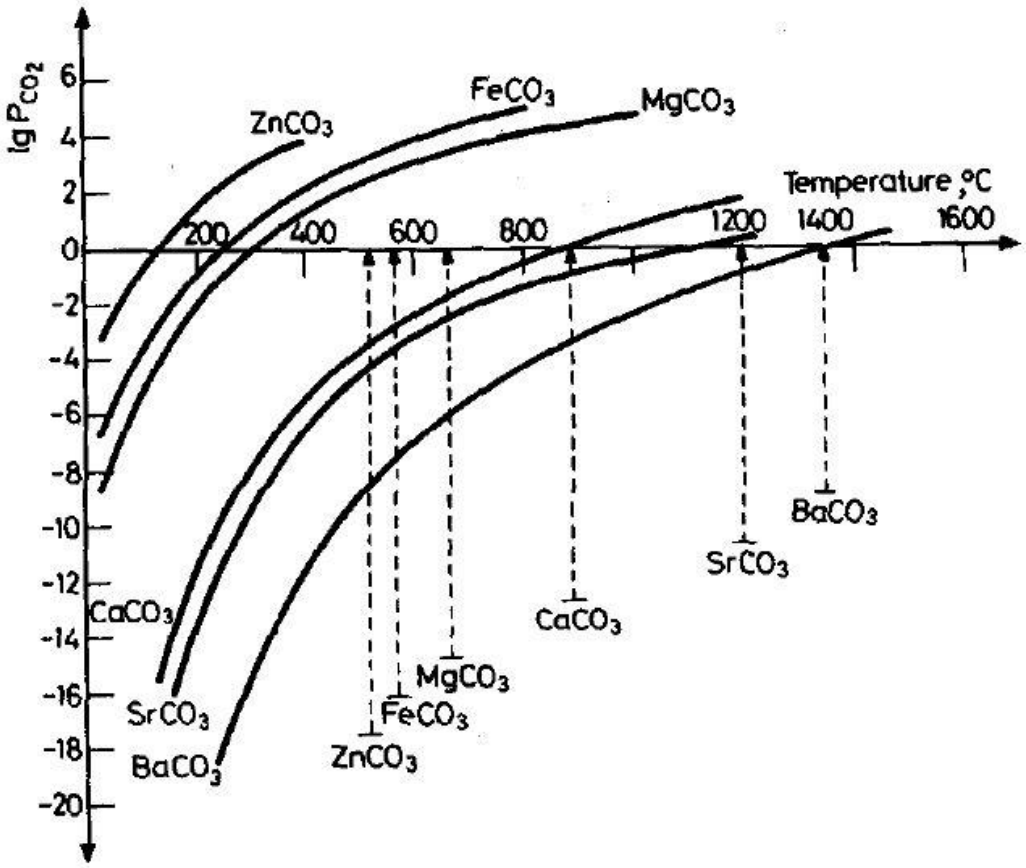

Figure 2.5: Carbonates decomposition temperatures as a function of p_{CO2} (Goldin and Kulikova, 1984)

3 Methodology

3.1 Limestone sample collection and preparation

Four limestones from southern Africa were sourced for use in this research. Three of the samples were high purity limestones and one of the samples was a dolomite. Two limestones, representing two separate quarry zones, were sampled and collected from Lime Acres in the Northern Cape province of South Africa. Another limestone sample was obtained from Handyman Lime, near Ndola in the Copperbelt province of Zambia. The dolomite stone was sampled and collected from the Mooiplaas quarry, west of Pretoria in South Africa. The sample naming is set out in Table 3.1 Additional information about the locations and formation information of the samples can be found in Appendix B.

Table 3.1: Nomenclature of samples and their sources.

Carbonate rock	Country	Province	Allocated name
Dolomite	South Africa	Gauteng province	Sample W
Limestone	South Africa	Northern Cape province	Sample X
Limestone	South Africa	Northern Cape province	Sample Y
Limestone	Zambia	Copperbelt province	Sample Z

From each quarry/lime works, stone was sampled and collected in two sizes, 30–50 mm (small sample size) and 70–125 mm (larger sample size). The samples were crushed and milled at the school of Chemical and Metallurgical Engineering. Each sample underwent chemical analysis at the quarry/lime producer it originated from.

3.2 Methods

Figure 3.1 is a graphical presentation of the sample preparation methods and analytical techniques used in this study. Additional analysis and tests included X–ray fluorescence (XRF) analysis

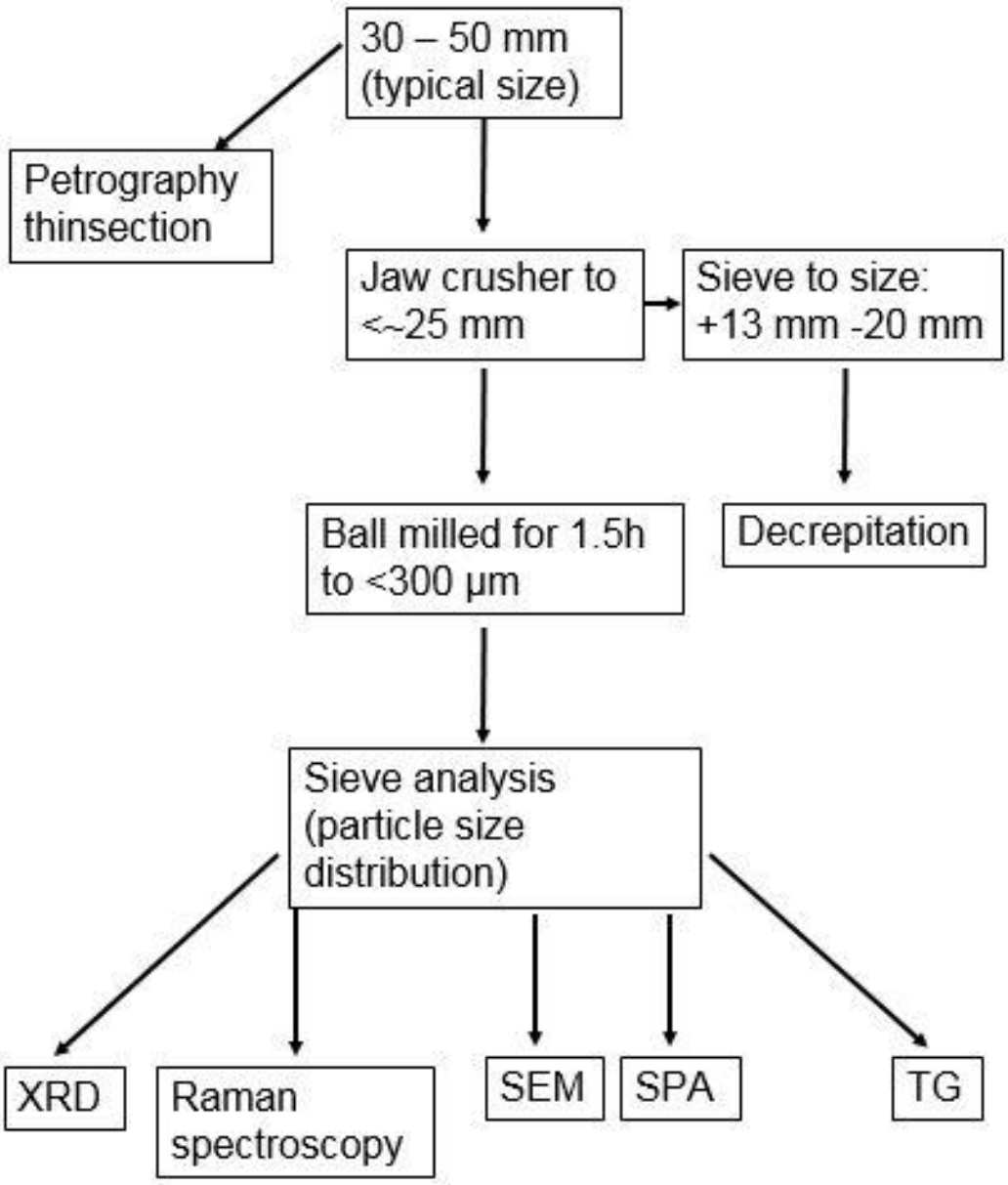

Figure 3.1: Powdered sample preparation and analysis route.

3.2.1 X–ray Fluorescence (XRF)

XRF analysis was performed at the on–site laboratory of each lime manufacturer except for Sample Z.

XRF analysis of sample Z was done at the University of the Witwatersrand at the Geoscience department. This analysis was done on a Panalytical PW2404 X–ray fluorescence spectrometer. Major elements were fused using Johnson Matthey Spectroflux 105 at 1100°C and raw data corrected using in–house software. The Norrish Fusion technique embedded in in–house software was used to determine major elements. Standard calibrations were made up using synthetic oxide mixtures and international standard rocks as well as in–house controls. Sample mass used was 0.35 gm and flux mass 2 gm. Calibration standards were primary International Reference Materials USGS series (USA) and NIM series (South Africa). Precision is taken as 1% for elements in abundance of greater than 5% by mass, and 5% for elements in abundance less than 5%. Please see Appendix D1 for the operating procedure of a XRF instrument.

3.2.2 Petrographic analysis (petrography)

Petrographic analysis was performed on the 30 – 50 mm stones and was done by Dr Penn–Clarke (see acknowledgment) of the Palaeontology Department at the University of the Witwatersrand. Thin sections were analysed and photographed using an Olympus BX41 petrographic microscope with an Olympus DP26 camera attachment housed at the School of Geosciences at the University of the Witwatersrand. Whole thin section micrographs were made using an Olympus BX63 microscope at the Microscopy and Microanalysis Unit. The micropetrography of each thin section was described in terms of mineralogy, grain size, grain contacts and relative abundance using visual estimation.

3.2.3 Sample preparation – Crushing and Milling

Stones of 30 – 50 mm in size were passed through a jaw crusher and then 1 kg of each sample was milled in a stainless steel laboratory ball mill (175 mm diameter and 222 mm length) with a uniform charge of stainless steel balls. The amount of each size ball used for milling varied based on what balls were available in the laboratory at the time of milling.

Each sample was milled for 1.5 h at a mill speed of 300 rpm. After milling all the fines and balls were extracted from the milling pot. The balls were separated from the fines in a stainless steel pan. The milling pot and the balls were rinsed with tap water and left to dry before the next milling.

3.2.4 X–ray Diffraction (XRD)

XRD analysis was performed on each sample at the Chemistry department of The University of the Witwatersrand. Analysis was done on a Bruker D2 Phaser desktop diffractometer. This diffractometer employs a sealed tube Cu X–ray source and is equipped with a Bruker Lynxeye PSD detector using a 2.5° secondary beam radial Söller slit and Ni filter. Appendix D3 explains the operating principle of a XRD instrument.

Hot stage XRD analysis was performed only on samples W, X and Y. Analysis was carried out with a Panalytical X–pert powder diffractometer using a Cu (kα, λ=1.5406 Å) and PixCEL 1–D detector operating in scanning line mode with an active length of 3.347° 2θ. Data was collected in the range from 10 – 50° 2θ. The samples were prepared as flat powders and placed inside an Anton–Paar HTK–1200N oven chamber. Each sample was heated from 50 °C (sample W)/100 °C (Sample X and Y) to 1200 °C in increments of 50 °C (sample W)/100 °C (Sample X and Y) and with a ramp rate of 150°C/min. After reaching the

temperature set point the sample was held for 10 minutes then scanned over the angular range with a collection time of 15 minutes.

3.2.5 Raman Spectroscopy

For each sample Raman analysis was carried out on two separate instruments – a Renishaw inVia Raman microscope and a ThermoFisher DXR™ 2 Raman microscope. For the Renishaw inVia Raman analysis a thin layer of powder was applied onto a microscope slide and 20 arbitrary points analysed for each sample. A laser power of 5 % at 514 nm was used to analyse the sample. Spectra were collected over the range of 100–1200 cm^{-1} with an exposure time of 10 seconds and 20 accumulations.

For the DXR Raman analysis, powder from each sample was again applied to a microscope slide and the slide placed under the microscope. A digital map of 5 points on each sample was made and then 10 spectra collected automatically from each point with the use of an automated sample table.

3.2.6 Scanning Electron Microscopy (SEM)

3.2.6.1 Scanning Electron Microscopy energy dispersive X–ray spectrometry (SEM–EDX)

SEM samples were prepared by lightly dabbing a sticky carbon stub on a surface containing the evenly spread sample. Any excess sample was blown off by compressed air to ensure only a thin layer of the sample on the stub. Because of the low conductivity of limestone, the carbon stubs containing the limestone powders were each covered with a very thin layer (~ 20 nm) of gold and palladium to increase conductance. A Carl Zeiss Sigma 300 FESEM instrument equipped with integrated Oxford X–act EDX detection was used for

the SEM. Images were captured at 1000 and at 4000 magnification with an acceleration voltage of 10 kV and a working distance of 6.7 mm.

3.2.6.2 Computer–Controlled Scanning Electron Microscopy (CCSEM)

CCSEM was used to do single particle analysis. CCSEM is an automated method by which each single particle in a sample is recognised by a Scanning Electron Microscope with the help of a powerful software package. The composition of each particle is then analysed using an EDX instrument and accompanying software. CCSEM combines the advantages of energy dispersive X–ray spectrometry (EDX) with those of digital image analysis on back scattered electron (BSE) micrographs for the automated measurements on hundreds or thousands of single grains.

For CCSEM single particles need to be visible to the EDX for analysis. To get single particles evenly spread on a carbon stub the following procedure was followed: CCSEM samples were prepared by suspending 10±2 mg of sample in 20 mL of methanol and the liquid suspension shaken for 30 seconds. The liquid suspension was drawn up by a pipette and one to two drops carefully placed on a stub containing black carbon tape. The methanol was allowed to evaporate and leave behind evenly spread single particles. Because of the distribution effect of larger particles sinking to the bottom of the suspension, mostly smaller particles were drawn up by the pipette and therefore ±90 % of particles in single particle analysis are –10 µm. This particle size limitation is dictated by the analysis method and the preparation of the samples needed for CCSEM.

The SEM section of the CCSEM analysis was performed by a Carl Zeiss Supra 40VP instrument and SmartSEM software. The EDX analysis was performed by an EDAX Apollo 40 SDD instrument and Genesis software. The “single particle analysis” application of the EDAX Genesis software was used to

analyse the chemical composition of each individual particle with the following microscope conditions: a 25 kV acceleration voltage and a 15 mm working distance. A 15 second spectrum was recorded for each particle.

Please see Appendix D4 for the operating principle of Scanning Electron Microscopes and Energy Dispersive X–ray analysis.

3.2.7 Decrepitation test

The decrepitation test was done according to guidelines set out by the Maerz™ Regulation No. 4 decrepitation test© (24–7–2015). The following procedure was executed:

a. Weigh out 250±1 g of +13mm –20mm stone onto a furnace crucible.
b. Heat oven to 114 °C.
c. Insert sample into oven.
d. After 10 minutes at 114±10 °C increase the oven temperature to 1000 °C (dolomite)/1050 °C (limestone)
e. Once oven reached 1000/1050 °C start the timer for 60 min. After 60 min let the oven cool down.
f. Wait for oven to cool to 114±10 °C and then take sample out of the oven and let cool further in a desiccator to ambient temperature.
g. Weigh total amount of stone in crucible = m_{burnt}
h. Sieve stone through a 11.2 mm sieve.
i. Collect and weigh what falls through the 11.2 mm sieve = $m_{decrepitated}$

$$\%\, decrepitation = \frac{m_{decrepitated}}{m_{burnt}} \frac{[g]}{[g]} \times 100\%$$

With the decrepitation test the disintegration tendency can be estimated for the same stone burning in a kiln. From industry experience the standard value of decrepitation for low maintenance operation is less than 10%. According to

Oates (2008) a 20 mm limestone (maximum size of stone in decrepitation test) would take 0.84 h to calcine at 1050 °C. 1 h was selected in order to ensure complete calcination. 1050 °C calcination temperature was selected because this is the temperature at which kilns typically operate.

3.2.8 Thermogravimetry (TG)

The TG analyses were done on a SDT Q600 TA instrument. The TA Q600 has a horizontal balance and furnace. The sample mass is monitored with a reference balance. The TA Q600 instrument can go from ambient temperature up to 1500 °C at a rate of 0.1 – 25 °C/min. The balance sensitivity is 0.1 µg. Appendix D2 explains the operation principles of a TG instrument.

A 40 µL alumina crucible was used for each TG run and an average of 10 ± 2 mg sample was used for every run. Nitrogen (100 kPa) flowrate was kept constant at 10 mL/min and the CO_2 flowrate was varied to meet the goal partial pressure. Three variables were investigated during the decomposition of the limestone and dolomite samples – heating rate final, temperature and CO_2 partial pressure. The dolomite decomposition was observed at 850 °C, 900 °C, 950 °C and 1000 °C at a CO_2 partial pressure of 0 bar (p_{CO2} = 0bar) . However at p_{CO2} = 1 bar the decomposition could not be observed before 950 °C and the method was adapted to observe decomposition of dolomitic limestone at 950 °C, 1000 °C, 1050 °C, 1100 °C and 1150 °C.

For the limestone samples, X, Y and Z, the temperatures investigated at p_{CO2} = 0 bar and p_{CO2} = 1 bar were the same. The final temperatures (T_f) at which decomposition was observed were 950 °C, 1000 °C, 1050 °C, 1100 °C and 1150 °C. Note that for Sample Z the full decomposition at 950 °C could not be observed at p_{CO2} = 1bar.

Decomposition of the carbonate rocks were investigated at the following CO_2 partial pressures: 0, 0.5, 1 and 1.5 bar. The CO_2 flowrates at 105 kPa were 0, 3.2, 10 and 29 mL/min for each partial pressure respectively. These partial pressures were selected because it was the most practical range of pressures allowed by the instrumental setup. The heating rate of the thermal gravimetric analysis was selected to be 15 °C/min in accordance with literature (Olszak–Humienik and Jablonski, 2015; Warne et al., 1981). Dolomite decomposition was investigated at 5 °C/min, 10 °C/min and 15 °C/min (0 bar CO_2 partial pressure) in order to see what effect the heating rate had on the decomposition behaviour. The TG method for each sample is summarised in Table 3.2

Table 3.2: Summary of TG variables of each sample.

Sample	Heating range [°C]	Increment [°C]	Heating rates [°C/min]	CO_2 partial pressure [bar]
W	850-1000	50	5,10,15	0, 0.5, 1, 1.5
X	950-1150	50	15	0, 0.5, 1, 1.5
Y	950-1150	50	15	0, 0.5, 1, 1.5
Z	950-1150	50	15	0, 0.5, 1, 1.5

850 °C was selected to be the lowest temperature for sample W (dolomite) because at the maximum partial pressure of 1.5 bar the dolomite is expected to decompose at 780–800 °C (Olszak–Humienik and Jablonski, 2015). 950 °C was selected to be the lowest temperature for samples X,Y and Z because at the maximum CO_2 partial pressure of 1.5 bar the limestone is expected to decompose at 920 °C (Eriksson, 2016). Therefore in order to witness the complete decomposition at all pressures the lowest temperature was selected to be 950 °C. 950 °C is also a very practical minimum temperature to investigate decomposition at since the modern shaft kilns operate between 950 °C and 1200 °C.

4 Results and discussion

4.1 Chemical composition of Carbonate Rock (XRF results)

X–Ray Fluorescence (XRF) is central to the assessment of a carbonate rock. XRF determines the chemical composition of a carbonate rock. A carbonate rock's chemical composition determines its calcination properties and behaviour. Knowledge of a limestone's/dolomite's chemical composition is integral to determining its suitability for use in a kiln. As a standard XRF reports the two most important elements (Ca and Mg) and impurities (Si, Fe and Al primarily) in a carbonate rock. XRF reports these elements as oxides (Ca and Mg converted to carbonates in Table 4.1 by molar proportions). Often XRF also reports Loss Of Ignition (LOI), but since Thermal Gravimetry (TG) analyses were done, the LOI was instead determined by TG. In this regard TG is complementary to XRF.

The chemical analyses of the carbonate rock samples are set out in Table 4.1. As mentioned in the methodology section most of the chemical analyses were performed by the on–site laboratories of the quarry operations and lime kiln sites from which the samples were sourced.

Table 4.1: Chemical analysis – carbonate rock samples (normalised).

Sample name	Compounds [%]								
	$CaCO_3$	$MgCO_3$	SiO_2	Al_2O_3	Fe_2O_3	Mn_2O_3	K_2O	SO_3	Total
W	54.13%	42.42%	1.26%	0.14%	0.78%	1.26%	-	0.01%	100
X	97.38%	1.54%	0.21%	0.04%	0.21%	0.57%	0.04%	0.01%	100
Y	98.20%	0.95%	0.06%	0.01%	0.17%	0.58%	0.02%	0.01%	100
Z	97.03%	0.97%	1.52%	0.24%	0.20%	0.02%	0.02%	-	100

Impurities occur as homogeneous or heterogeneous distributions. Homogeneous impurities contaminated the stone when the stone was first formed and occur in the ground mass of the stone as clay, silt, sand or quartz.

Heterogeneous impurities are impurities that occur in the pores and can be distinguished from the ground mass of the stone (Boynton, 1980).

Potassium and Magnesium have been identified in literature as two constituents that affect the behaviour of a carbonate rock in lime kilns, especially their potential to be hard burnt (Hogewoning et al., 2008). K_2O content of 0.01 – 0.03% and MgO content of 0.7 – 3% was found to have an effect. The reason why these minerals have an effect is as follows: “Dolomite or magnesite minerals and silica that contain potassium are present in the limestone in finely divided form as interstitial or edge fillings between the calcite crystals and remain in the same place during the calcination process. They form a boundary layer between the CaO crystallites and additional energy has to be applied to push the growth of the CaO interface beyond these foreign minerals.” (Hogewoning et al., 2008). The impurities of each sample are shown in Table 4.2 as pure elements and not as oxides.

Table 4.2: Impurities reported as pure elements and not as oxides.

Sample	Si [%]	Al [%]	Fe [%]	Mn [%]	K [%]
W	0.59	0.07	0.54	0.88	0.00
X	0.10	0.02	0.15	0.40	0.04
Y	0.03	0.01	0.12	0.40	0.01
Z	0.71	0.13	0.14	0.01	0.02

4.1.1 Dolomite (sample W) – Gauteng

Sample W is classified as a dolomite because $MgCO_3$ > 40% and $CaCO_3$ > 50% (Boynton, 1980) (also see the classification of limestones in the literature section). The high amount of MgO would decrease this sample’s susceptibility to sinter (Hogewoning et al., 2008). The high amount of Mn_2O_3 is due to the geology of the area where the sample originated and would most likely give the lime a brown colour upon calcination (Beukes, 1983). The high amount of Fe is also due to the geology of the sample’s origin (Klein and Beukes, 1989). The

Fe can occur homogeneously as iron carbonates (e.g. Ferroan Dolomite) or heterogeneously as pyrite or limonite (Boynton, 1980). Whether silica occurs in the ground mass or in pores is investigated in the petrographic section.

4.1.2 Limestone (Samples X and Y) – Northern Cape

Samples X and Y can both be classified as high purity limestones since their $CaCO_3$ content is 97 – 98.5 % (Boynton, 1980) (also see the classification of limestones in the literature section). The Manganese and Iron amount in samples X and Y is in accordance with literature – "The Ghaap Plateau facies carbonates are relatively manganese–rich containing more manganese than iron" (Beukes, 1987).

The high amount of MgO (>0.7%) and K_2O (>0.01%) in sample X would help prevent sintering of this limestone in a kiln (Hogewoning et al., 2008). Sintering is hard burning of the lime surface causing the lime to be less reactive. Sample Y contains less MgO and K_2O but still a significant amount to aid prevention of sintering in a lime kiln. The higher amount of CaO in sample Y would yield a purer product than sample X and have a lower heating value because it contains less impurity constituents. Whether silica occurs in the ground mass (homogeneous impurity) or in pores (heterogeneous impurity) was investigated in the petrographic section.

4.1.3 Limestone (Sample Z) – Zambia

Sample Z is classified as a high purity limestone (Boynton, 1980) because of its $CaCO_3$ content (>95%) but it should be noted that its silica content is indicative of a medium purity limestone. This stone corresponds to the "119 m–thick bedded grey limestone showing an alternation of dark and light layers (CaO=54.15 wt.%/ MgO=1.03 wt.%)" in the Kakontwe formation (Batumike Mwandulo et al., 2007).

Sample Z contains the most silica and alumina of all the limestones. The high amount of Si in the stone is due to the sandstone and siltstone in the upper Kipushi formation and lower Kaponda formation (Batumike Mwandulo et al., 2007).The higher amount of silica and alumina is likely to increase the onset temperature of sample Z in comparison to samples X and Y – this hypothesis is discussed in the Thermogravimetry (TG) section. Whether the silica occurs as part of the ground mass or in pores was investigated in the petrographic section.

Sample Z contains a similar amount of Fe to samples X and Y but less Manganese. These heavy metals are in agreement with the heavy metals occurring in the sample source region – “The Nguba and Kundelungu Group successions are also marked by numerous Zn–Pb–Cu or Cu–Ag–Au epigenetic deposits occurring in carbonates (Batumike Mwandulo et al., 2007).

4.2 Particle size distribution of milled carbonate rock samples

For each carbonate rock sample, stones of 30 – 50 mm in size were crushed and milled in preparation for the assessment methods that required a powder: XRD, Raman, SEM, CCSEM and TG. As particle size affects how samples behave in TG a particle size distribution was done on each sample.

The particle size distributions of the samples dolomite (W) and limestone (X, Y and Z) are shown below in Figure 4.1. The mean particle diameter and particle size range are shown in Table 4.3.

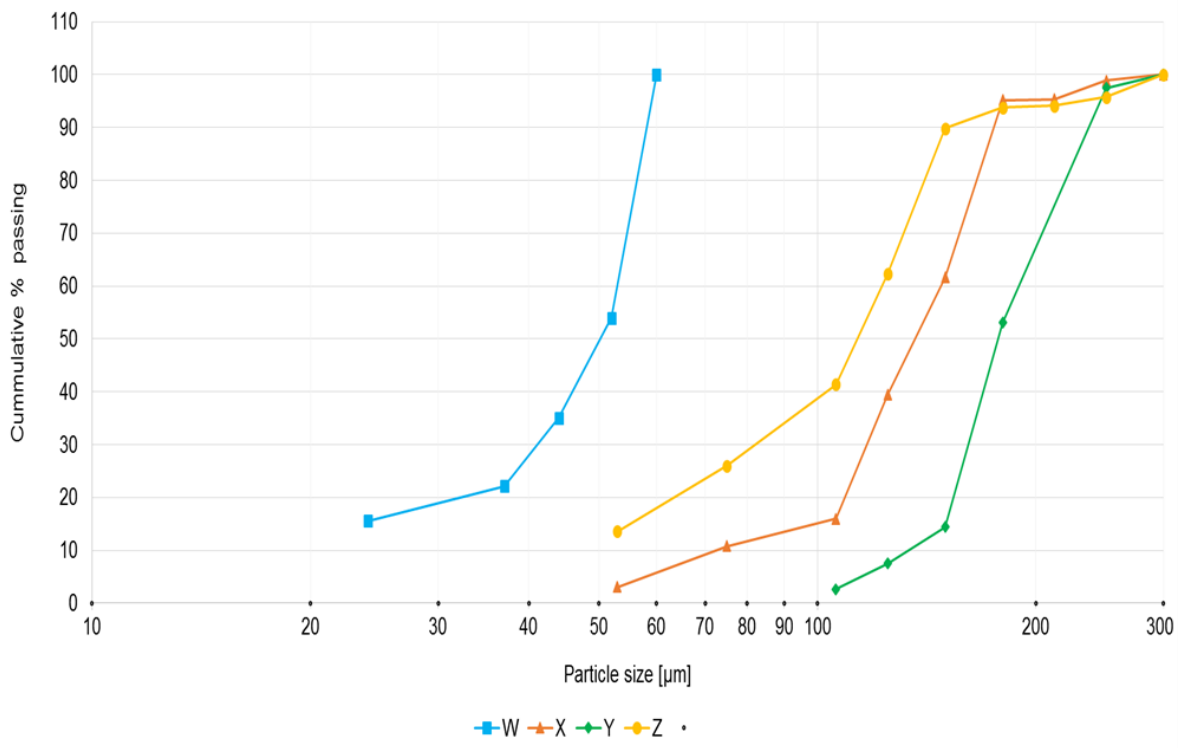

Figure 4.1: Particle size distribution of milled limestone and dolomite samples

Table 4.3: Carbonate content and milled characteristics of limestone and dolomite.

Sample	W	X	Y	Z
$CaCO_3$ content [%]	54.1%	97.4%	98.2%	97.0%
$MgCO_3$ content [%]	42.4%	1.5%	0.9%	1.0%
Groundmass crystals size [mm]	-	0.005 - 0.18	0.005 - 0.18	0.1 - 0.25
Grinding time [h]	1.5	1.5	1.5	1.5
Particle size range [µm]	1 - 60	1 - 300	1 - 300	1 - 300
d_{50} [µm]	50	137	178	114

4.2.1 Dolomite (Sample W)

Kristóf–Makó and Juhász (1999) investigated the decomposition of 10 g of dolomite that was ground in a 80 cm^3 laboratory planetary mill with 64.1 g of 10 mm stainless steel balls for a total grinding time of 1, 5 and 7 hours. According to Kristóf–Makó and Juhász (1999) dolomite ground for more than 1h results in

the development of a structurally distorted dolomite that decomposes in two stages – “Both MgI (690 °C) and MgII (580 °C) peaks (unresolved) can be observed after grinding for 1 h.”

The dolomite, sample W, was milled in a ball mill for 1.5 h and therefore the structure of the dolomite sample structure was distorted (Kristóf–Makó and Juhász, 1999). According to Kristóf–Makó and Juhász (1999) and Barcina et al. (1997) the structurally compromised (deformed) dolomite decomposes in two unresolved stages in an inert atmosphere. The $MgCO_3$ component is expected to decompose to MgO between 500 °C and 750 °C (Oates, 2008); and then $CaCO_3$ is expected to decompose to CaO from 900 °C onwards. The possible mechanisms of this two–stage decomposition were set out in the literature review section and the favoured mechanism is repeated here (Olszak-Humienik and Jablonski, 2015b):

$$CaMg(CO_3)_2 \rightleftarrows CaO + MgO + 2CO_2 \quad (16)$$

$$CaO + CaMg(CO_3)_2 \rightleftarrows MgO + 2CaCO_3 \quad (17)$$

$$2CaCO_3 \rightleftarrows 2CaO + 2CO_2 \quad (18)$$

The thermal decomposition of structurally sound dolomite is a one–step process which occurs close to 750 °C (Oates, 2008). This is further discussed in the Thermogravimetry section.

The reason why sample W (dolomitic limestone) had a narrower range with smaller particles is ascribed to the chemical and petrographic composition of

the rock. Dolomite and magnesite are known to result in much finer particles when crushed and ground because of the rhombic and anhedral grains that occur in dolomite (Harvey, 1970). This is confirmed by Marinoni et al. (2012) who found that dolomite was concentrated in 25 – 40 µm particles. The clay or silt that occurs in between the dolomite crystals breaks the surfaces up even more and is another cause of the grain sizes that are often smaller than10 µm (Harvey, 1970). The rock itself had a high hardness and brittleness which was observed during the preparation of cut specimens (cubes) for compressive strength testing.

4.2.2 Limestone (Samples X and Y): Northern Cape

Samples X and Y were both milled for 1.5h, as for sample W, but had a much wider range of particle sizes and S–curve distributions. The d_{50} values for X and Y differ by only 40 µm, which was expected considering their similar chemical composition and observed structure from petrographic study. Maximum decomposition rate is achieved when limestone particle size is minimized and when the decomposition occurs without mass transfer limitations (Borgwardt, 1985). The mean diameter of sample X is smaller than the mean diameter of sample Y. Therefore sample X is expected to decompose faster than sample Y or at a higher temperature in a thermogravimetric test.

4.2.3 Limestone (Sample Z): Zambia

Sample Z has a similar particle size range to samples X and Y along with an S–curve distribution. The particle sizes in the milled sample Z appear to be slightly smaller on average as is evident by the d_{50} value of 114 µm as compared to 137 µm and 178 µm of sample X and Y respectively. Because sample Z has the smallest d_{50} value of all the limestones, it is expected to decompose at a higher rate and lower temperature than samples X and Y or for a longer time at the same temperature in a thermogravimetric test.

4.3 X–ray Diffraction (XRD) and Raman Spectroscopy

Knowing the phase/compound in which impurities occur is of importance because this gives a more complete picture as to exactly how the elements that were identified in the XRF analysis occur. The bond strength between elements can also be deduced by determining in what combination elements occur: knowledge of the bond strength can help to explain if carbonate rocks will take a longer or shorter time to calcine. Knowing the phases/compounds also provides information on which impurities occur and enables predictions of how those impurities will affect the calcination to be made.

XRD is a qualitative method although the XRD spectra can be interpreted by the Rietveld refinement method (Rietveld, 1967) to be qualitative as well. The Rietveld refinement method was applied to the powdered XRD analysis in order to estimate the amount of minerals more accurately. XRD, however, cannot pick up trace amount crystals (<5%), while this can be done by Raman (Warren, 1990). By using Raman spectroscopy to identify trace phases (<5%), the assessment criteria for carbonate rocks are expanded from using only XRD to using XRD in conjunction with Raman spectroscopy. Raman can, however, only identify phases, not quantify them. Therefore Raman spectroscopy and X–ray Diffraction are used as complementary analytical techniques in this study. A summary of the identified phases from XRD and Raman analysis is given in Table 4.4.

Table 4.4: Identified phases from XRD and Raman analysis for samples W, X, Y and Z

	XRD phases present	Chemical Formula	Impurities	Raman phases present	Chemical formula	Impurities
W	Dolomite	$CaMg(CO_3)_2$		Dolomite	$CaMg(CO_3)_2$	
	Quartz	SiO_2	Si	Magnesite	$MgCO_3$	
	Siderite	$FeCO_3$	Fe	Calcite	$CaCO_3$	
	Calcite	$CaCO_3$				
X	Calcite	$CaCO_3$		Calcite	$CaCO_3$	
	Quartz	SiO_2	Si	Fluoborite	$Mg_3(BO_3)(F,OH)_3$	Mg
	Ferroan dolomite	$Ca(Mg,Fe)(CO_3)_2$	Fe	Thulite	$(Ca,Mn)_2Al_3(SiO_4)$	Mn,Al,Si
Y	Calcite	$CaCO_3$		Calcite	$CaCO_3$	
	Quartz	SiO_2	Si	Fluoborite	$Mg_3(BO_3)(F,OH)_3$	Mg
				Thulite	$(Ca,Mn)_2Al_3(SiO_4)$	Mn,Al,Si
Z	Calcite	$CaCO_3$		Calcite	$CaCO_3$ (trigonal crystal)	
	Quartz	SiO_2	Si	Aragonite	$CaCO_3$ (orthorhombic crystal)	
				Fluoborite	$Mg_3(BO_3)(F,OH)_3$	Mg
				Libethenite	$Cu_2(PO_4)(OH)$	Cu
				Graphite	C (hexagonal)	C
				Quartz	SiO_2	Si

The phases identified with XRD and Raman spectroscopy are discussed for each individual carbonaceous rock sample since each sample contains unique phases. The Raman shifts are then compared to Raman shifts of carbonate rocks in the literature.

As mentioned in the operating principle of Raman spectroscopy (Appendix D5), Raman is a qualitative analysis method that is used to identify phases and crystal structures.

Phases are identified by matching the Raman shifts (wavenumbers) to the spectra of known phases. Raman scans were conducted on two instruments. The results of the Renishaw inVia Raman instrument are reported here. The DXR instrument was used to corroborate the results of the Renishaw inVia instrument and to identify any phases not identified by the Renishaw inVia instrument. Raman scans were done on 20 different points for each sample.

The Raman shifts are reported in wavenumbers where wavenumber (unit: length^{-1}) is a unit independent of the speed of light as opposed to

frequencies/wavelengths. Each Raman shift is associated with a certain vibration/deformation in a molecule. In the case of carbonate rocks, there exists translation and stretching of molecules. Figure 4.2 and Figure 4.3 show two types of deformation that occur in carbonate molecules (Buzgar and Apopei, 2009). These shifts were identified by the Renishaw inVia Raman instrument.

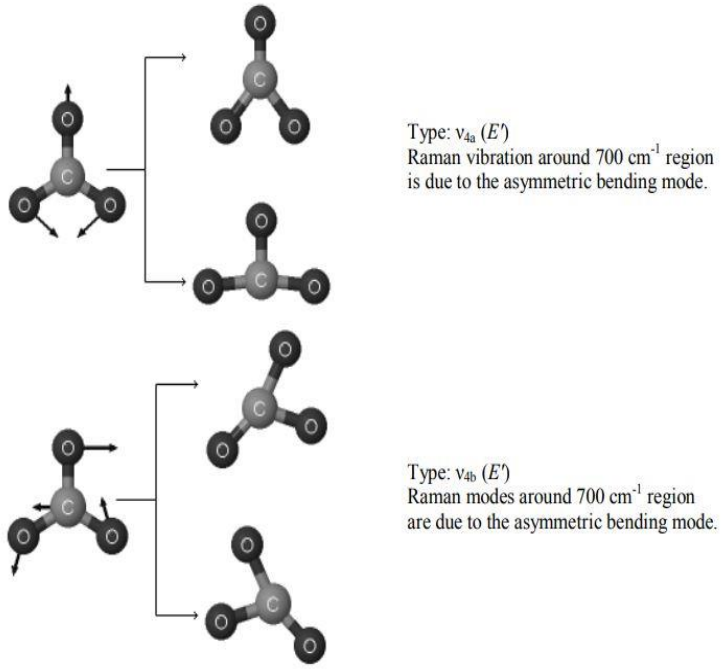

Figure 4.2: Asymmetric carbonate deformation – v4 (Buzgar and Apopei, 2009)

The positions of the wavenumbers are unique for each carbonate mineral and are thus diagnostic of their mineralogy. Owing to the very different strengths of the intra–CO_3^{2-} and inter–ionic forces, it might be expected that the Translational and Rotational modes have lower wavenumbers than those associated with internal modes (v_1 – v_4) (Gunasekaran et al., 2006). Minor shifts in wavenumber positions may be due to the effect of trace metal content and natural impurities present in the samples (Gunasekaran et al., 2006). The carbonate rocks in this study were characterized in the wavenumber range from 100 – 1200 cm^{-1}.

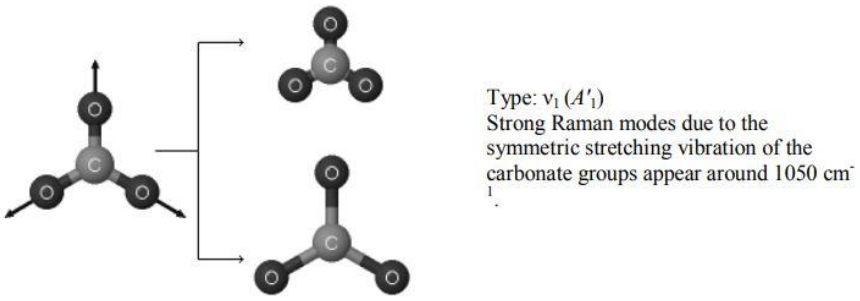

Figure 4.3: Symmetric carbonate deformation – v_1 (Buzgar and Apopei, 2009)

4.3.1 Dolomite (Sample W) – Gauteng

An XRD scan (Figure 4.4) of sample W showed that the sample consists of 96.3 % dolomite, 2.7 % quartz, 0.52 % siderite ($FeCO_3$) and 0.42 % calcite.

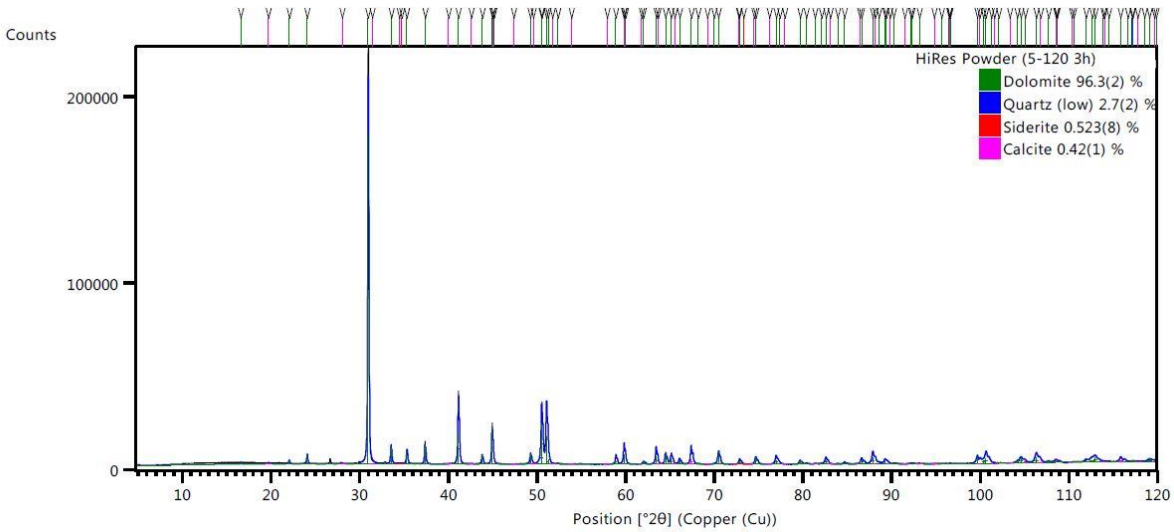

Figure 4.4: XRD spectrum of carbonate rock W

During Raman scanning (see Figure 4.5 and Figure 4.6) the two main matches for sample W were Magnesite ($MgCO_3$) and Dolomite ($CaMg(CO_3)_2$). Although Cobaltite (CoAsS) was a partial match for the Raman spectra of sample W, it was eliminated because of the absence of Arsenic and Cobalt in the XRF

results. It should be noted that petrographic analysis has shown that the sample contains pyrite in small amounts (<1%).

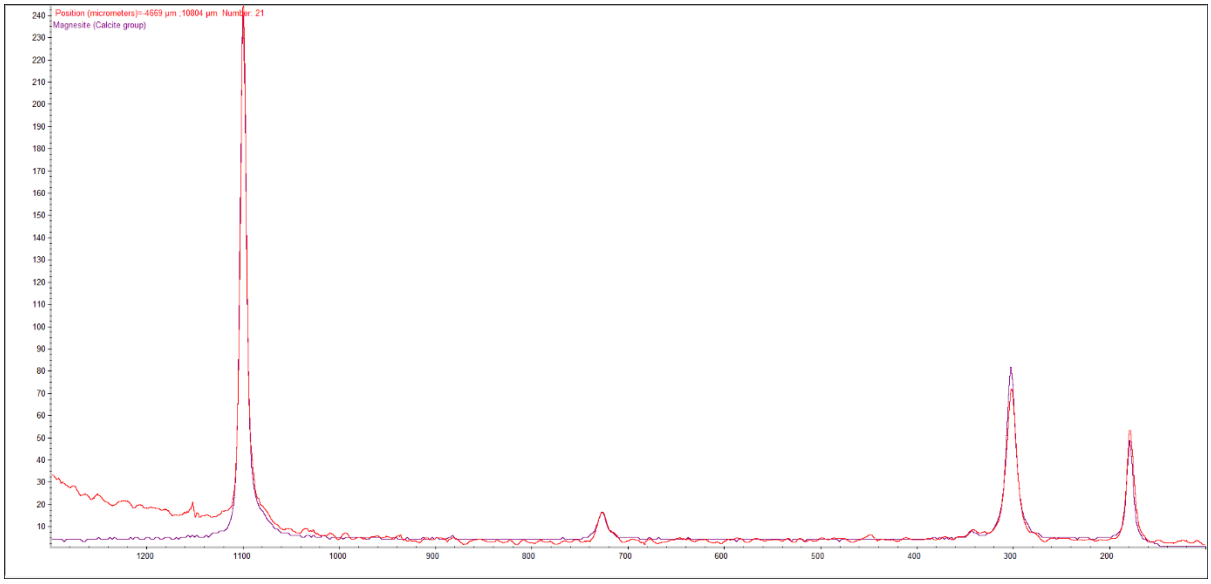

Figure 4.5: Magnesite (purple) match for Raman scan of sample W

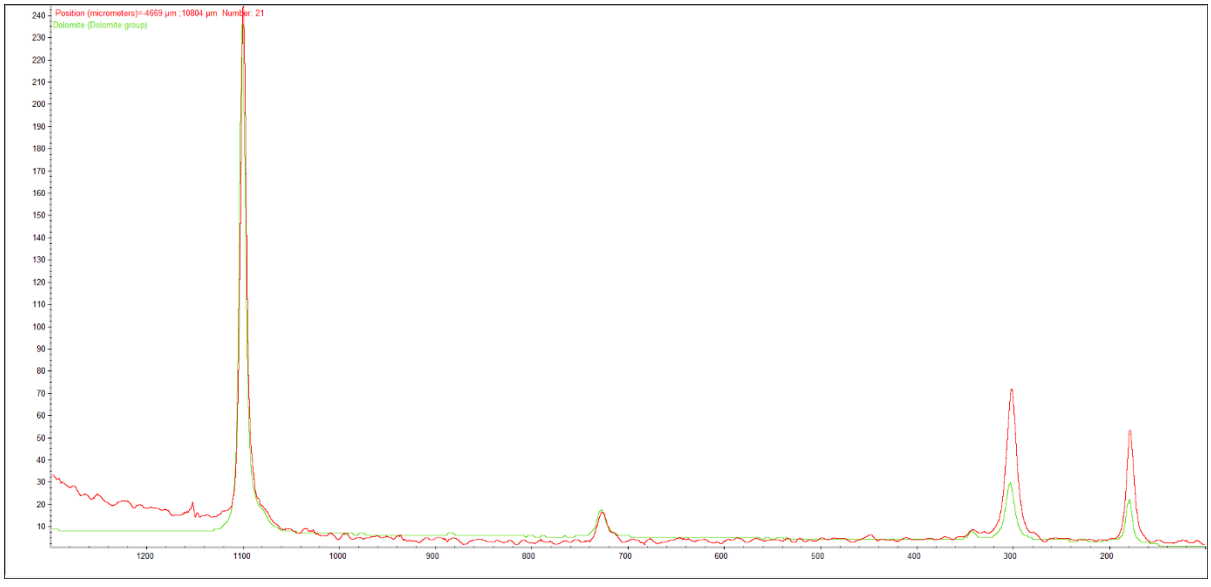

Figure 4.6: Dolomite (green) match for Raman scan of sample W

According to the XRF results in Table 4.1, $CaCO_3$ makes up 54.21% percent of sample W. With 0.42% being present as calcite (XRD results) this leaves (by difference) 53.79% of $CaCO_3$ in the sample to be present as dolomite

($CaMg(CO_3)_2$).

Table 4.5: The different phases in which $CaCO_3$ occurs in sample W

Phase	Analysis	$CaCO_3$ [%]
All phases	XRF	54.21%
Calcite	XRD	0.42%
Dolomite	By difference	53.79%

$FeCO_3$ (siderite) makes up 0.52 % (equivalent to 0.25% Fe) according to the XRD data. Iron is present as Siderite because of the oxidation state of Iron (Fe^{2+}) in the sample source geological region (Fischer and Knoll, 2009). However, according to the XRF results, sample W contains a total of 0.54 % Iron – therefore leaving 0.29% of Iron present in phases/minerals other than Siderite. One of these phases is Pyrite. Pyrite was identified in the petrography of sample W and was estimated to be present as <1%. The Iron which is not present as Siderite or Pyrite is therefore present as $Fe(OH)_3$ or Iron silicates according to geological information of the sample source region (Fischer and Knoll, 2009). The presence of Pyrite was supported by an unidentified peak during a Raman scan.

Only one of the 50 Raman scans done on the DXR instrument (see Methodology) showed an exception. As seen in Figure 4.7, the peak at ±370 cm^{-1} did not fit any matches and cannot be explained conclusively. It is suspected, however, to be a peak originating from the presence of pyrite. As mentioned previously, petrography identified a Pyrite phase in sample W. Pyrite has only two Raman shifts (of equal intensity), at 340 cm^{-1} and 370 cm^{-1} – (Refer to Figure 4.8 (rruff.info)). The intensity of the peaks in Figure 4.7 at 340 cm^{-1} and 370 cm^{-1} does not differ by much and the presence of pyrite is therefore confirmed. It is also known that Raman can identify numerous phases in one scan (see Appendix D3) and therefore the Pyrite phase is identified along with the Dolomite phase.

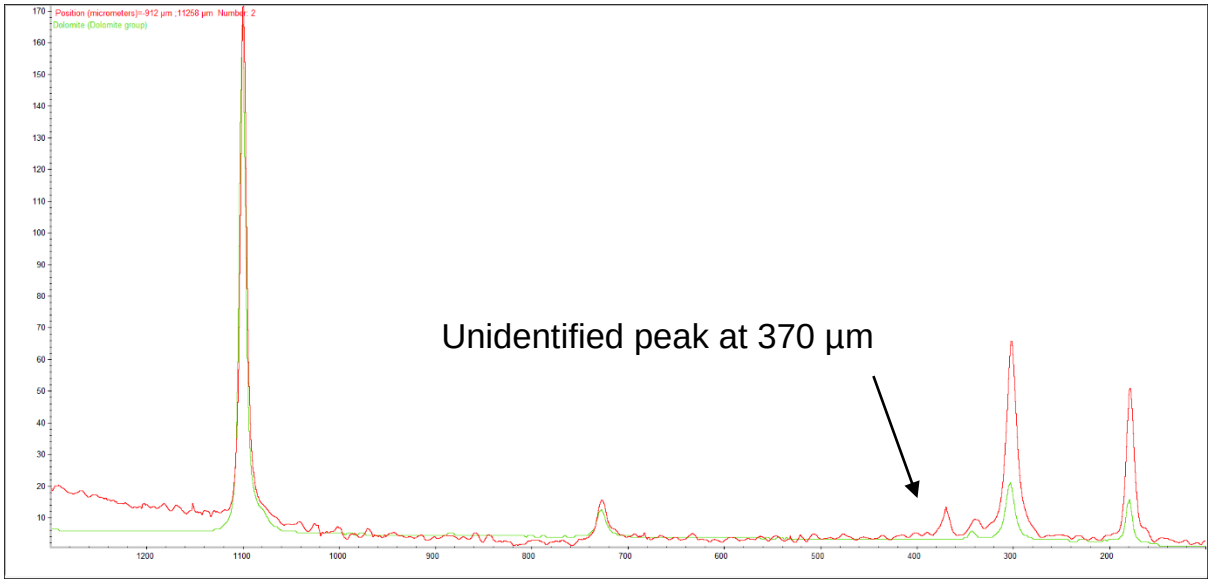

Figure 4.7: Raman scan of sample W (red) with an unidentified peak at ±370 µm

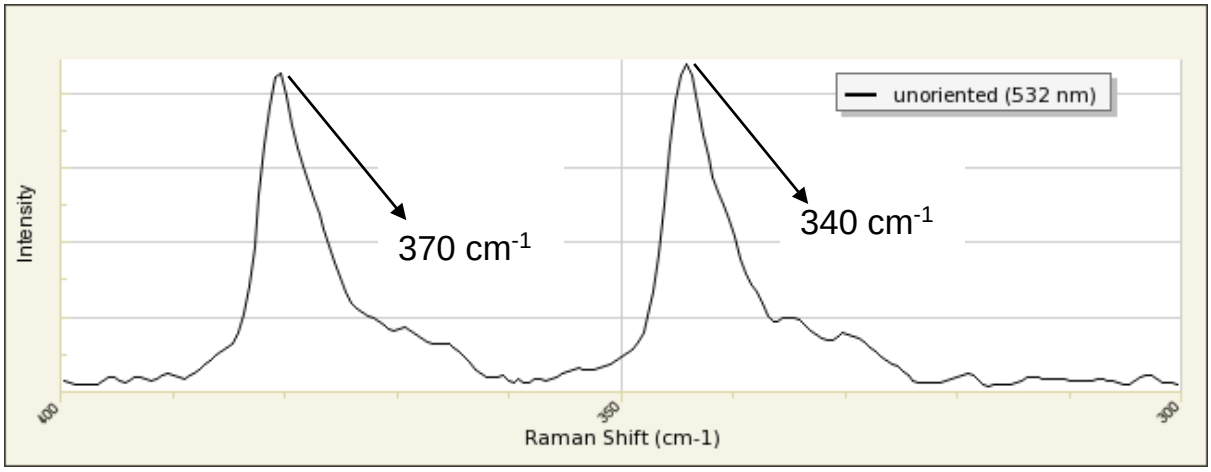

Figure 4.8: Raman scan of Pyrite between 300 cm^{-1} and 400 cm^{-1} (rruff.info)

The Raman wavenumbers of the dolomite sample are shown in Table 4.6. Limestone and dolomite have characteristic peaks at 155, 282, 712, 1086 and 1436 cm^{-1} (Krishnamurti, 1957). This work evaluated the Raman spectra only from 100 – 1200 cm^{-1}.

Table 4.6: Sample W (dolomite – Gauteng) wavenumbers

Wavenumbers (v) of Raman bands of dolomite			
Assignment	Ref [1]	Ref [3]	Sample W
T(Ca, Mg, CO_3)	187	179	174.2
T(Ca, Mg, CO_3)	309	304	292.1
v_4 - Asymmetric CO_3 deformation	733	725	723.1
v_1 - Symmetric CO_3 stretching	1106	1100	1096.5

R = rotational lattice mode, T = translational lattice mode

[1] = (Gunasekaran et al., 2006)

[3] = (Huang and Kerr, 1960)

In the dolomite, the major bands show a shift to higher numbers (Gunasekaran et al., 2006). The shifting of bands between dolomite and limestone for the samples in this study is shown in Table 4.77.

Table 4.7: Shifting of wavenumbers between limestone and dolomite

Structural deformation	Wavenumbers [cm^{-1}]	
	Limestone Sample Y	Dolomite Sample W
T(Ca, Mg, CO_3)	154.1	174.2
T(Ca, Mg, CO_3)	280	292.1
v_4 - Asymmetric CO_3 deformation	711.1	723.1
v_1 - Symmetric CO_3 stretching	1085.2	1096.5

The two lower wavenumbers (174 and 292 cm^{-1}) observed in the dolomite sample Raman spectra (Table 4.6) arise from the external vibrations of the CO_3 groups that involve translatory oscillations of those groups (Krishnamurti, 1957).

The larger wavenumbers at 723 and 1097 cm^{-1} arise from the internal vibrations of the CO_3 groups inside the crystal (Krishnamurti, 1957).

4.3.2 Limestone (Sample X) – Northern Cape

An XRD scan of limestone X (Figure 4.9) showed that it contains 99.23% Calcite and 0.77% Quartz.

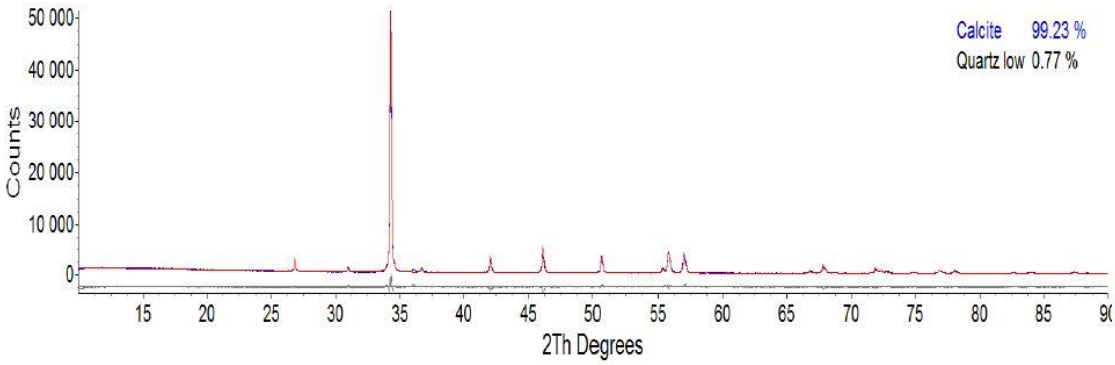

Figure 4.9: Matching phases for the XRD spectra of sample X

Raman scanning matched Calcite, Fluoborite, Thulite, and Eucryptite (Figure 4.10 – Figure 4.13) to the spectra of sample X. Eucryptite was eliminated as a possible phase because of the peak not matching at 162 cm^{-1} (Figure 4.13).

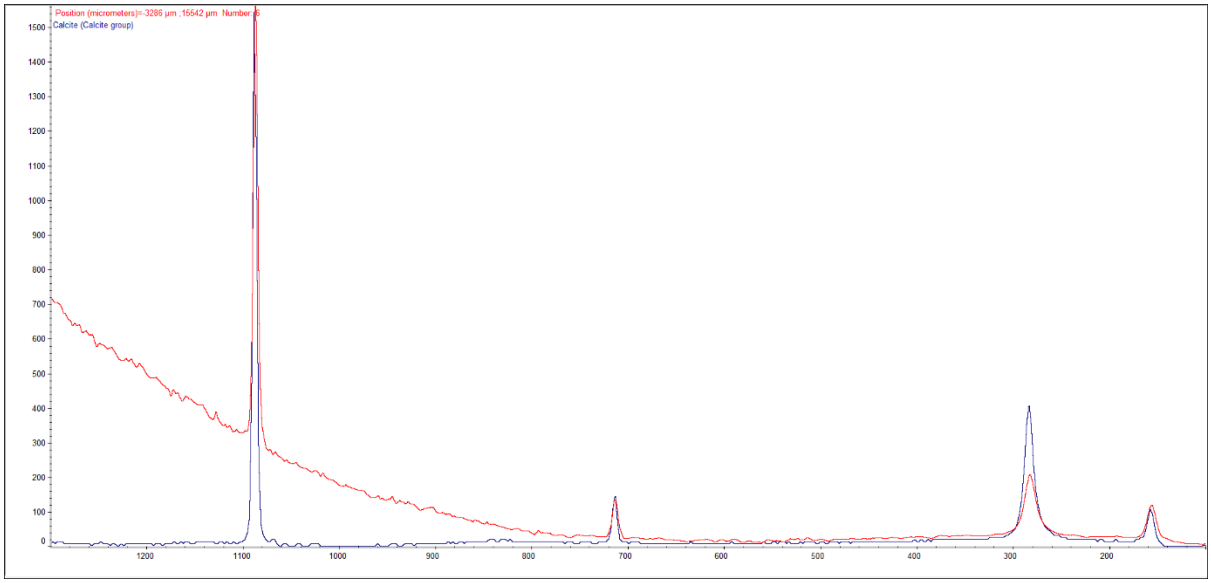

Figure 4.10: Calcite (blue) match for Raman spectrum of sample X (red)

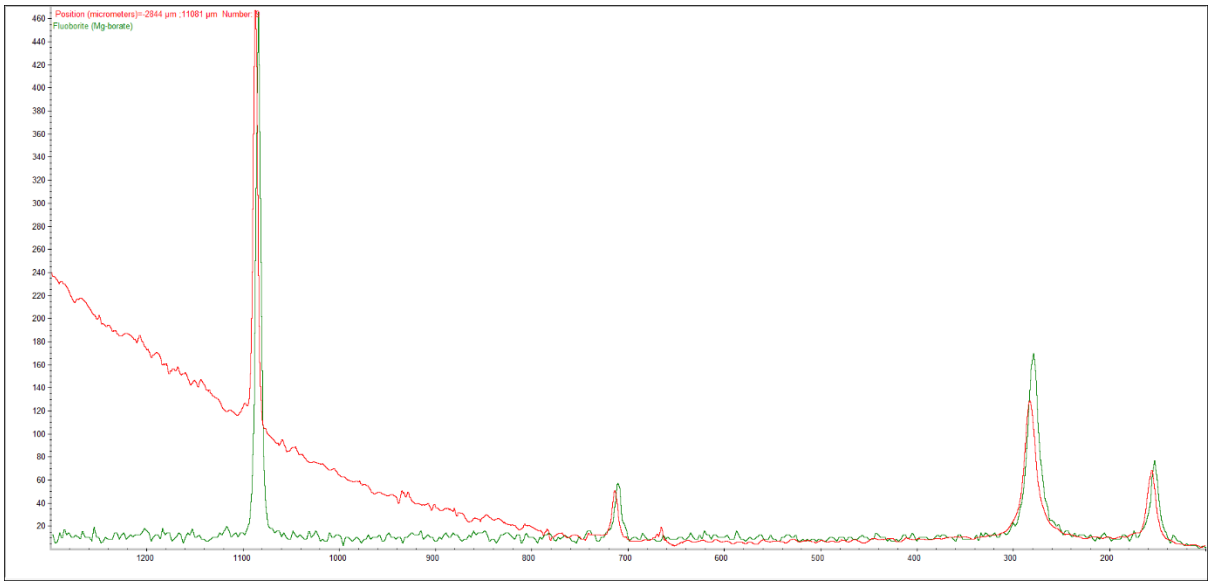

Figure 4.11: Fluoborite match (green) to Raman spectrum of sample X (red)

The amount of SiO_2 picked up by the XRD (0.77%) is more than what is reported in the XRF results (0.21%) because SiO_2 is not distributed uniformly throughout the sample. SiO_2 can occur as pure quartz or as part of a complex mineral. Raman spectroscopy is especially complementary in this case when it is necessary to establish whether SiO_2 occurs as pure quartz, as a mineral/clay or as quartz together with a mineral/clay.

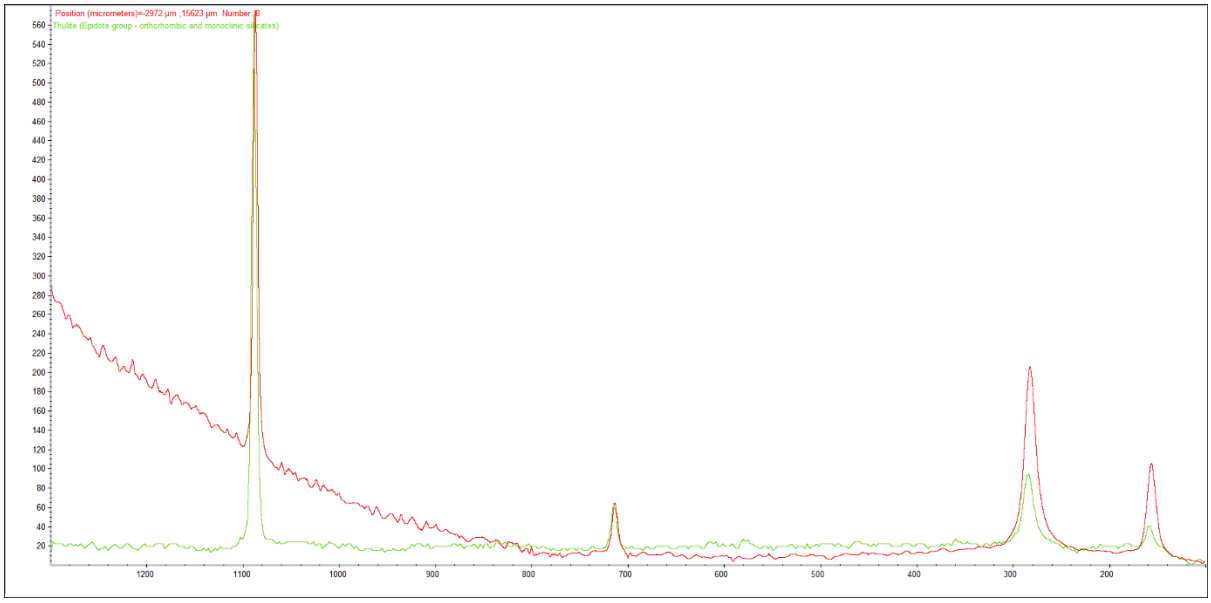

Figure 4.12: Thulite match (green) to the Raman spectrum of sample X (red)

As can be seen in Table 4.4, quartz was not identified in sample X by Raman analysis. Since 20 points were analysed on the Renishaw inVia Raman spectrometer and not one point contained a quartz phase it can be said with confidence that SiO_2 occurs in a mineral/clay form in sample X. Thulite was identified by Raman spectroscopy as the only Si–containing mineral and it is therefore concluded that Si occurs only as Thulite in sample X.

Thulite is the source of not only Silicon but also of Manganese in the sample. Manganese substitutes up to 2% of the Calcium in the limestone (Calvert and Pedersen, 1996). Thulite as the only Si–containing phase is supported by a routine calculation. According to XRF results Mn = 0.4% (Table 4.2) and if the amount of Si in Thulite is then calculated based on molar mass proportions

$$\%Si = \frac{MM_{Si}}{MM_{Mn}} \times \%Mn$$

$$= \frac{28.085}{(2 * 54.938)} \times 0.4\%$$

$$= 0.1\%$$

which is the same amount of Si reported by the XRF results (Table 4.1).

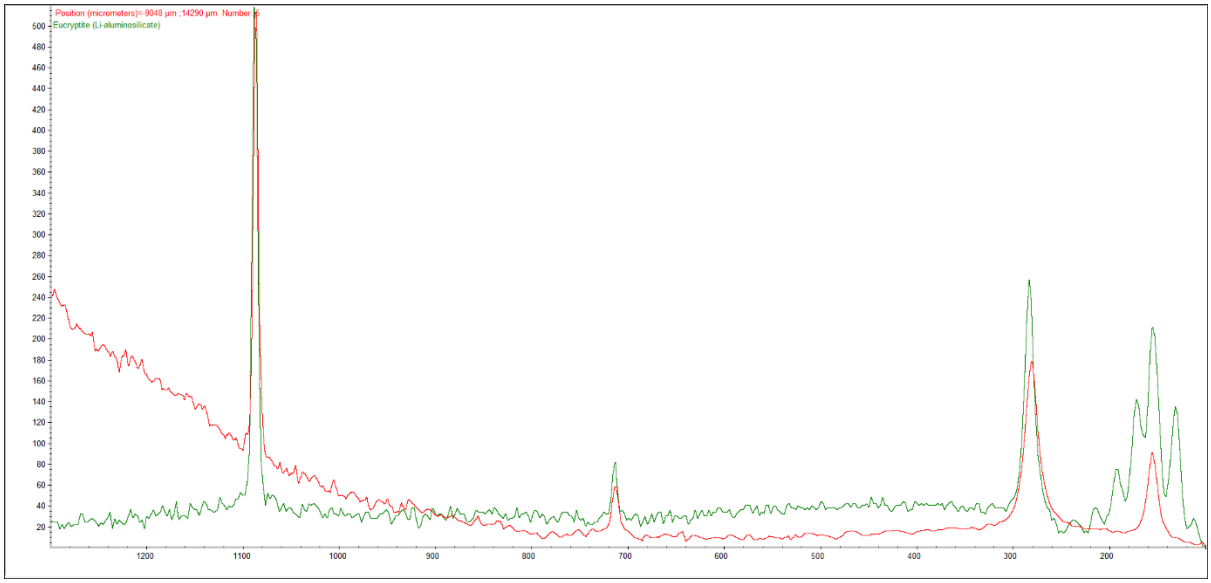

Figure 4.13: Eucryptite match (green) to Raman spectrum of carbonate rock X (red)

The presence of Thulite is further supported by geochemistry data. The Manganese in Thulite is present in the divalent state and thus corresponds to the geochemistry of the source area (Beukes, 1987). The occurrence of Manganese in a siliceous/chert mineral is explained by Beukes (1987) as follows:

"*…rimmed shelf margin stromatolitic mounds and columns would have been exposed to well–circulated ocean water. Therefore it is highly probable that the associated Manganese–rich dolomites and dolomitic limestones developed from Manganese–enriched marine phreatic water with intermediate*

alkalinity….the introduction of relatively large amounts of iron into these carbonates may have been related to the development of anaerobic conditions below the sediment–water interface which, according to Berner (1971), results in more acidic pore–water conditions. Such conditions would also explain the presence of replacement chert nodules and beds in the deep

Magnesium occurs as two minerals in sample X – Ferroan dolomite (Figure 4.14) and Fluoborite (Figure 4.11). The presence of Ferroan dolomite in the sample source area is confirmed by Beukes (1987). The exact reason why Magnesium occurs as Fluoborite is not certain and could form part of a future investigation. The black dots observed on the calcite during Raman scans are characteristic of Fluoborite and therefore provide further confirmation of the presence of Fluoborite.

Because of the geochemistry of the sample X source, Iron can occur as Siderite ($FeCO_3$), Iron silicates or Ferroan dolomite in sample X (Fischer and Knoll, 2009; Klein and Beukes, 1989). The source of the Iron is the Gamohaan Siderite–chert layer just above the intraclastic limestone layer that migrated into the limestone (Klein and Beukes, 1989). Another feature of the Siderite–chert layer is that some Iron is present as Ferroan dolomite. Ferroan dolomite in sample X was confirmed by XRD –refer to Figure 4.14. The Single Particle Analysis (SPA) was also used to determine more accurately in which form Fe is present. This is covered in detail in the SPA section.

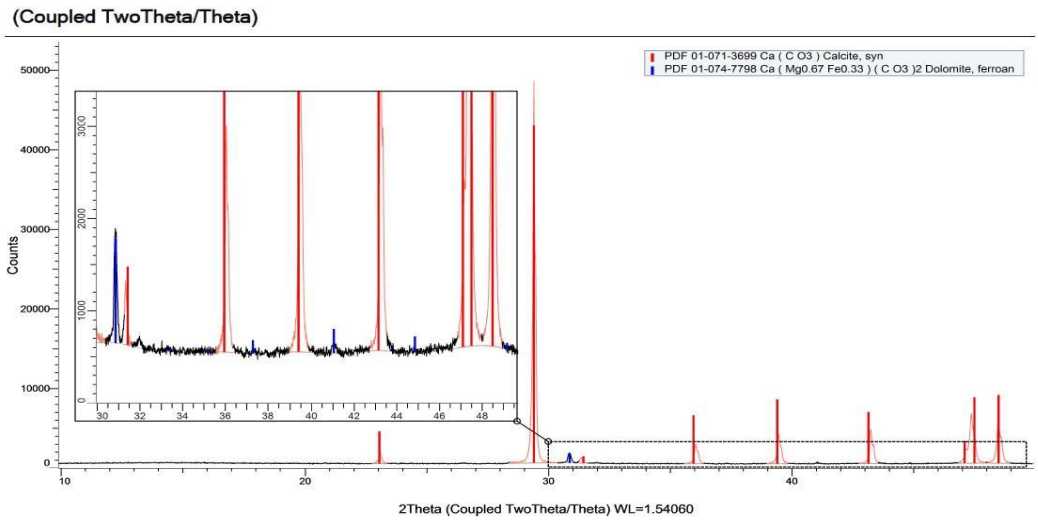

Figure 4.14: Ferroan dolomite match for XRD spectrum of sample X

The Raman wavenumbers of sample X are discussed together with wavenumbers of sample Y in the sample Y discussion because samples X and Y are both from the same source area.

4.3.3 Limestone (Sample Y) – Northern Cape

An XRD scan of sample Y (Figure 4.15) shows that the sample contains 99.65% calcite and 0.35% quartz.

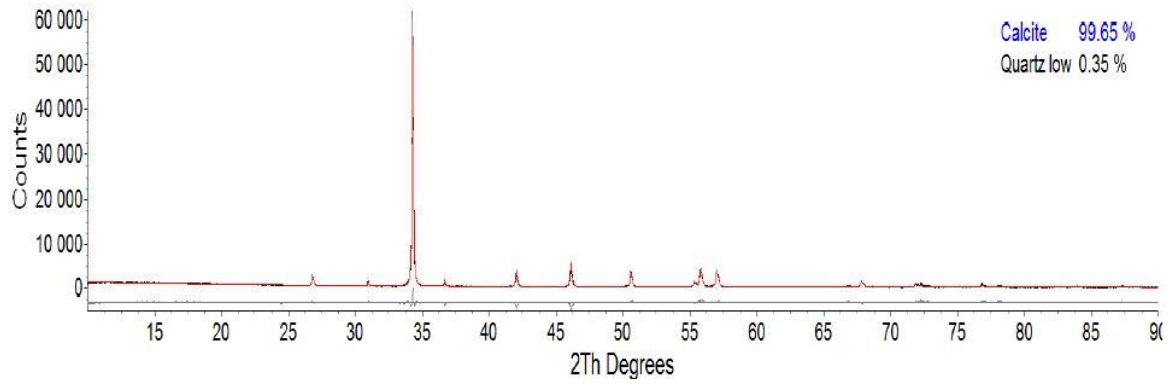

Figure 4.15: Matching phases for the XRD spectrum of sample Y

The Raman spectra of sample Y matched with Calcite (Figure 4.16), Fluoborite, and Thulite (Figure 4.17). The 0.95% $MgCO_3$ in the sample (Table 4.1) is present as a mineral – Fluoborite.

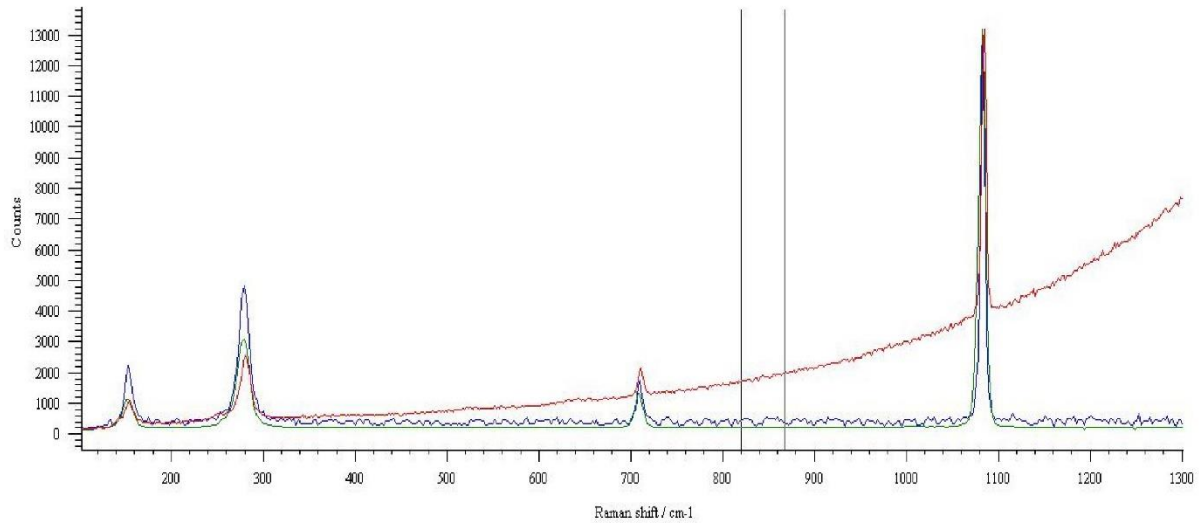

Figure 4.16: Calcite (green) and Fluoborite (blue) match for Raman spectrum of sample Y (red)

Sample Y contains 0.4 % Mn and 0.03 % Si (calculated from the oxide % in Table 4.1). Thus, according to the chemical formula of Thulite [$Mn_2Al_3(SiO_4)$], Si is expected to be 0.1%. This, however, is not the case. If Si does occur as Thulite it occurs only as a small percentage. Si therefore probably occurs as pure quartz. This statement is supported by the fact that Thulite often occurs along with quartz (Schaller and Glass, 1942). Because quartz was identified by XRD and Thulite by Raman spectroscopy (Figure 4.17) it is therefore concluded that Si occurs in both quartz and in Thulite. The Thulite in sample Y, just as in sample X, is the source of both Silicon and Manganese.

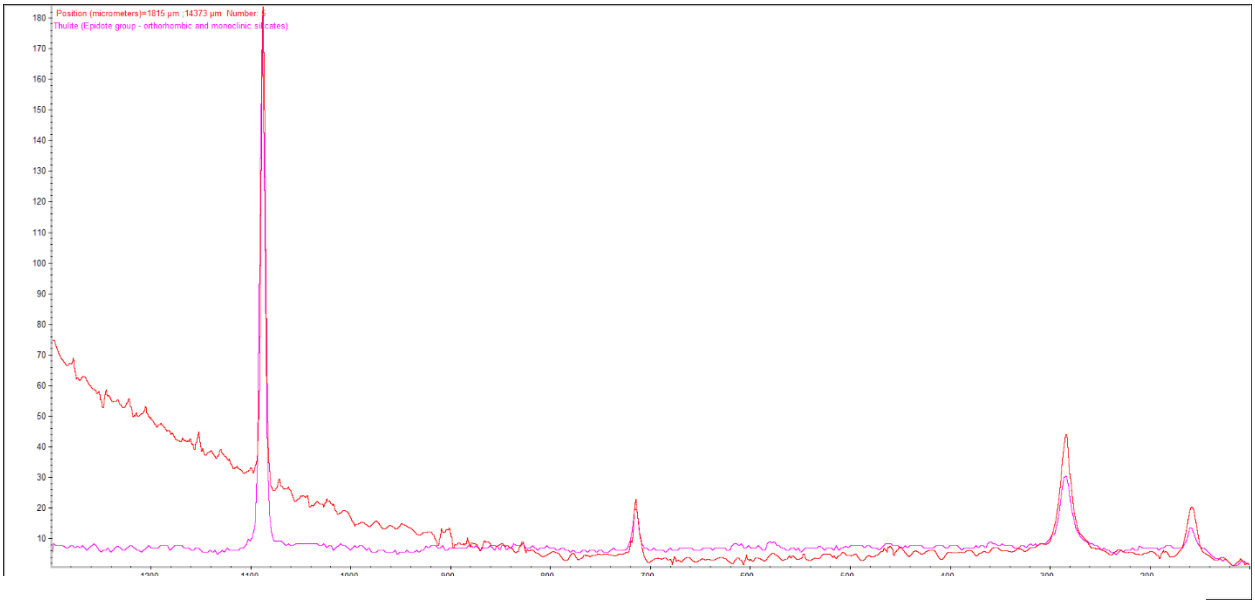

Figure 4.17: Thulite (purple) match for Raman spectrum of sample Y (red)

No Iron–containing phases were matched to the Raman spectrum of sample Y. XRF and SPA results proved however that Fe is definitely present in sample Y. It is therefore unclear in which mineral form Fe occurs in sample Y.

The wavenumbers of samples X and Y match closely the characteristic peaks of 155, 282, 712, 1086 and 1436 cm^{-1} (Krishnamurti, 1957). A wavenumber at 1436 cm^{-1} was not detected in this study because the Raman spectroscopy was only done from 100 – 1200 cm^{-1}. Raman bands at 282 cm^{-1} and 155 cm^{-1} are indicative of translations along the trigonal axis of the carbonate (Krishnamurti, 1957). The band at 155 cm^{-1} was not detected in sample X because sample X was analysed from 200 – 1200 cm^{-1}.

Table 4.8: Sample X and Y (limestone –Northern Cape) wavenumbers

Wavenumbers (v) of Raman bands of calcite I					
Assignment	Ref [1]	Ref [2]	Ref [4]	Sample X	Sample Y
T(Ca, CO_3)	162	155	156	-	154.1
T(Ca, CO_3)	288	281	283	279.3	280
v_4 - Asymmetric CO_3 deformation	716	711	713	711	711.1
v_1 - Symmetric CO_3 stretching	1092	1085	1085	1084.5	1085.2
Unidentified peaks	-	-		443.6	1014.3

R = rotational lattice mode, T = translational lattice mode

[1] = (Gunasekaran et al., 2006); [2] = (White and Farmer, 1974);

[4] = (Liu and Mernagh, 1990)

The only possible band found in literature that could match the unidentified band of sample X at 444 cm^{-1} (Table 4.8) is quartz which is known to appear at 461 cm^{-1} (Gunasekaran and Anbalagan, 2008). This is contradictory to the statement made earlier in this section that sample X does not contain Si in the quartz phase. However, quartz was identified in only 1 of the 20 points scanned by the Raman instrument. Therefore, the presence of quartz is explained by the fact that the quartz is not uniformly distributed in the sample.

The unidentified band of sample Y at 1014 cm^{-1} is considered to be due to a dolomitic phase (Sun et al., 2014), confirming the previously mentioned observation that sample Y also contains a dolomitic phase.

4.3.4 Limestone (Sample Z) – Zambia

XRD results of sample Z (Figure 4.18) show that it consists of 99.45% calcite and 0.55% Quartz.

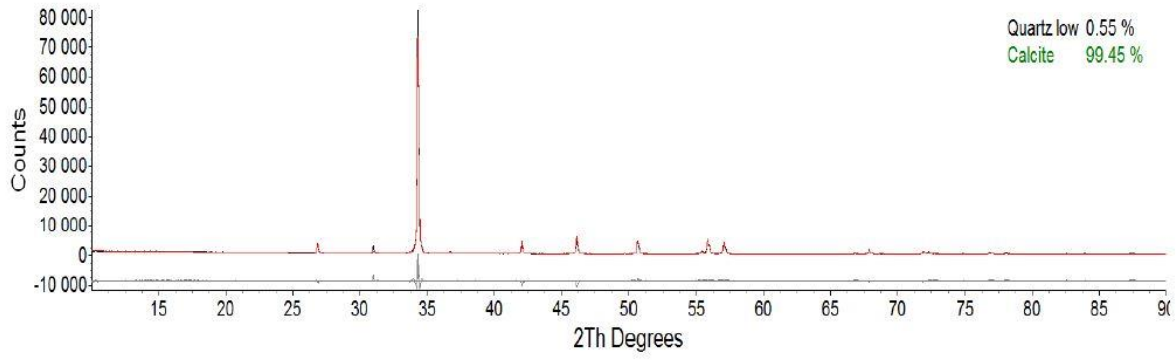

Figure 4.18: XRD spectrum of sample Z

Due to the project operations schedule, Raman scans of sample Z could not be done at the same time as samples W, X and Y. Raman scans of sample Z were however done at a later stage by Manchester Metropolitan University (see acknowledgements). Only the names of the matching phases for sample Z were saved, not the images. The Raman spectroscopy results showed that the sample Z spectra matched the phase spectra of Calcite, Aragonite, Fluoborite, Libethenite, Graphite and Quartz. To understand the array of phases occurring in sample Z it is necessary to look back to the geochemistry and diagenesis of sample Z.

The complete lithostratigraphy of the Kakontwe group is explained in the literature section. A summary of the Kakontwe formation is shown in Table 4.9.

Table 4.9: Relation of Kakontwe limestone formation

Nguba group	Muombe subgroup	Kipushi formation
		Kakontwe formation
		Kaponda formation
		Grand conglomerate (Mwale) formation

The Mwale formation which is situated below the Kaponda and Kakontwe formation is described by Batumike Mwandulo et al. (2007) as follows:

"*Sulphide–rich carbonaceous beds (pyrite and chalcopyrite) and a 10m–thick conglomeratic sandstone bed occur at the base and top of the formation, respectively. Quartz (11–12 vol.%), granite (7–9 vol.%), dolomite (4–6 vol.%), quartzite (3–4 vol.%), sandstones (1–2 vol.%), feldspar (0–1 vol.%) and mica schist (0–0.6 vol.%) clasts are randomly distributed in a dolomitic or carbonaceous shale matrix…In the Kipushi Pb–Zn–Cu mine, the Mwale formation contains sulphide–rich veinlets cutting across–bedding in shale beds.*"

This description offers an explanation for the occurrence of quartz, graphite and Libethenite (a Cu–containing mineral) in the limestone. The absence of any sulphur–containing minerals is especially peculiar since literature predicts these minerals (Batumike Mwandulo et al., 2007; Dechow and Jensen, 1965).

The presence of aragonite in sample Z can for the moment not be explained, but thermal techniques are able to give a better indication of whether aragonite is actually present. According to literature, aragonite transitions to calcite between 403 °C and 496 °C (Perić et al., 1996). Faust (1949) and Passe–Coutrin et al. (1995) reported 496 °C and 470 °C respectively as more specific temperatures for the transition of aragonite to calcite.

The reason for the occurrence of Fluoborite is not certain since the Magnesium–containing phase in the Kakontwe limestone is dolomite (Batumike Mwandulo et al., 2007; Binda and Van Eden, 1972; Mills, 2000). However, it is quite possible for Mg to occur in minerals other than dolomite. Thermogravimetric (TG) data offered more information on how Mg is present in the sample.

No Fe or Al–containing phases were identified by Raman spectroscopy even though XRF data showed that the sample contains Fe and Al. Variations in the distribution of impurities throughout the sample are a possible reason for this.

Literature indicated the presence of Iron oxides occurring in the dolomite of the Kakontwe formation (Batumike Mwandulo et al., 2007). Thus the Iron in sample Z identified by XRF analysis most likely occurs as Iron oxides.

4.4 Surface Characteristics

Scanning Electron Microscopy (SEM) and Electron dispersive X–ray spectroscopy (EDX) were used to determine the surface characteristics of the samples.

4.4.1 Dolomite – Sample W (Gauteng)

From Figure 4.19 it can be seen that the prepared carbonate rock sample W has a wide range of particle sizes, ranging from 1 µm up to 50 µm. There are fewer particles present from the upper part of the range: 50–60 µm. Particles in the lower end of the size range: 1–50 µm are predominantly present and this is in agreement with the particle size distribution where 50% of the particles are 50 µm or smaller. The decomposition characteristics are therefore expected to be closer to those of small particles than of larger particles.

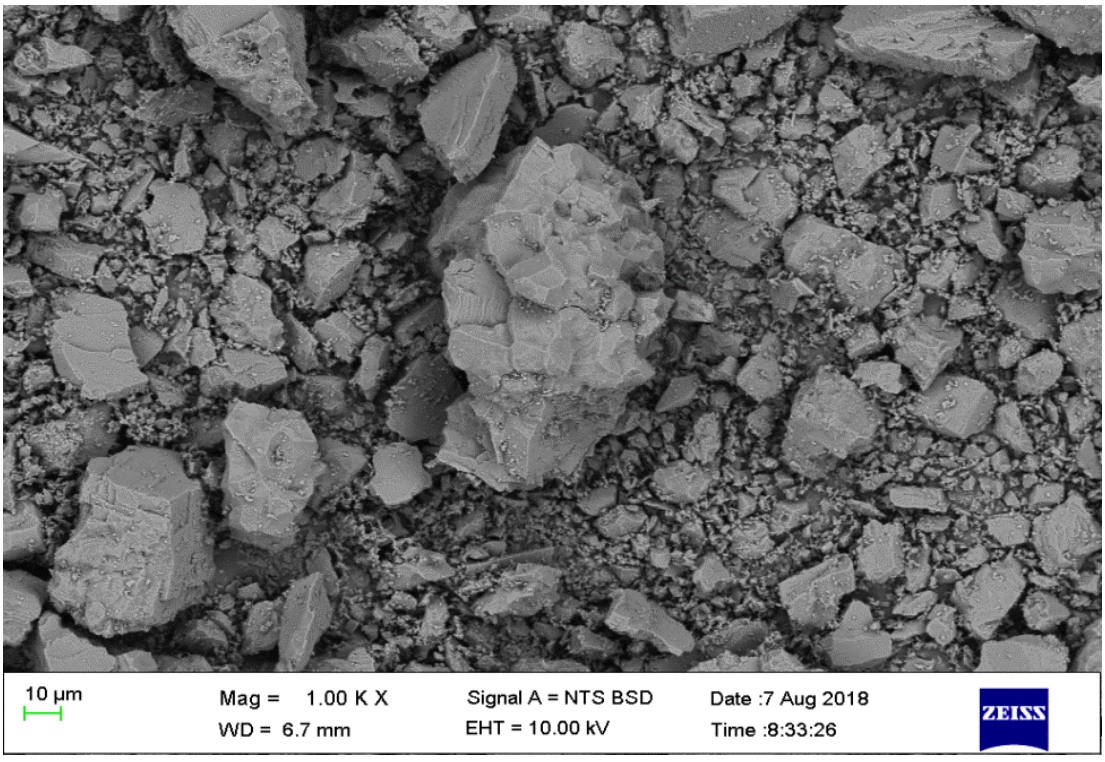

Figure 4.19: SEM image of carbonate rock W at 1000x. magnification

Figure 4.20 shows that very fine specks of powder, roughly 0.1–1 µm occur on larger particles. The very fine small particles would decompose readily under laboratory calcining conditions and would not have a significant impact on the decomposition rate. This sample could be classified as a magnesite according to the large proportion of uniform small (1–10 µm) grain sizes and the rhombic

shape of many of the particles (Harvey, 1970). However, because of the highly irregular fracture surface of the particles (Figure 4.20) and the relatively high silica content depicted in the XRF results it is more correctly classified as a clayey dolomite (Borgwardt and Harvey, 1972).

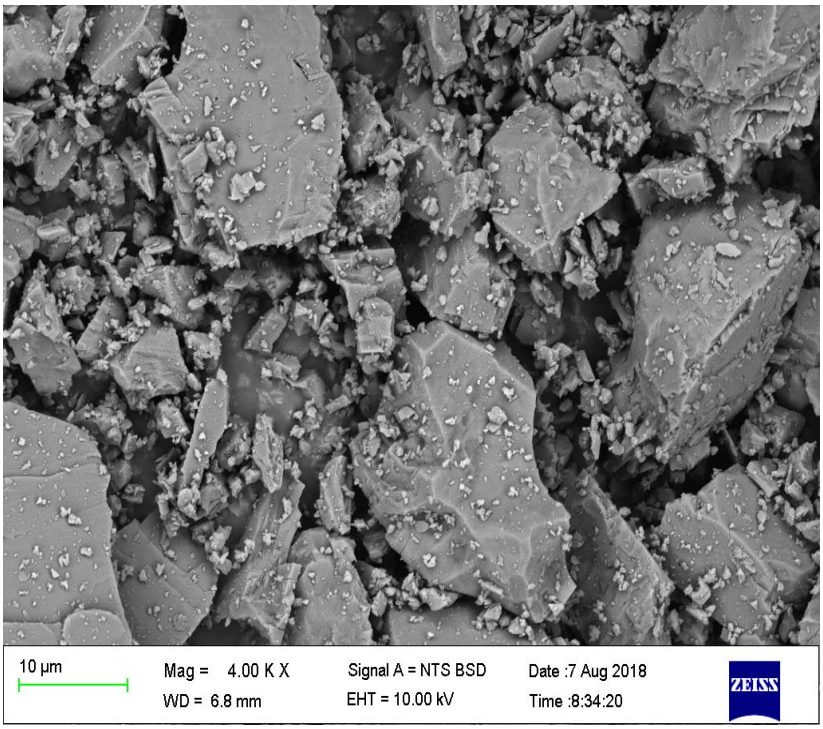

Figure 4.20: SEM image of carbonate rock W at 4000x magnification.

4.4.2 Limestone – Sample X (Northern Cape)

From Figure 4.20 it can be seen that a range of different particle sizes occurs in sample X. It is also clear that the particles are on average larger than the particles observed in sample W. This result confirms the particle size distribution analysis where the d_{50} size of sample X is 114 µm in comparison to 50 µm for sample W. In Figure 4.22, a particle of about 50 µm is shown and, just as in sample W, very fine specks of powder cover the larger particle. Sample X can be classified as a fine–grained calcitic limestone because of the

- grain boundaries that are distinctly curvilinear,

- the abundant sharp edges on the broken grains,

- cleavage steps on a few grains, and

- highly irregular surfaces with abundant tiny nooks and crevices (Harvey, 1970).

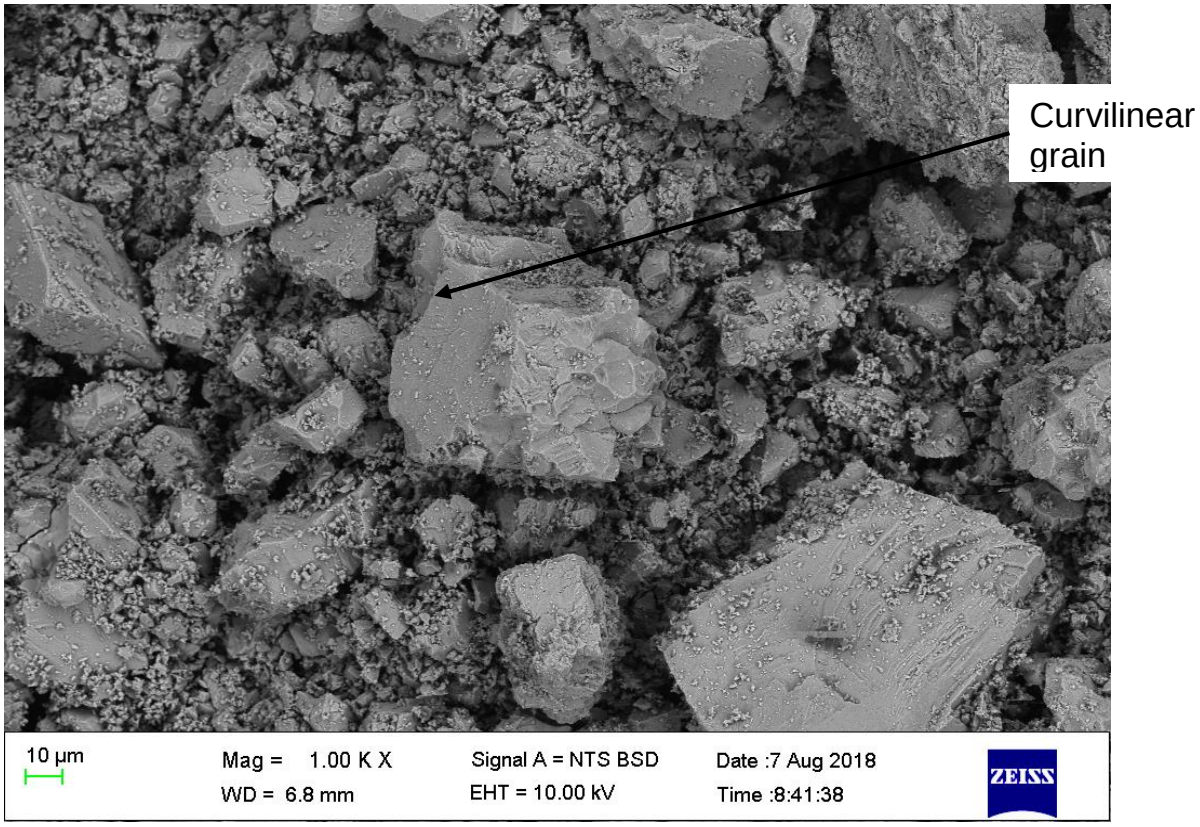

Figure 4.21: SEM image of carbonate rock X at 1000x magnification

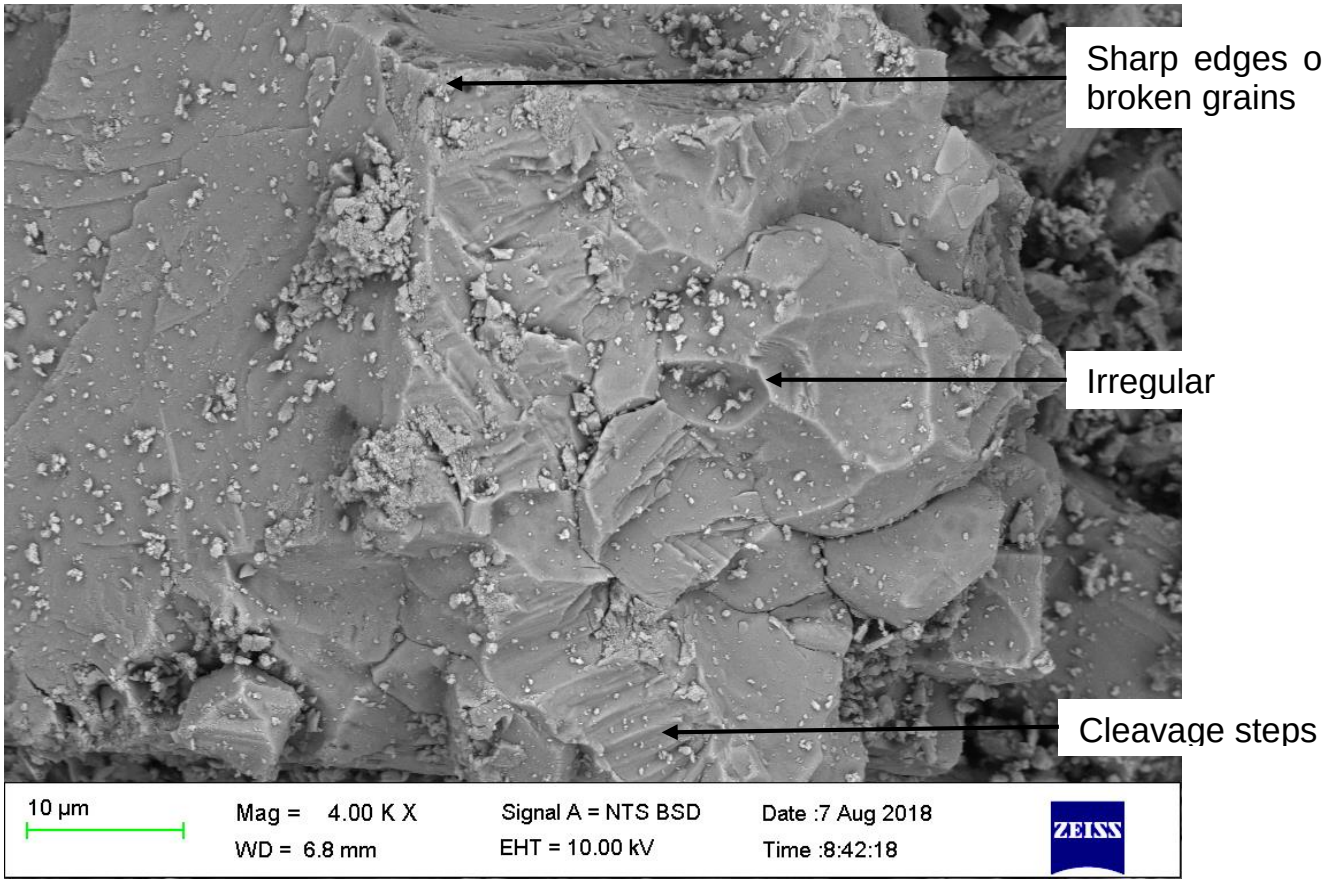

Figure 4.22: SEM image of carbonate rock X at 4000x magnification.

4.4.3 Limestone – Sample Y (Northern Cape)

A particle of roughly 150 µm is shown in Figure 4.23 and it can be clearly seen that larger particles are found in sample Y than in either sample X or W. This indicates a larger overall average particle size which is in agreement with the particle analysis that reports the d_{50} value of sample Y as 137µm. Smaller particles of 10–30 µm can be seen around the larger particle. Just as in samples W and X, small specks of powder are visible on the larger particles. The small specks of dust can be seen more clearly in Figure 4.24. Sample Y can also be classified as a fine grained calcitic limestone (Harvey, 1970). In Figure 4.24, some of the calcitic lamellae are clearly visible.

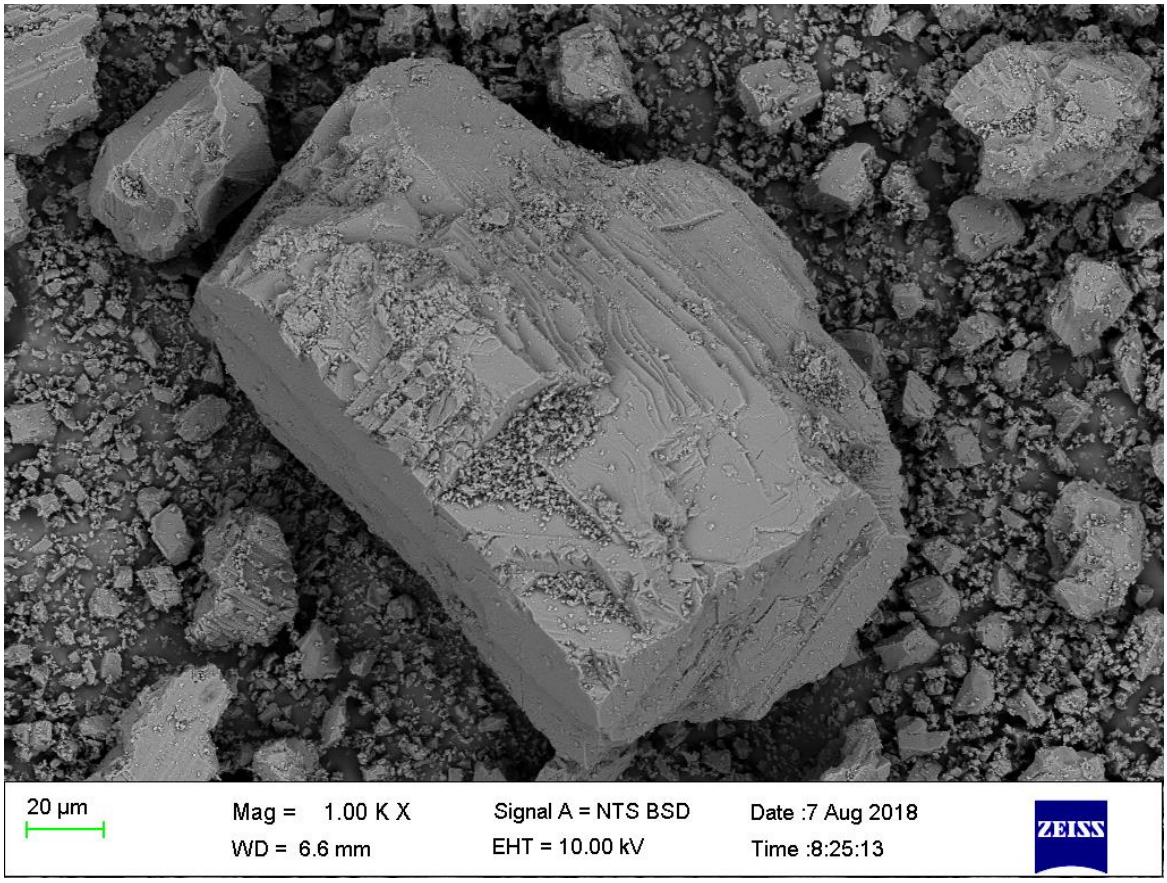

Figure 4.23: SEM image of carbonate rock Y at 1000x magnification.

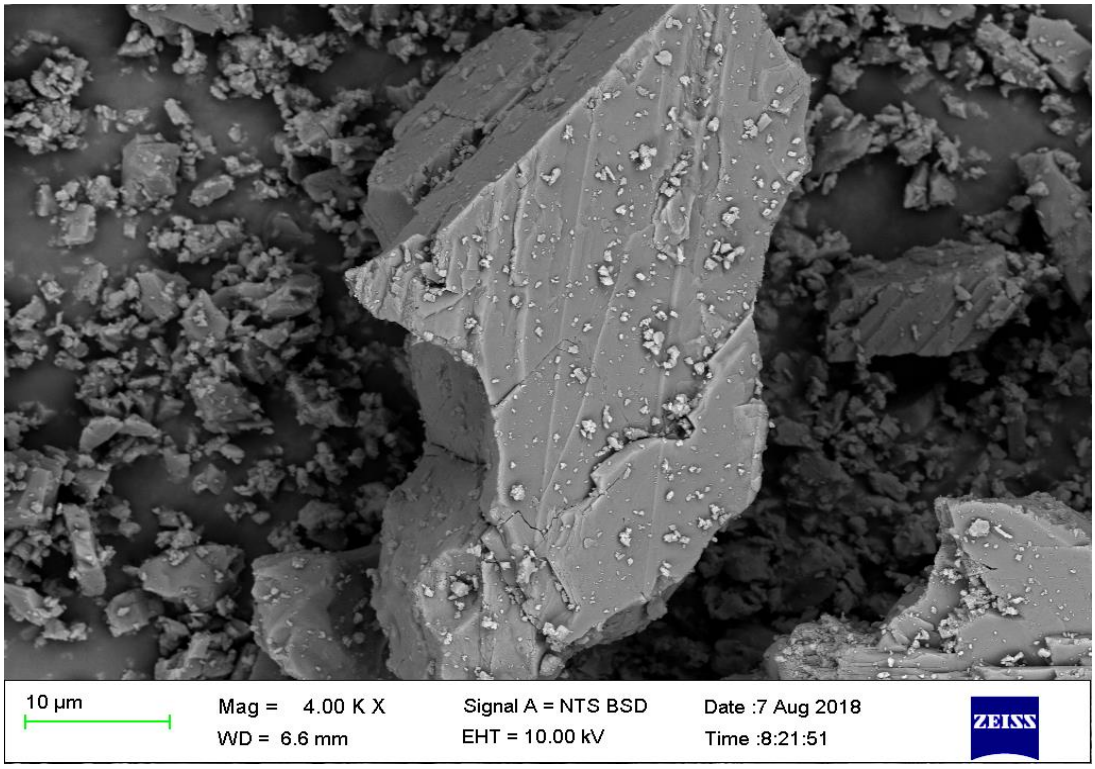

Figure 4.24: SEM image of carbonate rock Y at 4000x magnification.

4.4.4 Limestone – Sample Z (Zambia)

The 1000x and 4000x magnification SEM images of sample Z are shown in Figure 4.25 and Figure 4.26 respectively. A wide range of particle sizes can be seen in Figure 4.25.

Similar to the approach taken for sample X and Y, sample Z can be classified as a fine–grained calcitic limestone because of the i) sharp edges on the broken grains, ii) cleavage steps on a few grains, and iii) highly irregular surfaces with abundant tiny nooks and crevices (Harvey, 1970).

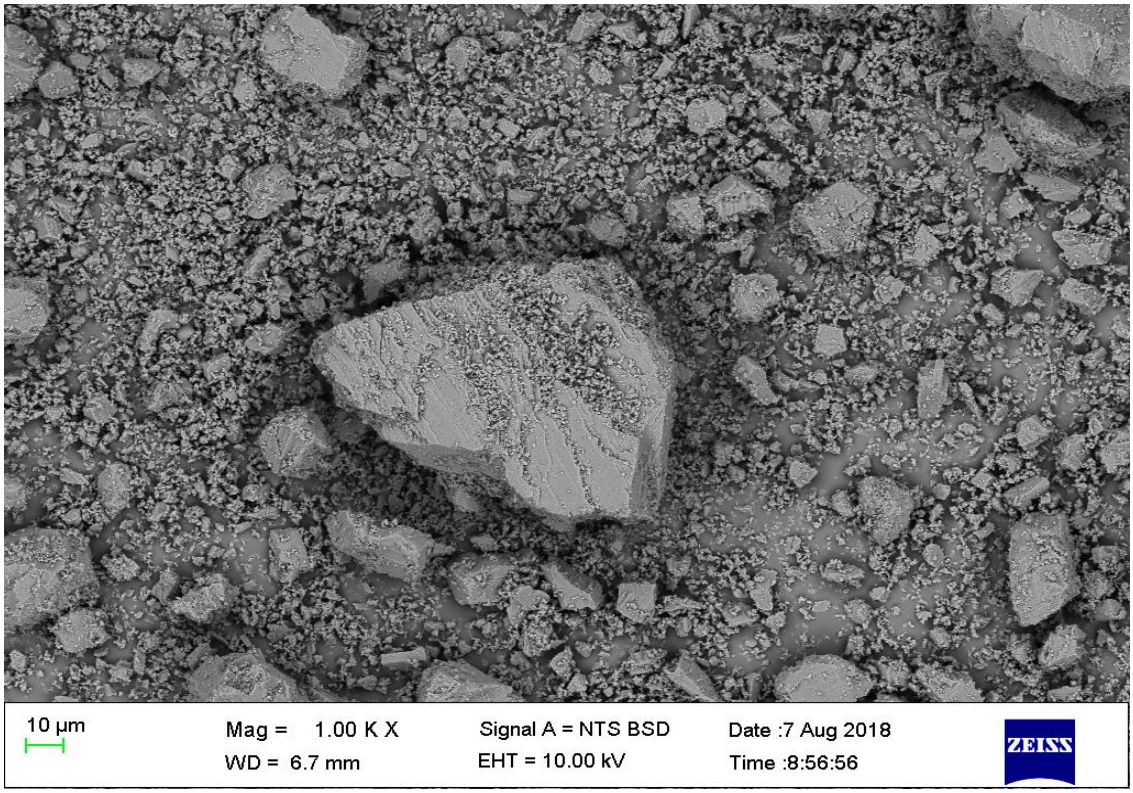

Figure 4.25: SEM image of carbonate rock Z at 1000x magnification

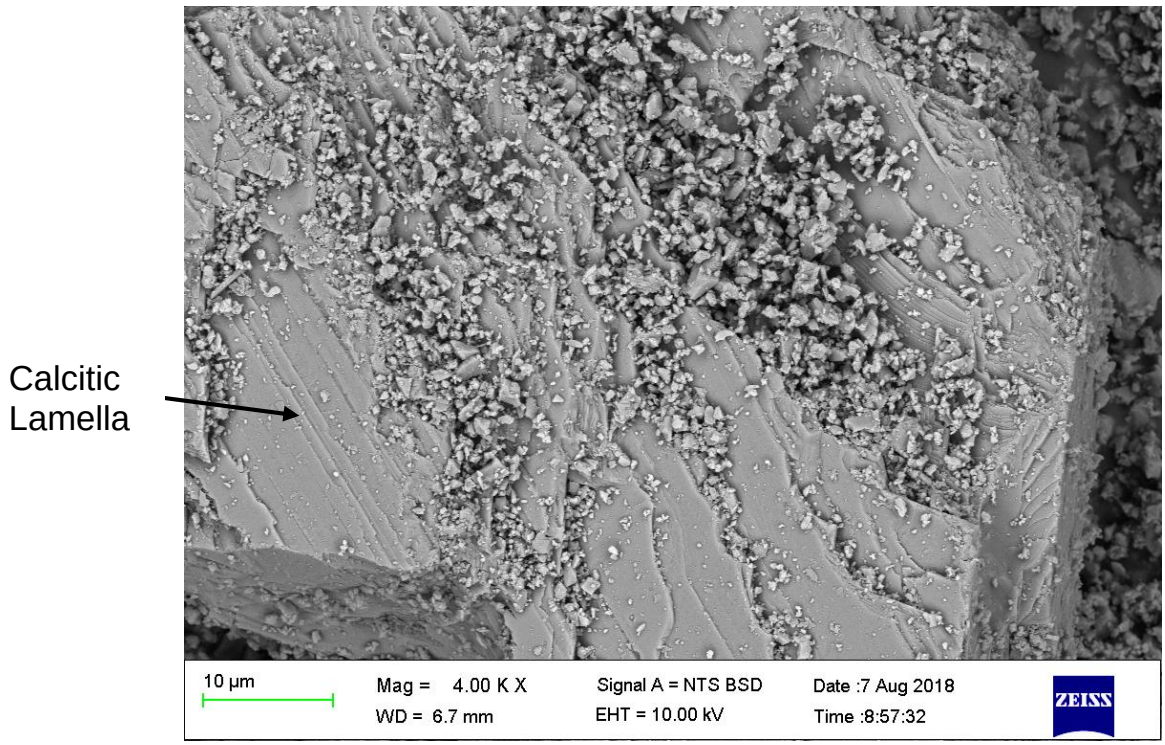

Figure 4.26: SEM image of carbonate rock Z at 4000x magnification

The calcitic lamellae are very clearly seen in the bottom left hand corner of Figure 4.26.

4.5 Single particle analysis (SPA)

SPA is a spectroscopic method used to analyse the chemical composition of individual particles of a powder. 1 – 10 µm size particles are required for this method. Each particle is scanned for elements and each element is then represented as a percentage of that particle. It can however happen that when the particle is very small and the scanning laser is larger than some particles, the laser often identifies the carbon tape on the stub as part of the particle. Figure 4.27 shows the SPA of samples Y, X and W.

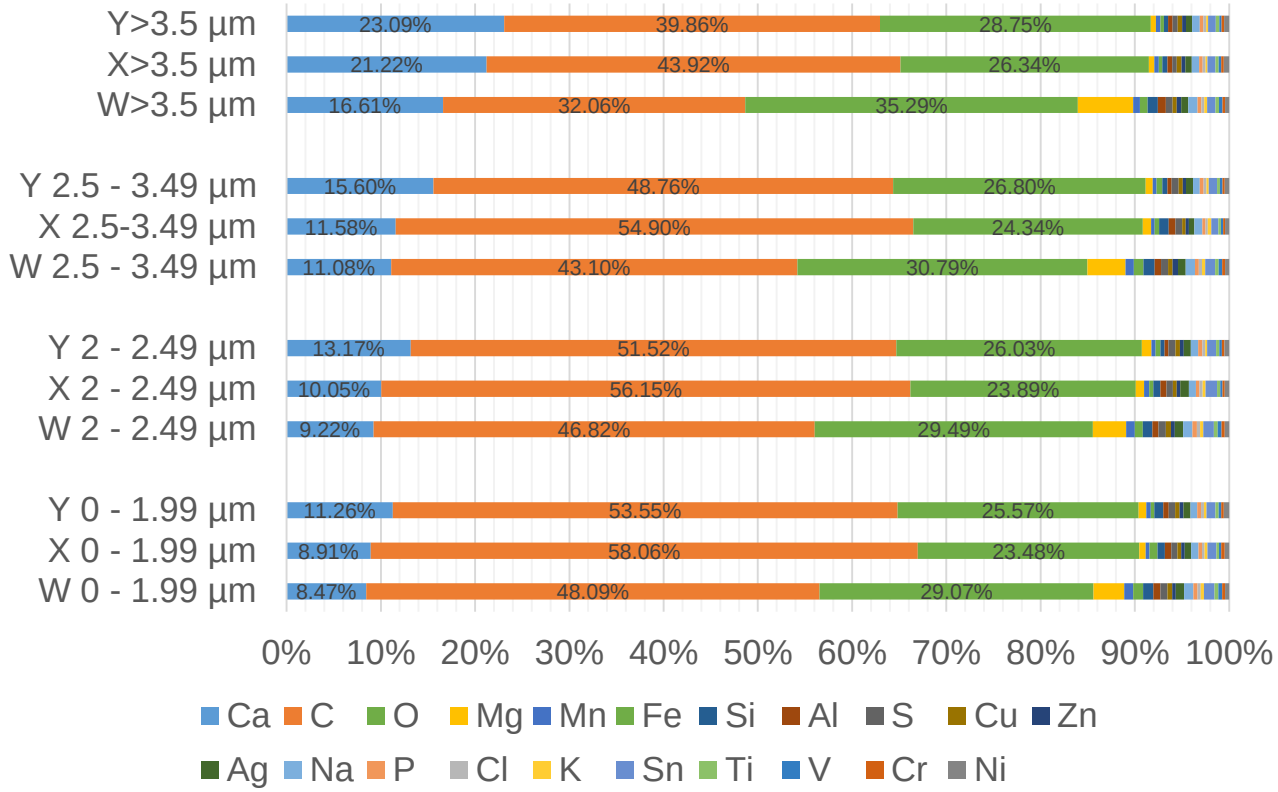

Figure 4.27: SPA of samples W, X and Y showing percentages of the main elements.

The main elements detected during Single Particle Analysis (SPA) were Ca, C, O and Mg. This is in accordance with the carbonate rocks X and Y being high purity limestones and sample W being a dolomite. As can be seen from Figure

4.27, sample W contains less Ca than samples X and Y for all particle sizes, and simultaneously contains more Mg for all the particle sizes. The reason for this is that sample W is a dolomite.

From molecular proportions it is expected that the mass percentage of C in a high purity limestone (95% – 98% $CaCO_3$) should be roughly 11.4% – 11.8%. The actual amount of measured C (Figure 4.27) ranges from 32% to 59%, and the amounts of the other elements present are therefore reduced in a corresponding manner.

A possible explanation for this observation is that additional carbon is detected during Single Particle Analysis (SPA) as a result of the carbon layer on the aluminium stub (used for sample presentation) in conjunction with the very small particle sizes that the method requires. The electron beam is typically 2µm in diameter, which is larger than some of the 1–2 µm particles. These particles therefore cover only part of the area exposed to the electron beam. The remaining area exposed to the electron beam is carbon and analysed as such by the EDX software (see Materials and Methods section for details on the EDX software). This idea is supported by the fact that the carbon content of larger particles is lower. The particles that are larger than the electron beam diameter can also contain more carbon because the particle is not centred exactly in the beam: the beam therefore interacts with only part of the particle and the rest of the beam interacts with the carbon on the SEM stub.

The Kandler method is not affected by this because it takes only elemental ratios into consideration and not the individual percentages.

From the SPA analysis, it can also be seen that the major trace elements are Mn, Fe, Si and Al. Another observation is that as the particle size increases, the mass ratio of Ca:O (calculated from molecular proportions) approaches the stoichiometric molar ratio of 0.83:1, being 0.8 in the size class of >3.5 µm.

As mentioned in the methodology section, the Kandler method interpreting technique was used to interpret the compositions of the single particles (SPA) and classify the particles into classes (compounds).

4.5.1 Kandler method

The Kandler method was applied to the SPA data to assist in the analysis of the data. Note that certain categories are tied to certain minerals (Table 4.10). Kandler et al. (2007) used transmission electron microscopy (TEM) to identify the phases in a particle and compared it to phases they deduced from the particle's chemistry. TEM was used instead of SEM because SEM can't identify phases, only elements. Figure 4.28 shows the Kandler results for the samples of this study. The relative amount of each phase in each Kandler class is shown in Figure 4.29. The various chemical structures of these phases are given in Figure 4.30.

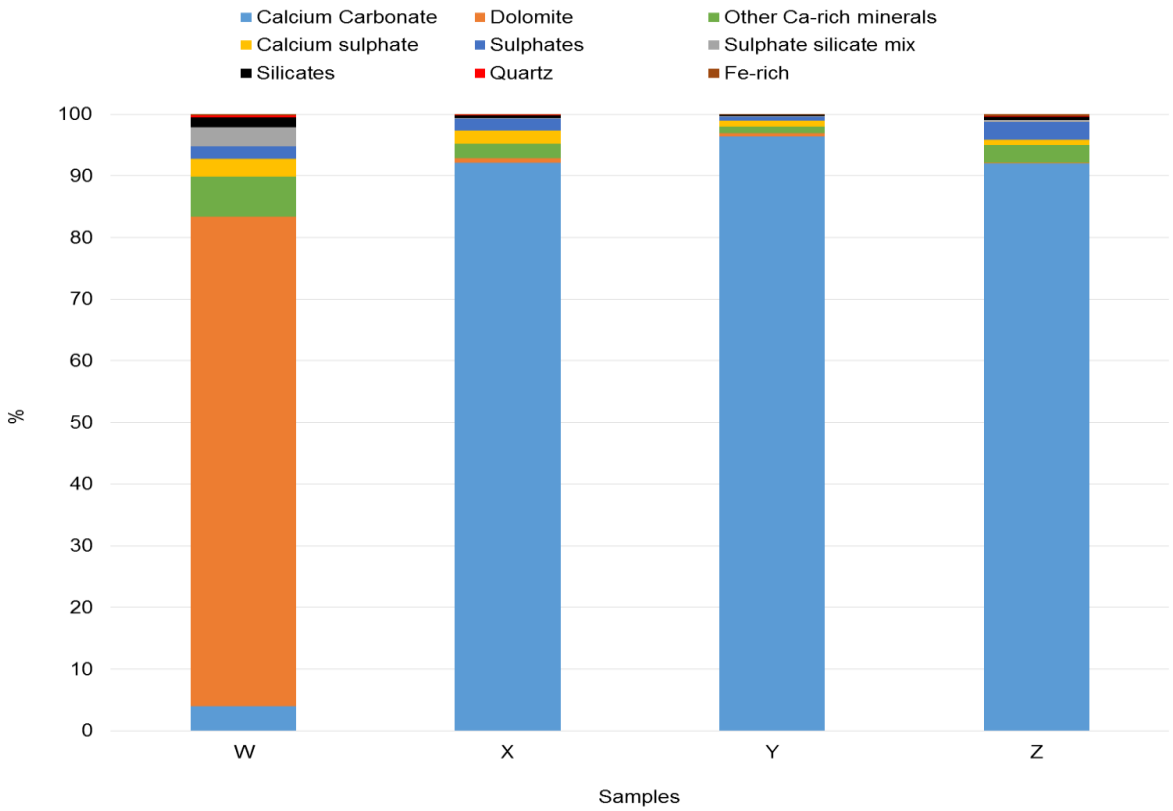

Figure 4.28: Kandler interpretation of the SPA results.

Table 4.10: Minerals associated with classification classes (Kandler et al., 2007).

Class name	Phases identified by TEM	Phases deduced from particle chemistry
Other Ca-rich minerals	-	Apatite
Sulphates	-	Blödite, löweite, glauberite, vanthoffite, mirabilite, thenardite, mascagnite
Sulphate silicate mixtures	-	Any silicate and sulphate
Silicates	Biotite, kaolinite, illite, muscovite, chloritoid, anorthite	Chlorite, albite, leucite, orthoclase, plagioclase, chrysotile
Quartz	Quartz	-
Fe-rich	Hematite	Ilmenite

Class name	Approx. composition, vol%
Iron-rich	40% hematite 30% illite 10% ilmenite 10% chloritoid 10% albite
Carbonates	75% calcite 15% dolomite 10% illite
Other calcium-rich	50% calcite 20% illite 10% dolomite 10% chloritoide 10% albite
Gypsum	90% gypsum 10% blödite
Quartz	85% quartz 15% illite
Silicates	55% illite 25% chloritoid 20% albite
Silicate sulfate mixtures	30% illite 30% blödite 20% glauberite 10% chloritoid 10% albite
Sulfates	60% blödite 30% glauberite 10% illite

Figure 4.29: Volumetric mineral composition of each class for aerosols studied by Kandler et al. (2007)

Phase name	Chemical formula	Phase name	Chemical formula
Apatite group	Fluorapatite: $Ca_5(PO_4)_3F$ Hydroxylapatite: $Ca_5(PO_4)_3(OH)$ Chlorapatite: $Ca_5(PO_4)_3Cl$ Carbonate-rich apatite/francolite:$Ca_5(PO_4,CO_3)_3(F,O)$	Biotite group	Annite: $KFe_3(AlSi_3)O_{10}(OH)_2$ Phlogopite: $KMg_3(AlSi_3)O_{10}(OH)_2$ Siderophyllite: $KFe_2Al(Al_2Si_2)O_{10}(F,OH)_2$ Eastonite: $KMg_2Al(Al_2Si_3)O_{10}(OH)_2$ Fluorannite: $KFe_3(AlSi_3)O_{10}F_2$ Fluorophlogopite: $KMg_3(AlSi_3)O_{10}F_2$
Blödite	$Na_2Mg(SO_4)_2 \cdot 4H_2O$	Plagioclase	$NaAlSi_3O_8$ - $CaAl_2Si_2O_8$
Löweite	$Na_{12}Mg_7(SO_4)_{13} \cdot 15H_2O$	Chrysotile	$Mg_3(Si_2O_5)(OH)_4$
Glauberite	$Na_2Ca(SO_4)_2$	Ilmenite	$FeTiO_3$
Vanthoffite	$Na_6Mg(SO_4)_4$	Kaolinite	$Al_2(Si_2O_5)(OH)_4$
Mirabilite	$Na_2SO_4 \cdot 10H_2O$	Anorthite	$Ca(Al_2Si_2O_8)$
Thenardite	Na_2SO_4	Muscovite	$KAl_2(AlSi_3O_{10})(OH)_2$
Mascagnite	$(NH_4)_2SO_4$	Chloritoid	$(Fe^{2+},Mg,Mn^{2+})Al_2(SiO_4)O(OH)_2$
Chlorite group	A generalized formula: $(X,Y)_{4\text{-}6}(Si,Al)_4O_{10}(OH,O)_8$ The "X" and "Y" in the formula represent ions, which might include: Fe^{+2}, Fe^{+3}, Mg^{+2}, Mn^{+2}, Ni^{+2}, Zn^{+2}, Al^{+3}, Li^{+1}, or Ti^{+4}. The composition and physical properties of chlorites vary as these ions substitute for one another in solid solution.	Illite group	Al-illite-hydromica: $KAl_2(AlSi_3O_{10})(OH)_2$ Ammersooite: $KAl_2(AlSi_3O_{10})(OH)_2$ Avalite: $KAl_2(AlSi_3O_{10})(OH)_2$ Brammallite: $(Na,H_3O)(Al,Mg,Fe)_2(Si,Al)_4O_{10})(OH)_2$ Illite Jade: $KAl_2(AlSi_3O_{10})(OH)_2$
Albite	$Na(AlSi_3O_8)$	Quartz	SiO_2
Leucite	$K(AlSi_2O_6)$	Hematite	Fe_2O_3
Orthoclase	$K(AlSi_3O_8)$		

Figure 4.30: Formulas of minerals identified by Kandler et al. (2007).

The value of SPA is realised when using the Kandler method of interpretation. The Kandler method uses ratios of elements in order to predict in which compound those elements occur for a defined particle (Kandler et al., 2007). The Kandler method does not simply take into account the elements that make up the compound, but also recognises the amount of other elements that are present, normally excluding C and O occurring in the sample. For example, for Gypsum the element ratio criteria are:

$|Ca+S|>0.5$ and $0.25<Ca/S<4$ and $Na/Ca<0.5$ (Kandler et al., 2007). A more complete set of criteria followed by the Kandler method is shown in Appendix C. The results from the Kandler interpretation can be seen in Figure 4.28.

The amounts of certain compounds differ from the XRF and XRD results due to the way in which the Kandler method interprets compounds and due to distribution of minerals upon milling. The Kandler method is utilised in this research, like most other analysing methods, to serve as a complementary method.

The following statements from Literature will be used to explain certain SPA and Kandler interpretation phenomena:

Explanation 1: "The relative contribution of sulphates and carbonaceous material increases with decreasing particle size" (Kandler et al., 2007)

Explanation 2: "Alumino–silicate clay minerals occur to a large extent as a dispersion of sediment of 0.1 – 10 µm particles concentrated in small size fractions i.e. below 20 µm" (Kandler et al., 2007).

Explanation 3: "Silica in the form of quartz and carbonates, chiefly calcite, ankerite and siderite, shows an enrichment in the particle size range 20 – 75 µm." (Raask, 1985).

4.5.1.1 Dolomite – Sample W (Gauteng) Kandler interpretation

As can be seen from Figure 4.28, sample W consists primarily of dolomite (80%). This is in agreement with the XRF and XRD analyses. The significant presence of Calcium carbonate (Calcite) does, however, not agree with the XRD/Raman results and the reason for this is clarified by explanation 3 above.

The "Other Ca–minerals" constitute a significant part in these small particles – 6.6%. Although Kandler et al. (2007) found in their study that these minerals largely constituted Calcite (50%) and illite (20%) – Figure 4.29, the "Other Ca–minerals" in this case most likely represents dolomite since sample W is a dolomite.

XRF analysis reported only 0.01% of SO_3 in sample W. The high amount of sulphur in the Kandler interpretation is accounted for by explanation 1 above. Thus, the 2.8% of "Calcium sulphate" and 2% of "Sulphates" are attributed to particle size and not a high occurrence of Sulphur in the sample. Sulphur does,

however, occur and it is postulated that the sulphur occurs with Iron instead of with Calcium. The petrographic analysis of sample W reported the presence of Pyrite and thus there is more evidence of Sulphur occurring with Iron than with Ca ("Calcium Sulphate") or Mg ("Magnesium Sulphate").

XRF analysis reported 0.54% Fe and XRD indicated 0.25% Fe in the form of Siderite ($FeCO_3$). The 0.2% of "Fe–rich minerals" in Figure 4.28 is similar to the amount of Siderite identified by XRD. Therefore Iron is confirmed to be present as Siderite.

It is suspected that Mn occurs in alumino–silicate compounds although this claim could not be backed up by the Raman analysis.

The 1.5 % of silicates identified by the Kandler method is very close to the 1.26% of SiO_2 reported by the XRF analysis. The 0.3% quartz is lower than the amount of quartz identified in the XRD analysis (2.7%). The reason for this was reported by Kandler et al. (2007) – in the statement, they remarked that "the same silicate minerals dominating the Silicates class were mixed with the materials dominating the other classes". Therefore the silica occurs as Iron– and alumino–silica minerals in the "Silicates" class instead of as quartz in the "Quartz" class. This finding is supported by the presence of alumino–silicates (see Figure 4.29 and Figure 4.28) which occur as 3.2% "Sulphate silicates". The high occurrence of alumino–silicates is supported by explanation 2 above. These alumino–silicates are also the source of the 0.07% of Al reported in the XRF analysis.

4.5.1.2 Limestone – Sample X (Northern Cape) Kandler interpretation

As expected from a high purity limestone, sample X consists mainly of $CaCO_3$ (Figure 4.28). Other notable classes in sample X are "Other Ca–rich minerals" (2.4%), "Calcium sulphate" (2.2%) and "Sulphates" (1.9%). The reasons for the

high occurrence of these minerals (Alumino–silicates and Sulphur) are given in explanation 1 above. The “Other Ca–rich minerals” are most likely Calcite or Calcium silicates (Beukes, 1977).

As discussed in the XRD/Raman section, Mg occurs in sample X as Fluoborite ($Mg_3(BO_3)(F,OH)_3$) and as Ferroan dolomite ($Ca(Mg,Fe)(CO_3)_2$). Dolomite does occur in the SPA results (0.7%) but this fact alone does not disprove the presence of Mg in Fluoborite form. The Kandler interpretation that was used did not account for Borates and therefore an accurate determination of the presence of Fluoborite could not be made in this case.

As discussed in the XRD/Raman section, Iron can occur in sample X as Siderite ($FeCO_3$), Iron silicates or Ferroan dolomite. The presence of “Dolomite” as well as “Fe–rich minerals” supports the XRD result of Ferroan dolomite in sample X. Since no other Iron–containing phases were recognised by the Raman analysis, it is likely that Iron occurs only as Ferroan dolomite and not in any silicates.

According to Figure 4.29, “Silicates” include Chlorite [$(X,Y)_{4-6}(Si,Al)_4O_{10}(OH,O)_8$] and “Silicate–sulphate mixtures” include Chloritoid [$(Fe^{2+},Mg,Mn^{2+})Al_2(SiO_4)O(OH)_2$]. Both Mn and Fe can possibly occur in these or other alumino–silicates. This result supports the Raman result of Mn occurring in a silicate form. The amount of Mn in the XRF analysis (0.4%) is the same amount of “Silicates” identified by the SPA, further supporting the deduction that Mn occurs as a silicate which was identified as Thulite ($(Ca,Mn)_2Al_3(SiO_4)$) in the Raman analysis.

XRF analysis reported 0.1% Si and 0.02% Al in sample X. The low percentage of “Sulphate silicates” but higher percentage of “Sulphates” in the Kandler interpretation indicates that silicates do occur but not in combination with Sulphur. According to the Kandler interpretation, 0.4% of “Silicates” are present

in sample X – Figure 4.28. The higher than expected occurrence of silicates is supported by explanation 2.

The low quantity of “Quartz” (0.1%) compared to the higher 0.4% “Silicates” supports the claim made in the XRD/Raman section that Si is present chiefly as a silicate in the mineral Thulite.

4.5.1.3 Limestone – Sample Y (Northern Cape) Kandler interpretation

XRF analysis reported 98.2% of $CaCO_3$ in sample Y. The Kandler interpretation of Sample Y is dominated by “Calcium Carbonate” (96.4%) which is in the Calcite phase according to XRD analysis. “Other Ca–rich minerals” are most likely calcite in such a high purity limestone (Figure 4.29). The high occurrence of Sulphate in 0.6% “Sulphates” and 0.9% “Calcium sulphate” is ratified again by explanation 1.

XRF results of sample Y reported 0.95% $MgCO_3$. From the XRD/Raman analysis it was originally postulated that sample Y contains Mg only as Fluoborite. This hypothesis is contradicted by the occurrence of 0.5% “Dolomite” in sample Y’s Kandler interpretation (Figure 4.28). Since sample X and sample Y are from the same geological area it is possible that the dolomite is not calcium magnesium carbonate but Ferroan dolomite. Neither dolomite nor Ferroan dolomite were identified by XRD or Raman spectroscopy, while Fluoborite was. Therefore no definite conclusion can be made regarding the phase in which Mg occurs.

Thulite ($(Ca,Mn)_2Al_3(SiO_4)$) is a phase which is known to occur in sample Y from Raman analysis, and thus Mn is present in an alumino–silica compound. It is not exactly certain in which form Fe is present in this sample.

XRF results reported only 0.03% of Si and 0.01 % Al in sample Y. Both the Si and Al XRF values for sample Y are half those of sample X. This fact is reflected in the Kandler “Silicates” and “Sulphates” which are half and less than half for Sample Y as compared to sample X. It is therefore suspected that the higher than expected 0.2% “Silicates” and 0.2% “Sulphate silicates” (Figure 4.28) resulted again for the reason given by explanation 2.

The absence of “Quartz” in the Kandler interpretation indicates that the quartz identified in the XRD analysis was a silicate compound and not pure quartz.

4.5.1.4 Limestone – Sample Z (Zambia) Kandler interpretation

As expected for a high purity limestone, sample Z consists mostly of $CaCO_3$. The “Other Ca–rich minerals” can be either Calcite or Aragonite because both these Calcium phases were identified during Raman scans.

XRF results reported 0.97% $MgCO_3$ in sample Z. The 0.2% “Dolomite” class (Figure 4.28) is most likely a trace phase in the sample and the phase in which some of the Mg occurs. However, Raman results proved the occurrence of Mg in the Fluoborite phase.

Although XRF analysis did not report on the presence of sulphur content, it is clear from the Kandler interpretation that sulphur does exist in sample Z. Lithostratigraphy of the geological source of sample Z corroborates this (refer to the XRD/Raman results and discussion). However, in such a high purity limestone, the Sulphur content is expected to be <1%. The high amount of Sulphur (2.8 % “Sulphates” and 0.8% “Calcium Sulphate”) as seen in Figure 4.28, is again resolved by explanation 1. Although Figure 4.29 shows that the main volumetric content of the “Sulphates” class is Blödite ($Na_2Mg(SO_4)_2{\cdot}4H_2O$), this phase is discarded based on the fact that no Na was identified in the XRF analysis. Blödite was considered as a potential Mg–

containing phase, and discarding this serves as additional evidence that Mg is present as Fluoborite ($Mg_3(BO_3)(F,OH)_3$) or dolomite.

XRF analysis reported 0.14% Fe in sample Z. XRD and Raman results did not report any Iron–containing phases. The “Iron–rich minerals” (Figure 4.28) by Kandler interpretation, is the highest for sample Z even though it contains about the same Fe as sample X and Y according to XRF data. Therefore, the Fe in sample Z is in Fe_2O_3 (Hematite) or $FeCO_3$ form. This fact does not exclude Fe from being present in alumino–silica compounds: it merely confirms that the Fe is present as more “Iron–rich minerals” in comparison to samples X and Y.

Although XRF analysis did not identify any trace amount of Copper, Raman analysis identified Libethenite ($Cu_2(PO_4)(OH)$) as a Copper–containing phase. The SPA and Kandler interpretation could not lend more information on the phase in which Copper is present. Copper is, however, likely to occur in sample Z since it is geologically located close to a large Copper deposit – (refer to the XRD/Raman results and discussion).

XRF results indicate the presence of 0.71% Si and 0.13% Al – a relatively large amount of Si and Al for a high purity limestone. The significantly higher Si and Al levels are evident in the “Silicates”, “Sulphate Silicates” and “Sulphates” which are higher for sample Z as compared to sample Y.

0.4% “Sulphate silicates” and 0.5% “Silicates” in Figure 4.28 confirm that Si and Al occur as alumino–silicates in sample Z – likely as illite or Chloritoid (Figure 4.29). Although no Al–containing phases were identified in sample Z, it is known that Plagioclase ($NaAlSi_3O_8$ – $CaAl_2Si_2O_8$) occurs in the Kaponda formation which is situated below the Kakontwe formation (Batumike Mwandulo et al., 2007). The absence of Na in the XRF results indicates that if plagioclase occurs in the sample, it is probably present as pure Anorthite ($CaAl_2Si_2O_8$). Anorthite is a Calcium Alumino–silicate and the presence of alumino–silicates is confirmed.

XRF results showed that sample Z contained 0.71% Si. XRD indicated a 0.55% quartz phase present in sample Z. This phase was confirmed by Raman scanning. These facts align with the petrographic analysis interpretation which described sample Z as containing quartz, mica and micrite allogens. However the Silicates: Quartz ratio from the Kandler interpretation is 5:1 showing that most of the Si occurs in alumino–silicates and not in quartz. Thus Quartz is a minor phase in sample Z.

A graphite phase was recognised during Raman scanning and was confirmed by the lithostratigraphy of sample Z's source.

4.6 Petrographic analysis of carbonate stone samples

Petrographic analysis offers information on the crystal structure, groundmass and pore structure of a carbonate rock – all of which are vital in assessing its behaviour in calcination. A summary of the petrographic analysis results is given in Table 4.11.

Table 4.11: Petrographic features of carbonate stone samples.

Sample	Colour	Classification	Calcite in pores	Calcite in stone mass	Pore features
W	Darkish grey	Micrite. No sparry calcite.	Secondary pore features that do not contain calcite.	Micritic ground mass.	Absence of any primary porosity features. Presence of secondary, post-depositional porosity features.
X	Whitish grey	Dismicrite.	Calcite present as sparite in stone mass (dismicrite) and crystallised in interconnected primary fenestrae		Interconnected primary pores
Y					
Z	Light grey	Sparite.	Calcite present as sparite in ground mas and crystallised sparite in pores. Medium to coarse calcite crystallised in primary and secondary pores that are not interconnected.	Sparry calcite ground mass. Allogens present.	No interconnecte primary and secondary pores

The classification of the carbonate rocks (Figure 4.31) from thin sections was based on the schemes by Folk (1962) as presented in Scholle and Ulmer–Scholle (2003).

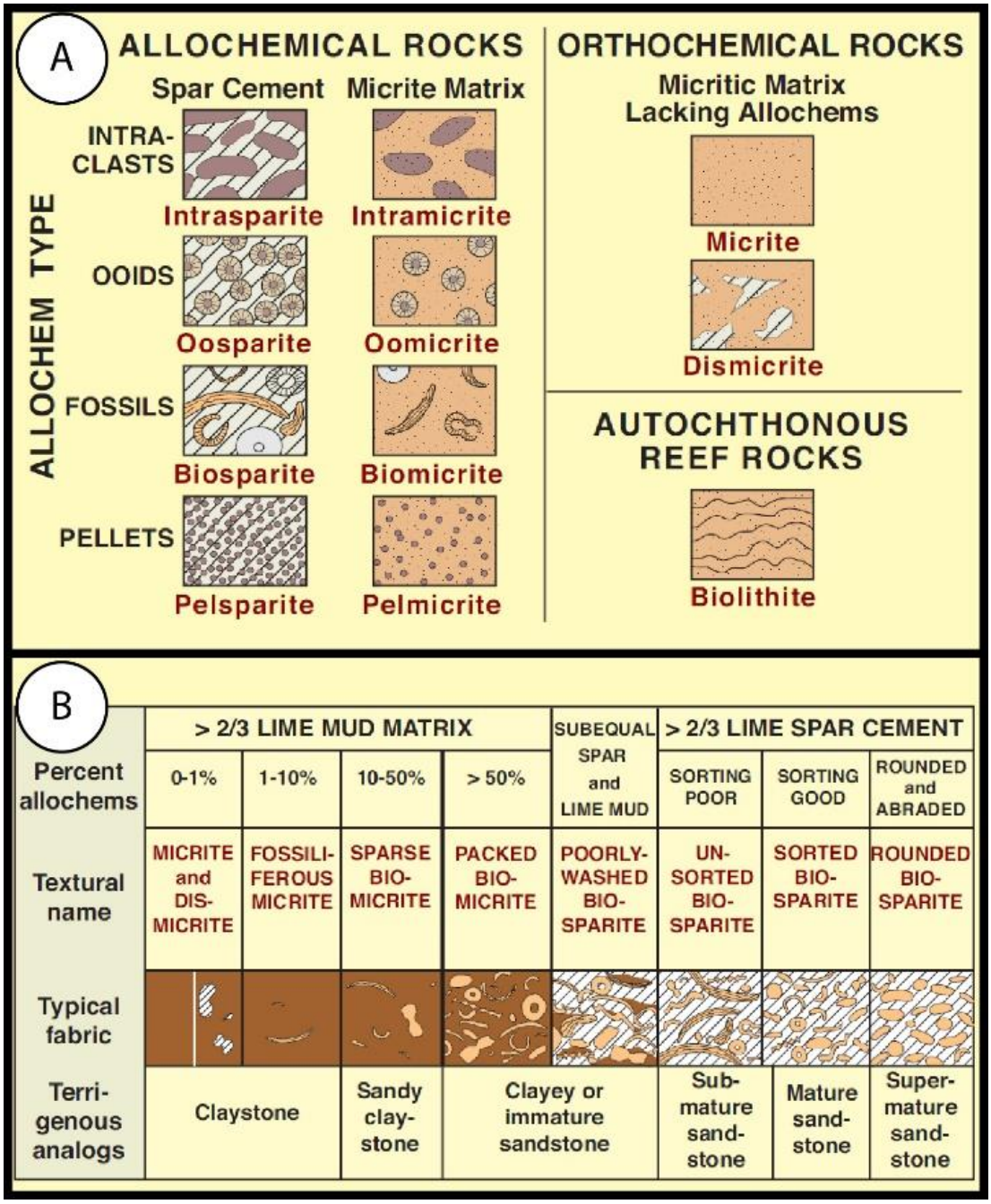

Figure 4.31: Graphic (A) and textural (B) classification schemes for carbonate rocks in thin section (Folk, 1962 in Scholle and Ulmer-Scholle, 2003).

Definitions of some terms are given below (Boggs Jr and Boggs, 2009).

Limestones:

Micrite: Carbonate mud (or lime mud) composed of very fine size (1~5 microns, 0.001~0.005 mm) calcite crystals. Modern lime mud consists mainly of aragonite, while ancient carbonate mud consists mainly of calcite. Lime mud may contain small amounts of fine–grained detrital minerals such as clay minerals, quartz, feldspar, and organic matters. Micrite may be present as a matrix among carbonate grains, or it may make up most or all of a limestone.

Sparite (sparry calcite): Clear calcite crystals typically larger than 62 μm. Large crystals (of the order of 0.02~0.1 mm) of calcite that appear clear or white viewed with a hand lens or in plane light under a polarizing microscope. Sparite can occur as large coarse crystal fill–ins or as individual fine crystals that make up stone fabric. It is formed during diagenesis. Sparry calcite crystals are distinguished from micrite by their larger size and clarity and from carbonate grains by their crystal shapes and lack of internal texture. The presence of sparry calcite cement in pore spaces indicates that grain framework voids were empty of lime mud at the time of deposition, suggesting deposition under high–energy flow conditions. Sparry calcite can also form by recrystallization of primary depositional grains and micrite during diagenesis.

Note: Micrites form as a matrix; sparry calcites form as a cement.

Microsparite: Calcite crystals theoretically between 5 and 62 μm, but mostly between 10 and 50 μm

Carbonate grains (Allochems): Carbonate grains typically range in size from silt (0.02 mm) to sand (up to 2mm), but larger particles such as fossil shells also occur.

Types of carbonate grains:

A. Rounded carbonate clasts cemented by sparry calcite.

B. Angular to sub–angular carbonate clasts in a micrite matrix.
C. Skeletal grains cemented with sparry calcite.
D. Normal ooids cemented with sparry calcite.
E. Radial ooids cemented with sparry calcite (white) and micrite (dark).
F. Pellets cemented with sparry calcite.

Dolomites:

Planar (idiotopic) dolomite: Rhombic, euhedral (well–formed) to anhedral (poorly formed) crystals.

Non–planar (xenotopic) dolomite: Non–planar, commonly anhedral crystals.

The porosity types were identified with the use of Figure 9.2 as done by Choquette and Pray 1970 as presented in Scholle and Ulmer–Scholle (2003).

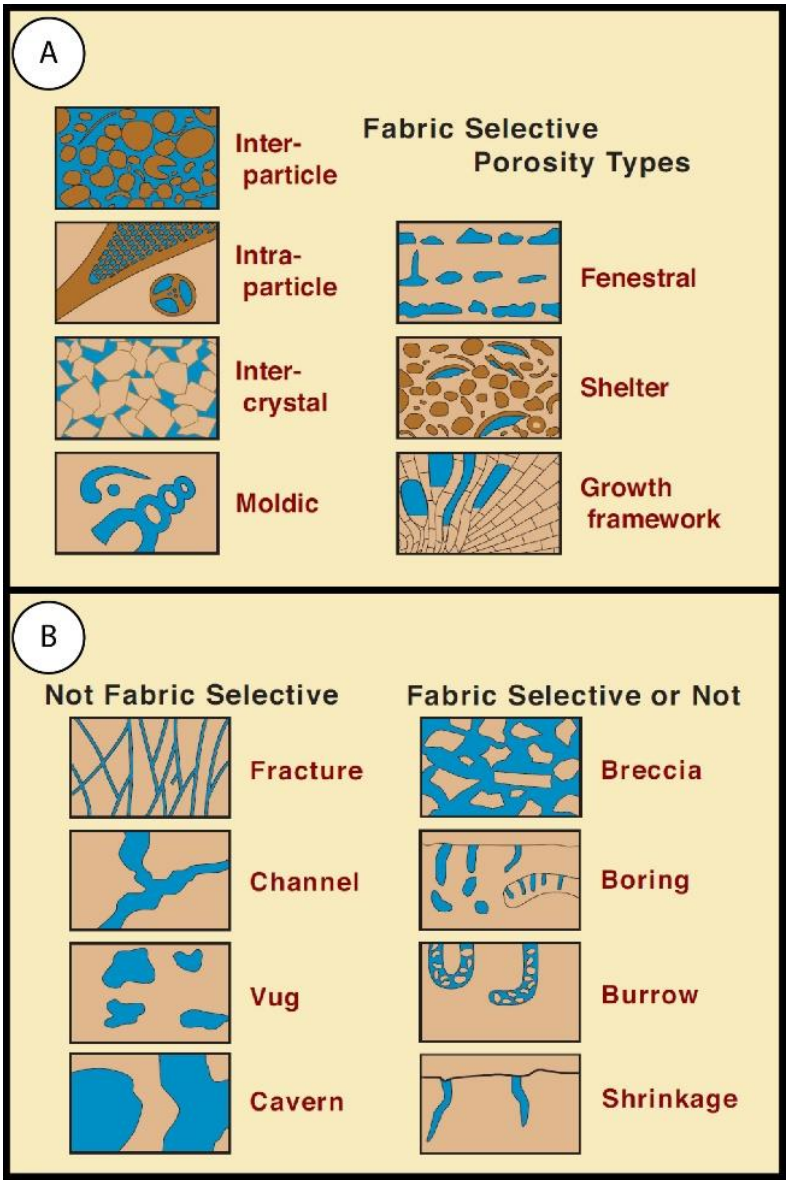

Figure 4.32: Primary (fabric-selective) (A) and Secondary (non-fabric-selective) (B) porosity types in carbonate rocks (Choquette and Pray, 1970 in Scholle and Ulmer-Scholle (2003).

The carbonate rocks can also be classified according to depositional texture as shown in Figure 4.33.

<table>
<tr><td colspan="5">DEPOSITIONAL TEXTURE RECOGNIZABLE</td><td>DEPOSITIONAL TEXTURE NOT RECOGNIZABLE</td></tr>
<tr><td colspan="3">Original components not bound together during deposition</td><td rowspan="3">Lacks mud and is grain supported</td><td rowspan="3">Original components were bound together during deposition ash shown by intergrown, skeletal mater, lamination contrary to gravity, or sediment-floored cavities that are roofed over by organic or questionable organic matter and are too large to be interstices</td><td rowspan="4">CRYSTALLINE CARBONATE

(Subdivide according to classifications designed to bear on physical texture or diagenesis)</td></tr>
<tr><td colspan="3">Contains mud
(particles of clay and fine silt sizes)</td></tr>
<tr><td colspan="2">Mud supported</td><td rowspan="2">Grain supported</td></tr>
<tr><td>Less than 10% grains</td><td>More than 10% grains</td></tr>
<tr><td>MUDSTONE</td><td>WACKSTONE</td><td>PACKSTONE</td><td>GRAINSTONE</td><td>BOUNDSTONE</td><td></td></tr>
</table>

Figure 4.33: Stone classification of carbonate rocks according to depositional texture (Dunham,1962).

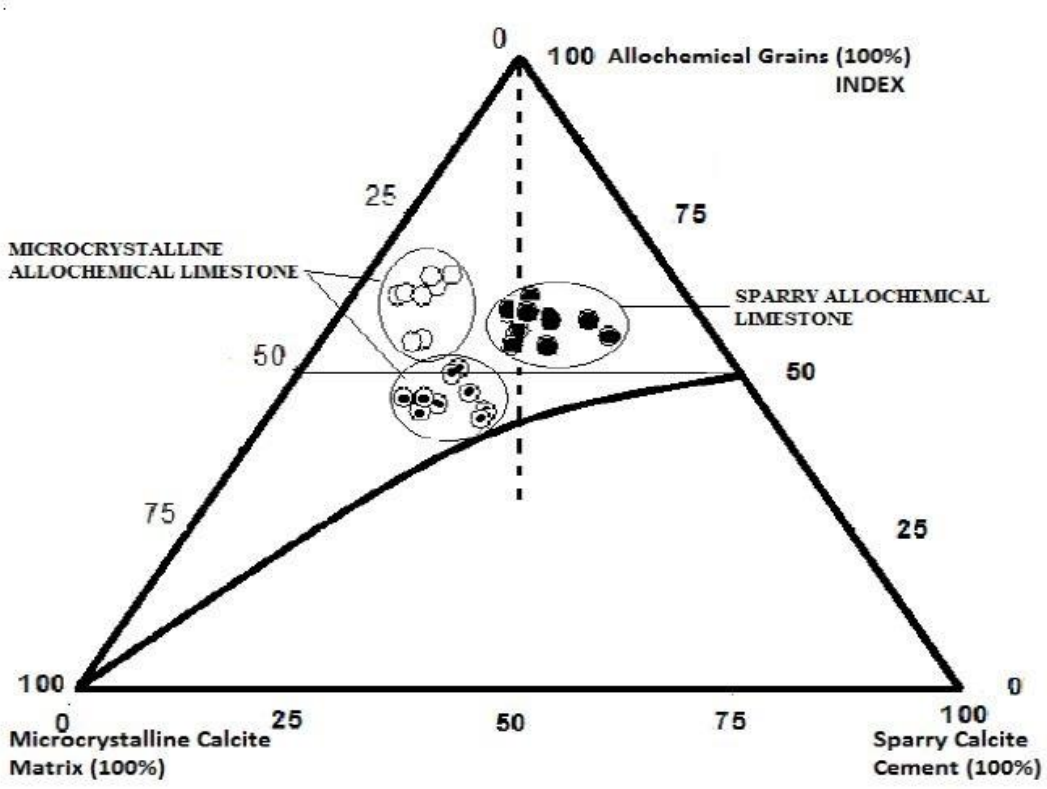

Figure 4.34: Phase diagram of different forms in which calcite can occur in limestones (Folk, 1959)

Note: “Mud–supported limestones are mudstones (i.e. lime mudstones) if they contain less than 10% carbonate grains and wackestones if they contain more

than 10% carbonate grains. Grain supported limestone that contain some micrite mud matrix are packstones. Grain supported limestones that lack mud matrix are grainstones." (Boggs Jr and Boggs, 2009).

A detailed description of the petrographic analysis of each of the rock samples are given in the next sections.

4.6.1 Dolomite – Sample W (Gauteng)

Sample W is a micrite – $CaCO_3$/mineral "mud". Sparite is absent in this sample (Figure 4.35 A and B). This sample consists of 85 – 95 % micrite (identified from Figure 4.35) and 5 – 15 % accessory authigenic mineral phases in the form of vein quartz and mud. Fenestrae and other primary pores (identified from Figure 4.35) are absent, offering a possible explanation to the hardness of the sample. Secondary porosity is however present as thin (0.2 – 0.5 mm thick) network fractures which are often occupied by crystallised vein quartz or altered micrite as clay mud (Figure 4.35 E and F). "Subhedral pyrite is present in sample W (G and H) as an accessory authigenic phase in very low relative abundances (<1%)." (Penn–Clarke, 2018).

According to Penn–Clarke (2018) the diagenetic history can be described as follows: "Calcite is restricted to micrite where it acted as a cement that bound mud–sized grains together during lithification. The generation of network fractures that permeate throughout carbonate rock W is interpreted to have occurred post–lithification as a secondary porosity feature. The presence of vein quartz that crystallised within these fractures is interpreted to represent a silica–rich fluid that migrated through the host rock, forcing open a network of cracks into which it precipitated, or altered micrite to clay mud. This fluid may have been responsible further for the precipitation of pyrite within sample W but this remains to be demonstrated."

According to Dunham (1962) (Figure 4.33) sample W is classified as a Mudstone because of the mud support structure and low percentage of grains.

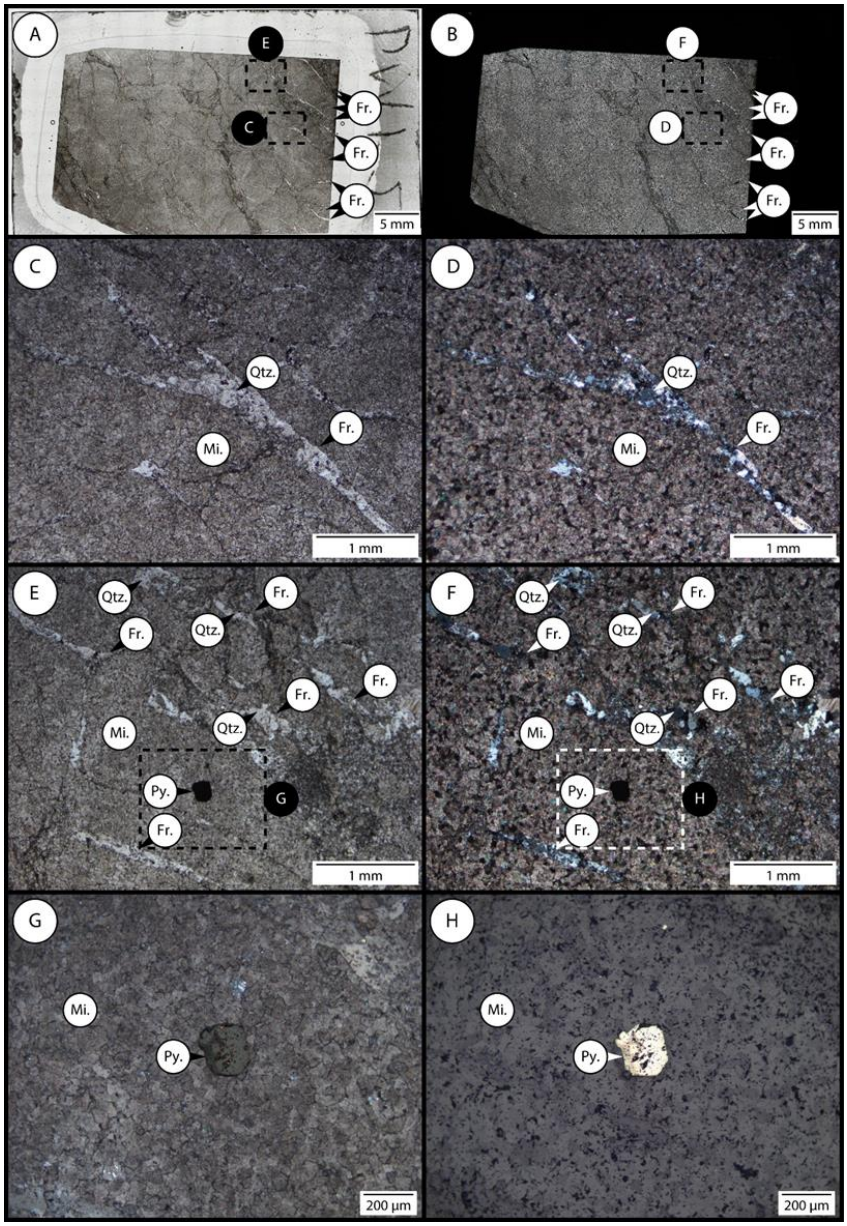

Figure 4.35: Petrographic features associated with sample W.

A – General overview of thin section showing networked fractures (Fr.) and overall, fine–grained micritic groundmass that typifies the sample. Plane polarised light, 4 x magnification. B – Same as A, but in cross–polarised light. C – Detail showing vein quartz infill (Qtz.) within fracture (Fr.) and overall micritic (Mi.) nature of the sample. Plane polarised light, 4 x magnification. D – Same

as C, but in cross–polarised light. E – Multiple quartz infilled (Qtz.) network fractures (Fr.) in micritic ground matrix (Mi.). Also shown is a subhedral authigenic pyrite grain (Py.). Plane polarised light, 4 x magnification. F – Same as E but in cross–polarised light. G – Transmitted photomicrograph showing detail of authigenic pyrite grain Plane polarised light, 10 x magnification. H – Same as G but in cross–polarised light.

4.6.2 Limestone – Sample X (Northern Cape)

Sample X is a dismicrite that is a mixture of sparite (calcite) and micrite (Mineral/$CaCO_3$ "mud") (Figure 4.37 A and B). The sample consists of roughly 50 % sparite and 50 % micrite. Most of the micrite occurs as micrite intraclasts (Figure 4.37 C and D). See Figure 4.36 for classification of clasts. The sparite (calcite) is in the form of coarse to very–coarse crystals that are of the size 0.3 – 1.8 mm (Figure 4.37 A and B). These crystals occur as a coarse mosaic solution cavity fill in interconnected fenestrae (pores) of 1 – 3.5 mm^2 cross section area. The coarse sparite grains in fenestral pore cavities often have angular–to–irregular, wavy intergranular contacts, some of which are stylolitic. The fenestrae (pores) are networked and oriented approximately parallel to the original laminations. Between these networked pores containing the solution cavity fills (sparite) and the micrite (mud), stylolites may be developed (Figure 4.37 E–H). Triangular pitting may be developed on certain very coarsely crystalline sparite grains (Figure 4.37 G and H). Silicate allogens (quartz, feldspar, lithic fragments, and micas) are rare and make up less than 1 % of the sample.

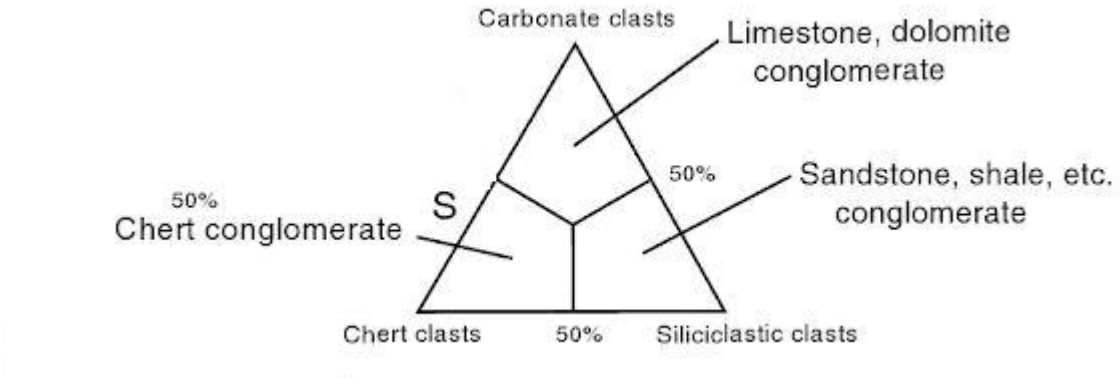

Figure 4.36: Classification of carbonate clasts. S = Sedimentary clasts. (Note: Conglomerates can be either clast-supported or matrix-supported.)

The diagenetic history can be described as: Sample X was originally a micrite with penecontemporaneous open pore spaces (fenestrae) distributed evenly throughout the ground mass. “Crystallisation of coarsely–to–very coarsely crystalline sparry calcite occurred within these fenestrae with percolation of bicarbonate–rich fluids.” “Much–finer grained calcite also acted as a cement between micrite grains during this phase. The hypothesis is that precipitation of sample X occurred with gradual burial and compaction in the subsurface.” (Penn–Clarke, 2018).

According to Dunham (1962) (Figure 4.33) sample X is classified as a Wackestone because of the micritic mud and the primary pore spaces filled with sparry calcite and microcrystalline sparite. The second classification (Figure 9.4) according to Folk (1959) is that sample X is a mixture between a microcrystalline calcite and a sparry calcite, lying halfway between the two corners on the bottom of the triangular phase diagram because of the lack of Allochems.

4.6.3 Limestone – Sample Y (Northern Cape)

Sample Y is compositionally and structurally similar to sample X and is also a fine dismicrite. It consists of ±60% micrite (mud) and ±40% coarse to very coarse crystalline sparite (calcite) (Figure 4.38 A and B). Sparite occurs as a coarse mosaic solution cavity fill in interconnected fenestrae (pores) of 0.2 – 2 mm^2 (Figure 4.38 C–F). The coarse sparite grains in fenestral pore cavities often have angular–to–irregular, wavy intergranular contacts, some of which are stylolitic. Silicate allogens (quartz, feldspar, lithic fragments, and micas) are rare and make up less than 1 % of the sample.

The diagenetic history can be described as: In a similar manner to sample X, “crystallisation of coarsely–to–very coarsely crystalline sparry calcite occurred within the fenestrae with percolation of bicarbonate–rich fluids. It is thought that percolation of fluids may have increased connectivity of pore spaces, or aided in expanding and interconnecting them.” “Much–finer grained calcite also acted as a cement between micrite grains during this phase. The hypothesis is that precipitation of sample X occurred with gradual burial and compaction in the subsurface.” (Penn–Clarke, 2018).

According to Dunham (1962) (Figure 4.33) sample Y is classified as a Wackestone because of the micritic mud and the primary pore spaces filled with sparry calcite and microcrystalline sparite. Its second classification (Figure 4.34) according to Folk (1959) is that sample Y is a mixture between a microcrystalline calcite and a sparry calcite, lying halfway between the two corners at the bottom of the triangular phase diagram because of the lack of allochems.

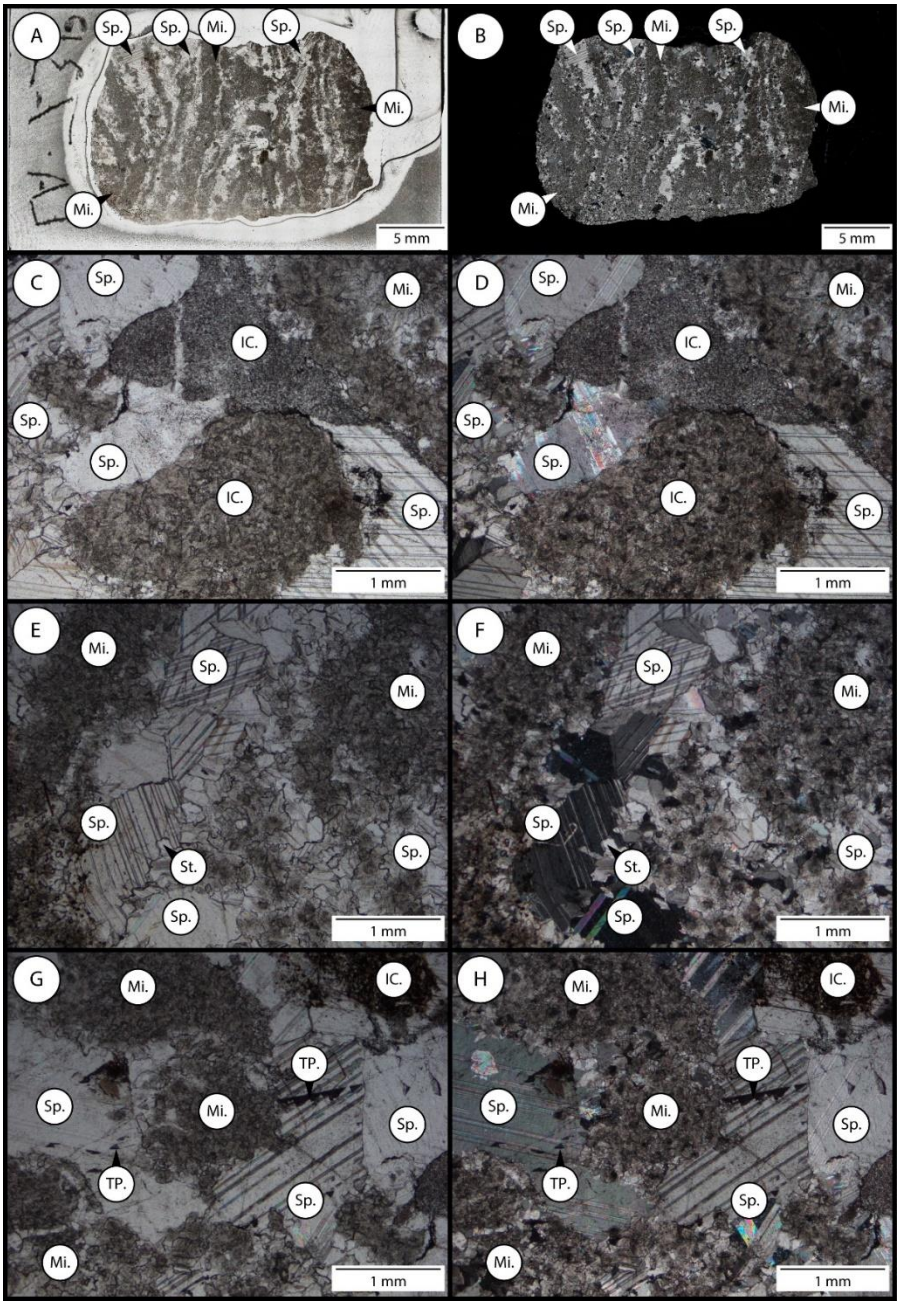

Figure 4.37: Micropetrographic images of carbonate rock X.

A – General overview of thin section showing organisation and connectivity of sparite (Sp.) in–filled fenestral pore spaces oriented approximately parallel to laminations as well as cross–cutting laminations. Overall ground matrix comprises micrite (Mi.). Plane polarised light, 4 x magnification. B – Same as A but in cross–polarised light. C – Detail showing relationships between micrite matrix (Mi.) and sparite infilled fenestrae (Sp.). Plane polarised light, 4 x

magnification. D – Same as C but in cross–polarised light. E – Detail of a large sparry calcite–infilled (Sp.) fenestra and its relationship with surrounding micrite (Mi.) matrix. Plane polarised light, 4 x magnification. F – Same as E but in cross–polarised light. G – Detail of triangular pits (TP.) within very coarsely crystalline sparite (Sp.). Also shown are stylolitic contacts between sparite and the micrite (Mi.) matrix. Plane polarised light, 4x magnification. H – same as G but in cross–polarised light.

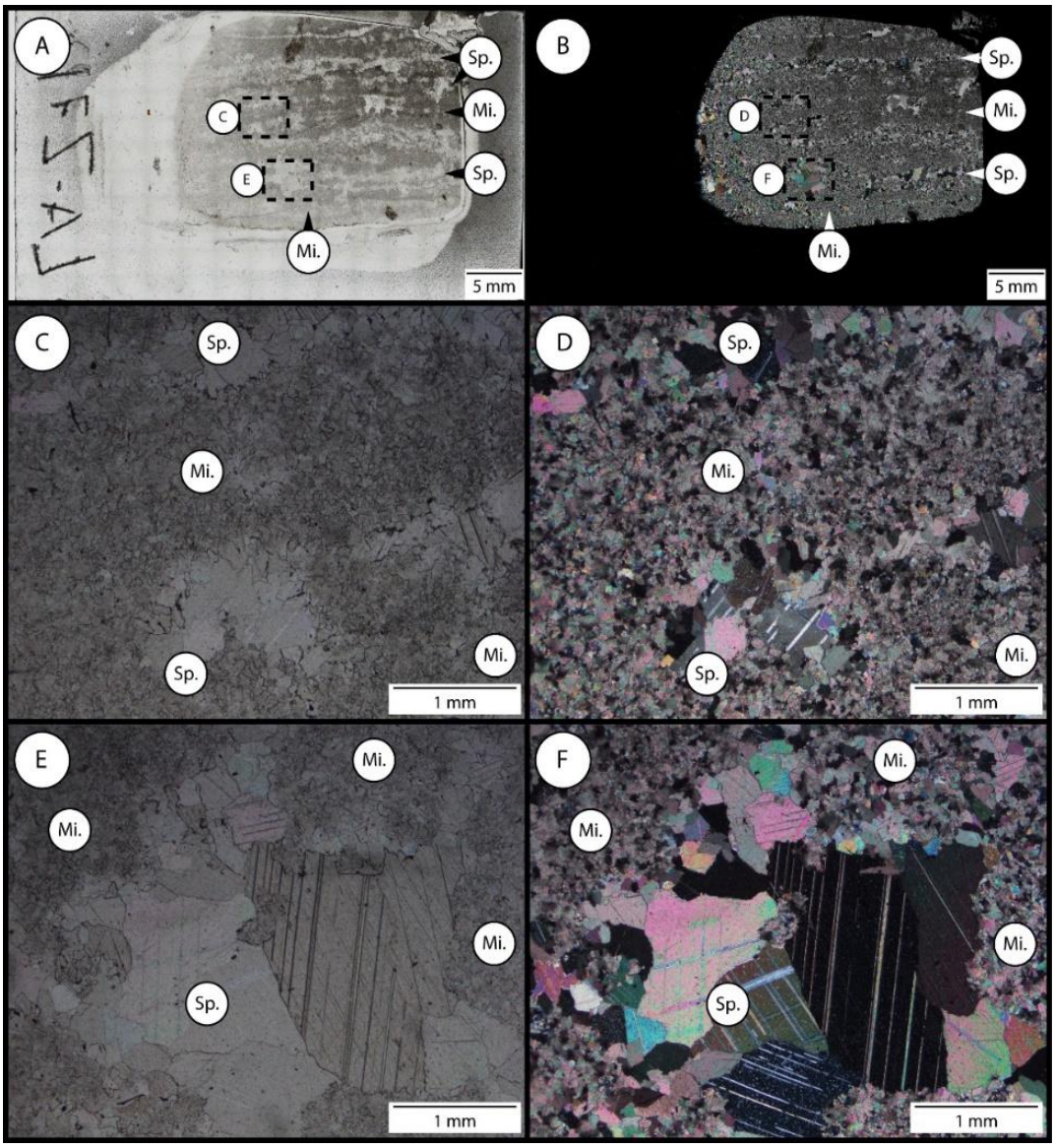

Figure 4.38: Micropetrographic images of carbonate rock Y.

A – General overview of thin section showing organisation and connectivity of sparite (Sp.) in–filled fenestral pore spaces oriented approximately parallel to laminations as well as cross–cutting laminations. Overall ground matrix comprises micrite (Mi.). Plane polarised light, 4 x magnification. B – Same as A but in cross–polarised light. C – Detail showing relationships between micrite matrix (Mi.) and sparite infilled fenestrae (Sp.). Plane polarised light, 4 x magnification. D – Same as C but in cross–polarised light. E – Detail of a large sparry calcite–infilled (Sp.) fenestra and its relationship with surrounding micrite (Mi.) matrix. Plane polarised light, 4 x magnification. F – Same as E but in cross–polarised light.

4.6.4 Limestone – Sample Z (Zambia)

Sample Z is compositionally and texturally different from samples W, X and Y. It is not a micrite or a dismicrite but a sparite (sparry calcite). Sample Z consists of >98% sparite (sparry calcite) and <2% allogens (Figure 4.39 A and B and G and H). The sparite (calcite) is present as fine to medium grains that are of the size 0.1 – 0.25 mm. The allogens are present as quartz, mica and micrite. Laminations (layering of stone less than 10 mm thick) are present in this sample but not in the other samples. Primary laminations are manifested in the sample as ripple cross–laminations that have been overprinted by sparite (Figure 4.39 A and B).

Sample Z also has primary pores, as in samples X and Y but they are not interconnected. Sample Z has non–interconnected secondary pores similar to sample W but these differ because they are thick fractures that are infilled with calcite. The primary pores (3.5 – 4.5 mm^2 cross section area fenestral cavities) are orientated parallel to the primary laminations (Figure 4.39 E and F) whereas the secondary pores (3.5 mm thick fractures) have a sub–parallel orientation to the primary laminations (Figure 4.39 C and D). “The pore spaces (primary as well as secondary) are not interconnected and are often infilled with medium to

coarse (0.3 – 0.5 mm) crystalline sparry calcite" (Penn–Clarke, 2018). Evidence suggests that late stage dissolution affected calcite in–filled fenestral pore features.

Its diagenetic history can be described as: "The crystalline nature of sparry calcite and its overprinting of primary sedimentary structures (ripple cross–lamination) suggest that the original calcite sand crystallised in place soon after sedimentation during cementation, and may have continued with burial to the subsurface. The rarity of fenestrae suggests that the host rock of sample Z had poor primary porosity. Crystallisation of medium–to–coarse grained mosaic–textured sparry calcite within primary pore spaces, such as fenestrae, took place, perhaps, at a later stage with gradual burial in the subsurface. The absence of stylolites suggests that sample Z has undergone minimal compaction with burial to the subsurface, post sedimentation and lithification. Late–stage fracturing, parallel to bedding, occurred post lithification, creating secondary fracture pore spaces that were later in–filled with mosaic–textured medium–to–coarse grained sparry calcite. Again, the mosaic–texture of sparry calcite within fracture–fill features suggests that this diagenetic phase took place in the subsurface. Dissolution of sparry calcite, specifically within vug–infilled cavities, represents the latest diagenetic stage of sample Z." (Penn–Clarke, 2018).

According to Dunham (1962) (Figure 4.33) sample Z is classified as a Grainstone because of the grainy sparite ground mass. The second classification is that sample Z is a sparry calcite (on the bottom right corner of the triangular phase diagram Figure 9.4) according to Folk (1959).

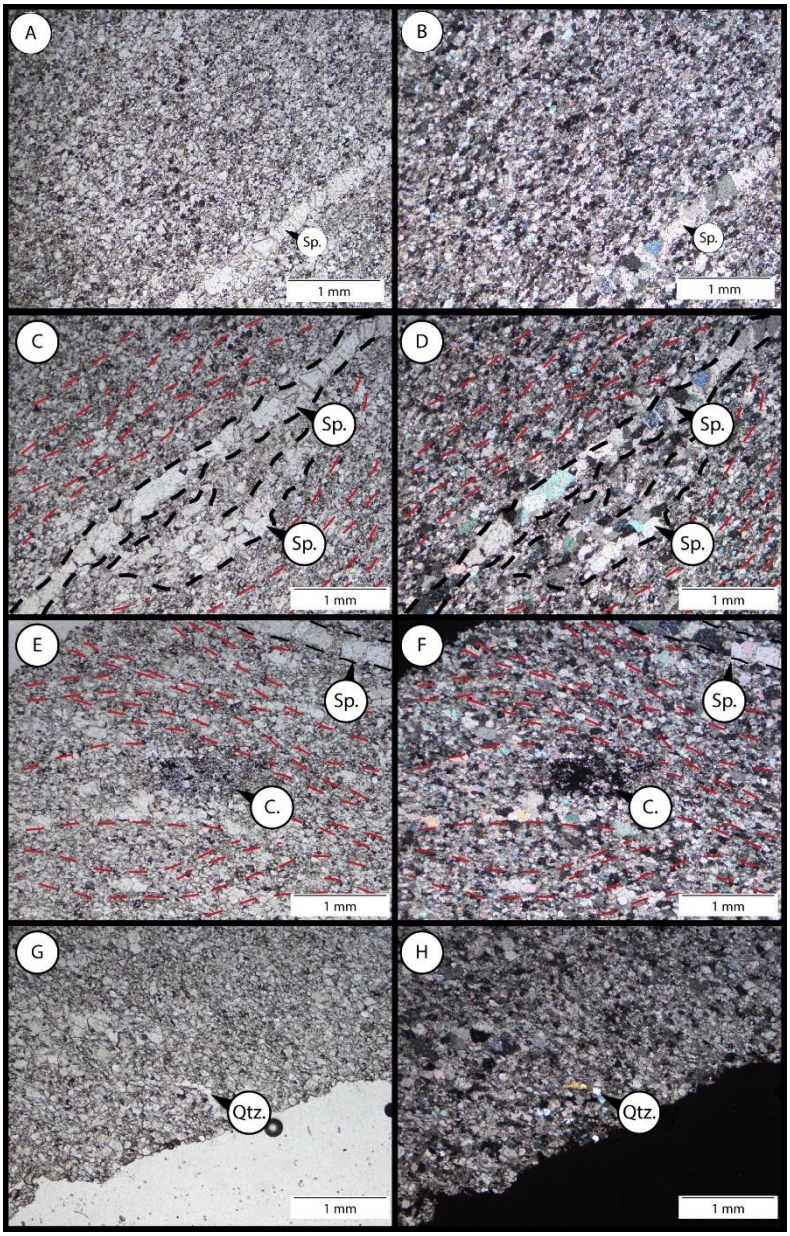

Figure 4.39: Petrographic features associated with sample Z.

A – General overview of the thin section showing fine–to–medium grained nature of sparry calcite ground mass, with primary ripple cross–laminations and sparry calcite infilled (Sp.) oriented subparallel to laminations (black dashed lines). Plane polarised light, 4x magnification. B – Same as A but in cross–polarised light. C – Detail of mosaic textured, medium–to–coarse grained sparry calcite (Sp.) infilled fractures, oriented subparallel to primary laminations. Plane polarised light, 4x magnification. D – Same as C but in cross–polarised light. E

– Open fenestral primary pore space cavity (C.) with secondary sparry calcite (Sp.) infilled fracture. Plane polarised light, 4x magnification. F – Same as E but in cross–polarised light. G – Rare quartz grains (Qtz.). Plane polarised light, 4x magnification. H – Same as G but in cross–polarised light.

4.7 Decrepitation Characteristics of carbonate rock samples

The decrepitation characteristic of a stone is an essential parameter in assessing the suitability of a stone for calcination in a lime kiln. Decrepitation of stone in shaft kilns can cause channelling within the kiln and consequently problems with product quality. Decrepitation in rotary kilns causes dust formation, resulting in loss of production mass. Decrepitation performance is classified according to Table 4.12 (Vola and Sarandrea, 2013).

Table 4.12: Classification of decrepitation performance of a carbonate rock (Vola and Sarandrea, 2013).

Amount of decrepitation	Classification
0 - 5 %	Excellent
5 - 15 %	Good
15 - 35 %	Acceptable but risky
>35%	Not acceptable

The decrepitation test was carried out by calcining 13.2 – 20 mm stone at 1000 °C (dolomite)/1050 °C for 1 hour. The burnt stone was then screened at 11.2 mm and the stone that passed 11.2 mm screening ($m_{decrepitated}$) was divided by the total amount of burnt stone (m_{burnt}). Thus

$$\%\, decrepitation = \frac{m_{decrepitated}}{m_{burnt}} \frac{[g]}{[g]} \times 100\%$$

The results for the decrepitation tests and overall average are shown in Table 4.13. According to the standard deviation and acceptable scientific practice it was necessary to do 3 decrepitation tests for each sample to get an overall

average. Sample W and Sample Z which showed the highest amount of decrepitation also showed the highest standard deviation. Sample Y's results were most consistent with a standard deviation of only 0.33%. Sample Z's results were most inconsistent with a standard deviation of 1.61%. However in a decrepitation test a standard deviation of 1.6% is within an acceptable region.

Table 4.13: Percent decrepitation in each stone sample after heating at 1050 °C for 1h

Decrepitation [%]	Sample W	Sample X	Sample Y	Sample Z
Test 1	5.8	4.4	5.5	12.6
Test 2	5.4	2.8	5.4	12.6
Test 3	7.5	3.7	6.0	15.4
Average [%]	6.2	3.7	5.7	13.5
Range [%]	2.1	1.6	0.6	2.8
Standard deviation [%]	1.13	0.79	0.33	1.61

Decrepitation is the process that occurs when crystals inside a limestone/dolomite expand upon heating and finally fracture, causing the stone to break up. The form in which calcite occurs, crystals or micrite, and primary pores are two factors affecting decrepitation (Hedin, 1954).

Crystalline limestone decrepitates the most (Hedin, 1954). Large crystals in limestone can even be converted completely to dust. Conversely, fine–grained limestone with small crystals of 2.5 mm or less generally resists the thermal stresses in the crystals without breaking up (Hedin, 1954).

Primary pores/fissures in between crystals assist in resisting decrepitation. These pores/fissures act as "expansion joints" leaving room for calcite crystals to expand without breaking down the integrity of the stone's matrix (Hedin, 1954).

Decrepitation is a physical phenomenon and chemical features of the stone have no effect on it (Boynton, 1980). The decrepitation of each stone can be

linked to two of the physical analysis techniques performed on the rock samples, petrography and SEM. Petrography lends a better understanding of the crystal structure while SEM lends a better understanding of the grain structure. The percentage of decrepitation is compared to the petrographic properties of each sample in Table 4.14.

Table 4.14: Petrographic features of the carbonate rocks compared to decrepitation.

	Sample W	Sample X	Sample Y	Sample Z
% Decrepitation Average (3 tests)	6.2	3.7	5.7	13.5
Micrite [%]	85 - 95	50	60	0
Grain size [mm]	0.001 - 0.005	0.005 - 0.18	0.005 - 0.18	0.1 - 0.25
Crystal size [mm]	No crystals	0.3 - 1.8	0.3 - 1.8	No crystals
Infilled Pore size [mm^2]	Only secondary pores	1.0 - 3.5	0.2 - 2.0	3.5 - 4.5

A detailed discussion on each of the carbonaceous rock samples is given in the next sections.

4.7.1 Dolomite – Sample W (Gauteng)

According to the SEM–EDS results, sample W is classified as a clayey dolomite with small uniform grain sizes. This feature of sample W allows the clayey dolomite (micrite) to act as a matrix between the small uniform particles and resist decrepitation of the stone.

The petrographic analysis showed that sample W is a micrite consisting of 85 – 95 % micrite (“mud”). Primary pores are absent but secondary pores are present as thin fractures often occupied by quartz or micrite.

It is reasoned that:

1. The absence of calcite *crystals* is the reason for the low amount of decrepitation happening in the rock (Hedin, 1954).

2. The micrite grains do not expand and break up as crystals would and in doing so the rock is less susceptible to decrepitation (Hedin, 1954).

3. The micrite “mud” grains expand and contract as a matrix, keeping the structural integrity of the stone intact. Large micrite grains are more likely to crumble upon calcination and in doing so contribute to decrepitation.

4. Secondary pores that are filled with silica/quartz prevent the expansion of grains and increase decrepitation.

4.7.2 Limestone – Samples X and Y (Northern Cape)

The physical appearance of the stone X before and after calcination for 1 hour at 1050 °C is shown in Figure 4.40. The colour of quicklime is a key determinant of its applications. The brown colour of the calcined stone is due to the presence of Manganese in the stone, confirming the Manganese reported in the XRF results.



Figure 4.40: Sample X before (left) and after calcination (right) at 1050 °C for 1 hour.

According to the SEM–EDS results, samples X and Y are both fine grained calcitic limestone. As mentioned above, these fine grains limit decrepitation because of their shrinking during calcination and maintaining the structural integrity of the stone.

The petrographic results showed that samples X and Y are dismicrite rocks – sparite crystals surrounded by micrite “mud”. The sparite exists as a mosaic of 0.3 – 1.8 mm coarse crystals in interconnected primary pores in both samples. These crystals expand upon heating and shrink upon calcination.

It is reasoned that:

1. The calcite crystals in the stone contribute towards decrepitation (Hedin, 1954).

2. The fact that the crystals are < 2 mm limits decrepitation (Hedin, 1954).

3. The interconnected primary pores act as expansion spaces for the calcite crystals and in doing so limit decrepitation (Hedin, 1954).

4. Sample X's larger pores (1 – 3.5 mm^2) offered more expansion space for the calcite crystals as opposed to sample Y's pores (0.2 – 2 mm^2) and therefore sample Y had a higher level of decrepitation (Ruckensteiner et al., 1995).

5. A fine–grained limestone with a higher amount of micrite (sample Y – 60%) decrepitates more than a fine–grained limestone with less micrite (Sample X – 50%).

Sample X had a larger range than sample Y, but with the standard deviation of 0.8% sample X has an upper limit of 4.5% decrepitation which is lower than the 5.4% lower limit of Sample Y (0.3% standard deviation). These numbers for decrepitation agree with literature for a packstone from South Africa (Vola and Sarandrea, 2013).

4.7.3 Limestone – Sample Z (Zambia)

The SEM–EDS results showed that sample Z can be classified as a fine grained calcitic limestone. These fine grains are larger than micrite grains but smaller than crystalline sparite (Folk, 1962).

The physical appearance of the stone before and after calcination for 1 hour at 1050 °C is shown in Figure 4.41. Although the structural integrity is already affected after calcination it is only observed after screening the quicklime.

The petrographic results show that sample Z consists of >98% sparry calcite. This means that all the calcite occurs as grains instead of as crystals or mud. The grains are fine to medium sized. Sparry calcite grains differ from micrite by

their larger size, and sparry calcite differs from carbonate grains by crystal shape and lack of internal texture (Folk, 1962). Micrites form as a matrix, while sparry calcite forms as a cement (Boggs Jr and Boggs, 2009). Sample Z also has non–interconnected primary and secondary pores.



Figure 4.41: Sample Z before (left) and after calcination (right) at 1050 °C for 1 hour.

It is reasoned that:

1. Because the sparry calcite is a cement the whole stone's structural integrity disintegrates as the sparry calcite grains move away from one another when shrinking during calcination. There is thus nothing holding the stone together anymore because the grains *are* the binding medium of the stone. This is in accordance with Ruckensteiner et al. (1995) who stated that increased disintegration can be expected for a limestone which is closely interstratified. Sample Z contains stratified sparry calcite.

2. According to the petrography results sample Z's pores are in–filled and pores are scarce in the rest of the stone. Thus the expanding sparite

crystals have little space to expand and cause the stone to break up, contributing to decrepitation.

3. A limestone consisting primarily of micrite and sparry calcite (sample Z) is expected to decrepitate more than a limestone consisting of large, coarse, mosaic calcite crystals and micrite (Ruckensteiner et al., 1995).

4. A high decrepitation value is expected from a fine– to medium–grained carbonate rock from Zambia (Vola and Sarandrea, 2013).

5. Literature showed that a sparry calcite with graphite inclusions from southern Africa is more prone to decrepitation (Vola and Sarandrea, 2013).

6. Sample Z will experience the most decrepitation during calcination whereas Samples X and Y would experience most decrepitation during heating (Ruckensteiner et al., 1995).

4.8 Thermogravimetry of carbonate rock samples

Thermogravimetry (TG) is a thermal analytical technique commonly used in the industry. TG is however useful in assessing a carbonate rock's suitability for use in a shaft kiln. TG assesses when and how a carbonate rock decomposes/calcines. TG measures the total mass loss (or Loss on Ignition as it is known in the industry), onset temperature, offset temperature, maximum peak temperature, decomposition rate, and decomposition stages. During heating calcination is observed as a mass loss.

4.8.1 Effect of different heating rates (applied only to Sample W)

During the heating rate investigation thermogravimetry was carried out in a nitrogen–only atmosphere (0 bar CO_2). The nitrogen at 100 kPa was at a flow rate of 10 mL/min. The flow rate is a relevant parameter because the CO_2 flowrate (constant pressure) was later adjusted to achieve the desired CO_2 partial pressures as mentioned in section 3.2.8. A sample of 10 ± 2 mg was used for each run. Mass loss was measured from 30 °C to 950 °C.

The first variable investigated was the rate of heating and how it affected the decomposition of a dolomite sample. As mentioned in section 3.2.8: Dolomite decomposition was investigated at 5 °C/min, 10 °C/min and 15 °C/min (0 bar CO_2 partial pressure) in order to determine whether the heating rate had an effect on the decomposition behaviour. This investigation was applied only to the dolomitic limestone in accordance with the project schedule. The results can be seen in Figure 4.42 and Table 4.15.

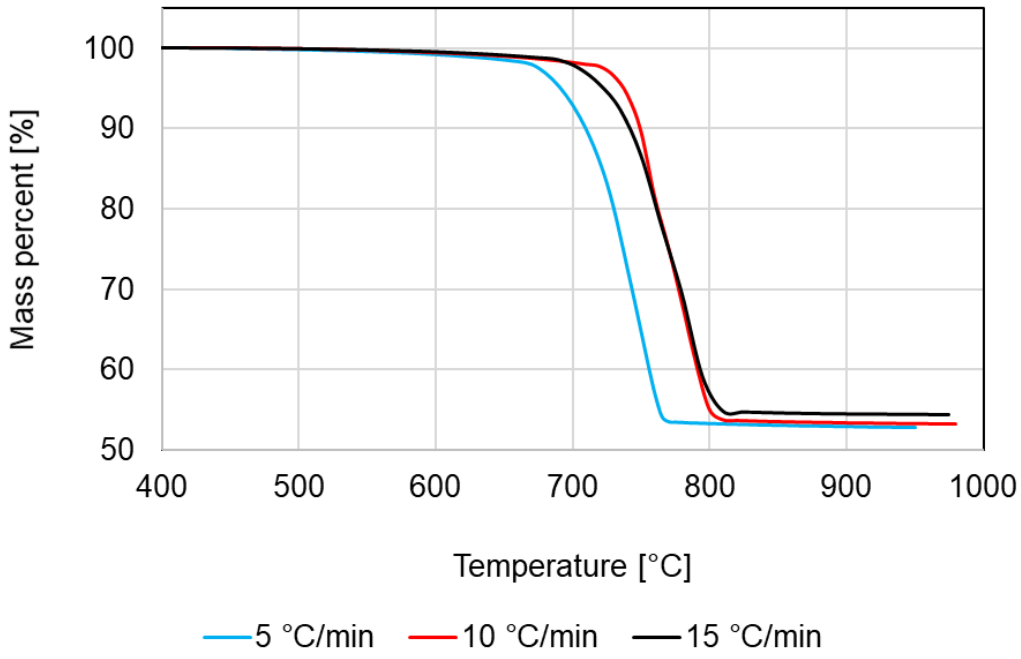

Figure 4.42: Decomposition of carbonate rock W at 5, 10 and 15 °C/min under a nitrogen atmosphere

Table 4.15: Decomposition of sample W up to 1000 °C at different heating rates.

Heating rate [°C/min]	Total weight loss [%]	Onset temperature [°C]	Offset temperature [°C]	Temperature range [°C]
5	47.32	662	790	89
10	46.75	738	870	132
15	45.64	728	885	157

From Figure 4.42 it can be seen that:

- Decomposition starts at a lower temperature for a rate of 5 °C/min as compared to 10 and 15 °C/min
- The rate of mass loss at the onset of calcination (slope at onset temperature) increases as the heating rate increases
- At a heating rate of 5 °C/min, the carbonate rock loses 0.57% more mass than at 10 °C/min, and 1.68% more mass than at 15 °C/min

Olszak–Humienik and Jablonski (2015) observed the same phenomenon in accordance with heating rates and onset decomposition temperatures. A possible reason for this occurrence is that at the higher heating rates, the carbonate rocks sinter more readily and this limits the rate of heat and mass transfer as the decomposition proceeds. “Due to the difference in dissociation temperatures of $MgCO_3$ and $CaCO_3$ the MgO is usually necessarily hard–burned in varying degrees before the CaO is formed due to retention at relatively high temperatures” (Boynton, 1980). The more limited the heat transfer the wider the range over which decomposition/calcination takes place because the heat takes longer to reach the core. Decomposition took place within 89 °C for a heating rate of 5 °C/min, 132 °C for a heating rate of 10 °C/min and 157 °C for a heating rate of 15 °C/min. This supports the statement that limited heat and mass transfer takes place as the heating rate was increased.

After establishing the heating rate effect on decomposition behaviour the temperature of the furnace was investigated. The goal of this was to determine whether there was any correlation between the heating rate and the extent of

calcination (how much mass was lost) at different furnace temperatures. These results are shown in Table 4.16 and Table 4.17. In Table 4.17 the specific decomposition of $MgCO_3$ (peak 1) and $CaCO_3$ (peak 2) was documented.

Table 4.16: Key characteristics of decomposition of sample W in 1 bar nitrogen-only atmosphere at different heating rates

Temp [°C]	Total mass change [%]	Onset temp [°C]	Offset temp [°C]
5 °C/min			
800	44.64	718.9	785
850	45.62	703.7	800
900	46.38	725.6	795
950	45.94	709.4	795
1000	47.32	701.3	790
10 °C/min			
800	42.37	719.6	-
850	46.13	714.6	810
900	44.52	720.7	840
950	47.28	718.4	840
1000	46.75	738.7	870
15 °C/min			
850	46.12	726.8	836
900	45.93	728.2	885
950	45.86	728.4	885
1000	45.64	728.3	885

No clear correlation emerged between the maximum temperatures and the % of decomposition (mass loss) of sample W for each heating rate. With increasing heating rates the maximum mass loss was observed to occur at lower temperatures. The temperature at which maximum mass loss occurred was lower for each heating rate class:

- for a heating rate of 5 °C/min maximum mass decomposition occurred at 1000 °C,

- for a heating rate of 10 °C/min maximum mass decomposition occurred at 950 °C,

- for a heating rate of 15 °C/min maximum mass decomposition occurred at 850 °C.

Table 4.17: Key characteristics of decomposition of sample W in 1 bar nitrogen atmosphere at different heating rates

Temp [°C]	Onset rate of change [%/min]	Max peak 1 [°C]	Max peak 2 [°C]
5 °C/min			
800	0.027	734.2	754.9
850	0.033	733.0	752.3
900	0.034	740.5	759.9
950	0.024	736.6	754.9
1000	0.023	736.9	752.0
10 °C/min			
800	0.037	744.2	774.6
850	0.038	747.5	767.5
900	0.059	753.6	774.5
950	0.075	750.1	775.1
1000	0.035	755.7	781.7
15 °C/min			
850	-	759.0	789.0
900	0.061	756.1	789.1
950	0.094	761.1	792.0
1000	0.078	757.1	790.2

4.8.2 Decomposition at different CO_2 pressures

As mentioned in 3.2.8, the decomposition of carbonate rocks was studied in a CO_2 atmosphere to simulate the CO_2 environment of a kiln and to study the decomposition effects that the CO_2 has on the carbonate rocks. Also, as mentioned a uniform heating rate of 15 °C/min was used for all the following TG analyses.

4.8.3 Sample W – Dolomite

4.8.3.1 p_{CO2} = 0 bar – Varying final temperature

Figure 4.43 shows that the decomposition of dolomite under a pure nitrogen atmosphere (p_{CO2} = 0 bar) occurred in one step.

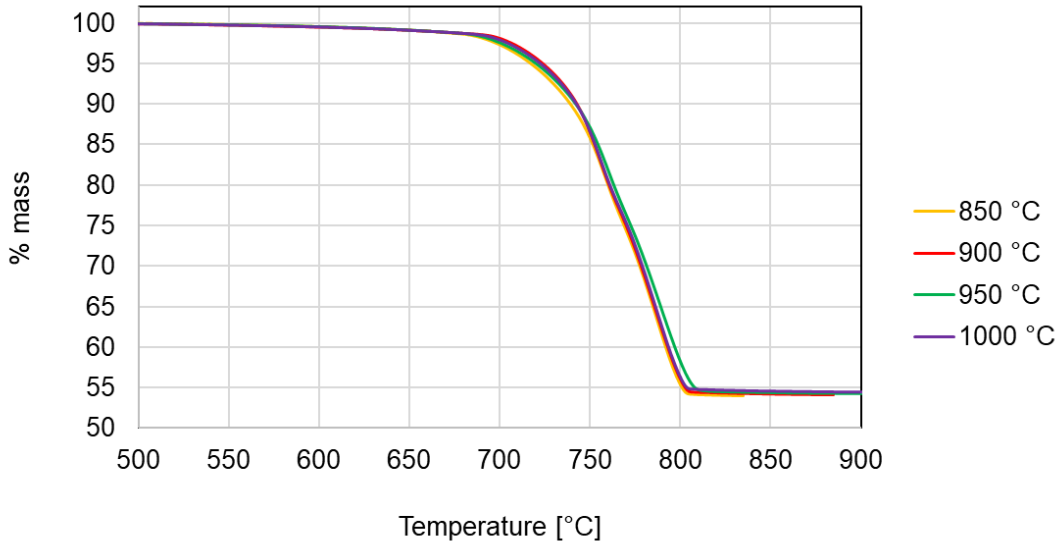

Figure 4.43: TG curve of the percent mass as a function of temperature for sample W decomposition – p_{CO2} = 0 bar. Heating rate 15 °C/min.

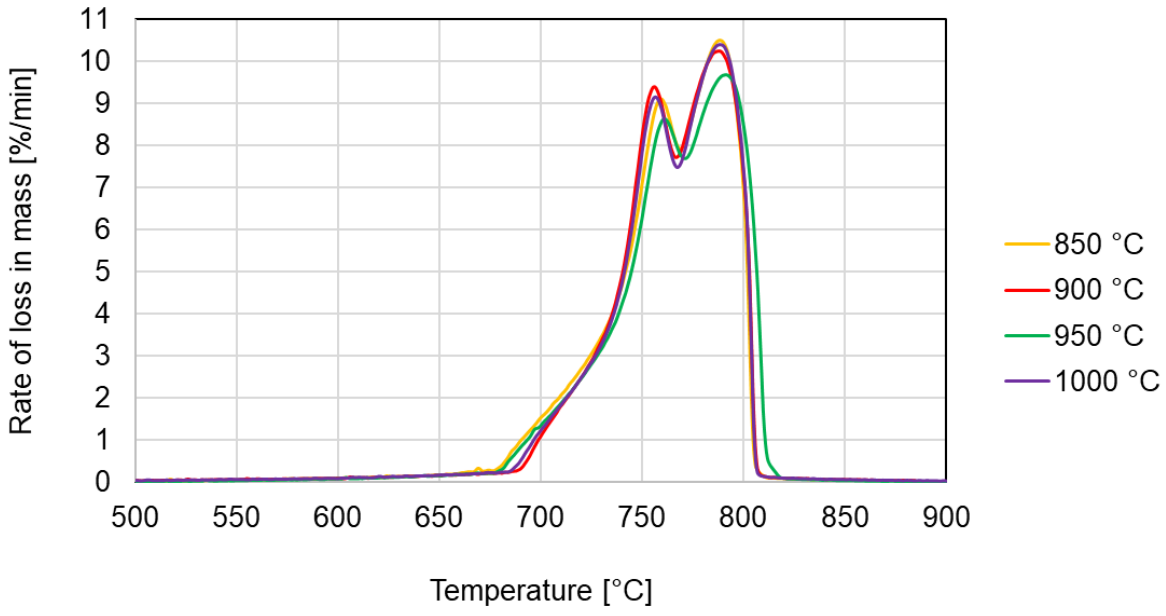

Figure 4.44: DTG curve of rate of loss in mass as a function of temperature for sample W decomposition – p_{CO2} = 0 bar. Heating rate 15 °C/min.

Further investigation using the rate of change in mass with temperature (Differential Thermogravimetry – DTG) showed that the decomposition actually occurred in two steps – Figure 4.44 The decomposition temperature of 700 °C – 800 °C is in accordance with a highly crystalline dolomite (Boynton, 1980), supporting the petrographic results that classified sample W as a micrite.

The overall decomposition was divided into two sub–steps according to temperature (Figure 4.44):

(i) 700 °C – 770 °C (770 °C is the saddle point) and

(ii) 770 °C – 850 °C

The first and second stages of decomposition occur at these temperatures and are in accordance with Barcina et al. (1997) and other literature (refer to the literature review section). The first stage was defined as all the mass loss from the onset temperature up to 770 °C, and the second stage as all mass loss from 770 °C until the offset temperature. The onset temperature is the temperature at which the slope of the derivative mass curve increases from 0. The offset temperature is the temperature at which the slope of the derivative mass curve returns to 0.

Table 4.18 shows the calculated expected mass loss from $MgCO_3$ and how it compares to the measured thermogravimetric (TG) mass loss over peak 1. Similarly, Table 4.19 shows the calculated expected mass loss from $CaCO_3$ and how it compares to the measured TG mass loss over peak 2. The calculated mass loss was based on the amount of MgO and CaO reported in the XRF analysis. XRF results reported 20.39 % MgO and 30.5 % CaO. As can be seen in Table 4.18, for $MgCO_3$ the measured amount of mass loss during TG matches the expected amount of mass loss very closely, 90 % or more. The mass loss of the second stage also matched the calculated mass loss very

closely, except at 950 °C. It is noted that the expected % of mass loss which did not occur in the first stage did occur in the second stage (last column of Table 4.18 and Table 4.19). It is therefore concluded that any $MgCO_3$ that did not decompose in the first stage, decomposed in the second stage.

Table 4.18: Calculated theoretical mass loss vs measured mass loss over peak 1.

Final Temp. [°C]	Measured total mass loss	Measured mass loss over peak 1	Measured: Peak1 loss/Tot loss	Calculated: Peak1 loss/Tot loss	Measured/calculated
850	39.3%	18.7%	0.48	0.48	0.99
900	39.8%	19.1%	0.48	0.48	1.00
950	39.0%	17.1%	0.44	0.48	0.91
1000	39.1%	18.5%	0.47	0.48	0.98

Table 4.19: Calculated theoretical mass loss vs measured mass loss over peak 2

Final Temp. [°C]	Measured total mass loss	Measured mass loss over peak 1	Measured: Peak2 loss/Tot loss	Calculated: Peak2 loss/Tot loss	Measured/calculated
850	39.3%	20.6%	0.52	0.52	1.01
900	39.8%	20.7%	0.52	0.52	1.00
950	39.0%	21.9%	0.56	0.52	1.08
1000	39.1%	20.6%	0.53	0.52	1.02

Hot stage XRD is an analytical method whereby XRD spectra of a material are gathered as the material is heated up. The hot stage XRD results (Figure 4.45) show, however, CaO and MgO peaks from 650 °C. Hot stage XRD confirmed the formation of MgO along with CaO as was observed in the TG results. The characteristic dolomite XRD peak at 31°, 41° and 45° ceased at 700 °C. The characteristic CaO XRD peak at ±31.5° and ±36.5° occurred from 650 °C and intensified after 770 °C indicating that more CaO formed after 770 °C. The MgO XRD peak at ±43° started occurring from 650 °C and then intensifies at 800 °C. The previous paragraph noted that $MgCO_3$ that did not decompose in the first stage decomposed in the second stage – see Figure 4.44. Therefore for Mg, the hot stage XRD data confirmed the TG data by showing production of MgO simultaneously with CaO after 800 °C. Post heating, the sample contained CaO

and MgO with a minor hexagonal Ca–Mg_2 phase in an approximate 1:1:0.06 ratio based on their Relative Intensity Ratios.

As mentioned in the literature study, the mechanism of dolomite decomposition is still much debated. From the above mentioned results it can be concluded that mechanism 3 (equations 8–10), as proposed by Britton et al. (1952) is followed (refer to section 2.4). In this mechanism, $MgCa(CO_3)_2$ decomposes to CaO and MgO at 700 °C – 770 °C. Almost immediate re–carbonation of the CaO to $CaCO_3$ takes place when CaO reacts with leftover dolomite and more MgO is formed. The $CaCO_3$ then decomposes at 770 °C – 850 °C. “Initial decomposition occurs at an interface, giving a solid solution (Mg,Ca)O, which soon breaks up into separate crystallites of magnesium oxide and of calcium oxide. The solid solution would probably have the pseudo–lattice of dolomite, and so long as this persists the carbon dioxide molecules would move to the exterior by a lattice migration, each molecule jumping from a lattice hole left by a previous molecule, to an adjacent one. If then the reaction is carried out rapidly so that the solid solution breaks up slightly or not at all whilst the experiment is in progress, a definite interface will be present” (Britton et al., 1952). Several authors have agreed that the (Mg,Ca)O interface breaks up into MgO and CaO (Cater and Buseck, 1985; Rodriguez–Navarro et al., 2012; Spinolo and Anselmi–Tamburini, 1989). The CaO undergoes re–carbonation on an interface which is located on separate CaO/$CaCO_3$ crystallites (Britton et al., 1952). The re–carbonation interface is not parallel with the decomposition interface (Britton et al., 1952).

A dolomite milled for 90 min, as the sample in this study was, is expected to have a peak temperature at 760 °C and 845 °C (Guzzo et al., 2019). The first peak of $MgCO_3$ decomposition agrees with literature. The second peak is lower possibly due to petrographic differences in the rock: the rock used in this study is from a different geological area as the rock used in the study of Guzzo et al. (2019).

The decomposition of dolomite in pCO_2 = 0 bar was repeated at 4 different furnace temperatures. Similar decomposition parameters were obtained for all temperatures as seen in Table 4.20.

Table 4.20: Characteristics of sample W's decomposition at pCO_2 = 0 bar

	Sample W, 0 bar CO_2			
	850 °C	900 °C	950 °C	1000 °C
Total mass change [%]	46	46	46	46
Onset temp [°C]	727	728	728	728
Max peak 1 [°C]	759	756	761	757
Max peak 2 [°C]	789	789	792	790
Offset temp [°C]	807	807	814	807
Decomposition range [°C]	80	79	86	79
Decomposition time [min]	5.35	5.26	5.70	5.25

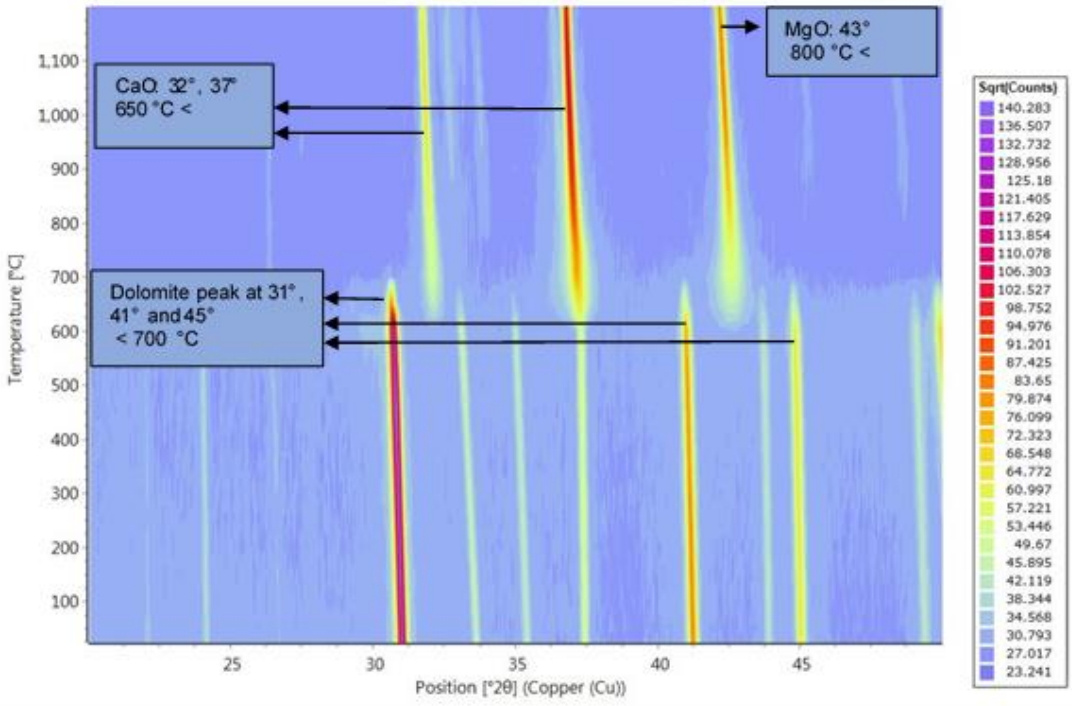

Figure 4.45: Hot stage XRD of sample W under an air atmosphere up to 1150 °C. Cu Kα.

4.8.3.2 p_{CO2} = 1 bar – Varying final temperature

Figure 4.46 and Figure 4.47 show clearly how the decomposition of sample W in an atmosphere with p_{CO2} = 1 bar occurs in two distinguishable steps.

The first step between 700 °C and 800 °is the decomposition of dolomite to MgO, CO_2 and $CaCO_3$. The mass loss of 22.6 % in this first step matches the expected mass loss from MgO of 22.14%. The onset temperature of the first step reaction, as recorded in Table 4.20, is in agreement with literature (Barcina et al., 1997a; Eriksson, 2016). In agreement with McIntosh et al. (1990) the first peak temperature is slightly lower in an atmosphere with p_{CO2} = 1 bar than in an atmosphere with no CO_2 (p_{CO2} = 0 bar). The first step is in accordance with equation 14 and the second step according to equation 15.

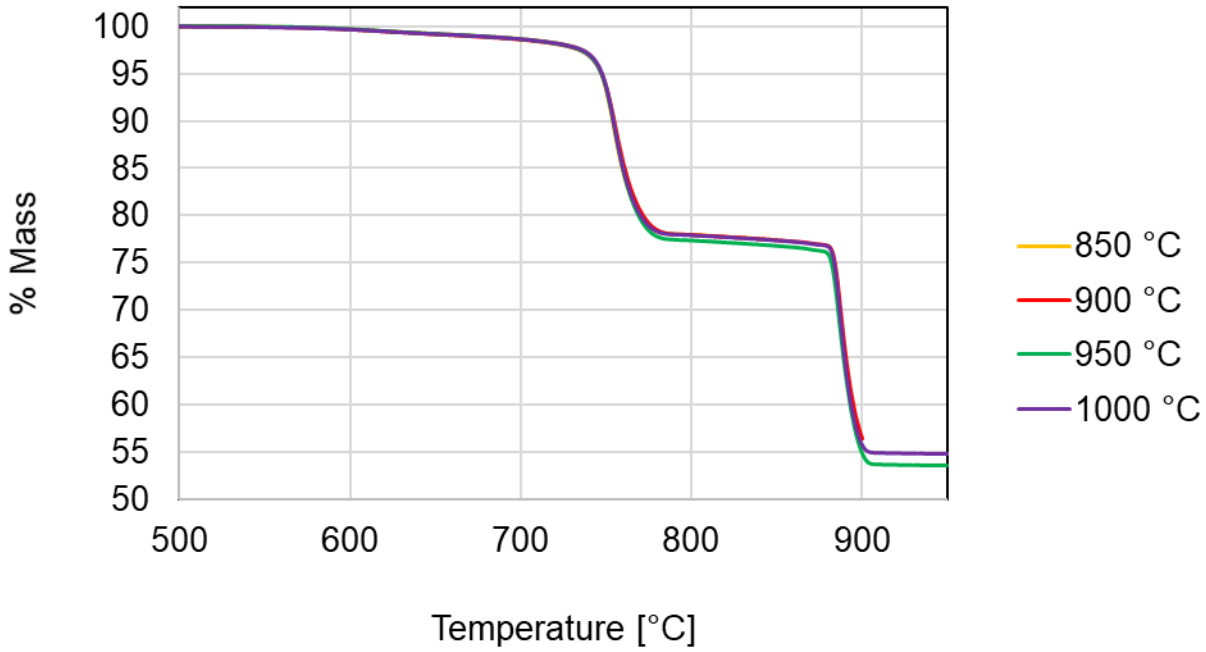

Figure 4.46: TG curve of percent mass as a function of temperature for sample W decomposition – p_{CO2} = 1 bar. Heating rate 15 °C/min

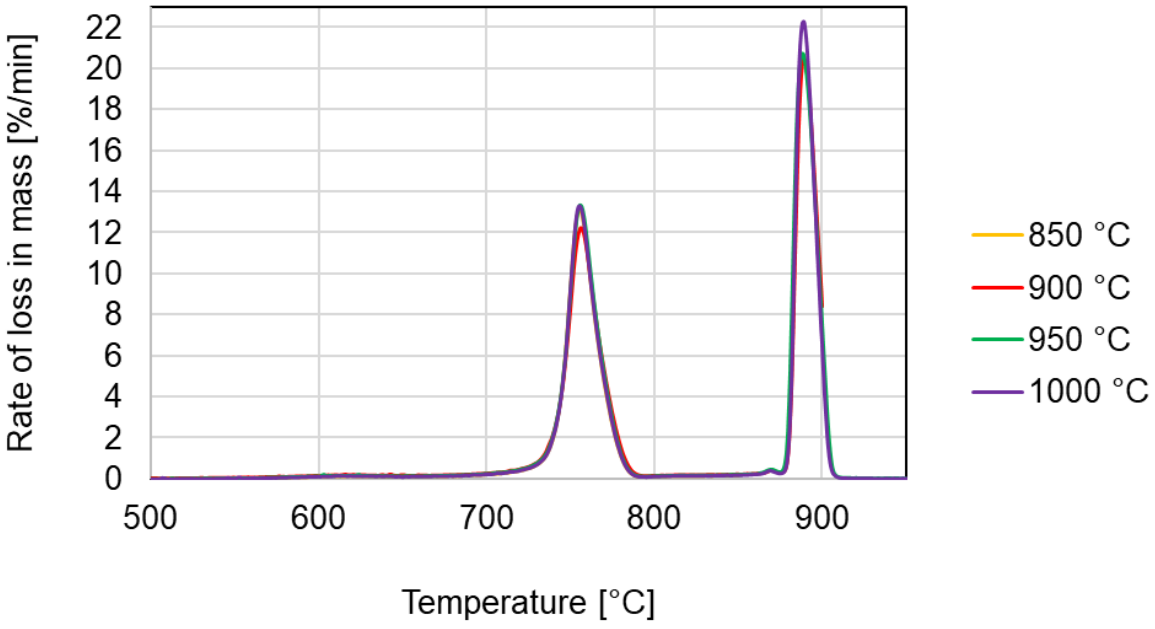

Figure 4.47: DTG curve of rate of loss in mass as a function of temperature for sample W decomposition – p_{CO2} = 1 bar. Heating rate 15 °C/min

The second step between 850 °C and 910 °C is the decomposition of $CaCO_3$ to CaO and CO_2. The onset temperature of this step (Table 4.21) is higher than predicted by literature (Barcina et al., 1997a; Eriksson, 2016). This is possibly because of a higher purity limestone.

Table 4.21: Characteristics of sample W's decomposition at p_{CO2} = 1 bar

	Sample W, 1 bar CO_2			
	850 °C	900 °C	950 °C	1000 °C
Total mass change [%]	23	44	46	45
Onset temp 1 [°C]	742	741	742	741
Max peak 1 [°C]	755	756	756	755
Onset temp 2 [°C]	N/A	881	880	879
Max peak 2 [°C]	N/A	889	888	888
Offset temp [°C]	785	900+	907	907
Decomposition range [°C]	43	159	165	166
Decomposition time [min]	2.90	10.59	11.00	11.05

As can be seen in Table 4.21 the maximum peak temperatures and onset temperatures do not vary greatly. The decomposition time is 11±0.05 min with the first step taking only 3 min of the total reaction time.

4.8.3.3 Comparison of p_{CO2} = 0 bar and p_{CO2} = 1 bar

Figure 4.48 compares the decomposition of sample W at p_{CO2} = 0 bar and p_{CO2} = 1 bar. From Figure 4.48 it can be seen how the first stage at p_{CO2} = 1 bar matches the first stage at p_{CO2} = 0 bar. It can also be seen how the two stages that were unresolved at p_{CO2} = 0 bar were resolved clearly at p_{CO2} = 1 bar.

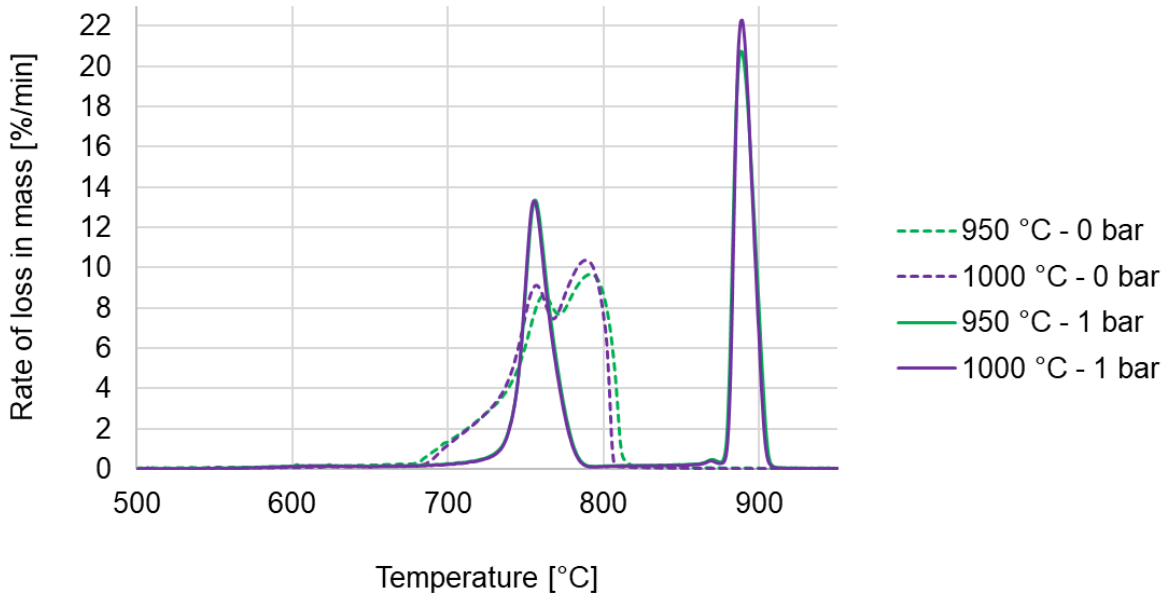

Figure 4.48: Sample W decomposition - 0 bar vs 1 bar p_{CO2}

The onset temperature and peak temperature for both stages is higher at p_{CO2} = 1 bar. The reason for these higher temperatures is thermodynamics. The Gibbs energy of the dolomite is given by the equation

$$\Delta G = \Delta G^{\circ} + RT\ln Q \qquad (19)$$

where $Q = pCO_2$

When the partial pressure of CO_2 is increased the total free Gibbs energy is higher and therefore more energy, i.e. a higher onset temperature, is required for the decomposition to proceed.

The higher peak temperature is attributed to diffusion rates of CO_2. If the diffusion rate of CO_2 out of the sample is fast then the pCO_2 in the sample holder approximates the pCO_2 in thermobalance i.e. 1 bar. This leads to a smaller driving force for the diffusion of the CO_2 and therefore a higher temperature was necessary. Thus, a lower pCO_2 requires a lower peak temperature

The rate of decomposition is higher for both stages at p_{CO2} = 1 bar. The rate of decomposition is a function of temperature and CO_2 diffusion rate. The rate at pCO_2 = 1 bar was higher because the decomposition temperature was higher.

For the second stage the rate of decomposition doubles when comparing p_{CO2} = 0 bar to p_{CO2} = 1 bar. The decomposition at p_{CO2} = 0 bar took approximately 5.5 min and at p_{CO2} = 1 bar approximately 11 min.

4.8.3.4 Impurities

Quartz and siderite were reported as impurities in the XRD results. Petrography proved pyrite as an impurity. The decomposition temperatures of quartz, siderite and pyrite at pCO_2 = 0 bar are respectively 1710 °C, 527 °C and 802 °C (Raask, 1985). The SPA showed that sample W does contain Al and Mn impurities as "silicates" and "sulphate silicates" (refer to Table 4.10 and Figure 4.29) but there is no clear indication as to exactly in what mineral the Al and Mn impurities occur.

The decomposition of quartz occurs at too high a temperature and will not be seen on a TG curve or derivative curve.

The decomposition of siderite is not seen on the TG curve because

(i) There is no small peak at 528 °C on the derivative curve

(ii) XRD reports 0.523 % of siderite present,

A mass difference of 0.523% occurred between 528 °C and 628 °C – Siderite could not have decomposed over such a wide range.

The decomposition of pyrite cannot be seen on the p_{CO2} = 0 bar curve because the decomposition of $CaCO_3$ is still in progress at that temperature. On the p_{CO2} = 1 bar curve there is also no small derivative peak at 528 °C.

On the p_{CO2} = 1 bar curve there is, however, a small derivative peak at 870 °C. This peak is most likely due to the decomposition of an ankerite ($Ca[Fe^{2+},Mg][CO_3]_2$) phase which, according to literature, decomposes at ~870 °C in a 50% CO_2 atmosphere (Warne, 1986).

4.8.4 Limestone – Sample X (Northern Cape)

4.8.4.1 p_{CO2} = 0 bar – Varying final temperature

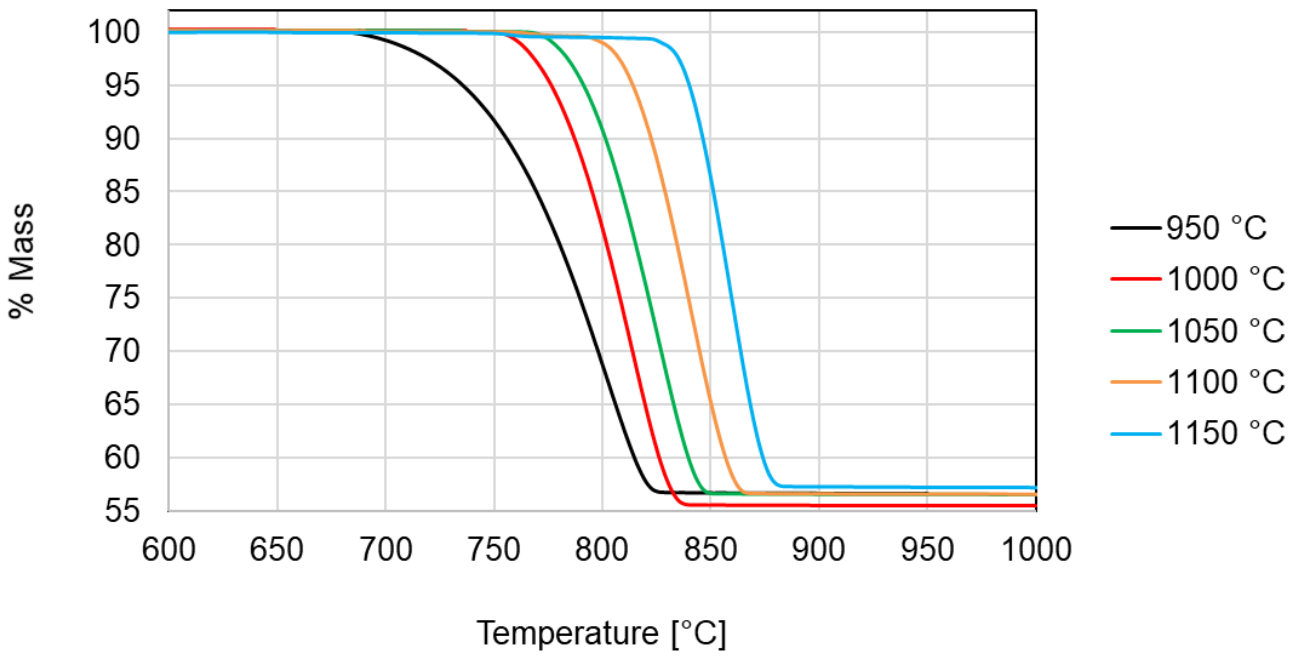

Figure 4.49: Percentage mass as a function of temperature for sample X decomposition – p_{CO2} = 0 bar. Heating rate 15 °C/min

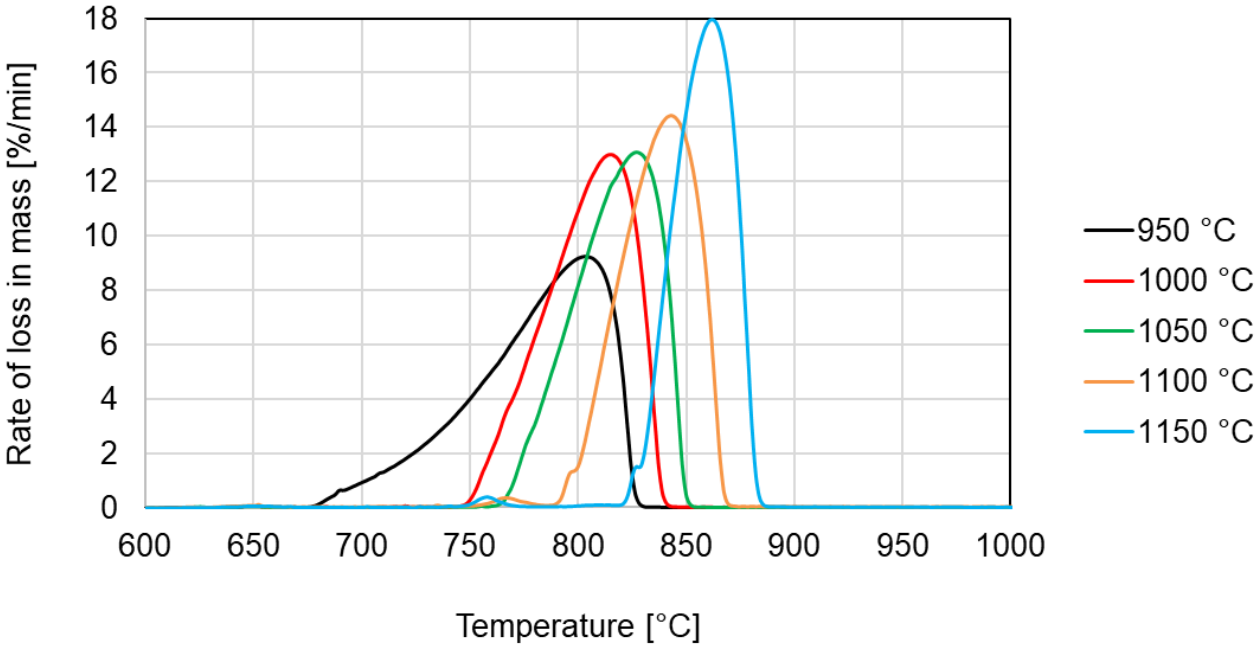

Figure 4.50: DTG curve as a function of temperature for sample X decomposition – p_{CO2} = 0 bar. Heating rate 15 °C/min

Figure 4.49 shows the total mass loss and Figure 4.50 shows rate of mass loss. In Figure 4.50 a small deflection in the curve at the onset temperature can be seen for the curves of 1100 °C and 1150 °C. The curve is level for a very short period at this temperature and thus the rate stays constant. A kind of “shoulder” appeared. This phenomenon is attributed to the way calcination takes place. Dissociation of the stone proceeds from the outside surface inward (Boynton, 1980). Usually the hot gases penetrate the limestone particle uniformly inwards on all sides. In actual fact, a certain amount of surface dissociation can occur at lower temperatures under low CO_2 partial pressures (Boynton, 1980).

“In order for dissociation to penetrate into the interior of the limestone, higher temperatures are necessary and further elevated for dissociation to occur in the core of the stone” (Boynton, 1980). The gas is the carrier of thermal energy. Therefore this study suggests that the rate of decomposition stays constant for a very short while at the onset temperature as the surface calcium carbonate dissociates. As the temperature is elevated further, the hot gases diffuse further

to the core of the stone causing decomposition to resume and the curve trends upwards again. The reason why this phenomenon is not seen at p_{CO2} = 1 bar is because the $CaCO_3$ on the surface is not favoured to dissociate in a CO_2 atmosphere according to the Gibbs energy principle. The CO_2 in the surrounding atmosphere in contact with the surface is already at 1 bar, forcing the dissociation reaction of $CaCO_3$ on the surface in the opposite direction.

A summary of the decomposition characteristics of sample X at p_{CO2} = 0 bar is given in Table 4.22.

Table 4.22: Characteristics of sample X's decomposition at p_{CO2} = 0 bar.

	Sample X, 0 bar CO_2				
	950 °C	1000 °C	1050 °C	1100 °C	1150 °C
Total mass change [%]	43	45	44	44	43
Onset temp [°C]	719	754	770	797	829
Max peak [°C]	803	815	827	843	862
Offset temp [°C]	827	840	851	868	884
Decomposition range [°C]	108	86	81	71	55
Decomposition time [min]	7.20	5.73	5.41	4.71	3.69

4.8.4.2 p_{CO2} = 1 bar – Varying final temperature

As can be seen in Figure 4.51 and Figure 4.52 the onset temperature, maximum peak temperature and range were similar for all temperatures to which the thermobalance was heated except 1050 °C which had a lower peak temperature. The onset temperature of 888±2 °C in an atmosphere of p_{CO2} = 1 bar is in agreement with literature (Eriksson, 2016). The 2 °C variance is attributed to measuring uncertainties and differences in study samples. 2 °C is a small difference considering that decomposition temperatures of different samples can differ up to 10 °C (Eriksson, 2016).

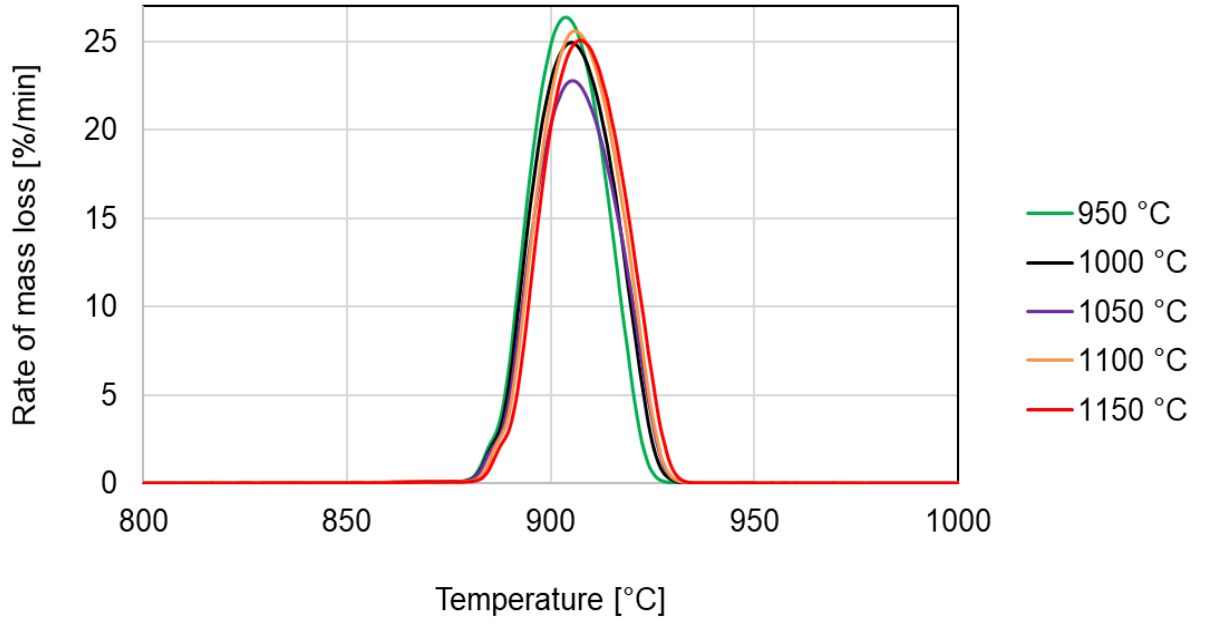

Figure 4.51: DTG curve as a function of temperature for sample X decomposition – p_{CO2} = 1 bar. Heating rate 15 °C/min

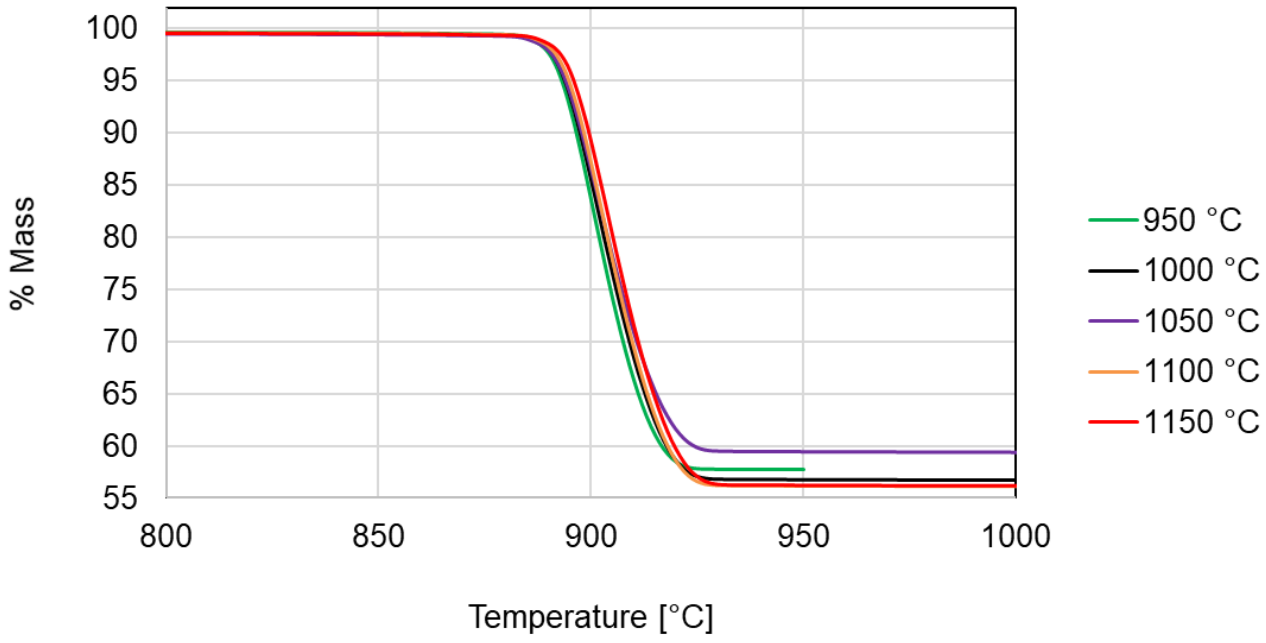

Figure 4.52: Percentage mass as a function of temperature for sample X decomposition – p_{CO2} = 1 bar. Heating rate 15 °C/min

In Figure 4.51 the “shoulder” appears again but less prominent. This is because the “shoulder” is an effect of temperature and not pCO_2. The hot temperature gas sinters the outside of the sample at first and only diffuses further into the sample as the temperature increases. “In order for dissociation to penetrate into the interior of the limestone, higher temperatures are necessary and further elevated for dissociation to occur in the core of the stone” (Boynton, 1980).

Table 4.23 shows specific details of the decomposition characteristics at different final thermobalance temperatures. The variances in total mass loss is attributed to measuring uncertainties and sample variations. It is noted that a T_f of 1050 °C yielded the lowest total mass loss and was most likely due to sintering. This amount of mass losses are in accordance with the total mass loss expected of a pure limestone (44% CO_2) and confirms the classification of sample X as a high purity limestone.

The decomposition time of sample X at p_{CO2} = 1 bar (2.75 min average) is 50% lower than at p_{CO2} = 0 bar (5.35 min average). An average decomposition time of 2.8 min was observed for all the final temperature runs except 950 °C when the decomposition time was 2.55 min.

Table 4.23: Characteristics of sample X's decomposition at p_{CO2} = 1 bar

	Sample X, 1 bar CO_2				
	950 °C	1000 °C	1050 °C	1100 °C	1150 °C
Total mass change [%]	42	43	41	44	44
Onset temp [°C]	887	887	887	888	890
Max peak 1 [°C]	904	905	905	906	907
Offset temp [°C]	925	929	930	930	932
Decomposition range [°C]	38	42	43	42	42
Decomposition time [min]	2.55	2.78	2.84	2.77	2.82

4.8.4.3 Comparison of p_{CO2} = 0 bar and p_{CO2} = 1 bar

At p_{CO2} = 0 bar there is a significant difference in the decomposition behaviour of sample X (see Figure 4.53). At 950 °C, the decomposition occurs at a slower rate and over a larger temperature range than for 1150 °C. The onset and peak temperatures are also lower for 950 °C than 1150 °C. This is because the rate is dependent on temperature and pCO_2. At a lower temperature and lower pCO_2 a lower rate of decomposition occurs.

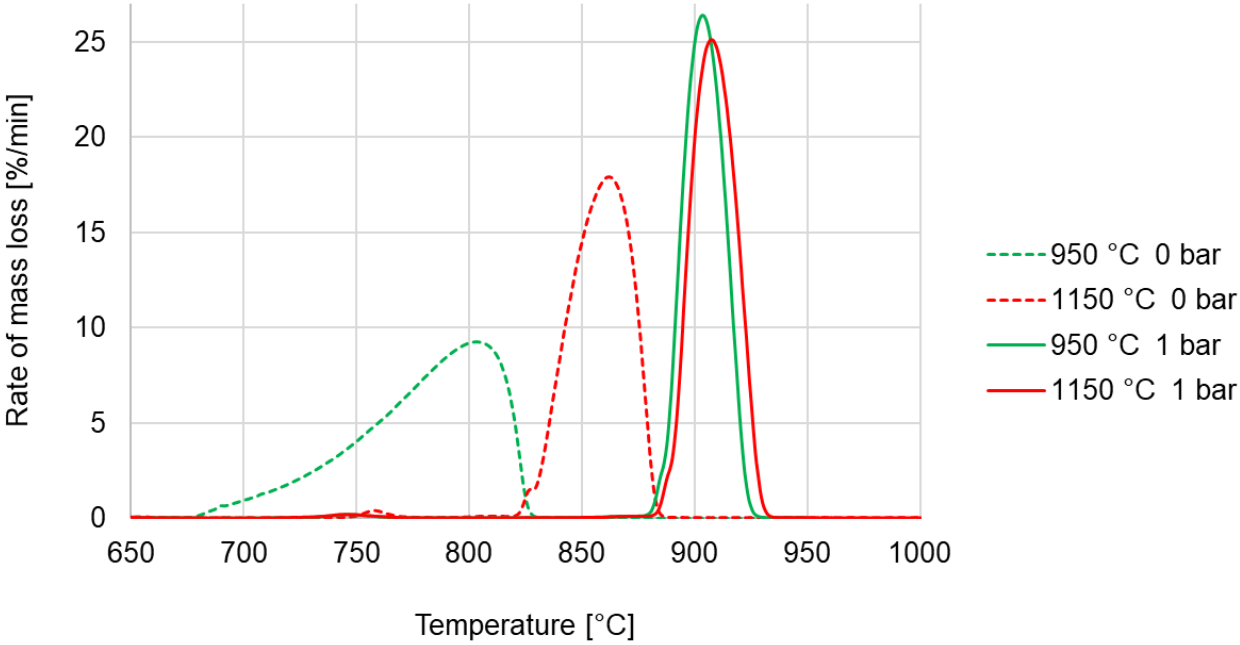

Figure 4.53: Sample X decomposition - 0 bar vs 1 bar p_{CO2}

At p_{CO2} = 1 bar the DTG curves for sample X's decomposition are very similar. This is because the CO_2 partial pressure played a larger role than temperature. Therefore the curves were very similar. For a thermobalance temperature of 950 °C, the peak temperature is slightly lower because at 1150 °C a higher peak rate could be achieved. The total mass loss at 1150 °C is, however, larger than at 950 °C.

4.8.4.4 Impurities

For the DTG graph at p_{CO2} = 0 bar, there is an interesting occurrence at final temperatures of 1100 °C and 1150 °C:

(i) A small peak at 766 °C (for T_f 1100 °C)

(ii) A small peak at 758 °C (for T_f 1150 °C)

Both these occurrences are indicative of the decomposition of impurities. These small peaks are not shown in the curve at other final temperatures because they would occur in the temperature decomposition range of $CaCO_3$ and therefore be overshadowed by the $CaCO_3$ curve.

For a T_f of 1100 °C, a mass change of 0.29% was recorded over the small peak at 766 °C. For a T_f of 1150 °C, a mass change of 0.32% was recorded over the small peak at 758 °C. This is likely due to the decomposition of ferroan dolomite. Milodowski et al. (1989) reported that a ferroan dolomite decomposed into $CaCO_3$, MgO and $MgFe_2O_4$ or Fe_3O_4. The decomposition onset temperature of ferroan dolomite depended on the Iron and Manganese content. They found that a ferroan dolomite with the structural composition $Ca_{1.007}Mg_{0.858}Fe_{0.113}Mn_{0.024}(CO_3)_2$ decomposed at 758 °C and a ferroan dolomite of structural composition $Ca_{1.001}Mg_{0.858}Fe_{0.002}Mn_{0.002}(CO_3)_2$ decomposed at 788 °C.

The decompositions of fluoborite (decomposition at 780 °C) and thulite (decomposition at 969 °C) was not registered on the TG curves.

4.8.5 Limestone – Sample Y (Northern Cape)

4.8.5.1 p_{CO2} = 0 bar – Varying final temperature

Figure 4.54 and Figure 4.55 indicate the decomposition behaviour of sample Y at thermobalance temperatures of 950 °C, 1000 °C, 1050 °C, 1100 °C and 1150 °C. The decomposition at 950 °C and 1000 °C have similar onset, peak and offset temperatures; unlike sample X where 1000 °C and 1050 °C had similar onset, peak and offset temperatures. A high purity limestone decomposes similarly at various temperatures due to homogeneity and the absence of impurities (Oates, 20118). The fact that this limestone decomposed in a similar manner at 950 °C, 1000 °C and 1050 °C is indicative of a high purity limestone. This was expected since the XRF analysis reported a high calcite purity in sample Y. At 1100 °C and 1150 °C sintering had a noticeable effect on the onset temperature.

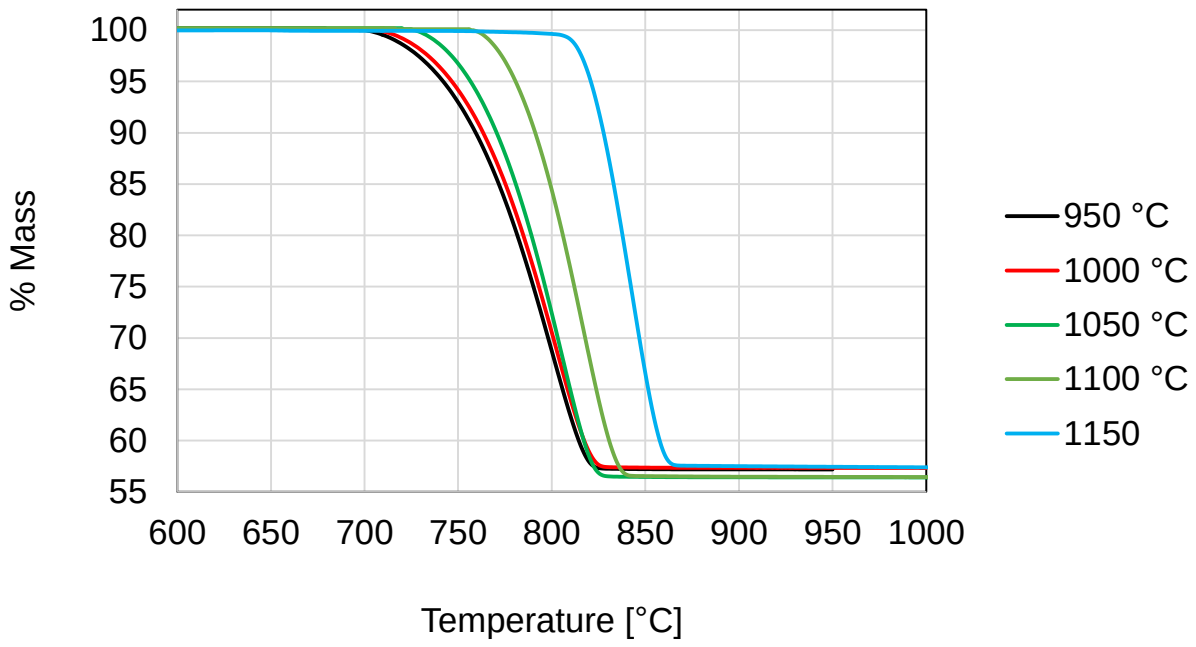

Figure 4.54: Percentage mass as a function of temperature for sample Y decomposition – p_{CO2} = 0 bar. Heating rate 15 °C/min

The decomposition rate reached a peak at 97 % of the decomposition temperature range for all temperatures except 1150 °C – see Figure 4.55. At 1150 °C the peak was achieved only at 99.5% of the decomposition range.

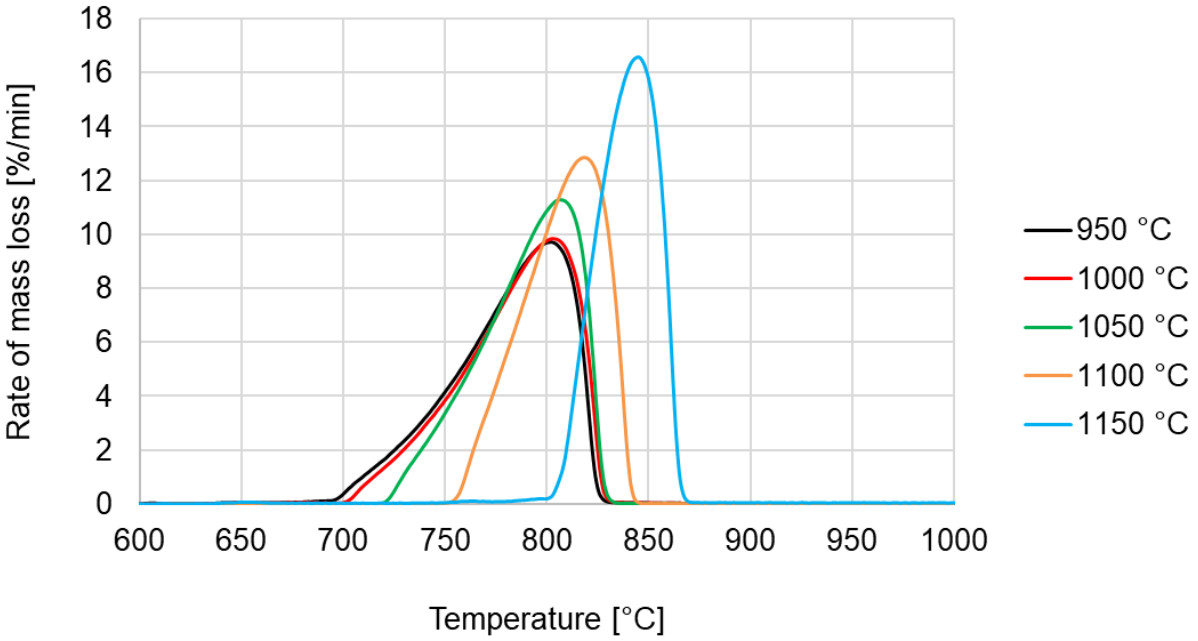

Figure 4.55: DTG curve as a function of temperature for sample Y decomposition – p_{CO2} = 0 bar. Heating rate 15 °C/min

As the final temperature increases the decomposition time decreases (Table 4.24). The decomposition time is 75 % shorter at 1150 °C than at 950 °C.

Table 4.24: Characteristics of sample Y's decomposition at p_{CO2} = 0 bar.

	Sample Y, 0 bar CO_2				
	950 °C	1000 °C	1050 °C	1100 °C	1150 °C
Total mass change [%]	43	43	44	44	43
Onset temp [°C]	721	726	734	756	806
Max peak [°C]	802	803	807	819	865
Offset temp [°C]	826	829	830	843	868
Decomposition range [°C]	105	104	96	87	62
Decomposition time [min]	7.00	6.90	6.38	5.82	4.11

4.8.5.2 p_{CO2} = 1 bar – Varying final temperature

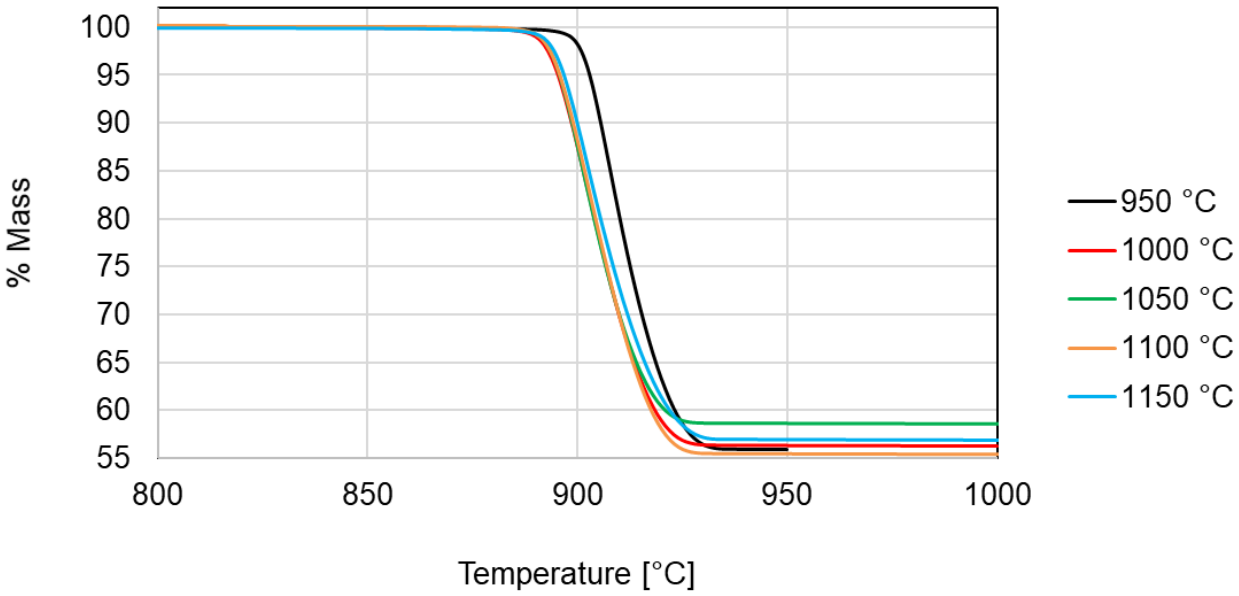

Figure 4.56: Percentage mass as a function of temperature for sample Y decomposition – p_{CO2} = 1 bar. Heating rate 15 °C/min

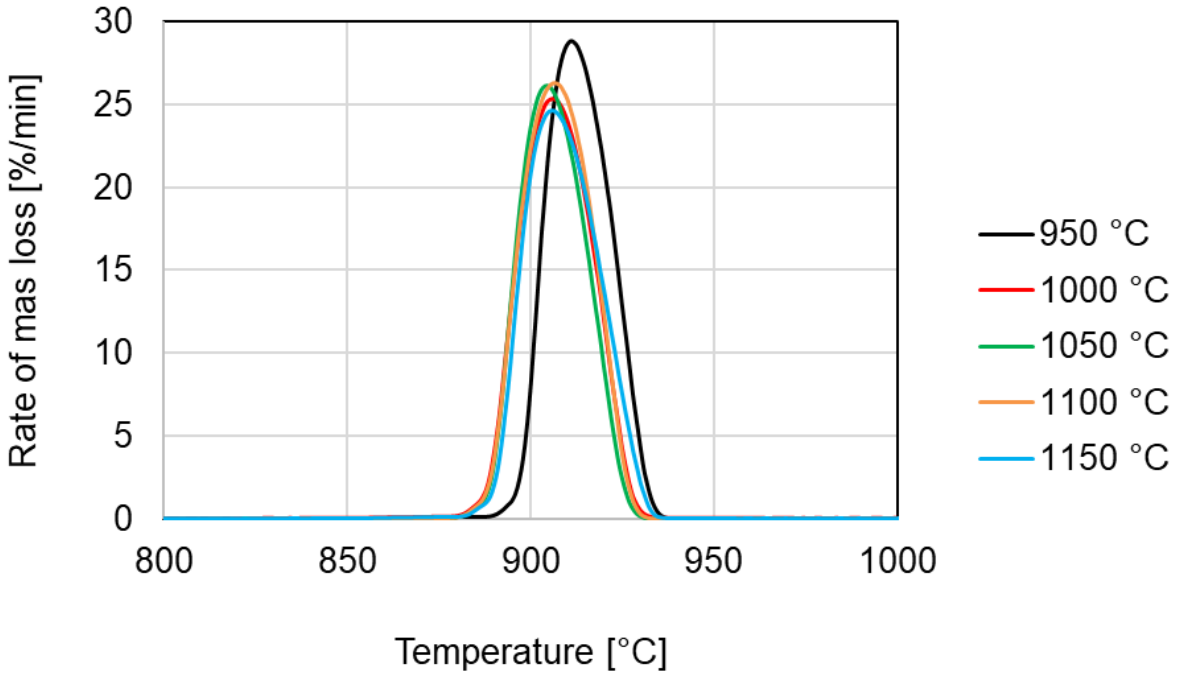

Figure 4.57: DTG curve as a function of temperature for sample Y decomposition – p_{CO2} = 1 bar. Heating rate 15 °C/min

As shown in Figure 4.56 and Figure 4.57, the decomposition behaviour at p_{CO2} = 1 bar is similar for all final temperatures except 950 °C. At 950 °C, the onset temperature, peak temperature and rate of decomposition are higher. The reason for this is unsure and literature does not offer any possible explanations.

The values in Table 4.25 agree with the decomposition characteristics that would be expected from a high-purity limestone. The onset temperature of 888±2 °C is the expected onset temperature of a limestone in a p_{CO2} = 1 bar atmosphere (Eriksson, 2016). In Figure 4.57, an important observation is that at all the thermobalance temperatures the maximum decomposition rate was reached at 905 °C except for a thermobalance temperature of 950 °C. At a thermobalance temperature of 950 °C the peak decomposition rate was reached at 912 °C. The difference at 950 °C is attributed to an uncertainty in measurement.

It is noted that in Figure 4.56, the 1050 °C final temperature curve shows a relatively lower total mass loss in relation to the other final temperatures. Table 4.25 shows all the mass losses and, as can be seen, the highest mass loss was achieved when the thermobalance was set to 1100 °C. Standard deviation of the mass losses measured is 1.2 %. Thus only the mass loss at 1050 °C is an outlier from the expected 44 % mass loss from a high purity limestone. Therefore kilns in industry could achieve a higher amount of available lime with a lower furnace setpoint i.e. 950 °C rather than a higher setpoint e.g. 1050 °C.

Table 4.25: Characteristics of sample Y's decomposition at p_{CO2} = 1 bar

	Sample Y, 1 bar CO2				
	950 °C	1000 °C	1050 °C	1100 °C	1150 °C
Total mass change [%]	44	43	42	45	43
Onset temp [°C]	898	889	889	889	890
Max peak [°C]	911	906	904	907	906
Offset temp [°C]	936	931	929	930	934
Decomposition range [°C]	38	42	40	41	44
Decomposition time [min]	2.56	2.82	2.64	2.74	2.90

4.8.5.3 Comparison of p_{CO2} = 0 bar and p_{CO2} = 1 bar

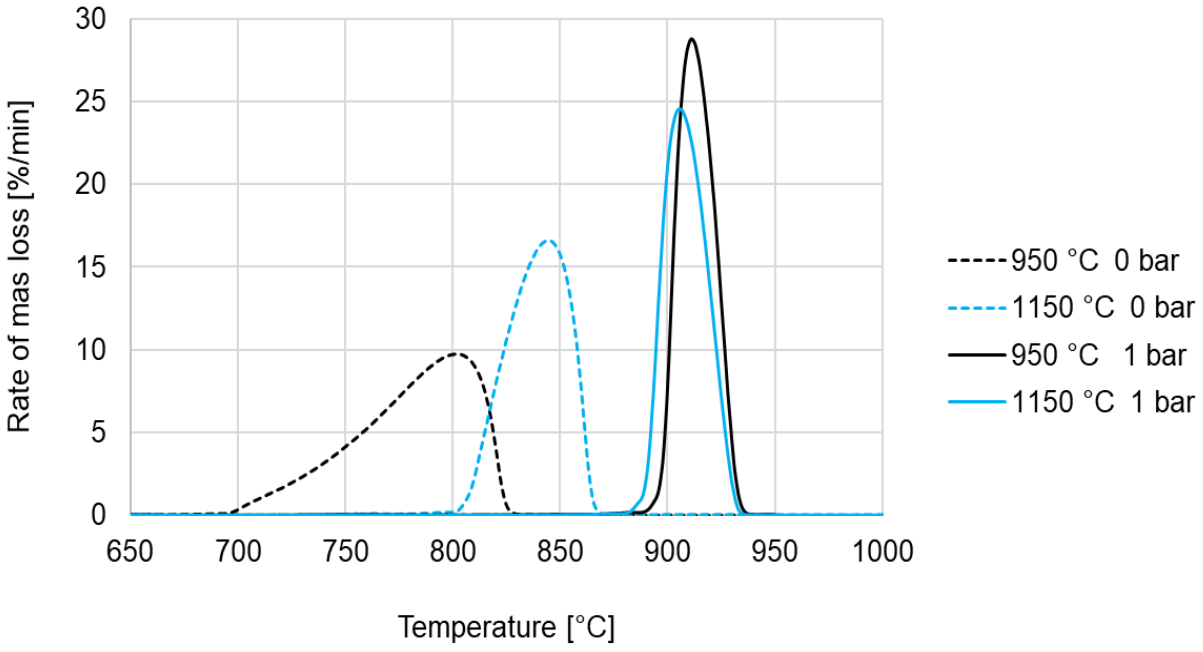

Figure 4.58: Sample Y decomposition – 0 bar vs 1 bar p_{CO2}.

At p_{CO2} = 0 bar Figure 4.58 shows that, like sample X, there is a significant difference between the derivative mass curves for 950 °C and 1150 °C. At 950 °C, the onset temperature and maximum peak temperature are lower, indicating a slower rate of decomposition. The larger temperature range of decomposition for 950 °C confirms the slower rate at 950 °C in comparison to 1150 °C. The onset temperature and peak temperature for 1150 °C are higher and the decomposition takes place at a faster rate, as is evident from the smaller temperature range of decomposition. Therefore temperature has a dominant effect on the decomposition rate at low pCO_2.

At p_{CO2} = 1 bar: The decomposition of 950 °C is more similar to 1150 °C than at p_{CO2} = 0 bar, but the difference is not as small as with sample X.

At p_{CO2} = 1 bar, the onset temperature, peak temperature and rate of decomposition are substantially higher for 950 °C than for 1150 °C. As

mentioned earlier, no obvious reasons exist for this much higher rate at 950 °C. The average mass loss is the same at both CO_2 partial pressures.

4.8.5.4 Impurities

No clear peaks on the derivative mass curves of sample Y that are indicative of impurities were identified. Raman results have, however, shown the presence of quartz, fluoborite and thulite.

The decomposition of fluoborite (decomposition at 780 °C) would be part of the $CaCO_3$ decomposition curve at p_{CO2} = 0 bar and would thus not be present as a separate peak on the TG curve if it were present. At p_{CO2} = 1 bar it would however show as a separate peak because it is outside the temperature range of $CaCO_3$ decomposition, but no peak was visible at that temperature. Thulite (decomposition at 969 °C) did not show as a TG peak at either of the CO_2 partial pressures.

4.8.6 Sample Z

4.8.6.1 p_{CO2} = 0 bar – Varying final temperature

Just as for the dolomite (Sample W, refer to section 4.8.3), the onset temperature, offset temperature, peak temperature and rate of decomposition was recorded at five different thermobalance set point temperatures for sample Z (Figure 4.59). As can be seen in Figure 4.59, the onset and peak temperature remain relatively constant for all final thermoblance temperatures but decreased for the final temperature of 1150°C. This decrease is attributed to uncertainty in measurement and no definite conclusions can be drawn from it.

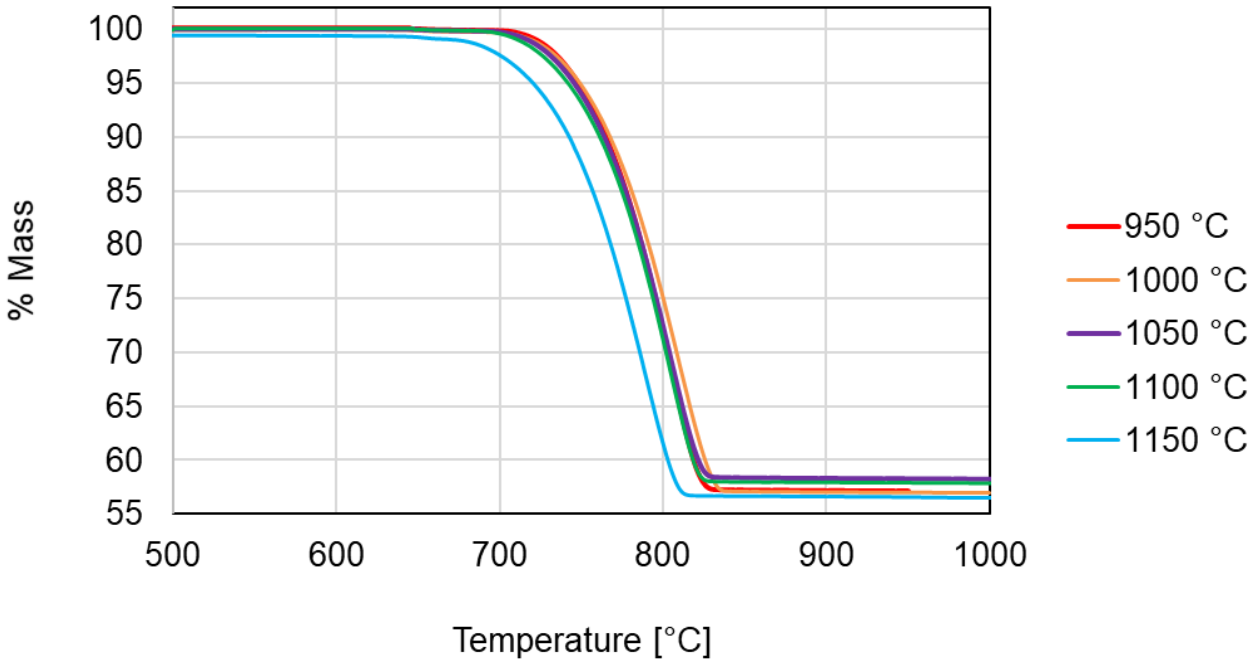

Figure 4.59: Percentage mass as a function of temperature for sample Z decomposition – p_{CO2} = 0 bar. Heating rate 15 °C/min

The decomposition rate (Figure 4.60) is similar for all final temperatures, except for 1000 °C and 1150 °C. For 1000 °C and 1150 °C, the decomposition rate was slightly lower than for the other thermobalance temperatures. The highest rate of decomposition was achieved at 950 °C. The variance is attributed to uncertainty in measurments.

Table 4.26 gives a summary of the main features of sample Z's decomposition at different final temperatures. As can be seen, the only outliers, due to uncertainty in measurement, were 1000 °C and 1150 °C. It is important to note that the shortest decomposition time was at 950 °C and 1100 °C.

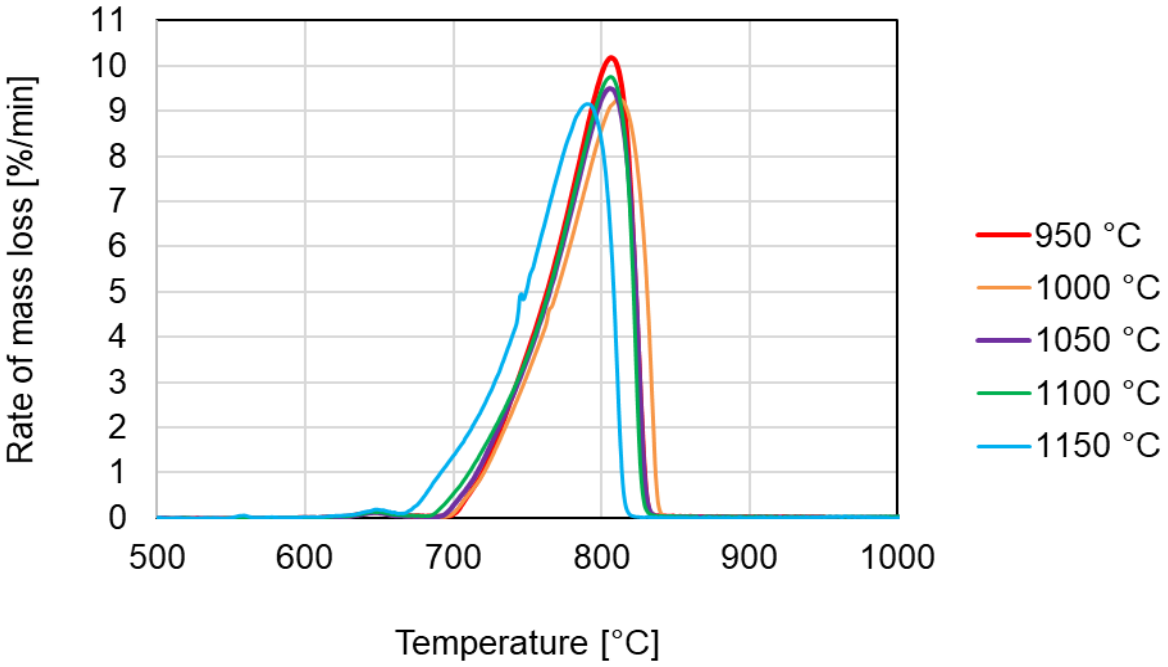

Figure 4.60: DTG curve as a function of temperature for sample Z decomposition – p_{CO2} = 0 bar. Heating rate 15 °C/min

Table 4.26: Characteristics of sample Z's decomposition at p_{CO2} = 0 bar.

	Sample Z, 0 bar CO2				
	950 °C	1000 °C	1050 °C	1100 °C	1150 °C
Total mass change [%]	43	43	42	42	43
Onset temp [°C]	730	730	729	728	710
Max peak [°C]	806	812	806	806	790
Offset temp [°C]	831	839	831	829	817
Decomposition range [°C]	101	109	102	101	107
Decomposition time [min]	6.76	7.24	6.80	6.73	7.16

4.8.6.2 p_{CO2} = 1 bar – Varying final temperature

The decomposition behaviour of sample Z at p_{CO2} = 1 bar is much different from the decomposition behaviour at p_{CO2} = 0 bar. For this reason, the strange decomposition behaviour of sample Z at p_{CO2} = 1 bar is attributed to how CO_2 is displaced from the stone during the calcination of the limestone crystals as is also evident in Figure 4.61. It is only at higher CO_2 partial pressures that the decomposition behaviour changes.

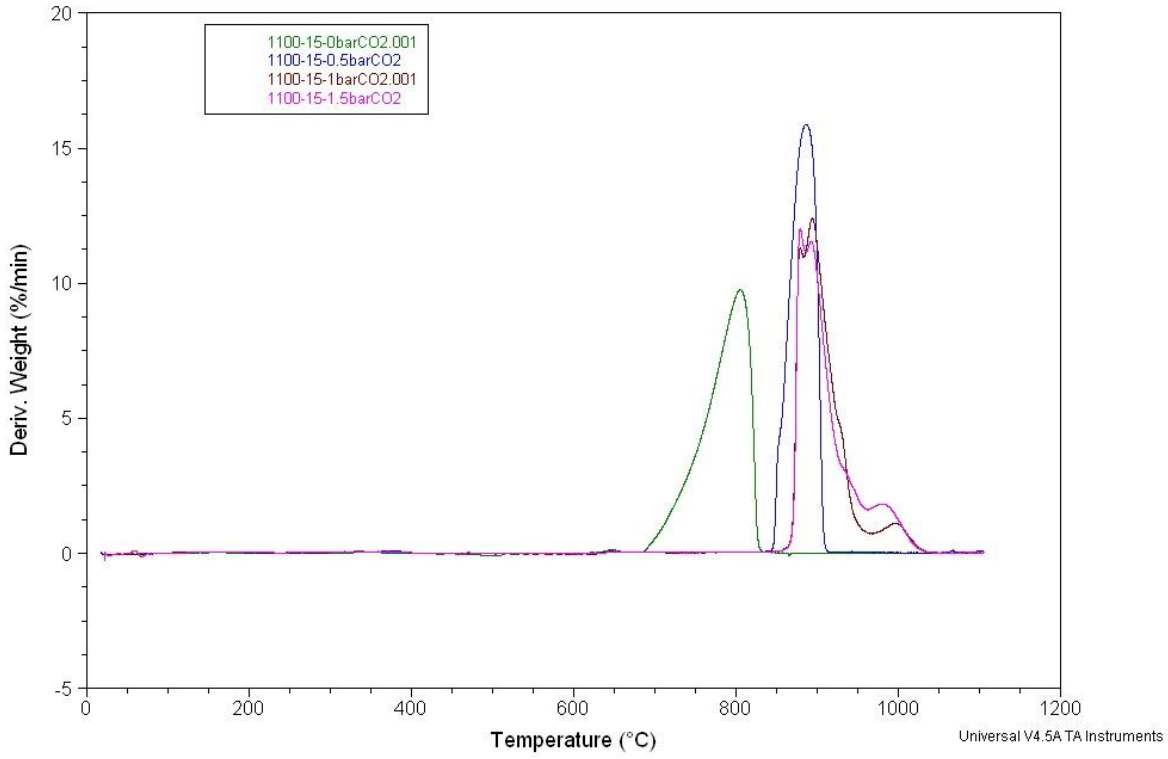

Figure 4.61: Decomposition of sample Z at different CO_2 pressures

The movement of CO_2 is impacted by the microstructure and petrography of the limestone (Alaabed et al., 2014; Lech et al., 2009; Marinoni et al., 2015; Soltan, 2011; Soltan and Serry, 2011)

According to the petrography section, sample Z is a sparry calcite with an original rarity of primary voids that later filled with sparry calcite. The primary

pores are not interconnected. Sample Z also contains large secondary fractures that were filled in with coarse calcite.

The overall decomposition of sample Z is shown in Figure 4.62. The rate of mass loss offers more information on the mechanism of the decomposition. From Figure 4.63, the decomposition of sample Z at p_{CO2} = 1 bar can be divided into 4 stages: 850 °C – 880 °C, 880 °C – 898 °C , 898 °C – 960 °C and 960 °C – 1050 °C.

1. Stage 1: 850 °C – 880 °C

The limestone decomposes as expected from a high purity limestone, with the decomposition rate increasing from 850 °C and reaching a peak at 880 °C.

2. Stage 2: 880 °C – 898 °C

At 880 °C, a peak forms and the rate of decomposition decreases until 885 °C. At 885 °C, a saddle point occurs and the rate of decomposition changes from decreasing to increasing. The rate of decomposition increases from 885 °C up to 898 °C.

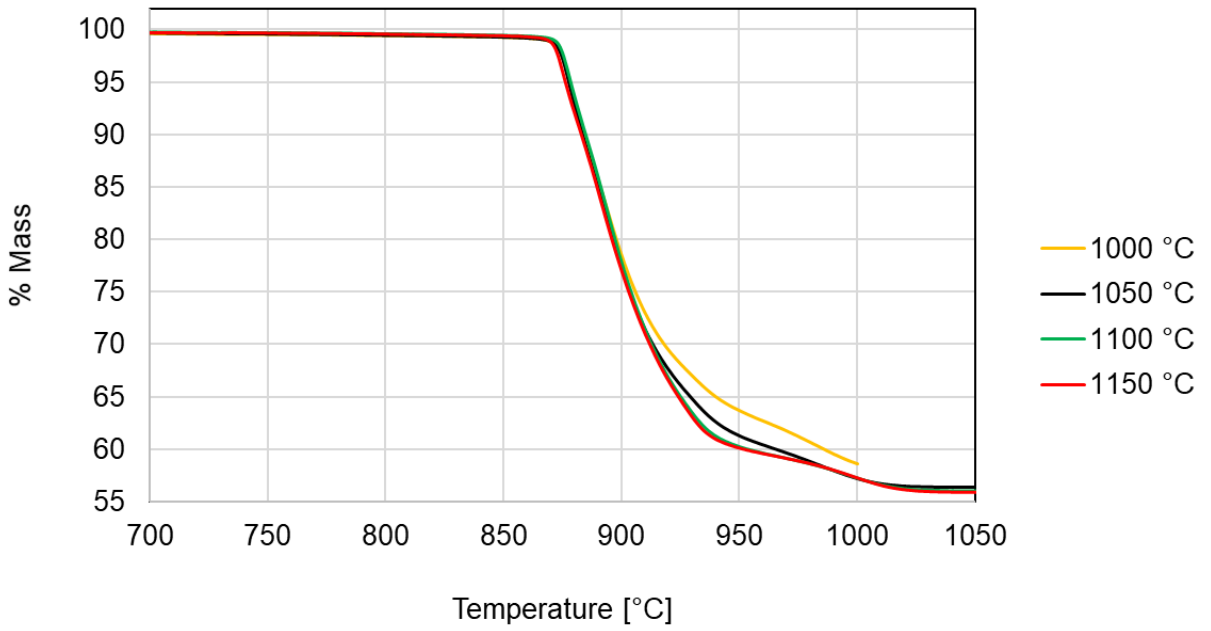

Figure 4.62: Percentage mass as a function of temperature for sample Z decomposition – p_{CO2} = 1 bar. Heating rate 15 °C/min

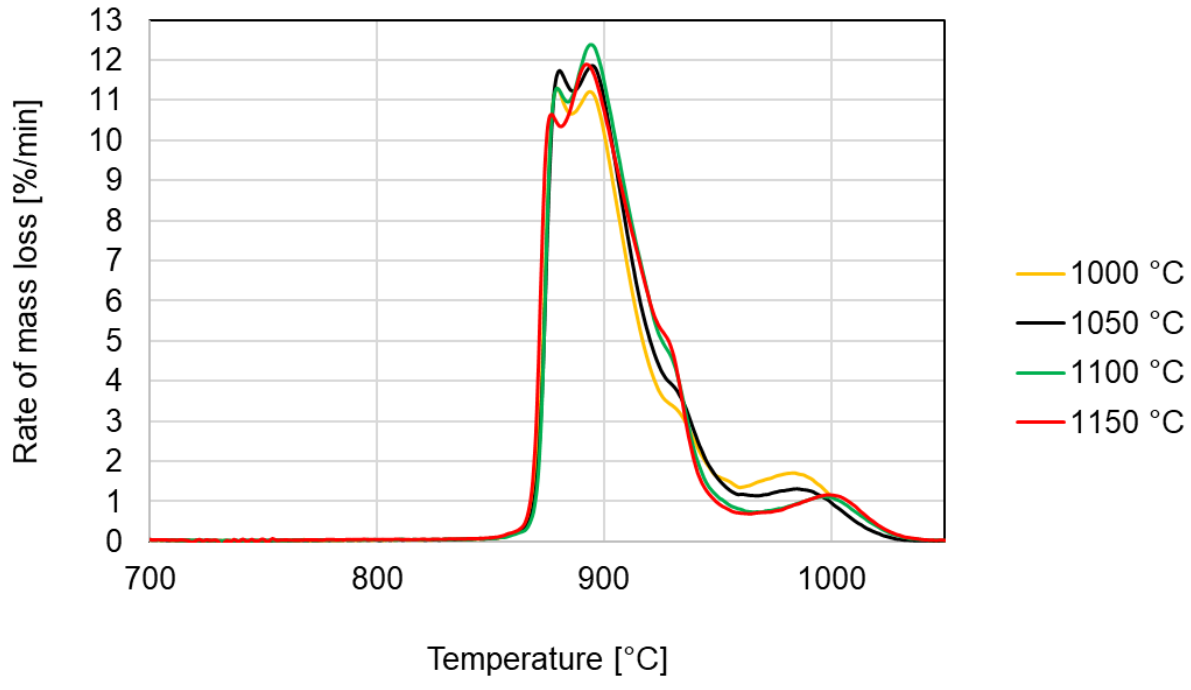

Figure 4.63: DTG curve as a function of temperature for sample Z decomposition – p_{CO2} = 1 bar. Heating rate 15 °C/min.

Since this behaviour of a grainstone has not been reported before in any of the literature that was examined during the course of this study, a unique explanation had to be devised and the explanation is reasoned as follows:

Throughout this explanation it is important to keep in mind the petrographic classification of sample Z. Sample Z was classified as a grainstone limestone (Dunham, 1962) with fine to medium calcite grains (0.1–0.25 mm) making up the groundmass of the stone. Primary laminations are manifested in the stone as ripple cross–laminations that have been overprinted by sparite. The stone is characterised by poor primary porosity.

As the heat penetrates a limestone particle from 850 °C – 880 °C it starts the decomposition from the outer layer inwards towards the core as CO_2 simultaneously migrates outwards through the lime pores. However, the decomposition reaches a maximum at 880 °C and then the decomposition rate is slowed down up to 885 °C. Decomposition is still occurring from 880 °C – 885 °C, but at a slower rate. The rate of decomposition in this instance is determined by how the movement of the CO_2 out of the particle is affected by the microstructure of the stone.

The rate of decomposition decreases when the CO_2 within the particle cannot diffuse quickly enough out of the particle and in doing so slows down the forward reaction of calcination. This occurs when the CO_2 has a limited number of paths out of the particle and that is exactly what happens at 880 °C. This research reasons that at 880 °C the liberated CO_2 pressure exiting the particle is the same as the atmospheric pressure, creating unfavourable conditions for the forward decomposition reaction. The reaction thus slows down. As the reaction temperature continues to increase to 885 °C, micro–cracks are formed, providing additional paths for the exiting CO_2 to escape more easily. This decreases the overall CO_2 pressure in the particle and favours the forward decomposition reaction again, increasing the rate of decomposition.

This research reasons that:

At 880 °C: heat starts to penetrate the larger calcite crystals (that are deposited in the secondary fractures); by the time the CO_2 is expelled from the larger crystals the fine, smaller calcite crystals have started overburning to a small degree and closed potential pores for CO_2 to escape, forcing CO_2 to take longer routes to escape. This explanation is supported by the fact that as the T_f increases, overburning occurs more readily and the first peak reaches a maximum earlier. Previous work by another author agrees with this result: “decomposition is retarded by the heterogeneous nature of the calcite grains” (Silva et al., 2010).

At 885 °C: As the heat is further increased, at 885 °C micro–cracks in the groundmass start forming, allowing CO_2 to escape more easily and thus the decomposition rate increases again from 885 °C to 898 °C. This phenomenon is supported by literature: “The presence of euhedral–subhedral calcite crystals in the sparite matrix of the limestone microstructure enhances the formation of triple junction fractures, which also contribute in lowering the activation energy with accelerating lime liberation.” (Soltan and Serry, 2011).

Stage 3: 898 °C – 925 °C

At 898 °C: the maximum rate of decomposition that is possible for this sparite groundmass grainstone is achieved. Sample Z is a sparry calcite groundmass limestone with few pores and thus does not achieve a very high decomposition rate (Lech et al., 2009).

From 898 °C – 925 °C: the rate of decomposition decreases whereupon it reaches a small plateau at 925 °C. The reason for this small plateau is unclear and plausible reasons can be investigated in distinct research projects in the future.

From 925 °C – 960 °C: the rate of decomposition keeps decreasing as the available amount of $CaCO_3$ decreases and as the CO_2 finds it harder to escape through the outward lime that has started to slightly overburn, with closing of pores.

3. Stage 4: 960 °C – 1050 °C

At 960 °C, an unexpected saddle point occurs, whereafter the rate of decomposition increases again to form a peak at 985 °C for T_f = 1000 °C/1050 °C and up to 1000 °C for T_f = 1100 °C/ 1150 °C (Table 4.27). After this peak the decomposition rate decreases again to 1050 °C as expected (Figure 4.63).

The explanation for the saddle point is reasoned as follows:

As the decomposition rate slows down to 960 °C, more and more lime pores are closed up by slight overburning since the temperature keeps increasing. This temperature increase is reasoned to be the cause of a second stage of micro–cracks forming (Lech et al., 2009). These micro–cracks give new pathways for CO_2 and increase the rate at which CO_2 can escape. This sudden escape of CO_2 decreases the partial pressure of CO_2 in the particle unexpectedly and forces the calcination reaction once again in a forward direction at a faster rate. This causes the last bit of undecomposed $CaCO_3$ to decompose at a quicker rate but as it decomposes the $CaCO_3$ creates CO_2 again, increasing the partial pressure of CO_2 again, and in so doing forcing the calcination reaction to slow down again after it reached a maximum at 985°C/1000°C.

The lower peak for T_f = 1100 °C/1150 °C is attributed to the fact that at higher temperatures more lime is overburned. Thus even though micro–cracks ease the release of CO_2 it blocks other pores in the lime as escape routes for the CO_2 thereby having an overall lower peak.

Table 4.27: Characteristics of sample Z's decomposition at pCO2 = 1 bar.

	Sample Z - 1 bar CO2			
	1000 °C	1050 °C	1100 °C	1150 °C
Total mass change [%]	41	44	44	44
Onset temp [°C]	871	871	871	869
Max peak 1 [°C]	880	880	880	877
Max peak 2 [°C]	894	894	894	892
Max peak 3 [°C]	984	986	1000	999
Offset temp [°C]	1000+	1015	1021	1022
Decomposition range [°C]	129	144	150	153
Decomposition time [min]	8.63	9.62	9.99	10.21

4.8.6.3 Comparison of p_{CO2} = 0 bar vs p_{CO2} = 1 bar

At p_{CO2} =0 bar: Figure 4.64 (dotted line) shows that a higher final temperature of 1150 °C has a higher onset and peak temperature but not a higher rate than 1000 °C. The decomposition times are similar for 1000 °C and 1150 °C.

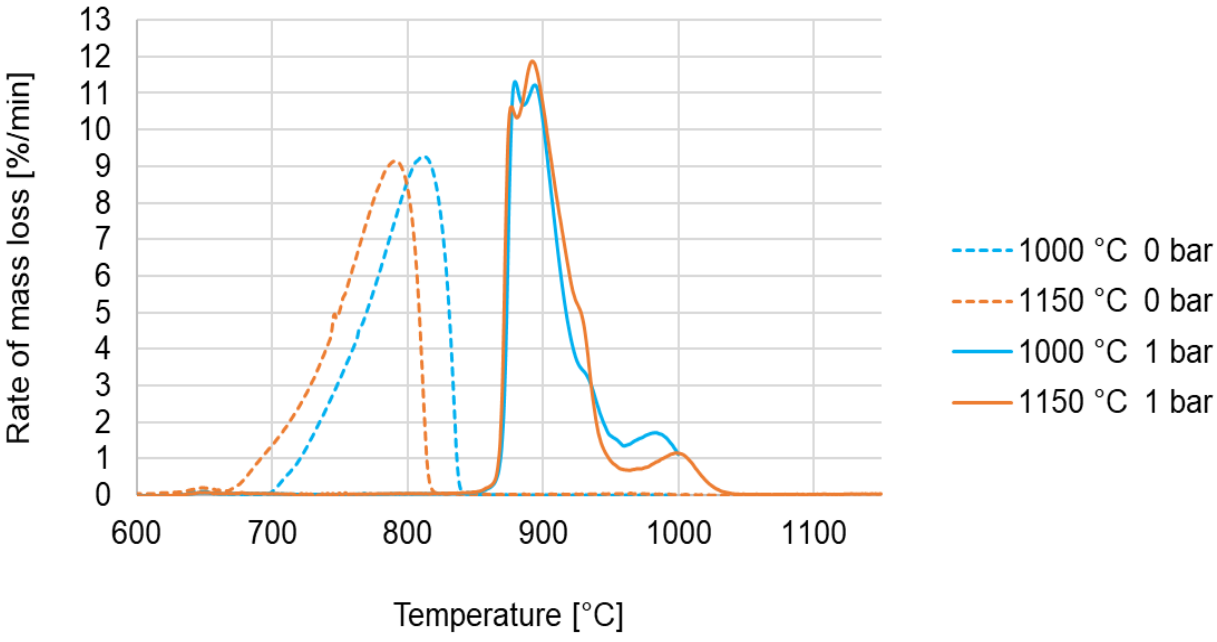

Figure 4.64: Sample Z decomposition - 0 bar vs 1 bar pCO2.

At p_{CO2} = 1 bar: Figure 4.64 shows that the onset temperature is the same for 1000 °C and 1150 °C. The first peak is slightly higher for 1000 °C due possibly to later onset of overburning of the already–formed lime. The second peak is

higher for 1150 °C in comparison to 1000 °C. This is due to larger and/or more cracks forming at higher temperatures. The third peak is lower for 1150 °C due to more overburning happening at 1150 °C, making it difficult for CO_2 to escape fast. It can also be noted that the small plateau at 925 °C onsets at a higher rate for T_f = 1150 °C. The reason for this is still unclear. Lastly, the rate at p_{CO2} = 1 bar is higher than the decomposition rate at p_{CO2} = 0 bar. A higher CO_2 pressure during limestone decomposition is known to yield a higher decomposition rate (Boynton, 1980).

4.8.6.4 Impurities

Raman reported Fluoborite, Libethenite, Graphite and Quartz as impurities. Single particle analysis also showed Iron–containing minerals and a minor dolomite phase. Some inorganic phases and their Curie decomposition temperatures are shown in Figure 4.65 (Milodowski et al., 1989).

Compound	T_c (°C)
$\alpha - Fe_2O_3$	675
$\gamma - Fe_2O_3$	585
Fe_3O_4	585
$MgFe_2O_4$	440
$MnFe_2O_4$	300
Mn_3O_4	230
$Mn_{0.91}Mg_{0.09}Fe_2O_4$	313 [a]
$Mn_{0.40}Mg_{0.60}Fe_2O_4$	384 [a]
$Mn_{0.35}Mg_{0.65}Fe_2O_4$	391 [a]

[a] Values predicted for decomposition products of siderite [26].

Figure 4.65: Decomposition temperatures of inorganic phases that might occur in limestone (Milodowski et al., 1989).

From Figure 4.66, three small peaks can be observed: At ~165 °C, ~648 °C and at ~745 °C. The peak observed at 165 °C is attributed to the de–hydroxylation of a hydrate. It is unsure exactly which mineral–hydrate this is.

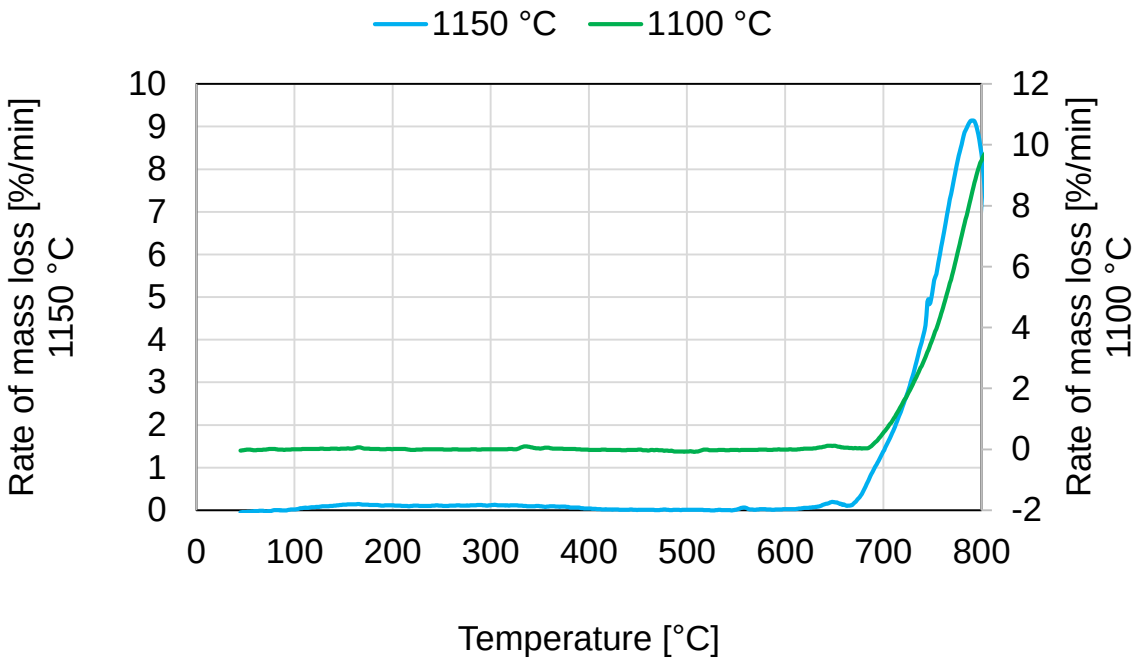

Figure 4.66: DTG curve of sample Z at p_{CO2} = 0 bar showing impurity peaks

According to Serry et al. (2008b), during the decomposition of limestone a thermal peak between 300 °C – 700 °C indicates the de–hydroxylation of Iron and clay minerals into free Fe_2O_3, Al_2O_3 and SiO_2. More specifically, at 250 °C – 350 °C, a peak indicates the de–hydroxylation of hydrated Iron oxides, while a peak at 460 °C or higher indicates the decomposition of clay minerals e.g. illite (Serry et al., 2008a). The same author noted that Goethite [$Fe^{3+}O(OH)$] decomposition occurs between 300 °C and 350 °C (Milodowski et al., 1989). Milodowski et al. (1989) confirmed the transition of various Fe/Mn phases between 300 °C and 400 °C – these transitions are observed as tiny disturbances in the curves in Figure 4.66.

The presence of Iron oxides in sample Z was established in the SPA section and therefore the peak at 333 °C is most likely the decomposition of an Iron mineral or an Iron–hydrate mineral.

The SPA also confirmed the occurrence of alumina silicates in sample Z. In fact it was found that more Si occurs in alumino–silicates than in the quartz phase.

Thus, the decomposition peaks at 516 °C and 555 °C are attributed to the decomposition of clay and alumino–silicate minerals into free Iron(III) oxide, Alumina and Silica. It could also be the decomposition of Siderite ($FeCO_3$) which decomposes between 510 °C and 570 °C (Warne and Dubrawski, 1990).

Mass losses between 600 °C and 800 °C can be attributed to magnesium–containing and dolomite phases (Serry et al., 2008a). Thus the decomposition peaks at 648 °C and 745 °C are likely to be the Fluoborite and dolomite phases decomposing. However, many alumino–silicates also decompose above 700 °C and thus it could be an alumino–silicate that decomposes at 745 °C.

4.9 Comparison

4.9.1 At p_{CO2} = 0 bar

4.9.1.1 Onset temperature

The onset temperature for the samples increases in the following order: W<Y<Z<X (Figure 4.67). The onset temperature for sample W is lowest as expected for a dolomite. Vola et al. (2018) proved that the higher the micrite:sparite ratio, the lower the activation energy in an atmosphere of air. The onset temperatures for sample Y and Z are, however, very similar: this is surprising since sample Y has a micritic groundmass and sample Z has a groundmass. These results prove that in a nitrogen atmosphere the micrite:sparite ratio does not affect the activation energy of decomposition as it does in an air atmosphere (Vola et al., 2018).

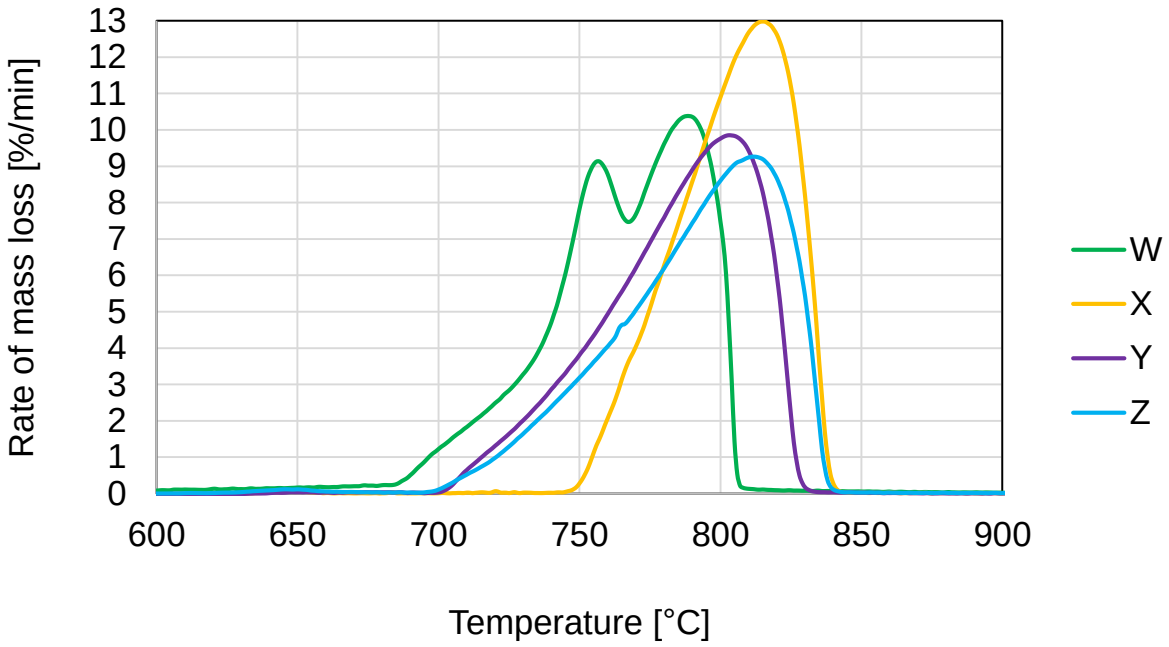

Figure 4.67: Decomposition of samples W, X, Y and Z at p_{CO2} = 0 bar up to 900 °C.

In the XRF section, it was hypothesised that sample Z would have a higher onset temperature because of its high alumina and silica content. This hypothesis is proved incorrect from the TG results.

The higher onset temperature of sample X, as compared to sample Y, is due to it having a higher activation energy. A higher micrite:sparite ratio results in a lower activation energy (Marinoni et al., 2015) and thus sample Y has a lower onset temperature than sample X. The onset temperature of sample X is also possibly due to a high amount of impurities in comparison with sample Y (Kantiranis et al., 1999). However, samples Y and Z, having very similar onset temperatures, disprove the hypothesis that onset temperature is affected by impurities in this sample – impurities only affect the available lime (Boynton, 1980).

4.9.1.2 Peak temperature

The peak temperatures are all very similar for limestones X, Y and Z due to the fact that calcite in each sample decomposes at the same temperature in an inert atmosphere where the rate of CO_2 escape is not affected.

4.9.1.3 Decomposition rate

In the particle size distribution section, it was hypothesised that sample Z would decompose faster or at a lower temperature than samples X and Y because it had the smallest d_{50} value of the limestones (Borgwardt, 1985). This hypothesis is dismissed because sample X actually has the highest rate of decomposition instead of the expected sample Z. In addition, samples X, Y and Z all have similar peak decomposition temperatures. Sample X, which is from the same limestone deposit as sample Y, and has a lower d_{50} value, does however decompose faster than sample Y as predicted in the sample size distribution section.

The decomposition rate of limestones is known to be dependent on the microstructure of limestone (Lech et al., 2009). Limestones with larger, more inter–connected pores have higher rates of decomposition (Lech et al., 2009). Less compact limestones, like micritic limestones, are also known to create "macrocracks" upon calcination more easily and ease the flow of CO_2 out of the stone, thereby increasing the rate of decomposition (Lech et al., 2009). From Figure 4.67, it can be deduced that, in a N_2 atmosphere, sample X has the most favourable microstructure for the movement of hot gases into the particles and the escape of CO_2 out of the particles. Sample X's decomposition rate is the highest at p_{CO2} = 0 bar. The much higher rate of decomposition of sample X in comparison to sample Y is however contrary to Soltan (2011) in a specific regard – Soltan (2011) stated that micrite has a slower decomposition rate when

associated with considerable portions of impurities. Sample X contains more impurities than sample Y and is expected to decompose at a slower rate.

Samples Y and Z have larger decomposition ranges because of the slower rate they at which they decompose.

4.9.2 At p_{CO2} = 1 bar

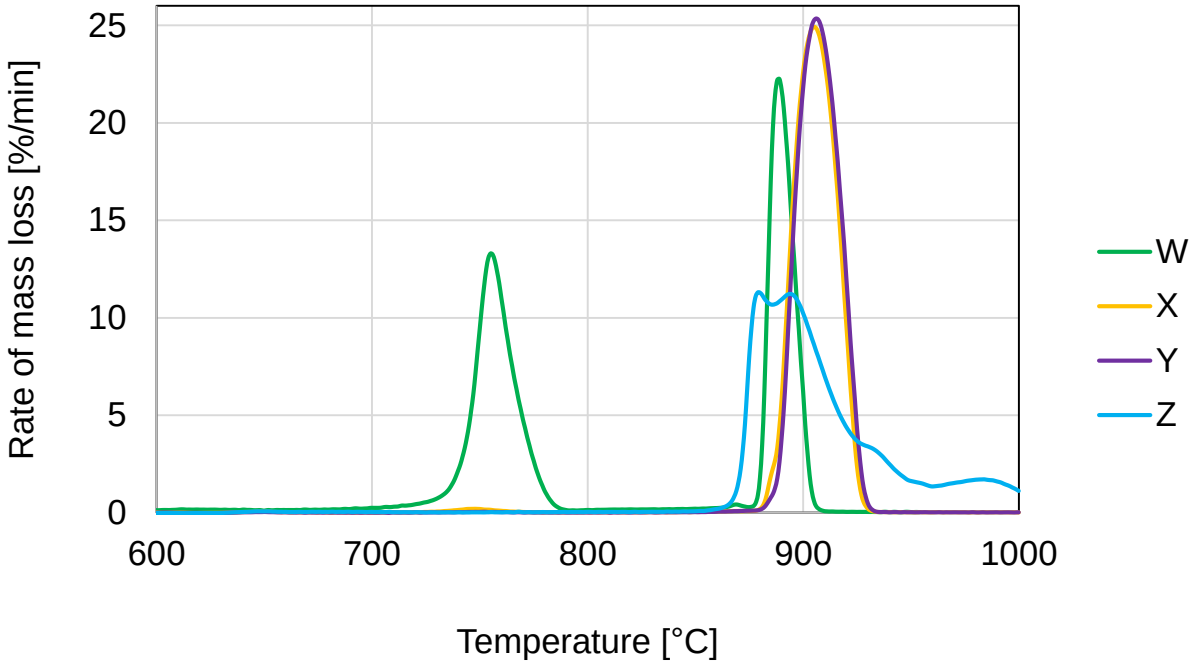

Figure 4.68: Decomposition of samples W, X, Y and Z at p_{CO2} = 1 bar up to 1000 °C

4.9.2.1 Onset temperature

Figure 4.68 shows how sample W decomposes in two clear stages in a CO_2 atmosphere – $MgCO_3$ decomposition onset at 741 °C and $CaCO_3$ decomposition onset at 880 °C.

Samples X and Y both start decomposing at 888 °C, as expected from high purity limestones (Boynton, 1980).

Sample Z starts to decompose at the lowest temperature – 870 °C. The reason for this early onset is because sample Z has a lower activation energy due to the high amount of sparite in the limestone (Vola et al., 2018).

It is noted that the very small peak of sample X at 748 °C, that coincides with the Magnesite decomposition of sample W, confirms the presence of a dolomite phase in sample X.

4.9.2.2 Peak temperature

At p_{CO2} = 1 bar, calcite is expected to decompose at 890 °C (Eriksson, 2016).

For the decomposition of $CaCO_3$:

- Sample W has a peak at 888 °C
- Samples X and Y have a peak at 906 °C
- Sample Z has peaks at 880 °C and 894 °C

These differences in the decomposition of $CaCO_3$ in each sample are attributed possibly to the microstructure of each sample. Samples W, X and Y have micritic groundmasses. Sample Z has a sparitic groundmass (larger crystals than micrite). However, the decomposition temperature results are not in accordance with literature which states that the activation energy of a micritic groundmass stone is less than the activation energy of a sparitic groundmass stone. Thus, the decomposition temperatures cannot be explained by their groundmass fabrics.

Limestone that decomposes at lower temperatures yields more reactive lime (Beruto et al., 2010). From the peak temperatures in Figure 4.68, it can be deduced that sample Z would be more reactive than samples X and Y. Knowing that a higher amount of impurities in a limestone yields a less reactive lime (Boynton, 1980), it can be said that sample Y would be more reactive than sample X. Thus the reactivity of the lime produced from these limestones would increase in the order X<Y<Z.

4.9.2.3 Decomposition rate

The calcite decomposition in sample W (dolomite) reaches a high decomposition rate due to the micritic groundmass (Vola et al., 2018) and dolomite phase occurring in the stone (Lech et al., 2009).

Figure 4.68 shows that the decomposition curves for samples X and Y are the same and are the highest compared to samples W and Z. This result illustrates that samples X and Y both form more and/or larger microcracks/macrocracks in a CO_2 atmosphere to allow better escape of CO_2 from inside the particle to the outside (Lech et al., 2009). Literature has also shown that a micritic groundmass favours a faster decomposition rate as opposed to a sparitic groundmass (Marinoni et al., 2015; Vola et al., 2018). Some of the microcracks formed in sample X are very possibly due to the dolomite phase occurring in the sample (Alaabed et al., 2014; Lech et al., 2009).

Sample Z's decomposition rate decreases because of the quick sintering of the outside of the larger sparite crystals (as mentioned in the discussion on the decomposition of sample Z). Sample Z has a limited distribution of pores causing macrocracks to occur only occasionally. They are caused by a heterogeneous distribution of the grain sizes. At 885 °C and 960 °C, "reactivated macrocracks provide pathways for fast CO_2 diffusion during calcination." (Lech et al., 2009; Silva et al., 2010; Soltan and Serry, 2011).

5 Conclusions

This research set out to learn how the key physical and chemical properties of the limestone used in lime shaft kilns could be utilised in assessing the suitability of a stone source for kiln operation. In order to do this, a range of physical, analytical and thermal tests was conducted to set up a set of assessment criteria.

5.1 Correlation between stone properties and its behaviour in thermal environments

The microstructure and pores of each carbonate rock observed by petrographic analysis were both vital in the explanation of the decrepitation and decomposition behaviour of the stones. Stones with micritic groundmass and larger pores decomposed at a high rate and showed lower decrepitation values.

The impurities identified by XRF, XRD, Raman Spectroscopy and Single Particle Analysis had no direct correlation to the thermal decomposition of the carbonate rocks but did offer information on some minor peaks observed during Thermal Gravimetric Analysis. No direct correlations could be made between the values of decrepitation and the amount of impurities.

All the limestones used in this research were of high purity but, as was evident from the Thermal Gravimetric Analysis, they all acted very differently under calcining conditions. The other analyses done on the stones were crucial in explaining the individualistic behaviour of each stone in the Thermal Gravimetric Analysis.

5.2 Criteria for assessment of the suitability of carbonate rock types for calcination in modern vertical kilns

This research illustrated that petrographic analysis, in conjunction with decrepitation tests and Thermogravimetry, is essential in assessing a limestone's suitability for use in a shaft kiln. The chemical analyses act in a complementary way to the thermal analyses and visual analysis (petrography), offering chemical explanations for observations. The XRF analysis, XRD analysis, Raman spectroscopy and Single Particle Analysis all served as complementary techniques to the Petrography and thermal tests. It is therefore important to have a combination of chemical, visual (petrography) and thermal tests.

The XRF analysis is a standard test applied in industry but, in conjunction with other tests, it can offer even more information. The XRF analysis in this research identified the elements present in each stone. The phases in which those elements are present were determined subsequently by XRD and Raman Spectroscopy. This research showed how Raman spectroscopy can be used as a complementary procedure to XRD by identifying trace phases which XRD could not identify.

Single Particle Analysis was most useful in determining in which phase Si and Al are present in the stones. This data is important since alumino–silicates often occur in limestones.

The assessment of the microstructure and pore structure of the stone by Petrography proved to be vital in assessing the suitability of a stone for use in a shaft kiln. The petrographic analysis offered explanations for the decrepitation behaviour of each stone.

Decrepitation tests assessed the break–up of stone on heating. This is a very important characteristic of the stone since this is a deciding factor in the use and operation of a shaft kiln. Thermal Gravimetric Analysis assessed the onset, peak and offset temperature of every stone under different calcining conditions as well as their decomposition behaviours and impurities.

Use of this complete set of criteria offers valuable information on the suitability of a carbonate rock for use in a shaft kiln. These criteria are helpful during the decision making process in determining whether the stone can be used in a shaft kiln, as well as during kiln operation to achieve the most efficient kiln performance.

6 Recommendations and future work

A research project on decrepitation alone can be undertaken in which the effect of chemical and physical properties on decrepitation can be studied. This study can include the effect of temperature on decrepitation and compressive strength. An investigation can also be launched into determining the cause of the plateau in the decomposition curve of sample Z (refer to TG of sample Z).

7 Significance of this work

The hypothesis of this work was to gain a better understanding of the physical and chemical characteristics of the rock types and to assess why the stone used in shaft kilns behaves in a certain way. As summarised in the concluding statements, the criteria assessment developed in this work offers to kiln manufacturers and operators in the industry a better understanding of carbonate rocks, their properties and their suitability for use in a shaft kiln. It allows current rotary kiln operators a means to assess their stone for use in a shaft kiln to make the potential technology shift. It also offers information to

current shaft kiln operators on which assessment criteria can be utilised to optimise their current operation.

8 Presentations and publication

A presentation on this research was given at the International Lime Association (ILA) Information Exchange Forum 2018 in Cape Town, South Africa (refer to Appendix E for abstract of work presented at conference). The presentation sparked interest at the conference to the extent that the German journal ZKG International requested a paper on the topic.

9 References

Agnello, V., 2005. Dolomite and Limestone in South Africa: Supply and demand.

Alaabed, S., Soltan, A.M., Abdelghany, O., Amin, B.E.M., El Tokhi, M., Khaleel, A., Musalim, A., 2014. United Arab Emirates limestones: impact of petrography on thermal behavior. Miner Petrol 108, 837–852. https://doi.org/10.1007/s00710-014-0329-3

Barcina, L.M., Espina, A., Suarez, M., Garcia, J.R., Rodriguez, J., 1997. Characterization of monumental carbonate stones by thermal analysis (TG, DTG and DSC). Thermochimica Acta 290, 181–189.

Batumike Mwandulo, J., Cailteux, J.H., Kampunzu, A.B., 2007. Lithostratigraphy, basin development, base metal deposits, and regional correlations of the Neoproterozoic Nguba and Kundelungu rock successions, central African Copperbelt.

Berner, R.A., 1971. Principles of chemical sedimentology. McGraw-Hill Companies.

Beruto, D.T., Botter, R., Cabella, R., Lagazzo, A., 2010. A consecutive decomposition–sintering dilatometer method to study the effect of limestone impurities on lime microstructure and its water reactivity. Journal of the European Ceramic Society 30, 1277–1286. https://doi.org/10.1016/j.jeurceramsoc.2009.12.012

Beukes, N.J., 1987. Facies relations, depositional environments and diagenesis in a major early Proterozoic stromatolitic carbonate platform to basinal sequence, Campbellrand Subgroup, Transvaal Supergroup, Southern Africa. Sedimentary Geology 54, 1–46.

Beukes, N.J., 1983. Palaeoenvironmental setting of iron-formations in the depositional basin of the Transvaal Supergroup, South Africa, in: Developments in Precambrian Geology. Elsevier, pp. 131–198.

Beukes, N.J., 1977. Transition from siliciclastic to carbonate sedimentation near the base of the Transvaal Supergroup, northern Cape Province, South Africa. Sedimentary Geology 18, 201–221.

Binda, P.L., Van Eden, J.G., 1972. Sedimentological evidence on the origin of the Precambrian Great conglomerate (Kundelungu tillite), Zambia. Palaeogeography, Palaeoclimatology, Palaeoecology 12, 151–168.

Boggs Jr, S., Boggs, S., 2009. Petrology of sedimentary rocks. Cambridge University Press.

Borgwardt, R.H., 1985. Calcination kinetics and surface area of dispersed limestone particles. AIChE Journal 31, 103–111.

Borgwardt, R.H., Harvey, R.D., 1972. Properties of carbonate rocks related to sulfur dioxide reactivity. Environmental Science & Technology 6, 350–360.

Boynton, R.S., 1980. Chemistry and technology of lime and limestone.

Bresciani, P., Colombari, V., Gabriele, V., Sarandrea, L., 2016. Analyse to excel. International Cement review.

Britton, H.T.S., Gregg, S.J., Winsor, G.W., 1952. The calcination of dolomite. Part II.—The thermal decomposition of dolomite. Transactions of the Faraday Society 48, 70–75.

Buzgar, N., Apopei, A.I., 2009. The Raman study of certain carbonates. Geologie Tomul L 2, 97–112.

Calvert, S.E., Pedersen, T.F., 1996. Sedimentary geochemistry of manganese; implications for the environment of formation of manganiferous black shales. Economic Geology 91, 36–47.

Cater, E.D., Buseck, P.R., 1985. Mechanism of decomposition of dolomite, Ca0. 5Mg0. 5CO3, in the electron microscope. Ultramicroscopy 18, 241–251.

Cheng, C., Specht, E., Kehse, G., 2007. Influences of the origin and material properties of limestone on its decomposition behaviour in shaft kilns. ZKG INTERNATIONAL 60, 51–61.

de Villiers, J.P.R., Lu, L., 2015. XRD analysis and evaluation of iron ores and sinters, in: Iron Ore. Elsevier, pp. 85–100.

Dechow, E., Jensen, M.L., 1965. Sulfur isotopes of some central African sulfide deposits. Economic Geology 60, 894–941.

Dollimore, D., Dunn, J.G., Lee, Y.F., Penrod, B.M., 1994. The decrepitation of dolomite and limestone. Thermochimica acta 237, 125–131.

Dunham, R.J., 1962. Classification of carbonate rocks according to depositional textures.

Eriksson, M., 2016. Characterization of kiln feed limestone by dynamic heating rate thermogravimetry. International Journal of Mineral Processing 147, 31–42.

Faust, G.T., 1949. Differentiation of aragonite from calcite by differential thermal analysis. Science 110, 402–403.

Fischer, W.W., Knoll, A.H., 2009. An iron shuttle for deepwater silica in Late Archean and early Paleoproterozoic iron formation. Geological Society of America Bulletin 121, 222–235.

Folk, R.L., 1962. Spectral subdivision of limestone types.

Folk, R.L., 1959. Practical petrographic classification of limestones. AAPG Bulletin 43, 1–38.

Gill, R., 2014. Modern Analytical Geochemistry: an introduction to quantitative chemical analysis techniques for Earth, environmental and materials scientists. Routledge.

Goldin, D.M., Kulikova, G.V., 1984. On the dissociation mechanism of carbonates and their isomorphous mixture. Journal of thermal analysis 29, 139–145.

Gunasekaran, S., Anbalagan, G., 2008. Spectroscopic study of phase transitions in natural calcite mineral. Spectrochimica Acta Part A: Molecular and Biomolecular Spectroscopy 69, 1246–1251. https://doi.org/10.1016/j.saa.2007.06.036

Gunasekaran, S., Anbalagan, G., Pandi, S., 2006. Raman and infrared spectra of carbonates of calcite structure. Journal of Raman Spectroscopy: An International Journal for Original Work in all Aspects of Raman Spectroscopy, Including Higher Order Processes, and also Brillouin and Rayleigh Scattering 37, 892–899.

Guzzo, P.L., Marinho de Barros, F.B., de Arruda Tino, A.A., 2019. Effect of prolonged dry grinding on size distribution, crystal structure and thermal decomposition of ultrafine particles of dolostone. Powder Technology 342, 141–148. https://doi.org/10.1016/j.powtec.2018.09.064

Harvey, R.D., 1970. Petrographic and mineralogical characteristics of carbonate rocks related to sorption of sulfur oxides in flue gases. Environmental geology no. 038.

Hashimoto, H., Komaki, E., Hayashi, F., Uematsu, T., 1980. Partial decomposition of dolomite in CO2. Journal of solid state chemistry 33, 181–188.

Hedin, R., 1954. Changes occuring in the limestone during heating before dissociation. Svenska forskningsinstitutet för cement och betong vid Kungl. Tekniska högskolan.

Hogewoning, S., Wolter, A., Schmidt, S.-O., 2008. Dependence of hard burn potential on limestone properties (Part 2). ZKG international 61, 84–93.

Huang, C.K., Kerr, P.F., 1960. Infrared study of the carbonate minerals. Am. Mineral 45, 311–324.

Kandler, K., Benker, N., Bundke, U., Cuevas, E., Ebert, M., Knippertz, P., Rodríguez, S., Schütz, L., Weinbruch, S., 2007. Chemical composition and complex refractive index of Saharan Mineral Dust at Izaña, Tenerife (Spain) derived by electron microscopy. Atmospheric Environment 41, 8058–8074. https://doi.org/10.1016/j.atmosenv.2007.06.047

Kantiranis, N., Tsirambides, A., Filippidis, A., Christaras, B., 1999. Technological characteristics of the calcined limestone from Agios Panteleimonas, Macedonia, Greece. Materials and Structures 32, 546–551.

Klein, C., Beukes, N.J., 1989. Geochemistry and sedimentology of a facies transition from limestone to iron-formation deposition in the early Proterozoic Transvaal Supergroup, South Africa. Economic Geology 84, 1733–1774.

Kök, M.V., Smykatz-Kloss, W., 2008. Characterization, correlation and kinetics of dolomite samples as outlined by thermal methods. Journal of Thermal Analysis and Calorimetry 91, 565–568.

Kontoyannis, C.G., Vagenas, N.V., 2000. Calcium carbonate phase analysis using XRD and FT-Raman spectroscopy. Analyst 125, 251–255.

Krishnamurti, D., 1957. The Raman spectrum of calcite and its interpretation, in: Proceedings of the Indian Academy of Sciences-Section A. Springer, pp. 183–202.

Kristof, E., Juhasz, A.Z., Vassanyi, I., 1993. The effect of mechanical treatment on the crystal structure and thermal behavior of kaolinite. Clays and Clay Minerals 41, 608–612.

Kristóf-Makó, É., Juhász, A.Z., 1999. The effect of mechanical treatment on the crystal structure and thermal decomposition of dolomite. Thermochimica Acta 342, 105–114. https://doi.org/10.1016/S0040-6031(99)00290-7

Kuisma-Kursula, P., 2000. Accuracy, precision and detection limits of SEM-WDS, SEM-EDS and PIXE in the multielemental analysis of medieval glass. X-ray Spectrometry 29, 111–118.

Lech, R., Wodnicka, K., Pedzich, Z., 2009. Effect of the limestone fabric on the fabric development in burnt lime (Part 2). ZKG international 62.

Liu, L.-G., Mernagh, T.P., 1990. Phase transitions and Raman spectra of calcite at high pressures and room temperature. American Mineralogist 75, 801–806.

Marinoni, N., Allevi, S., Marchi, M., Dapiaggi, M., 2012. A Kinetic Study of Thermal Decomposition of Limestone Using In Situ High Temperature X-Ray Powder Diffraction. Journal of the American Ceramic Society 95, 2491–2498.

Marinoni, N., Bernasconi, A., Della Porta, G., Marchi, M., Pavese, A., 2015. The role of petrography on the thermal decomposition and burnability of limestones used in industrial cement clinker. Miner Petrol 109, 719–731. https://doi.org/10.1007/s00710-015-0398-y

McCauley, R.A., Johnson, L.A., 1991. Decrepitation and thermal decomposition of dolomite. Thermochimica acta 185, 271–282.

McIntosh, R.M., Sharp, J.H., Wilburn, F.W., 1990. The thermal decomposition of dolomite. Thermochimica Acta 165, 281–296. https://doi.org/10.1016/0040-6031(90)80228-Q

Mills, J., 2000. A technical discussion of mining operations in the lime and cement industries of Zambia and Malawi (PhD Thesis). University of Nottingham.

Milodowski, A.E., Morgan, D.J., Warne, S.S.J., 1989. Thermal analysis studies of the dolomite-ferroan dolomite-ankerite series. II. Decomposition mechanism in flowing CO2 atmosphere. Thermochimica Acta 152, 279–297.

Mitchell, C., 2002. An African perspective on aglime.

Mitchell, C., 2000. Industrial mineral resources of Zambia.

Muller, A., Stark, J., 1989. CALCINATION OF LIMESTONE POWDERS IS SUSPENSION. ZEMENT-KALK-GIPS 42, 93–95.

Oates, J.A., 2008. Lime and limestone: chemistry and technology, production and uses. John Wiley & Sons.

Olszak-Humienik, M., Jablonski, M., 2015a. Thermal behavior of natural dolomite. J Therm Anal Calorim 119, 2239–2248. https://doi.org/10.1007/s10973-014-4301-6

Olszak-Humienik, M., Jablonski, M., 2015b. Thermal behavior of natural dolomite. J Therm Anal Calorim 119, 2239–2248. https://doi.org/10.1007/s10973-014-4301-6

Passe-Coutrin, N., N'Guyen, P., Pelmard, R., Ouensanga, A., Bouchon, C., 1995. Water desorption and aragonite—calcite phase transition in scleractinian corals skeletons. Thermochimica Acta 265, 135–140.

Penn-Clarke, C., 2018. Micropetrographic characterisation of various carbonate rocks (Internal report). University of the Witwatersrand.

Perić, J., Vučak, M., Krstulović, R., Brečević, L., Kralj, D., 1996. Phase transformation of calcium carbonate polymorphs. Thermochimica Acta 277, 175–186.

Piringer, H., 2017. Lime Shaft Kilns. Energy Procedia 120, 75–95.

Raask, E., 1985. Mineral impurities in coal combustion: behavior, problems, and remedial measures. Taylor & Francis.

Rietveld, H.M., 1967. Line profiles of neutron powder-diffraction peaks for structure refinement. Acta Crystallographica 22, 151–152.

Ritchie, N.W., 2013. Is Scanning Electron Microscopy/Energy Dispersive X-ray Spectrometry (SEM/EDS) Quantitative? Scanning 35, 141–168.

Rodriguez-Navarro, C., Kudlacz, K., Ruiz-Agudo, E., 2012. The mechanism of thermal decomposition of dolomite: New insights from 2D-XRD and TEM analyses. American Mineralogist 97, 38–51. https://doi.org/10.2138/am.2011.3813

Ruckensteiner, G., Burczeck, J., Ludwig, U., 1995. Factors affecting the stability of the internal structure when burning limestone. ZEMENT-KALK-GIPS 48, 342–348.

Schaller, W.T., Glass, J.J., 1942. Occurrence of pink zoisite (thulite) in the United States. American Mineralogist: Journal of Earth and Planetary Materials 27, 519–524.

Schobert, H., 2013. Chemistry of fossil fuels and biofuels. Cambridge University Press.

SEM introduction to scanning electron microscopy [WWW Document], n.d. URL https://www.understanding-cement.com/sem-introduction.html (accessed 1.8.18).

Serry, M.A.K., Abu-Zeid, M.M., SHARAF EL-DIN, A.A.M., Soltan, A.M.M., 2008a. Egyptian limestones for quicklime manufacture. Part 1 Characterization of limestone samples for quicklime manufacture. ZKG international 61, 68–77.

Serry, M.A.K., Abu-Zeid, M.M., Sharaf-ElDin, A.A., Soltan, A.M.M., 2008b. Egyptian limestones for quicklime manufacture. Part 2: Factors influencing the rate of active-lime liberation of technological samples. ZKG international 61, 61–71.

Silva, M., Specht, E., Schmidt, J., Al-Karawi, J., 2010. Influence of the origin of limestone on its decomposition temperature and on the specific heat capacity and conductivity of lime. High Temperatures–High Pressures 38.

Soltan, A.M.M., 2011. Petrographic modelling of Egyptian limestones for quicklime manufacture. Arab J Geosci 4, 803–815. https://doi.org/10.1007/s12517-009-0095-4

Soltan, A.M.M., Serry, M.A., 2011. Impact of limestone microstructure on calcination activation energy. Advances in Applied Ceramics 110, 409–416.

Spinolo, G., Anselmi-Tamburini, U., 1989. Nonequilibrium calcium oxide-magnesium oxide solid solutions produced by chemical decomposition. The Journal of Physical Chemistry 93, 6837–6843.

Sun, J., Wu, Z., Cheng, H., Zhang, Z., Frost, R.L., 2014. A Raman spectroscopic comparison of calcite and dolomite. Spectrochimica Acta Part A: Molecular and Biomolecular Spectroscopy 117, 158–162. https://doi.org/10.1016/j.saa.2013.08.014

Vola, G., Bresciani, P., Rodeghero, E., Sarandrea, L., Cruciani, G., 2018. Impact of rock fabric, thermal behavior, and carbonate decomposition kinetics on quicklime industrial production and slaking reactivity. Journal of Thermal Analysis and Calorimetry 1–27.

Vola, G., Sarandrea, L., 2014. Lime Reactivity Study. World Cement.

Vola, G., Sarandrea, L., 2013. New materials characterization for industrial lime manufacturing. ZKG international 62–70.

Vola, G., Sarandrea, L., Della Porta, G., Cavallo, A., Jadoul, F., Cruciani, G., 2017. The influence of petrography, mineralogy and chemistry on burnability and reactivity of quicklime produced in Twin Shaft Regenerative (TSR) kilns from Neoarchean limestone (Transvaal Supergroup, South Africa). Miner Petrol 112, 555–576. https://doi.org/10.1007/s00710-017-0542-y

Warne, S.S.J., 1986. Applications of variable atmosphere DTA (in CO2) to improved detection and content evaluation of anhydrous carbonates in mixtures. Thermochimica acta 109, 243–252.

Warne, S.S.J., Dubrawski, J.V., 1990. Applications of thermal analysis methods to iron minerals in coal—A synthesis. Thermochimica Acta 166, 337–341.

Warne, S.S.J., Morgan, D.J., Milodowski, A.E., 1981. Thermal analysis studies of the dolomite, ferroan dolomite, ankerite series. Part 1. Iron content recognition and determination by variable atmosphere DTA. Thermochimica Acta 51, 105–111.

Warren, B.E., 1990. X-ray Diffraction. Courier Corporation.

White, W.B., Farmer, V.C., 1974. The infrared spectra of minerals. Mineralogical Society Monograph 4, 105–06.

Appendices

Appendix A: Sample preparation and analyses flowsheet

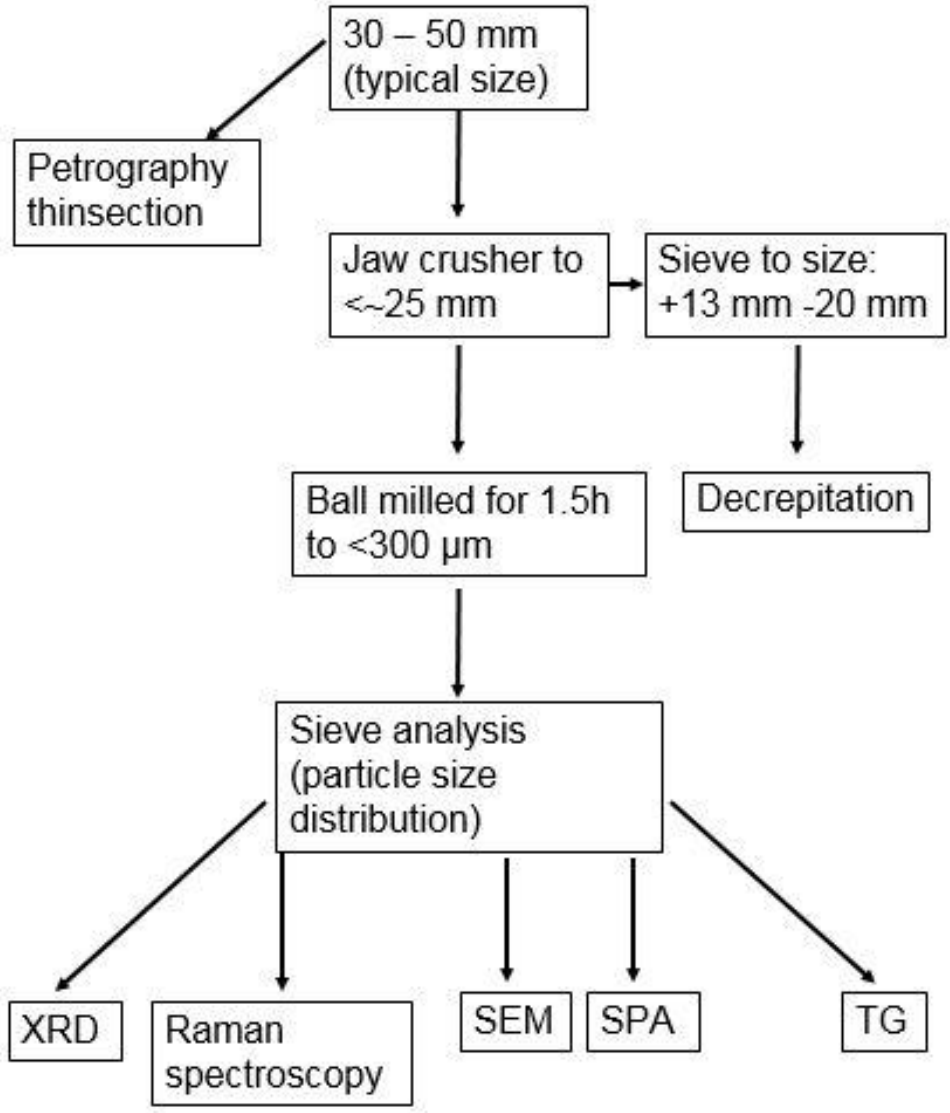

Figure A1: Flow diagram of sample preparation and test plan

Appendix B: Lime plant locations

Appendix B1: South African map with locations of limestone sources

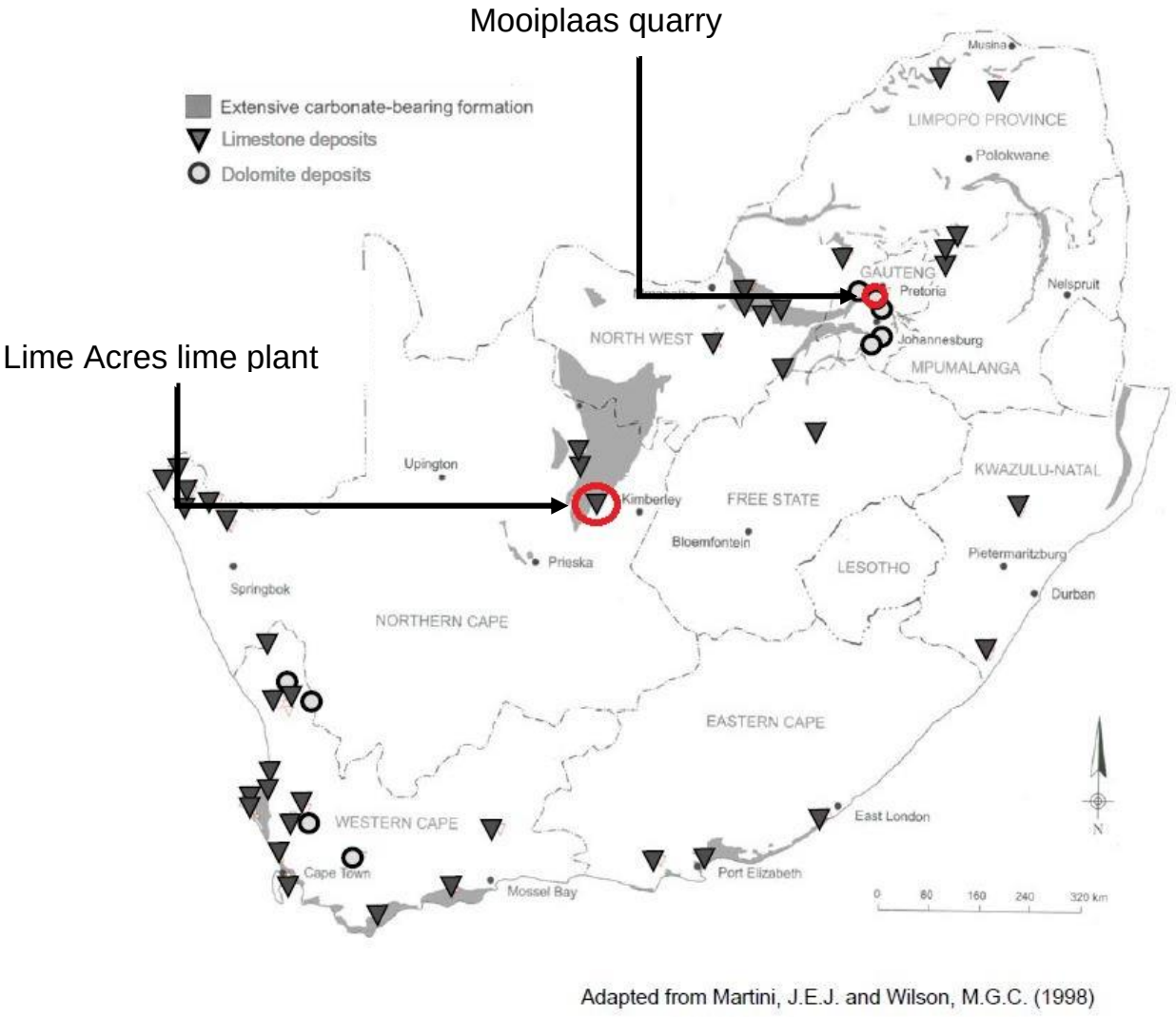

Figure B1: Locations of limestone and dolomite samples sourced from South Africa (Agnello, 2005)

Appendix B2: Location and formations of the Ghaap Group

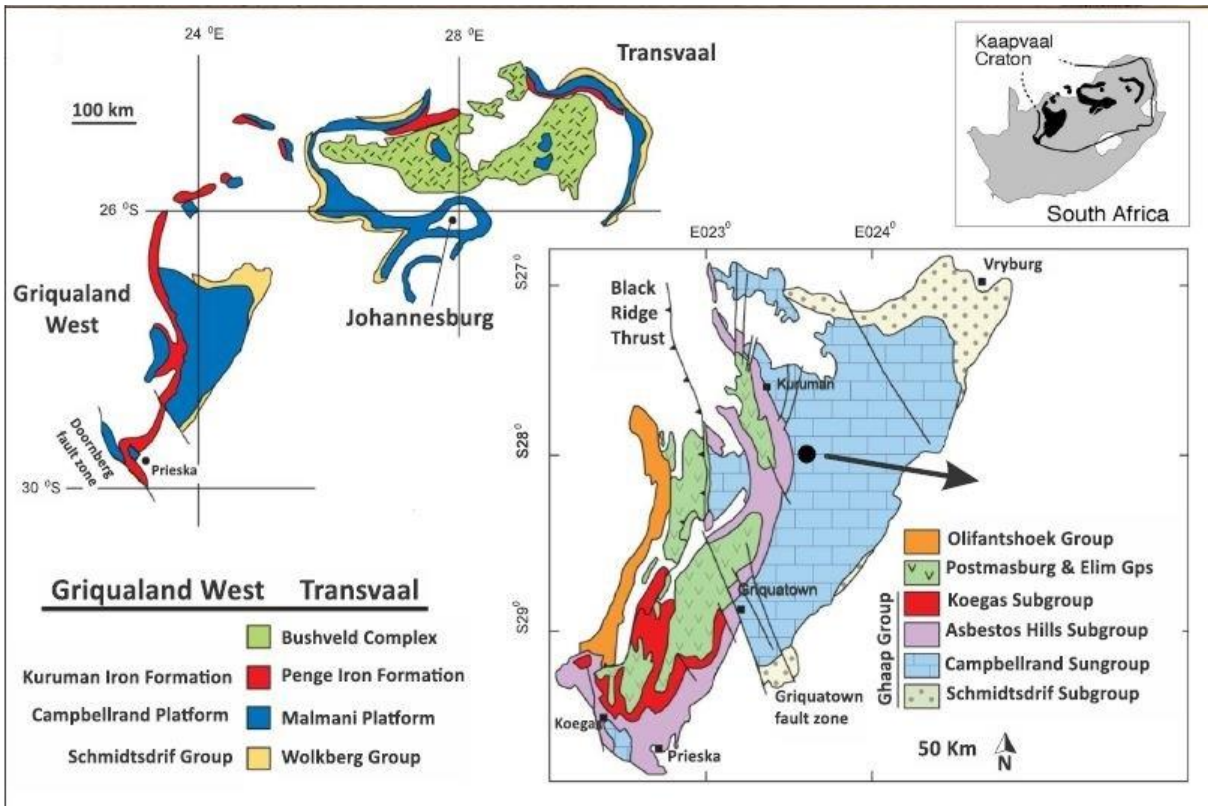

Figure B2: Location of Lime Acres member in the Campbellrand subgroup (Vola et al., 2017)

Appendix B3: Lithostratigraphy and age of the Ghaap Plateau and Transvaal basin

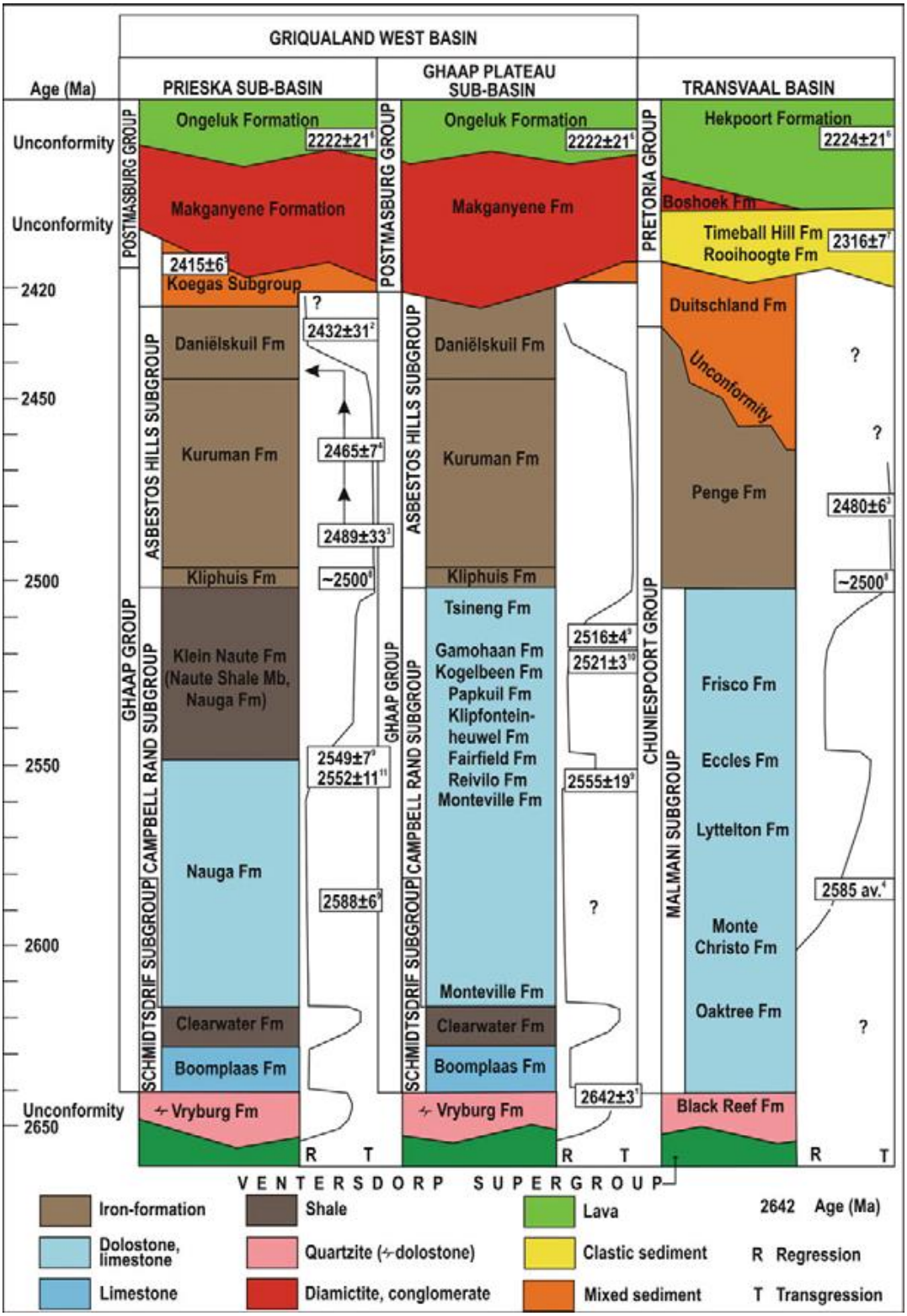

Figure B3: Lithostratigraphy of South African limestone formations

Appendix B4: Thickness and position of formations in the Ghaap plateau

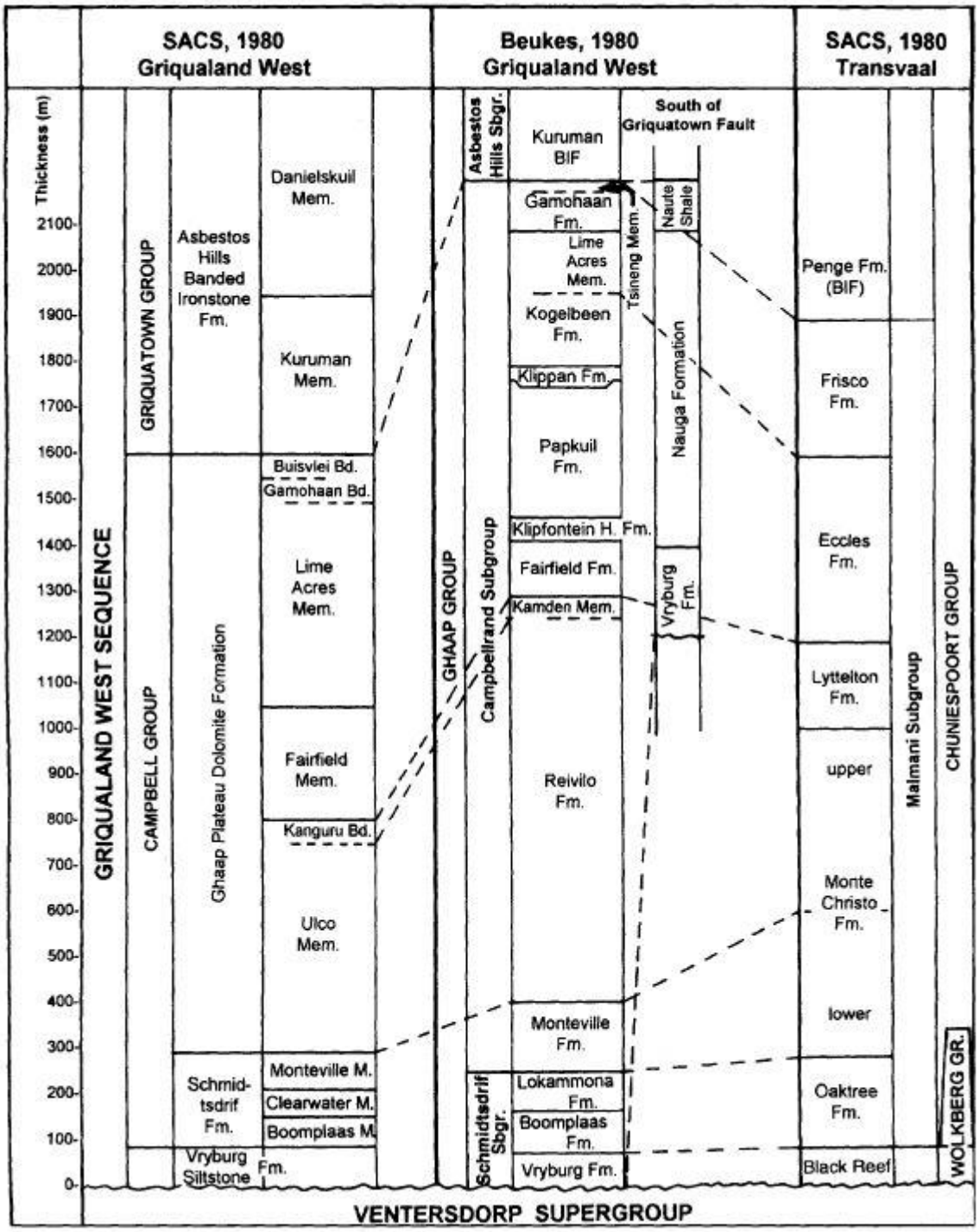

Figure B4: Position of Lime Acres formation in the Ghaap plateau (Altermann and Wotherspoon, 1995).

Appendix B5: Zambian map with locations of limestone deposits

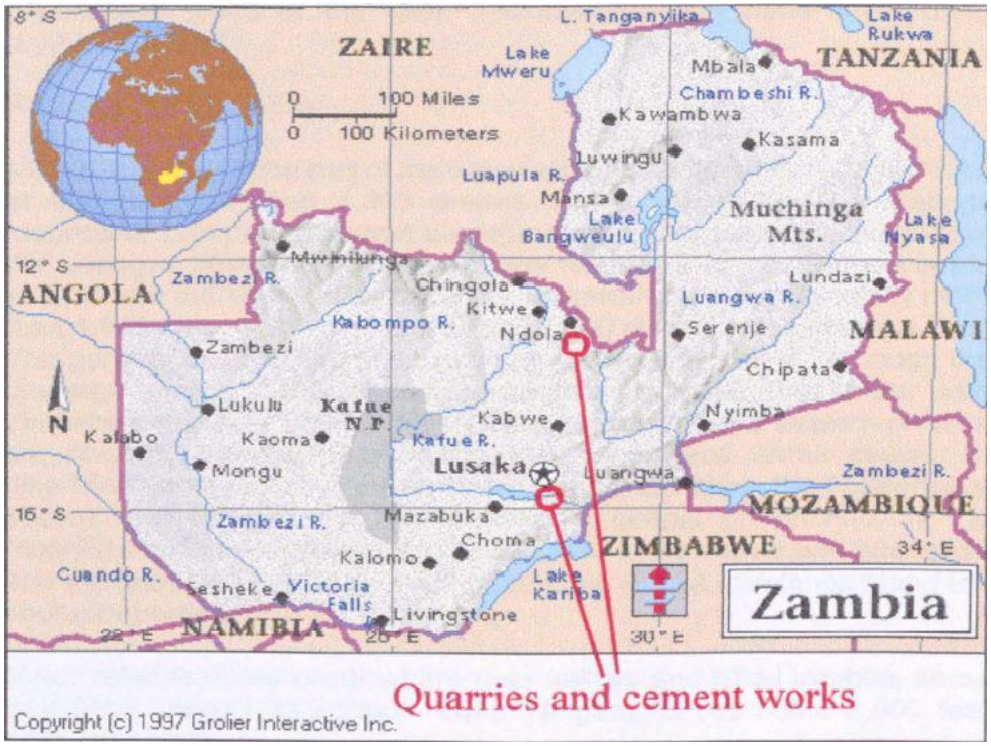

Figure B5: Location of Ndola in Zambia (Mills, 2000)

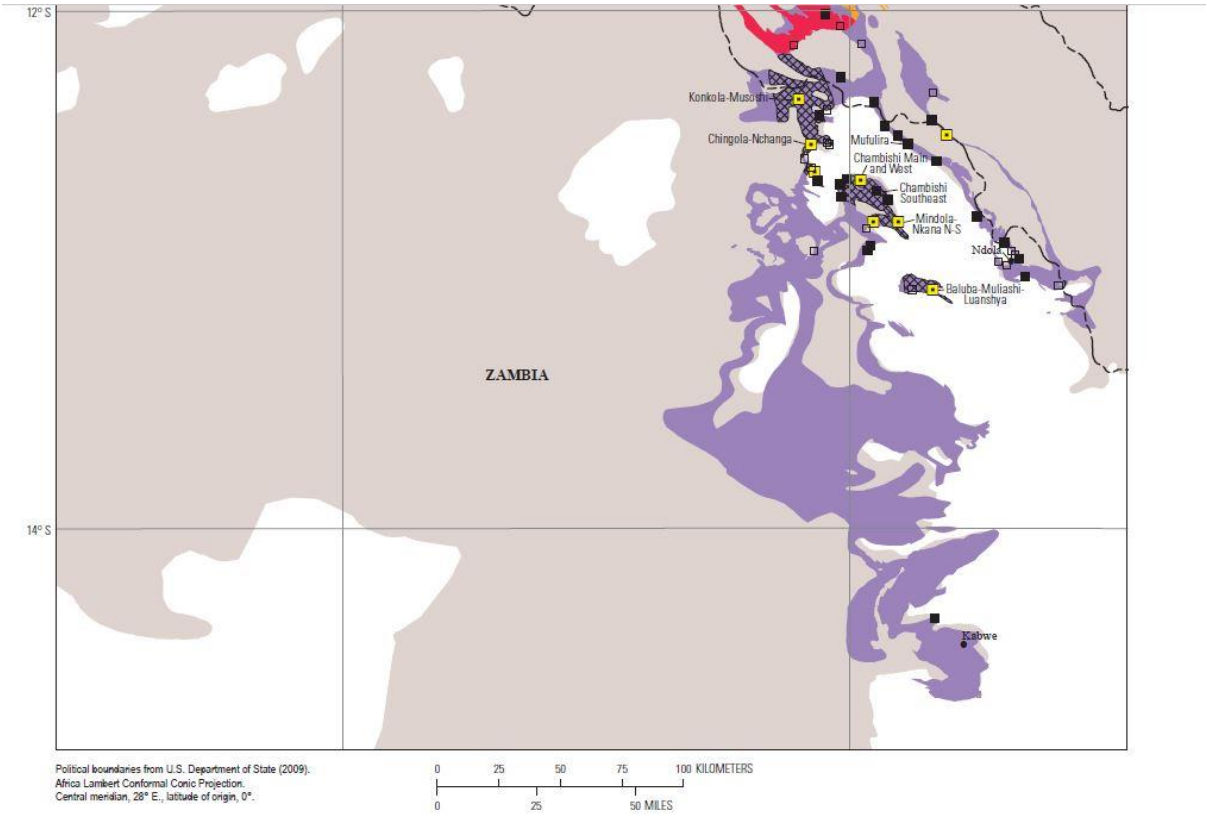

Figure B6: Location of limestone deposits (black squares) in Zambia (Zientek et al., 2014)

Appendix B6: Location of Handyman Lime relative to Ndola lime



Fig B7: Location of Handyman's Lime in Zambia (Google Earth)

Appendix B7: Lithostratigraphy of the Katanga supergroup in Zambia

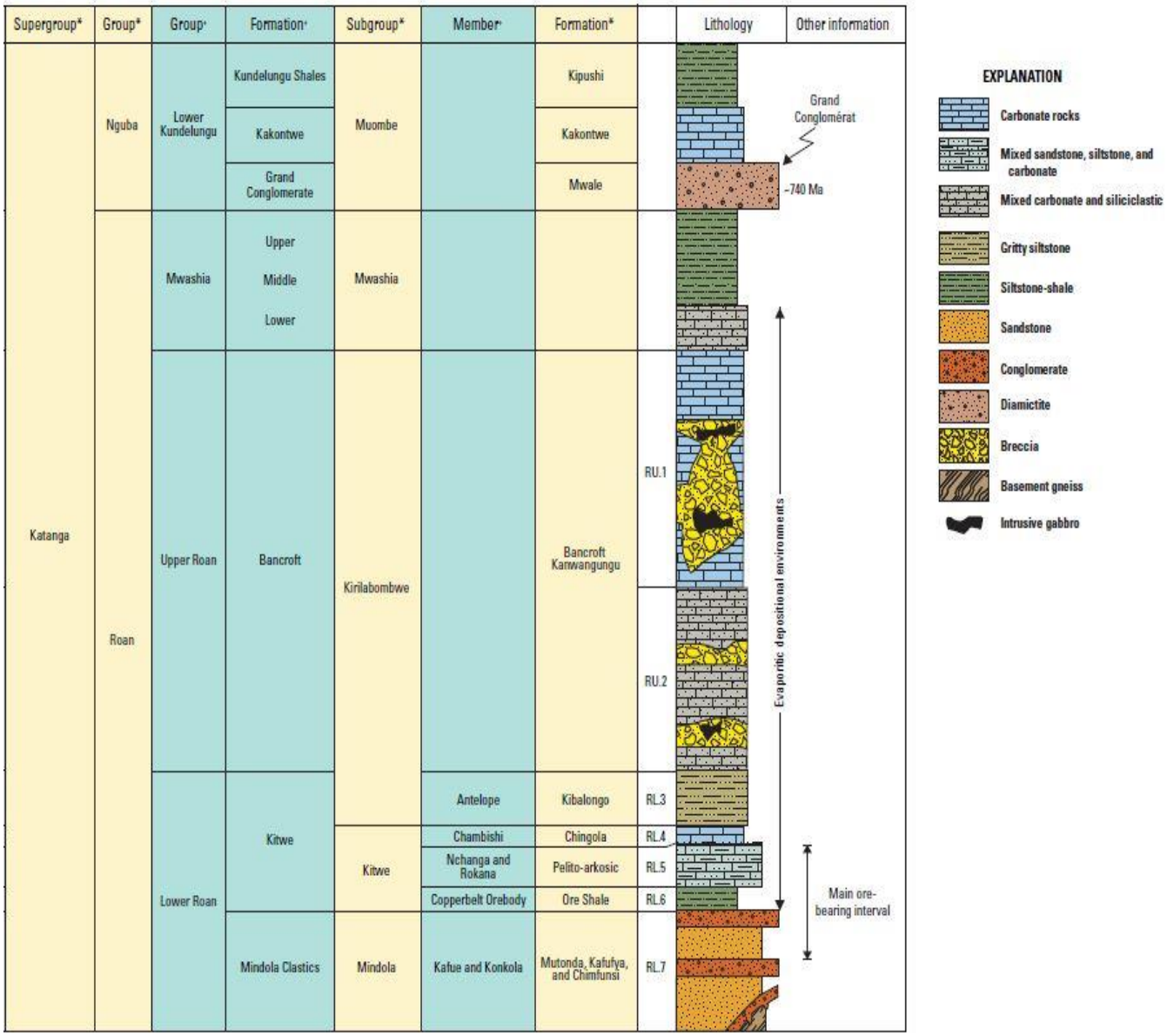

Figure B8: Lithostratigraphy of Ndola region limestone formations (Zientek et al., 2014).

Appendix B8: Age and thickness of the formations in the Katanga supergroup

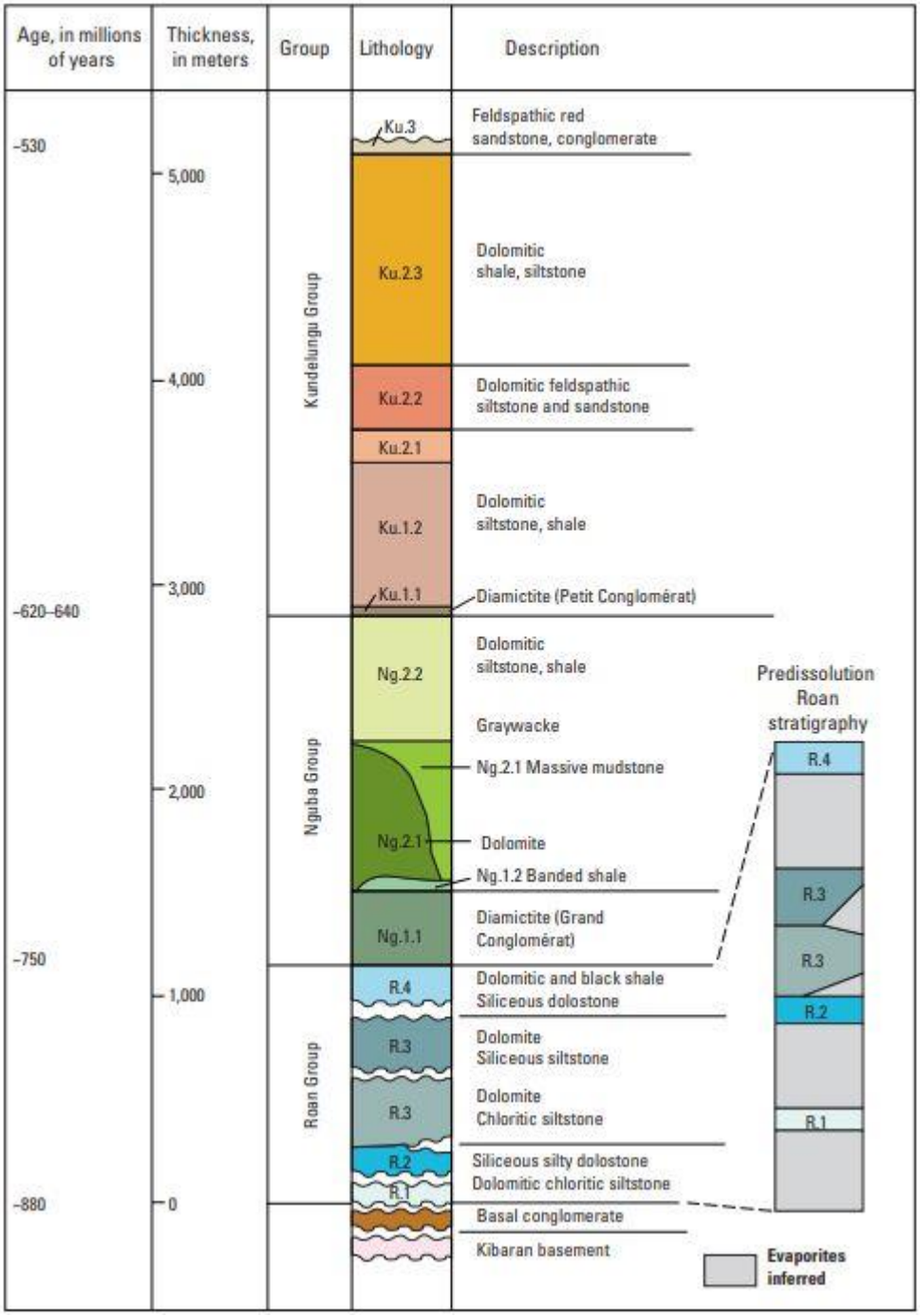

Figure B9: Age and thickness of limestone formations in the Ndola region (Zientek et al., 2014).

Appendix C: Criteria of Kandler classification system

Class name	Criteria	Phases identified by TEM	Phases deduced from particle chemistry
Iron-rich	$\|Fe\| > 0.15$ and $Si/Fe < 1$ and $Ti/Fe < 1.33$	Hematite	Ilmenite
Titanium-rich	$\|Ti\| > 0.3$ and $Na/Ti < 1$ and $Mg/Ti < 1$ and $Al/Ti < 1$ and $Si/Ti < 1$ and $S/Ti < 1$ and $Fe/Ti < 1$		Rutile
Carbonates	$[\|Ca + Mg\| > 0.5$ and $0.33 < Mg/Ca < 3]$ or $[\|Ca\| > 0.5$ and $Mg/Ca < 0.33$ and $Si/Ca < 0.5$ and $S/Ca < 0.25$ and $P/Ca < 0.15]$	Dolomite	Calcite
Other calcium-rich	$\|Ca\| > 0.25$ and $Si/Ca < 0.5$ and not in class carbonates or gypsum		Apatite
Gypsum	$\|Ca + S\| > 0.5$ and $0.25 < Ca/S < 4$ and $Na/Ca < 0.5$		Gypsum
Halite	$\|Na + Cl\| > 0.5$ and $S/Na < 0.375$ and $S/Cl < 0.5$ and $Si/Cl < 0.5$	Halite	
Quartz	$\|Si\| > 0.5$ and $Mg/Si < 0.2$ and $Al/Si < 0.2$	Quartz	
Silicates	$\|Si\| > 0.2$ and $Na/Si < 0.7$ and $Mg/Si < 1.33$ and $Al/Si < 1.33$ and $K/Si < 0.5$ and $Ca/Si < 0.5$ and $Ti/Si < 0.5$ and $Fe/Si < 0.5$ and $\|P + S + Cl\| < 0.2$ and not in class quartz	Biotite, kaolinite, illite, muscovite, chloritoide, anorthite	Chlorite, albite, leucite, orthoclase, plagioclase, chrysotile
Sulfate silicate mixtures	$\|Na + S + Mg + Al + Si + K + Ca\| > 0.7$ and $0.6 < S/Si < 2$		Any silicate and sulfate
Sulfates	$\|S\| > 0.5$ and $Cl/S < 0.3$ and $Si/S < 0.5$ and $Fe/S < 0.5$ and not in class gypsum		Blödite/löweite, glauberite, vanthoffite, mirabilite/thenardite, mascagnite
Carbonaceous	$\|\|C + O\|\| > 0.97$		
Other	Not in other class		Alunite, periclase/magnesite, spinel

All elemental ratios based on moles; $|X|$ = total atomic content of element X relative to all other elements analyzed (except C and O); $\|X\|$ total atomic content of element X relative to all other elements analyzed (including C and O).

Figure C1: Kandler original classification criteria (Kandler et al., 2007).

Appendix D: Operation principles of analysis methods

Appendix D1: X–ray Fluorescence (XRF)

X–ray Fluorescence is an X–ray analysis technique used primarily for the identification of different elements in a sample. XRF can identify individual elements as well as molecules and complex chemical structures. XRF can be used on solids as well as liquids. XRF is particularly well–suited for investigations that involve:

- bulk chemical analyses of major elements (Si, Ti, Al, Fe, Mn, Mg, Ca, Na, K, P) in rock and sediment

- bulk chemical analyses of trace elements (>1 ppm; Ba, Ce, Co, Cr, Cu, Ga, La, Nb, Ni, Rb, Sc, Sr, Rh, U, V, Y, Zr, Zn) in rock and sediment

An XRF instrument fire an X–ray beam (incident beam) at a sample. Some of the X–rays are absorbed and some scattered. The incident X–ray beam is typically generated from a Rhodium source, although Tungsten and Chromium can also be used. The X–rays that are absorbed by the sample is done in a manner that is characteristic of the sample's chemistry. The excited electrons emits (fluoresce) different energies because of electrons being displaced. The electrons are displaced as follow: the atoms in the sample absorb X–ray energy by ionizing, ejecting electrons from the lower (usually K and L) energy levels. The ejected electrons are replaced by electrons from an outer, higher energy orbital. When this happens, energy is released due to the decreased binding energy of the inner electron orbital compared with an outer one. This energy release is in the form of emission of characteristic X–rays indicating the type of atom present. The generated X–ray can be detected by and Energy Dispersive (EDX) detection system or by a Wavelength Dispersive (WDX) detection system. The WDX system filters out individual X–ray by their energies through

the use of crystals whereas the EDX system continuously and repeatedly count and plot the number of X–rays at each energy. The WDX detection system is advantageous in the sense that it can detect a range of elements simultaneously and also because it has an up to thirty times higher energy (spectral) resolution than EDX. A disadvantage of the WDX system is that it has a severe reduced efficiency and higher costs.

Most elements have, however, more than one electron shell and thus there is more X–rays and consequently a much wider variety of peaks observed during XRF as opposed to XRD. XRF has several disadvantages, one of which is that Sodium is generally the lowest element that can be analysed with this technique. Also, because of scattering, background radiation and matrix effects, this technique is used primarily qualitative instead of quantitative. (Gill, 2014)

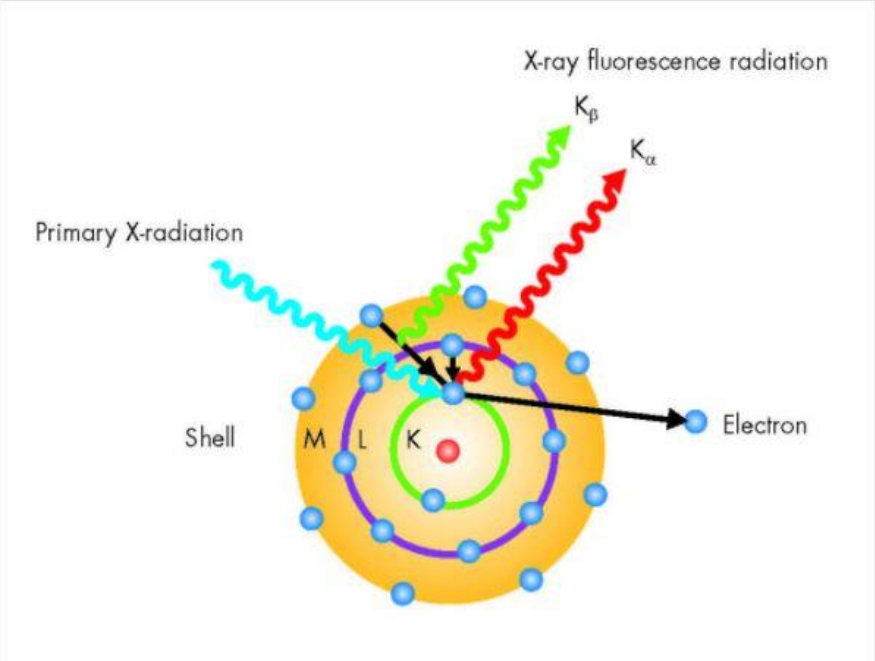

Figure D1: Effect of X-rays on electrons in sample. (“X-Ray Fluorescence Spectroscopy (XRF) – Basics,”)

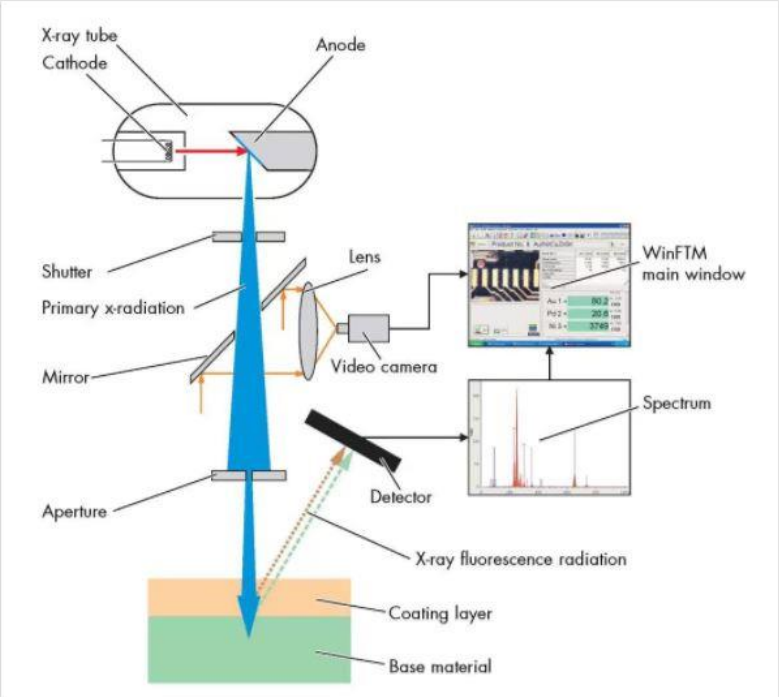

Figure D2: XRF instrument setup.

Appendix D2: Thermogravimetry (TG)

Thermal gravimetric analysis is a thermal analysis technique which is able to provide information about the sample's thermal decomposition/stability, molecular make–up, morphology and phase transitions. In a thermogravimetric analysis, a specific sequence is applied. This sequence programmes the instrument to go up to a specified temperature at a specified heating rate. The change in mass (mass loss) caused by the thermal decomposition of the sample, is constantly measured over the time. The heat flux inside the TGA furnace can also be measured during an analysis. The most volatile components that are present in the sample are the first ones that cause the mass loss, followed by the (heavier) non–volatile components in the sample. The temperature range and heating rate is determined by the (sample and the sample properties) that is being investigated. TGA is performed under in a N_2, air, argon or CO_2 atmosphere. An inert atmosphere is normally chosen for

explosive samples so that combustion of the sample is prevented when reaching high operating temperatures. The data from the analysis is shown in a thermogram (a graph), wherein the initial percentage mass of the sample is shown (on the Y–axis) versus the time [min] or temperature [°C] (on the X–axis). A characteristic decomposition curve is often obtained from samples.

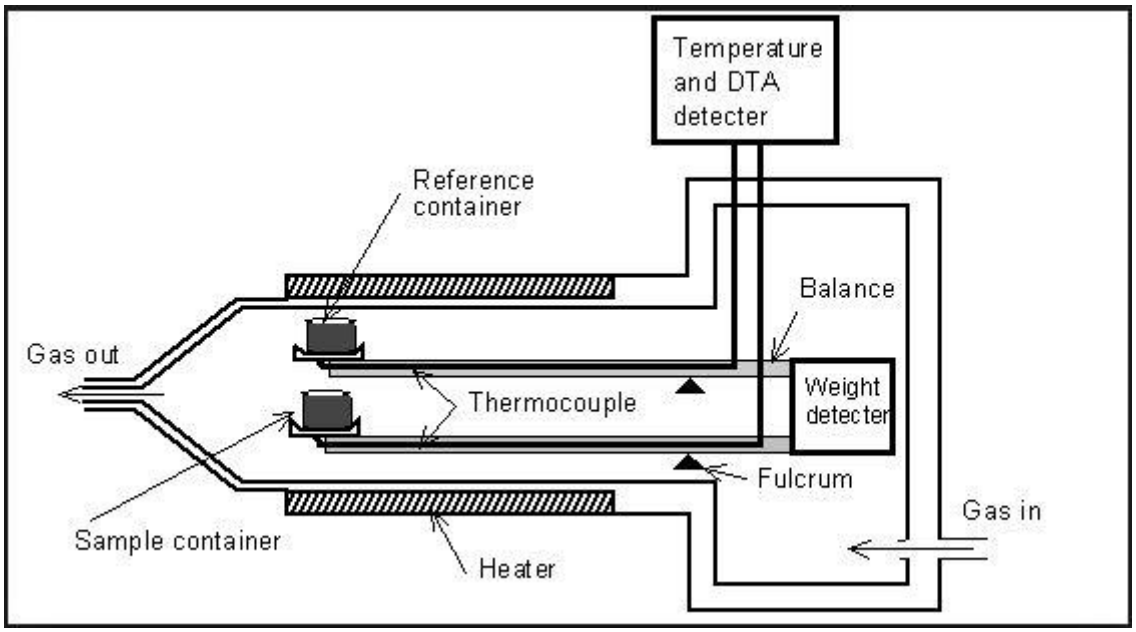

Figure D3: TG instrument setup (Murasawa et al., 2012).

Appendix D3: X–ray Diffraction (XRD)

“Powder X–ray diffraction (XRD) analysis uses a monochromatic beam of X–rays to irradiate a sample with the X–ray source and detector making variable angles with normally a flat sample. The diffracted X–rays from the crystal planes in the powdered phases that will be measured by a detector will show up as peaks of variable intensities at specific diffraction angles. Each phase or mineral will have a unique diffraction pattern that is a function of its crystal structure, its crystallite size, and its lattice strain, if present.

The intensity I_{hkl} of a diffraction peak is a function of a number of factors and is expressed in abbreviated form as the following equation:

$$I_{hkl} = S \times M_{hkl} \times LP \times A \times P_{hkl} \times F_{hkl}$$

where *S* is the scale factor that equates the experimental diffraction pattern to the calculated pattern. It is a function of the crystal structure of the phase and the quantity of the phase in a mixture, M_{hkl} is a multiplicity factor that depends on the number of times that symmetrically equivalent reflections overlap in a diffraction pattern, *LP* is a combined term depending on the geometry of diffraction and the partial polarization of the X–ray beam, *A* is a correction for the absorption of the X–ray beam, P_{hkl} is the preferred orientation correction term that corrects for possible deviations from the random orientation of crystallites in the sample due to their shape, F_{hkl} is the structure factor that is defined by the crystal structure. The structure factor is a function of the scattering power of the constituent atoms and their positions and is given by

$$F_{hkl} = \sum_{n=1}^{N} f_n \, e^{2\pi i(hx+ky+lz)}$$

where f_n is the atomic scattering factor of the nth atom; *x*, *y*, and *z* is the position of the *n*th atom. The diffraction peaks are further affected by instrumental and sample effects that cause broadening so that the combination of all these gives the peak profiles that are observed in the experimental diffraction pattern." (de Villiers and Lu, 2015)

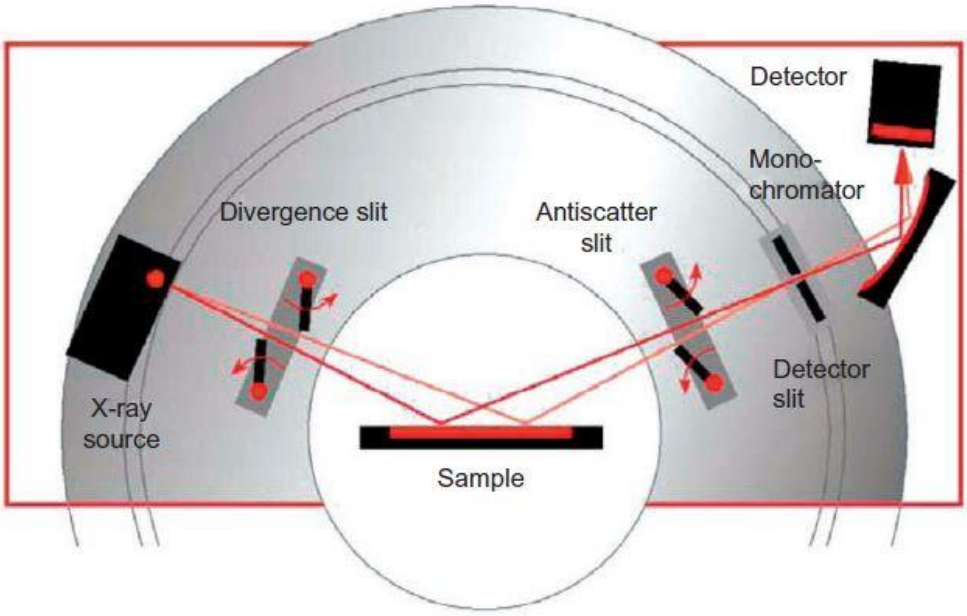

Figure D4: The Braggs-Brentano geometry used in modern diffractometers (Bruker AXS)

Appendix D4: Scanning Electron Microscopy (SEM)

Scanning Electron Microscopy – Energy Dispersive X–ray microscopy (SEM–EDX) is a technique used to observe the microstructure and crystallinity of samples. The SEM provides information about the sample's crystal– and microstructure and EDX provides information about the sample's chemical composition. These images can show detailed parts down to 25 Angstroms. Materials such as minerals and metals are interesting to examine, using this technique.

The scanning electron microscope operates at high vacuum (for stability) and a beam of electrons is emitted by a field emission gun. The field emission gun operates by charging a cathode (tungsten filament) with a current big enough to overcome the 4.5 eV work function of tungsten. The area of the filament from

which electrons are emitted is controlled by a Wehnelt cap. The electrons are then accelerated toward an anode at a speed of 0.1 – 20 kV (1 kV most commonly used). The Wehnelt cap and the anode together act as an electrostatic lens to focus the emitted electrons. After the anode the electron beam is ‘’thinned’’ through a series of electromagnetic lens. The electron beam excite electrons on the surface of the sample which are then released – these released electrons are called secondary electrons. Secondary electrons are in the nanometre range. The more secondary electrons are emitted the clearer the surface of the sample can be seen. The sample is typically at an incline to the incoming electron beam so as to ensure maximum secondary electron yield and thus high resolution. These secondary electrons are directed towards a detector that consists of a faraday cage, followed by a photocathode and a photomultiplier. The processing unit then maps the topographic surface of the sample based on the strength of the secondary electrons received. The upper surface specificity of SEM makes it ideal for imaging topographic contrast – the signal from 'unseen' parts is slightly lower than the signal from areas directly 'seen' by the detector; these will appear slightly darker, known as shadowing contrast. SEM images are in black–and–white. It is essential for a sample to be conductive in order to observe it with SEM.

Scanning electron microscopy can simultaneously make use of the energy dispersive spectroscopy (EDX) function: a complementary energy–dispersive x–ray detector. The x–ray detector works on the same principle as the XRD instrument (above).The x–ray detector is positioned to intercept x–rays emitted from the sample when the electron beam generated x–rays within the sample. These x–rays have energies that are characteristic for each element in the sample. One can find out which element are present in a sample once the SEM–EDX has determined the energy content of the x–rays. When EDX is used along with SEM a high acceleration voltage of electrons are used in order to induce X–rays. The disadvantage of a higher acceleration voltage is a lower surface resolution of the sample. EDX must not be confused with wavelength dispersive

X–ray fluorescence (WDXRF). The main difference between WDXRF and EDX is the energy resolution – up to 30 times higher energy resolution used for WDXRF (Kuisma–Kursula, 2000; Ritchie, 2013).

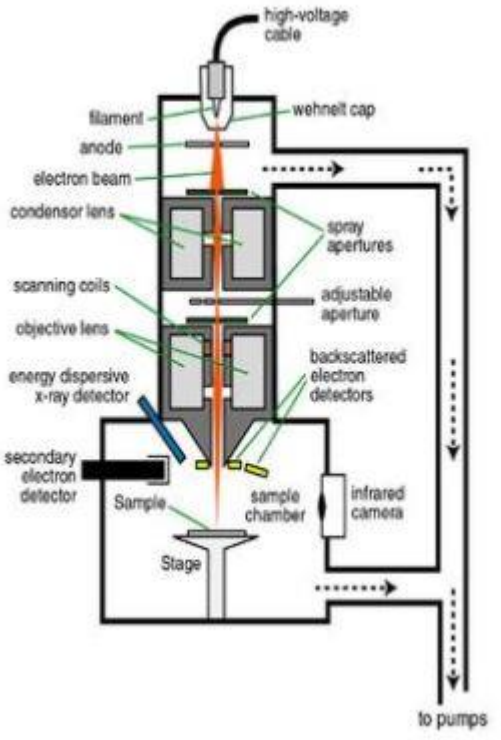

Figure D5: SEM-EDX instrument setup and operation principle

Appendix D5: Raman spectroscopy

Raman spectroscopy (Raman scattering) is a qualitative surface technique used primarily to identify phases and crystalline polymorphs e.g. calcite, aragonite and vaterite. Raman utilises a laser scattering technique that is used to identify and characterize molecules. It is predominantly applicable to the qualitative and quantitative analyses of covalently bonded molecules but quantitative Raman analysis is rarely used because of the cheaper option of quantitative absorbance methods.

Raman can be done on solids liquids and gases. Its main advantage is that it is non–destructive and non–invasive. Another advantage of Raman scattering is that it can detect multiple species in a single measurement.

Disadvantages of Raman is that it requires precise position if certain molecules occur only in certain regions, and not all species are Raman active. A big drawback of Raman spectroscopy is fluorescence. Fluorescence can easily overwhelm the Raman signal and lead to false results. The minimizing of fluorescence is essential when using Raman spectroscopy. This is why Raman spectroscopy is normally done in dark space and where non–reflective materials are used to analyse the sample on.

Raman spectroscopy identifies molecules based on the vibrational energy that is unique for every chemical bond. The identification and characterisation is done by scattering photons off of the molecules and measuring the scattered photon’s energy to see how it interacted with the vibrational state of the chemical bonds in the molecules. Raman spectroscopy gives information complimentary to Infrared spectroscopy.

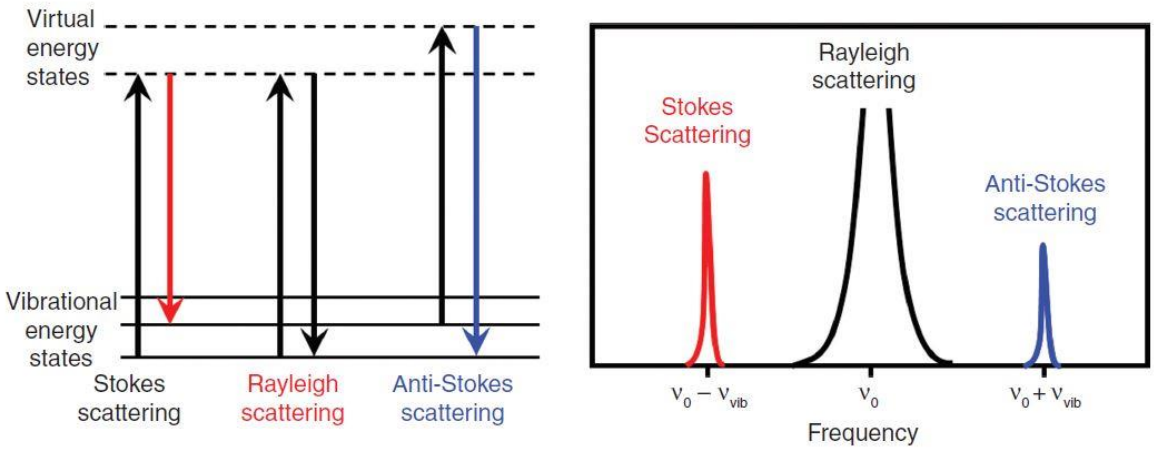

Figure D6: Types of Raman scattering and their corresponding frequencies (Kim et al., 2017)

A Raman scattering uses a monochromatic light, usually a laser in the visible light range source to emit photons. These photons contain an energy $h\upsilon_o$. Once a photon collides with a molecule a collision occurs and the photon's energy changes/stay constant by scattering in one of 3 ways: Rayleigh scattering, Inelastic scattering (Stokes), Elastic scattering (Anti–stokes).

Rayleigh scattering: A change of photon direction but not energy. Usually the collision is elastic and the scattered photon retains its original energy $h\upsilon_o$ leaving the molecule in its original energy state v=0.

Inelastic scattering: Transfer of energy from the photon and transferred to the molecule. In a very small fraction of collisions part of the photon energy is used to increase the vibrational energy of the molecule from v=0 to v=1. The scattered photon then has the energy $h\upsilon_o - h\upsilon_{vib}$ and is scattered at the frequency $\upsilon_o - \upsilon_{vib}$.

Elastic scattering: Transfer of energy from molecule to photon. A fraction of the molecules are in an excited vibrational state (v=1). During a collision there is a

small probability of the molecule transferring its excess vibrational to the photon. The photon is thus scattered at the frequency $\upsilon_o + \upsilon_{vib}$.

Raman scattering is done by illuminating the sample with a laser beam. The scattered light (post–collision) is collected with a lens and sent through a monochromator. Wavelengths close to the laser wavelength due to Rayleigh (elastic scattering) is the filtered out with a notch or band pass filter, while the rest of the collected light is dispersed onto a detector. The software package then plots the scattered light intensity vs energy difference from excitation line. These differences from the excitation line are called Raman shifts.

Raman shifts are reported in wavenumbers and not in light frequency/energy because spectroscopic instruments are typically calibrated in terms of wavelength, independent of the value for the speed of light. Wavenumbers ($\Delta\omega$) have units of inverse length expressed as cm^{-1}. The spectral wavelength recorded by the detector λ_1 is converted to wavenumber using the equation

$$\Delta\omega = \frac{1}{\lambda_0} - \frac{1}{\lambda_1}$$

Where $\Delta\omega$ is the wavenumber (Raman shift), λ_0 is the excitation wavelength from the light source, and λ_1 is the scattered Raman wavelength recorded by the detector.

Appendix E: ILA conference abstract

ILA General Assembly **Cape Town** **10 – 12 October 2018**

Paper offered for inclusion in the topic "CO_2 emission reduction"
For submission to:
https://icsevents.eventsair.com/ilaassembly/callforpapers/Site/Register

Title

Developing knowledge of limestone and dolomite sources and assessment of suitability for calcination in vertical kilns in Southern Africa

Authors

Potgieter, EM and Gaylard, JM
School of Chemical and Metallurgical Engineering
University of the Witwatersrand
Johannesburg

Abstract

The production of lime in modern shaft kilns of the PFR type has increased significantly over the past few years driven by the low heat consumption of these kilns together with their ability to produce lime of competitive quality. In South Africa, where lime has been produced mainly in rotary kilns since the mid–1950's, the most recent large–scale kiln project has seen the installation of two PFR kilns.

Whatever kiln type is utilised, the starting point for efficient kiln operation is knowledge – not only of the kiln fuel but especially of the limestone or dolomite used as kiln feed.

It is general practice for kiln suppliers to conduct a range of established empirical tests to assess and confirm the suitability of the kiln feed material during project design and planning. There are, however, indications in some cases that – in spite of these tests – kiln operating problems attributed to the feed stone have occurred unexpectedly during the commissioning and early operating stages.

A research project is therefore being undertaken at the University of the Witwatersrand to investigate a range of chemical and physical tests for developing knowledge of limestone and dolomite sources and for use in the assessment of suitability for vertical kiln operation. These tests include petrographic analysis and x–ray diffraction, microscopic structure examination, thermogravimetric analysis, decrepitation and compressive strength.

This is a new approach in South Africa to provide a comprehensive evaluation of lime kiln feed stone properties. The real value of this research will be realised by linking the results to actual kiln operating phenomena which are observed.